Spectroscopy of luminescent nanoparticles and interactions with organic molecules for imaging and therapy

Daniel Raphael Cooper

Department of Physics

McGill University, Montreal

April 2014

A thesis submitted to McGill University in partial fulfillment of the requirements for the degree of

Doctor of Philosophy

ACKNOWLEDGEMENTS

My sincere thanks to Prof. Jay Nadeau for welcoming me into her lab, introducing me to the wide world of nanoparticles, and helping me to navigate the oft-stormy waters of academia. This work would not have been possible without her support, guidance and patience.

Thanks of course to all the members of the Nadeau lab past and present, exemplary teammates all. My gratitude to Dr. Sam Clarke for imparting me with the knowledge of his QD synthesis wizardry, as well as Rafael Khatchadourian and Anil Kumar for their stalwart good-naturedness. Special thanks to Eve-Marie Marie Monique Dumas for sharing a comparable fondness for sushi and especially for translating the abstract for this work. My appreciation to Jenna Blumenthal, who assisted me with a zany idea one summer. Our latest incarnations have been formidable – thanks to Elaine Zhang, Lina Carlini, Devesh Bekah and Wilson Poon for rounding out the graduate students' squad, Soon Hyang Park and Olivier Amzallag for doing our dirty work, and especially Dr. Hicham Chibli for humoring me during the occasional chemistry rant and TEM marathon. Thanks to Prof. Mike Hallett and the rest of the Systems Biology Training Program for taking a chance on me and providing funding.

For the most recent work, I am grateful to Prof. Stephen Bradforth and Prof. Colin Hill for their support and guidance, and to Tyler Zhang, Marcel Georgin and Konstantin Kudinov for their fortitude during vigorous data collection at USC. Assistance with the TCSPC apparatus offered by Anirban Roy and Saptaparna Das was greatly appreciated.

I would be remiss to exclude the plethora of artists and friends who have made the last few years exceptional. In particular, the members of The Unsettlers and the staff and patrons of Grumpy's deserve special mention. Ben, Brie & Genevieve made this a better place to be. Gern f., the best bartender in the city, guaranteed a hospitable haunt. To all of the other musicians who have kept me rapt in awe – Cécile Doo-Kingué, Cindy Doire, David Simard, Gabrielle Papillon, Corinna Rose, Lisa Malachowski, Alex Silver, Sarah Jane Scouten, Jenny Berkel – keep doing what you do so well. An extra-special thanks to Dave Gurnsey and Laura Cooper for indulging my own musical fancy, and to Hadi Adel and Bob Chatelain for providing us with a venue and audience on more than one occasion.

Lastly, thanks for my incredibly supportive family. They are ever a source of comfort and goodwill.

ABSTRACT

The emergence of nanomaterials has had a profound effect on the scientific community, reflected in the ever-increasing number of dedicated 'nanojournals.' Biomedical applications of nanoparticles are numerous, and include imaging as luminescent probes or contrast agents, biosensing, drug and gene delivery and photodynamic therapy (PDT), among others. Luminescent semiconductor nanocrystals, known as quantum dots or QDs, were among the first varieties produced and remain the most popular choice for imaging due to their versatile optical properties. While it has long been recognized that QDs exhibit sensitivity to photoinduced processes involving interactions with organic molecules and oxygen species in aqueous environments, results in these complex systems are often contradictory. Two of the most popular QD compositions, CdSe/ZnS and CdTe, have redox potentials that permit interactions with relevant chemical species, frequently resulting in considerable fluctuations in their spectroscopic properties. By conjugating QDs to the small molecule electron donor dopamine (DA) and using time-resolved fluorescence spectroscopy, we have studied the dynamics governing photoenhancement of QD luminescence by biomolecule-mediated production of reactive oxygen species (ROS), implicating their involvement through oxygen deprivation and the action of antioxidants. This 'photosensitization' was further studied using electron paramagnetic resonance (EPR) and chemical assays to discern between types of ROS and the consistency of various probes. It has been proposed that dense luminescent nanoparticles could also be used in conjunction with radiation therapy to not only provide dose enhancement, but also as a means to improve delivery and indirect activation of PDT agents through scintillation energy transfer. While many scintillators have been studied in bulk for radiation detection and other purposes, the study of nanoscintillators is in its infancy. Current QD preparations, despite their notable photostability, have poor radiation hardness. Luminescent lanthanide-doped insulators are among the proposed alternatives, as they are relatively biocompatible and chemically stable. $Ce_xLa_{1-x}F_3$ is a heavy, fast scintillator that shows promise for radiation-assisted PDT, but exhibits complex luminescence mechanisms that depend highly on the crystalline quality and Ce^{3+} dopant concentration. We report novel synthesis techniques and surface chemistry for $Ce_{0.1}La_{0.9}F_3/LaF_3$ and CeF_3/LaF_3 core/shell nanoparticles, and explore their mechanisms of photoluminescence as well as energy transfer to bound and unbound photosensitizer molecules in aqueous solutions. We found that Ce^{3+} excitation efficiently relays energy to photosensitizers through a multi-step cascade, results that have important implications for the design of nanoscintillator systems.

ABRÉGÉ

L'arrivée des nanomatériaux a eu un effet profond sur la communauté scientifique, reflété par l'apparition accélérée de journaux scientifiques « nano-spécialisés ». Les applications biomédicales des nanoparticules sont nombreuses et incluent l'utilisation en imagerie entant que sondes luminescentes ou d'agent de contraste, la bio-perception, la livraison de médicament ou de gênes ainsi que pour la thérapie photo-dynamique (TPD) et autres. Des nanoparticules semiconductrices luminescentes nommées points quantiques (PQs) ont été parmi les premières variétés produites et restent le choix le plus populaire pour l'imagerie, dû à leurs propriétés optiques polyvalentes. Quoiqu'il soit reconnu depuis longtemps que les PQs soient sensibles aux procédés induits par la lumière impliquant l'interaction avec des molécules organiques et des espèces d'oxygène en environnement aqueux, les résultats dans ces systèmes complexes sont souvent contradictoires. Deux des compositions les plus populaires des PQs, CdSe/ZnS et CdTe, ont un potentiel de réduction qui permet l'interaction avec les espèces chimiques pertinentes causant souvent des fluctuations considérables de leurs propriétés spectroscopiques. En conjuguant les PQs à la petite molécule donneuse d'électron dopamine (DA) et en utilisant la spectroscopie de fluorescence résolue en temps, nous avons étudié les dynamiques gouvernants l'amélioration de la luminescence des PQs causée par la production d'espèces réactives d'oxygène (ERO) provenant de la médiation de biomolécules, démontrant ainsi leur implication par la privation d'oxygène et l'action d'antioxydants. Cette « photosensibilization » fût étudiée plus en profondeur par résonance paramagnétique électronique (RPE) et par analyse chimique afin de distinguer les différents types d'ERO et l'uniformité d'une variété de sondes. Il a été proposé que les nanoparticules luminescentes denses pourraient être utilisées avec la radiothérapie pour non seulement bonifier l'effet de la dose mais aussi afin d'améliorer la livraison et d'activer indirectement les agents de la TPD à l'aide d'un transfert d'énergie par scintillement. Quoique les scintillateurs aient été amplement étudiés pour la détection de radiation et autres raisons, la recherche à ce sujet en est encore à ses débuts. Malgré la photostabilité notable des préparations courantes de PQs, leur résistance à la radiation est faible. Les isolants luminescents aux lanthanides font partie des alternatives proposées puisqu'ils sont relativement biocompatibles et stables chimiquement. $Ce_xLa_{1-x}F_3$ sont des scintillateurs lourd et rapide et sont prometteurs pour la TPD assistée par radiation, mais présentent des mécanismes de luminescence complexe qui dépendent grandement sur la qualité cristalline de la particule et la concentration de Ce^{3+}. Nous présentons une nouvelle technique de synthèse et une nouvelle chimie de surface pour les nanoparticules $Ce_{0.1}La_{0.9}F_3/LaF_3$ et CeF_3/LaF_3 et nous explorons leurs mécanismes de photoluminescence ainsi que le transfert d'énergie pour lier et défaire des molécules photosensibilisatrices en solution aqueuse. Nous avons trouvé que l'excitation de Ce^{3+} transfert l'énergie vers les photosensibilisateurs de façon efficace par une cascade de plusieurs étapes. Ces résultats ont des implications importantes pour la conception de systèmes nanoscintillants.

TABLE OF CONTENTS

LIST OF TABLES AND FIGURES

CONTRIBUTION OF AUTHORS

The content of this thesis is adapted from published or submitted manuscripts in which the student made a substantial contribution. Unless noted below, the experiments described are the sole work of the authors. Additional contributions are described in the acknowledgements of the relevant chapters, but will be reiterated here. In most cases, J. Nadeau (McGill University, Montreal) had significant input into the experimental design and implementation.

Chapter 2. Synthesis of QDs was performed in conjunction with Samuel J. Clarke (McGill University, Montreal); preparation of QDs and bioconjugates was performed in conjunction with Lina Carlini and Jay L. Nadeau (McGill University, Montreal); TCSPC measurements were performed in conjunction with Diana Suffern and Rupesh Parbhoo (University of Southern California, Los Angeles, CA) and Lina Carlini and Jay L. Nadeau (McGill University, Montreal); analysis was performed in conjunction with Stephen E. Bradforth (University of Southern California, Los Angeles, CA), Lina Carlini and Jay L. Nadeau.

Chapter 3. Synthesis of QDs and preparation of bioconjugates was performed in conjunction with Jay L. Nadeau; EPR measurements were performed in conjunction with Nada M. Dimitrijevic (Argonne National Laboratory, Lemont, IL); bioassays, imaging and analysis were performed by Jay L. Nadeau and the student.

Chapter 4. Synthesis of LnNPs, surface chemistry and photoluminescence experiments performed by the student.

Chapter 5. Synthesis of LnNPs and preparation of bioconjugates was performed by the student; TEM images were acquired by Hicham Chibli and David Liu (McGill University, Montreal) under the direction of the student; TCSPC measurements were performed in conjunction with Konstantin Kudinov (University of Southern California, Los Angeles, CA); analysis was performed in conjunction with Pooja Tyagi (McGill University), Stephen E. Bradforth and Jay L. Nadeau.

Chapter 6. Synthesis of LnNPs was performed by the student; scintillation measurements were performed by Konstantin Kudinov, Colin K. Hill and Stephen E. Bradforth (University of Southern California, Los Angeles, CA); CFAs performed by Tyler Zhang, Colin K. Hill and the student (preliminary).

Chapter 1

Introduction

1. Introduction

1.1 Introduction

Over the past few decades, nanotechnology has become an integral part of many areas of research. Nanoscience is primarily concerned with the study of materials at length scales of 1-100 nm – in this nanoscale regime, the properties of a material may change significantly compared to the bulk, often due to the increased influence of surface effects. Concomitant developments in the understanding of nanoscale behaviors and advances in fabrication and characterization techniques have fostered the rapid expansion of nanoscience. A broad distinction can be made between nanostructures that are grown on or patterned from substrates, such as those used in many physics applications, and nanoscale 'particles' produced and suspended in solution as colloids.

The application of nanotechnology to biology and medicine results in multidisciplinary research at the forefront of biology, chemistry and physics. Colloidal luminescent nanoparticles offer a valuable alternative to traditional small molecule and protein fluorescent probes, providing distinct advantages for imaging. With relatively simple chemical strategies, nanoparticles can be modified with a variety of molecules that provide a broad range of additional functionalities like targeting, biosensing, energy and charge transfer, drug or small molecule delivery, or often, a combination. Though nanomaterials have been swiftly adopted for such purposes, their interactions with biological species are complex and incompletely understood.

Spectroscopy, the study of interactions between radiation and matter, is instrumental for the understanding of nanomaterials. Because of the high surface to volume ratio of nanoparticles and the associated sensitivity to their local environment, many interactions manifest as distinct changes in spectroscopic measurements at the single-particle and ensemble levels.

This thesis will focus on the photophysical properties of luminescent nanoparticles, as well as their behaviors in the presence of or conjugated to organic molecules that are relevant to targeting, imaging and/or therapeutic applications. The purpose of this introductory chapter is to provide background relevant to the published work in the following two chapters, including basic principles of photoluminescence, some common and advanced spectroscopic techniques, and fundamental theory of luminescent semiconductor nanoparticles.

1.2 Principles of photoluminescence and spectroscopic techniques

Luminescent materials, sometimes referred to as fluorophores for organic compounds or phosphors for inorganic compounds, are those that emit light in response to chemical or physical stimuli other than heat. Here we will focus on luminescence in response to absorption of light, particularly **fluorescence**, which results from electronic relaxation of the excited singlet state of a material to the ground state. There are a number of associated physical phenomena which can be succinctly presented by a Jablonski diagram, as shown in Figure 1.1 for a typical organic fluorophore. An electron in the ground state of the fluorophore (S_0) can absorb light energy to be promoted to an excited singlet state (S_1, S_2,…S_n), whereupon it first loses energy through vibrational relaxation, also known as internal conversion, relaxing to the lowest vibrational level of the first excited state S_1. This process typically occurs within a picosecond, with the excess vibrational energy converted into heat. This state is relatively long-lived, on the order of nanoseconds, and from this point, a number of things may occur. The first is relaxation to the ground state either with (radiative) or without (nonradiative) emission of a photon. Radiative relaxation typically only occurs with significant yield from the lowest excited state of a given multiplicity, a principle known as Kasha's rule. For this reason, the emission wavelength is typically independent of the excitation wavelength. Nonradiative relaxation occurs through

quenching by high-energy vibrations of solvents or other organic species, or more complex mechanisms.

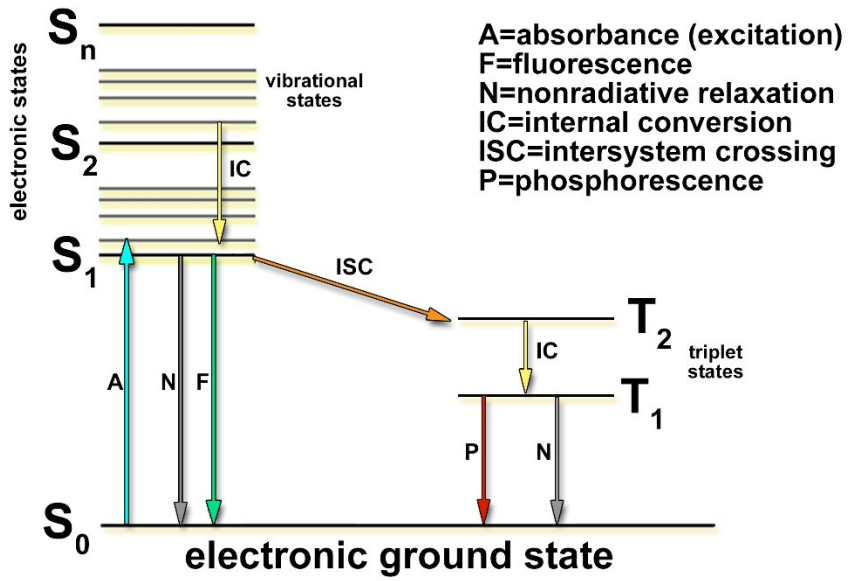

Figure 1.1 Jablonski diagram illustrating the radiative and nonradiative relaxation pathways and rates for a typical fluorophore after excitation by light. Absorption of light (A) excites an electron from the ground state (S_0) to a higher energy state (S_1, S_2,…S_n), whereupon it will undergo vibrational relaxation or internal conversion (IC) to the lowest excited state. From there, de-excitation can occur through non-radiative (N) or radiative pathways, including fluorescence (F) which occurs through singlet state relaxation, or phosphorescence (P), which may occur after intersystem crossing (ISC) to an excited triplet state (T_1, T_2,…T_n).

If the excited singlet state instead transitions to an excited triplet state (changing the spin multiplicity), it is referred to as intersystem crossing. In most simple fluorophores, this process is unlikely to occur. One notable exception is the class of molecules referred to as 'photosensitizers,'

which are characterized by their high probability of intersystem crossing, allowing them to readily react with water, biomolecules, or molecular oxygen, which is unusual for existing in a stable triplet state. Note that a high triplet yield generally means a low fluorescence quantum yield, as the processes are competitive, though delayed fluorescence may also occur if intersystem crossing occurs a second time, restoring the excited singlet state. Radiative recombination from the excited triplet state is referred to as **phosphorescence**, and occurs at microsecond to second time scales. Photosensitizers and photosensitization will be discussed in more detail in the following chapters.

Basic fluorescence properties are encompassed by a handful of physical values[1]. The spectral difference between the absorption and emission band maxima of the same electronic transition is referred to as the **Stokes shift**. Importantly, this difference enables isolation of excitation and emission wavelengths using dichroic mirrors in simple optical systems, one of primary principles of fluorescence microscopy. The **extinction coefficient** ε is a measure of how strongly light is absorbed by a species at each wavelength and is a characteristic of the material itself. It is typically reported as molar absorptivity (in units of $L \cdot mol^{-1} \cdot cm^{-1}$) or mass absorptivity (in units of $L \cdot g^{-1} \cdot cm^{-1}$). The **fluorescence quantum yield** (QY) Φ is defined as the ratio of the number of photons emitted by fluorescence to the number of photons absorbed, giving the probability of photon emission per excitation, or emission efficiency. Experimental determination of QY values is routinely done by comparison to a reference substance with a well-established QY, typically having been determined with an integrating sphere. Note that many molecules and other materials can absorb light without any resultant emission. The product of the quantum yield and the extinction coefficient gives the **brightness**, valuable for quantitative comparison of materials and evaluating their usefulness for imaging. The **fluorescence lifetime** τ is the characteristic time constant of the time-resolved fluorescence decay – in some cases

monoexponential, as with some isolated fluorophores, but often multiexponential in complex systems, as will be discussed in Chapters 2-5.

1.2.1 Absorption and steady-state fluorescence

The most basic spectroscopic measurements include ultraviolet-visible (UV/vis) absorption as well as steady-state fluorescence, both of which are routinely acquired in lab settings using fairly simple photometers. Photometers generally consist of one or more continuous light sources such as xenon flash lamps; monochromators to select narrow wavelength bands; and CCD or PMT detectors, covering excitation and emission wavelengths of ~200-800 nm. Absorbance and fluorescence values are shown as spectra with an amplitude as a function of wavelength.

The absorbance of a liquid substance, as measured by a typical spectrophotometer, is a unitless quantity defined as the negative logarithm of the fraction of light transmitted through a sample, I/I_0, where I_0 is the intensity of incident (excitation) light and I is the intensity of the detected light.

$$A = -\log(I/I_0) = \varepsilon l c \tag{1.1}$$

This relation is known as the Beer-Lambert law. The right-hand side relates the absorbance value to a concentration c of absorbers with extinction coefficient ε for a path length l. This linear relationship assumes that the absorbers do not interfere with each other and generally holds true for values of A < 2 (corresponding to 1% transmission), though in practice values of 0.2-0.8 are typically preferred. If either the concentration c or absorptivity ε of a sample is known and the other unknown, the unknown value can easily be determined by measuring the absorbance A with a known path length (typically 1 cm). The absorbance is sometimes referred to as optical density, or OD.

Special care must be taken for absorbance and fluorescence measurements in the ultraviolet ($\lambda < 400$ nm), as many solvents and organic molecules (including the polymers that comprise many cuvettes and multiwell plates) have significant absorption and possible fluorescence in this region, as will be discussed in Chapters 4-6 and Appendix B.

1.2.2 Time-resolved fluorescence and energy transfer

While steady-state fluorescence measurements provide essential information, time-resolved measurements often provide additional insight into photoluminescence mechanisms and the factors that affect them. The QY of an emitter can be considered as the ratio of radiative relaxation rate k_r to the sum of radiative and all nonradiative rates Σk_{nr}, which can also be equated to the product of the radiative rate and the fluorescence lifetime τ:

$$\Phi = \frac{k_r}{k_r + \sum k_{nr}} = k_r \tau \tag{1.2}$$

From this relationship, it can be seen that if the radiative rate is unchanged, changes in the time-resolved fluorescence lifetimes are indicative of changes to nonradiative relaxation channels, either through quenching, energy or charge transfer, or a combination. In the case of Förster resonance energy transfer (FRET), the efficiency of the transfer is given by[2]:

$$\eta = \frac{k_{ET}}{k_{ET} + k_r + \sum k_{nr}} = \frac{1}{1 + (d/R_0)^6} \tag{1.3}$$

where k_{ET} is the rate of energy transfer. R_0 is referred to as the "Förster distance" and the definition can be found in Section 4.3.2. FRET is a nonradiative process that arises from dipole-dipole coupling of a fluorescent donor at a distance d to an acceptor (which need not be luminescent). It is not of central importance to the first half of this work, but will be further discussed in Section 4.3.2.

Time-correlated single photon counting (TCSPC) is a technique for time-resolved fluorescence measurements that delivers excitation via ultrashort pulse lasers, providing picosecond to nanosecond resolution of the dynamics of a system. Assuming essentially simultaneous excitation of a collection of emitters, they will subsequently fluoresce at different time points. By collecting the individual photons at known points, a decay curve can be constructed that has some exponential dependence. As many pulses are delivered to the sample, a histogram with time bins is produced, reflecting the excited state lifetime associated with radiative relaxation. While fluorophores typically have simple decay patterns, nanoparticles often show complex behaviors that cannot be discerned from steady-state measurements (see Section 1.5), making TCSPC an essential tool for their study. The design of a standard apparatus is shown in Figure 1.2, and the specifics of the experimental setup used in this work are provided in the appropriate sections.

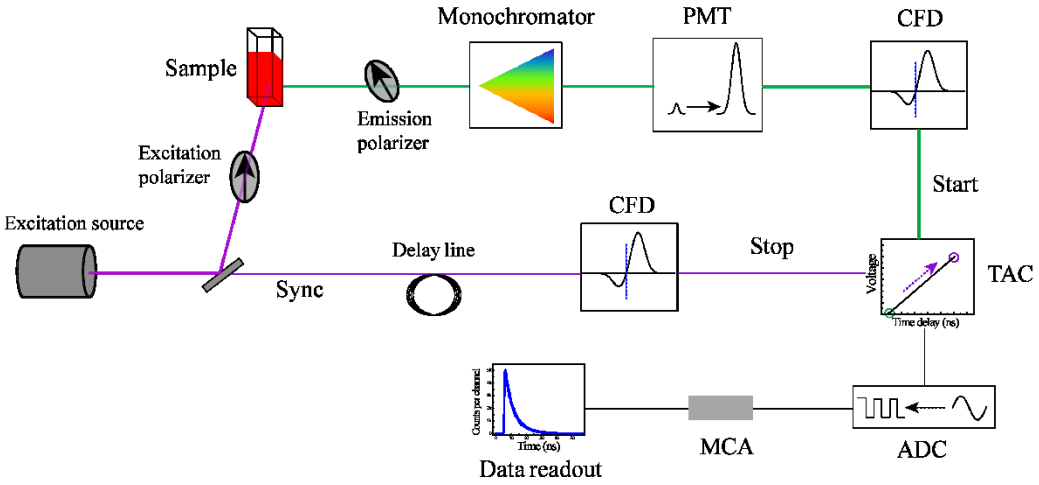

Figure 1.2 Schematic of a TCSPC setup. PMT = photomultiplier tube, CFD = constant fraction discriminator, TAC = time-to-amplitude converter, ADC = analog-to-digital converter, MCA = multi-channel analyzer.

1.2.3 Electron paramagnetic resonance

Electron paramagnetic resonance (EPR) spectroscopy is a technique to investigate the presence of unpaired electrons, and is analogous in principle to nuclear magnetic resonance (NMR) with excited electron spins rather than atomic nuclei. In the presence of an external magnetic field, the magnetic moments of unpaired electrons align either parallel or antiparallel to the field (with spin quantum numbers m_s = -½ or ½ respectively). Due to the Zeeman effect, the alignments are separated by an energy E proportional to the strength of the field B_0 and can be reversed by absorption or emission of a photon with energy equal to the difference:

$$h\nu = \Delta E = g_e \mu_B B_0 \tag{1.4}$$

where g_e is the g-factor for a free electron (g_e = 2.0023) and μ_B is the Bohr magneton. The basic principle is illustrated in Figure 1.3. This forms the guiding principle of EPR – detecting unpaired electrons by continuously exposing a sample to electromagnetic radiation (typically microwaves) in the presence of a magnetic field and measuring the absorbance. Either the wavelength or the field can be varied – typically the field is varied for a fixed radiation wavelength. Unpaired electrons do not occur in isolation, and in practice there are confounding factors that affect the energy levels, including ensemble effects and spin-orbit coupling with atomic nuclei.

Because free radicals of interest, such as reactive oxygen species, are often short-lived, spin traps can be employed to provide stable reporters of cumulative radical production. Spin traps are organic molecules that possess nitrone groups that can react with free radicals to either generate or extinguish stable paramagnetic nitroxide spin adducts that can then be evaluated with EPR with greater temporal lenience.

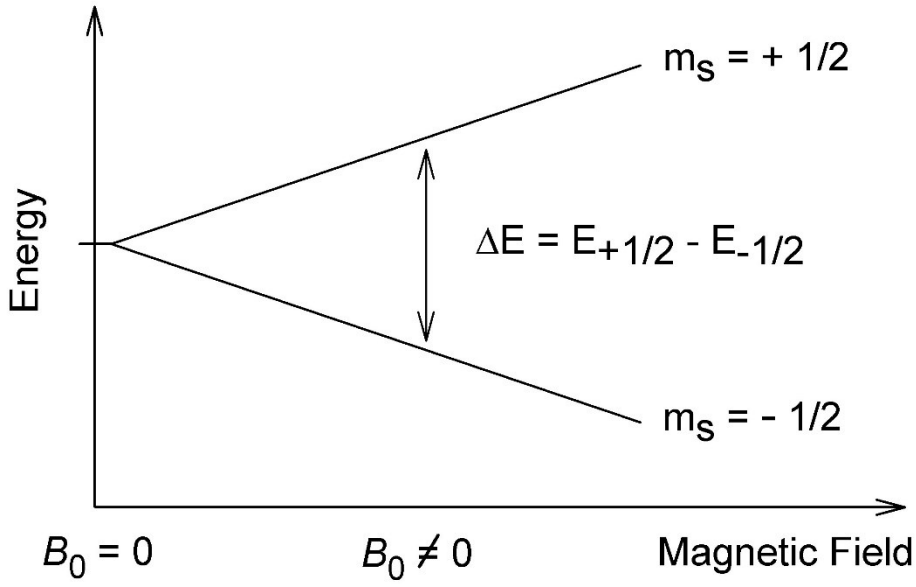

Figure 1.3 The Zeeman effect for unpaired electrons in an external magnetic field. As the field strength increases, the energy difference between electrons with magnetic moment aligned either parallel (m_s = -½) or antiparallel (m_s = ½) to the field increases. Absorption of a photon of energy equal to the difference manifests as an absorbance feature in the EPR spectrum.

1.3 Fluorescent probes

While there are many fluorescent molecules that can label specific cell components, they are often toxic to the cell. The advent of novel fluorescent probes has had a profound effect on cell and molecular biology studies through improved imaging possibilities. In 1962, Osamu Shimomura and colleagues reported the discovery and properties of a green fluorescent protein (GFP) that had been isolated from *Aequorea victoria* jellyfish[3]. Several research groups, including that of Martin Chalfie, pursued the adaptation of GFP into a useful bioprobe[4, 5, 6, 7]. When the crystal structure of GFP was reported in 1996[8, 9], elucidating the nature of the chromophore and its environment, it became possible to make drastic improvements to the properties of GFP and pave the way for the

development of a library of multicolored variants. For the discovery and development of GFP, Osamu Shimomura, Martin Chalfie and Roger Y. Tsien were awarded the Nobel Prize in Chemistry in 2008. GFP and its variants have since become ubiquitous in biology research, owing to their biocompatibility and ability to "label" proteins of interest through basic molecular biology techniques, greatly enhancing the potential for imaging biological targets through fluorescence microscopy[10]. Many of the latest variants have high extinction coefficients (between 40,000 and 100,000 $M^{-1}cm^{-1}$) and quantum yields (>0.5), but can be hindered by their considerable bulk (~27 kDa) and low photostability.

Colloidal luminescent nanoparticles (NPs) have emerged as an alternative to FPs for applications where probe size control, tunability of optical properties, large extinction coefficients and/or photostability are paramount. Early efforts focused on semiconductor nanoparticles, commonly known as quantum dots or QDs[11], which have since become widespread. Other recently-developed inorganic compositions such as doped insulators allow for less conventional imaging possibilities, such as upconversion (photoluminescence with anti-Stokes shift) or scintillation (radioluminescence), which will be discussed further in Chapters 4-6. Most recently, organic NPs such as "graphene QDs" (GQDs) or "C-dots" have emerged[12, 13, 14], which display excitation-dependent emission and excellent biocompatibility.

1.4 Quantum dots

Semiconductor nanocrystals that are small enough to experience three-dimensional quantum confinement of excitons (electron-hole pairs) are colloquially referred to as quantum dots, or QDs. A variety of colloidal QD compositions can be manufactured, including II-VI materials such as CdS and ZnO, IV-VI materials such as PbS and PbSe, III-V materials such as GaN, InAs and InP, as well as ternary alloys such as CuInS and CdSeS. Each composition possesses distinct properties,

and taken together, QDs are perhaps the most well-studied classification of nanoparticle. The majority of colloidal QD research has focused on direct gap II-VI semiconductors consisting of metal chalcogenides such as CdSe, CdTe and ZnS. Typically, QD cores are protected and 'passivated' by a shell consisting of a different material. CdSe QD cores are typically modified with ZnS shells that have the same wurtzite (hexagonal) crystal structure as the core, reducing lattice mismatch. The conduction and valence band edges of the CdSe core lie within the band gap of the ZnS shell, forming what is known as a "Type I" core/shell structure. "Reverse Type I" refers to a structure with the core having a band gap wider than the shell, and with the shell band edges lying within those of the core. In "Type II" structures, the band edges are offset, with the core edges lying either higher or lower than those of the shell. A notable exception to the typical core/shell structure is CdTe, which maintains its brightness when modified for suspension in aqueous solution. In this work, we will only be concerned with Type I structures or 'bare core' QDs. The Type I shell provides a barrier that is transparent to the emission from the QD core – by passivating dangling bonds on the core surface, the QY can be improved, accompanied by a red shift of the core emission. The physical shielding is also important for preventing aggregation and photo-induced anodic decomposition of the core, as the release of Cd^{2+} ions has been thoroughly implicated in the cytotoxicity of QDs that contain it.

Reference [15] provides a thorough overview of the first decade of QD development for biological applications. While cadmium-based QDs have proven helpful for many applications, their toxicity remains a terminal deterrent to their translation into clinical environments. Many alternative compositions of luminescent NPs have emerged in recent years, including a variety of Cd-free QDs such as InP/ZnS (currently under investigation by members of our lab[16, 17]).

1.4.1 Physical & optical properties

The defining characteristic of QDs is that their optical properties are directly related to their physical dimensions. In a bulk semiconductor of band gap E_g, excitation with light of energy $h\nu > E_g$ results in the excitation of an electron from the valence band to the conduction band, leaving a positively-charged localized region (hole). Electrons and holes can function as charge carriers, while electron-hole pairs bound by Coulombic attraction are referred to as excitons. The creation of an exciton is also associated with a spatial separation between the pair, known as the **exciton Bohr radius**. This value is influenced by the effective mass of the electron and hole as well as the relative permittivity of the material. As the physical dimensions of a single crystal approach the exciton Bohr radius, quantum confinement effects become significant and the properties of the material become highly size-dependent. For CdSe (bulk band gap 1.74 eV), the radius is 53 Å; for CdTe (bulk band gap 1.44 eV), it is 75 Å – so CdTe QDs approach the Bohr radius value at larger sizes than CdSe. Confinement results in properties that begin to resemble those of single molecules. In a 3D bulk material, the electron density of states is continuous and proportional to the square root of the energy:

$$\rho_{3D}(E) = \left(\frac{m_e}{\hbar^2}\right)^{3/2} \frac{\sqrt{2E}}{\pi^2} \tag{1.5}$$

where m_e is the effective electron mass. In a 0D structure such as a QD, with quantum confinement in all spatial dimensions, the exciton can be likened to a 'particle in a box.' The density of states then becomes discrete and quantized with quantum numbers n, m, l[18]:

$$\rho_{0D}(E) = 2\sum_{n,m,l} \delta(E - \varepsilon_{n,m,l}) \tag{1.6}$$

Figure 1.4a shows a representation of the effect of quantum confinement on the density of states for idealized 3D, 2D (quantum wells), 1D (quantum wires) and 0D systems. The additional

confinement energy results in a progressive broadening of the band gap compared to the bulk as the size of the QD decreases. An analytical approximation for the lowest excited 1*s* state (the first exciton absorbance peak) was reported by Brus in 1990[19]:

$$E_{1s}(r) = E_g + \frac{\hbar^2\pi^2}{2r^2}\left(\frac{1}{m_e} + \frac{1}{m_h}\right) - \frac{1.8e^2}{\varepsilon_r r} + \cdots \quad (1.7)$$

where E_g is the band gap of the bulk semiconductor, r is the QD radius, m_e and m_h are the effective electron and hole masses, and ε_r is the relative permittivity of the material. The second term is the quantum localization energy and is proportional to $1/r^2$. The third term describes the Coulomb attraction between an electron-hole pair and has a $1/r$ dependence. These terms provide an estimate of the band gap of a QD in the strong confinement regime. In practice, the dependence of the emission wavelength on QD size is more complex, and is shown for some common QD compositions in Figure 1.4b. As the band gaps of bulk CdSe and CdTe are near the low energy limit of the visible spectrum, QD preparations show emissions that span much of the visible range, emitting at higher energies (lower wavelengths) as the QD size decreases. The absorbance of QDs is very broad and the emission is narrow and symmetric, as shown in Figure 1.4c.

Seminal work by the group of Xiaogang Peng provided an experimental basis for easy characterization of CdSe and CdTe QDs by establishing simple relationships to estimate the QD diameters and extinction coefficients from the absorbance spectra[20]. Using the wavelength value λ (in nm) corresponding to the first excitonic absorbance peak, QD diameters (in nm) are estimated according to the following:

$$\text{CdSe: } D = (1.6122 \times 10^{-9})\lambda^4 - (2.6575 \times 10^{-6})\lambda^3 + (1.6242 \times 10^{-3})\lambda^2 - (0.4277)\lambda + 41.57 \quad (1.8)$$

$$\text{CdTe: } D = (9.8127 \times 10^{-7})\lambda^3 - (1.7147 \times 10^{-3})\lambda^2 + (1.0064)\lambda - 194.84 \quad (1.9)$$

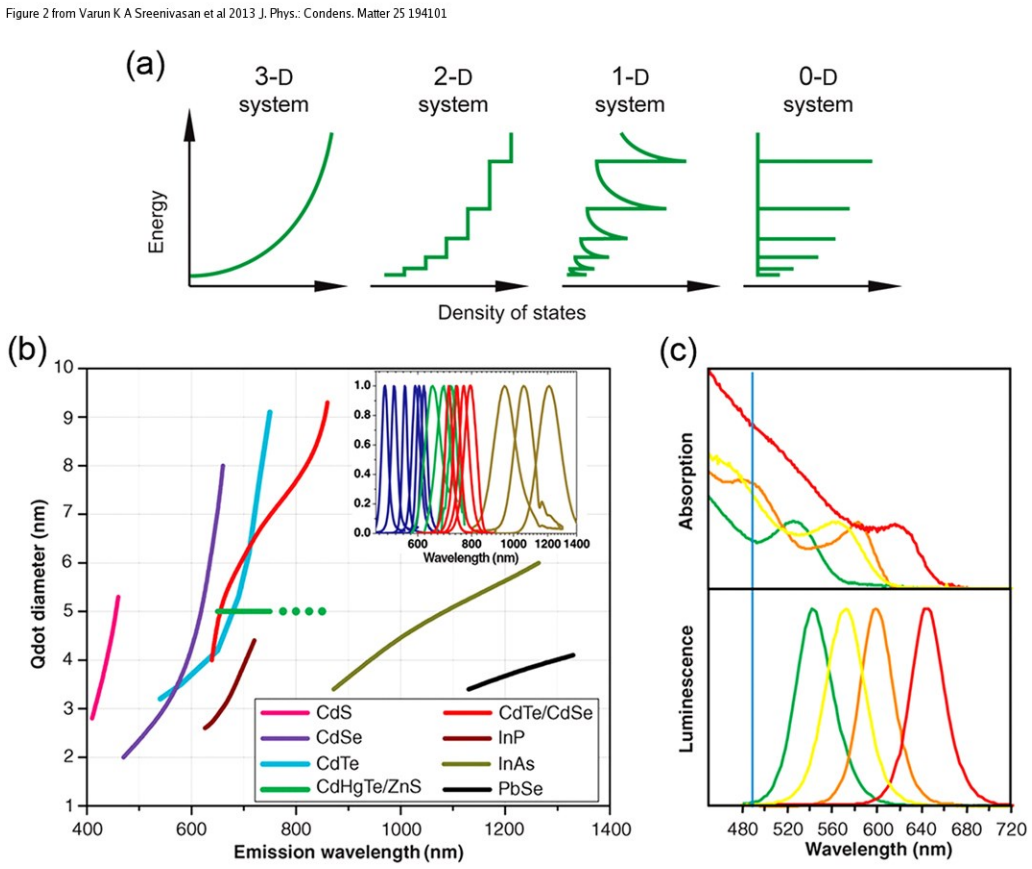

Figure 1.4 Some electronic and optical properties of QDs. (a) Electron density of states for idealized semiconductors with varying confinement. Note the 3D (bulk) density of states is continuous, whereas the 0D (QDs) is discrete, reminiscent of atomic energy levels. (b) QD emission wavelengths with varying sizes for a selection of materials. As QDs become smaller, the confinement potential results in higher energy emission. (c) Characteristic absorption and photoluminescence spectra of QDs of different sizes. Reprinted with permission from reference [21].

The extinction coefficients ε (λ) (in units of $M^{-1}cm^{-1}$, with D in nm) can then be determined with the simple relations:

$$\text{CdSe: } \varepsilon = 5{,}857 \cdot D^{2.65} \tag{1.10}$$

$$\text{CdTe: } \varepsilon = 10{,}043 \cdot D^{2.12} \tag{1.11}$$

In combination, these relations allow for straightforward estimation of two basic properties of QDs and QD concentrations by using the Beer-Lambert law. Given the typical sizes of QDs, it is apparent that they have ε values that are comparable to or exceed most FPs (typically >80,000 $M^{-1}cm^{-1}$).

An interesting behavior of QDs is fluorescence intermittency, or **blinking**[22]. It is especially relevant for single-particle tracking and quantum information processing purposes and has attracted a considerable amount of interest in the past several years[23, 24, 25, 26, 27, 28, 29, 30, 31, 32, 33], though the mechanisms have yet to be fully unraveled. It is related to competition between radiative and nonradiative relaxation processes, believed to arise from the concurrent formation of multiple excitons which ultimately result in the ejection of an electron or hole, creating a charged state of the QD. If new excitons are then formed, they will decay through fast, nonradiative pathways, known as Auger recombination. When the neutral state of the QD is restored, so too is its tendency to fluoresce. Recently, it has been proposed that surface-associated 'hot electron' traps constitute a distinct second mechanism[34, 35, 36]. While blinking is not of central importance to this work, it is worthwhile to note that the small thiol molecule β-mercaptoethanol has been used with QDs as an "anti-blinking" reagent, the mechanisms of which have been recently studied by our group[37, 38].

1.4.2 Surface chemistry & bioconjugation

Synthesis of colloidal QDs is ordinarily accomplished through organometallic routes, where organometallic precursors are dissolved in a system comprised of high-boiling point organic solvents and hydrophobic surfactants. These methods result in highly crystalline, monodisperse nanocrystals with excellent optical properties[39]. Under these conditions (as-synthesized, in organic

solvent), the QDs are highly stable and fluoresce with high efficiency for years. For most investigations that do not include a biological component, QDs are simply used as such. Monodispersity is of particular importance to investigations of fundamental properties and mechanisms, due to their considerable dependence on the QD size. For use in aqueous environments, the QD surface coating must be modified or replaced. Synthesis of QDs directly in aqueous systems is also possible[40, 41, 42], though these routes provide less reliable control over the crystallinity, size and luminescence of the QDs. For this reason, it is often preferred to synthesize QDs through organometallic routes, and then make them water-dispersible through ligand exchange or other reactions[43]. Ligand exchange involves mixing the organic-phase QDs (coated with organophosphates such as trioctylphosphine and/or fatty acids such as oleic acid) with an aqueous solution containing a hydrophilic ligand, typically a small thiol molecule like mercaptoacetic acid (MAA, aka thioglycolic acid)[44], 3-mercaptopropionic acid (MPA)[45] or mercaptosuccinic acid (MSA, aka thiomalic acid)[46]. A large excess of these ligands will replace the hydrophobic surfactants by the law of mass action, with the reduced thiol groups forming strong bonds with the QD surface and "solubilizing" the QDs. This also allows for control over the terminal functional groups of the QD coatings, which determine the potential for bioconjugation reactions and influence other biological interactions. The ligands listed above possess terminal carboxylic acid groups, but similar ligands can be chosen for positively-charged amine functionality (mercaptoethylamine[47], aka cysteamine) or zwitterionic options with both amine and carboxylic acid groups (cysteine[48] or penicillamine[49]). While the surface charge itself has further implications for biological environments, these ligands all provide a compact coating for the QDs, and do not substantially increase the hydrodynamic size beyond that of the QD itself. One drawback with such charge-stabilized QDs is their sensitivity to pH and ionic strength in

solution. Additionally, replacement of native surfactants with thiol ligands and transfer to aqueous solution often results in decreased QY and photostability of the QDs[45, 50]. Bidentate ligands such as dihydrolipoic acid (DHLA) can provide enhanced long-term colloidal stability due to their high affinity for the QD surface[51, 52, 53], but can be less effective at preventing interactions with other molecules because of their lower density, providing less charge and steric hindrance[54]. A depiction of common surfactants and ligands is shown in Figure 1.5.

Alternatives to direct ligand exchange include encapsulation of the as-synthesized QDs with amphiphilic polymers[55, 56] as well as silanization, the formation of a shell of crosslinked silane molecules around the QD[57]. While these methods also confer water-dispersibility along with high stability, the coatings are substantially larger, increasing the hydrodynamic size of the QDs significantly and creating a larger barrier for surface-attached molecules. For protection against non-specific interactions, these coatings are favorable, but not necessarily when investigating energy and electron transfer of the QD to surface molecules. For many biological purposes, there are also distinct advantages to keeping the NPs as compact as possible[58].

Pendant functional groups allow for the attachment of a variety of molecules through the formation of covalent bonds, a process known as bioconjugation. A common strategy for bioconjugation using NPs is the formation of an amide or peptide bond between an amine and carboxylate group, a dehydration (condensation) reaction that can be mediated by a class of crosslinkers called carbodiimides. For water-dispersible NPs, the most popular choice is the water-soluble zero-length crosslinker 1-ethyl-3-(3-dimethylaminopropyl)carbodiimide (EDC), which has been used to conjugate small molecules for sensing, targeting and/or photosensitization[46, 59, 60, 61, 62], peptides[63], proteins[64], and antibodies[65] to QDs.

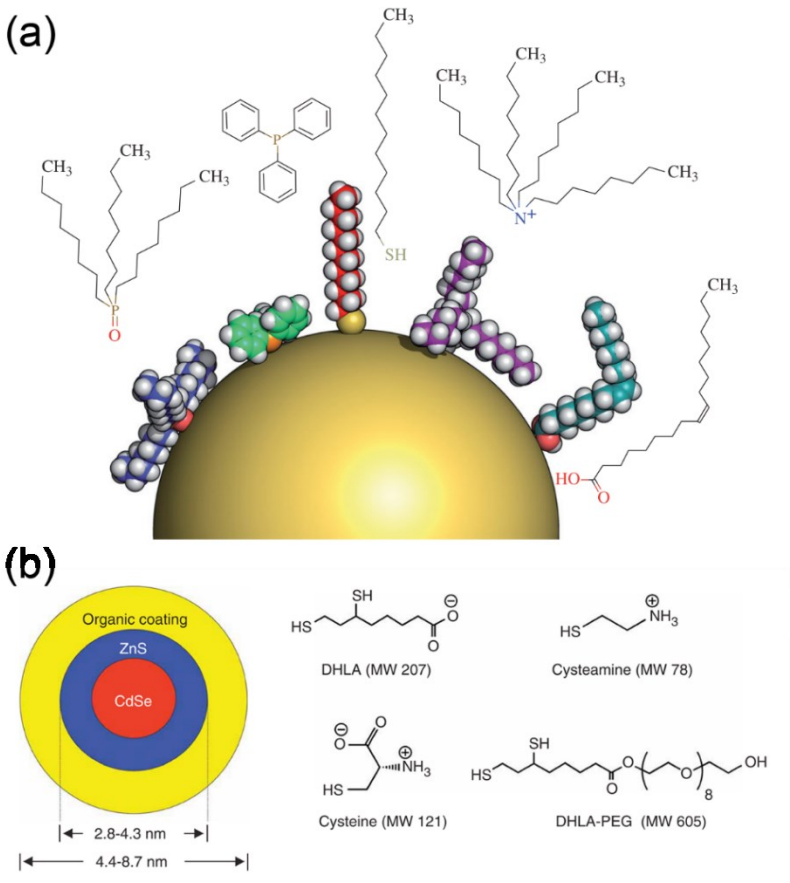

Figure 1.5 Cartoon depiction of some common colloidal QD surface coatings. (a) Hydrophobic coatings that function as surfactants for organometallic QD synthesis, coordinating the metal surface in a variety of ways. Shown left to right are trioctylphosphine oxide (TOPO), triphenylphosphine (TPP), dodecanethiol (DDT), tetraoctylammonium bromide (TOAB) and oleic acid (OA). Reprinted with permission from reference [66]. (b) Selected monodentate and bidentate hydrophilic thiol ligands for "solubilizing" QDs. Ligands bind the QD surface through the thiol groups, and can provide a range of functionalities to the QD, including terminal amines (cysteamine), carboxylates (DHLA, and others like MPA) or both (cysteine). PEGylated ligands provide additional stabilization and biocompatibility to the QDs. Small thiol ligands do not substantially increase the hydrodynamic size of QDs. Reprinted with permission from reference [58].

1.5 Context and motivation

In the years preceding the research conducted in Chapters 2 & 3, there was a remarkable boom in the study of QDs applied to biological systems as imaging probes, biosensors and to a lesser extent for possible therapeutic applications[11, 15, 67, 68, 69, 70, 71, 72, 73, 74, 75, 76]. QDs were investigated for optical applications ranging from single molecule and organelle tracking[77], to *in vivo* cancer targeting and imaging[69]. Though they have easily proven to be valuable alternatives to typical fluorescent dyes, quantitative evaluation of QDs exposed to physiological conditions requires careful consideration. Though the total ionic strength/osmolarity remains fairly constant in biological compartments, there are considerable variations in the ionic composition and pH/oxidation potential of different structures, associated with both normal and pathological conditions, in addition to the myriad physical and chemical influences of biomolecules. Tailoring QDs to specific purposes often involves significant modification of their surface coatings, which can complicate prediction of photophysical behaviors. The photoluminescence of QDs is known to be exquisitely sensitive to a number of factors, particularly trap states, which frequently act as fast non-radiative de-excitation channels for photogenerated charge carriers.

Trap states arise in a number of ways, and can strongly interact with photogenerated electrons and holes due to the delocalized nature of excitations in QDs. Bulk-type traps (those found within the volume of a crystal) occur from impurities, point defects and localized stresses, and can occupy energy levels spanning the band gap of the material and into the valence/conduction bands. These and other trap types occur at the material surface, and are of critical importance to nanoscale crystals. Early reports suggested dangling bonds of surface ions as the origin of localized trap states for photogenerated electrons and holes[19, 78]. In practice, colloidal QDs are passivated to a large extent by ligands, such as charged or polar organic

molecules that covalently bind the surface ions. Surfactant ligands such as TOPO (Fig. 1.5a) are known to coordinate to Cd sites and passivate their electron trapping tendency, while electrons from surface Se dangling bonds were suggested to lead to mid-gap or "deep trap" states that compete with band-edge recombination in favor of lower energy deep trap emission, by first capturing photogenerated holes (resulting in fast, ps lifetime emission) followed by excited state electrons, leading to a secondary long-lived emission (up to μs lifetimes)[79]. Long-lived band edge recombination may also result from nominally spin-forbidden decay of excited state electrons to the so-called "dark exciton" triplet state, with emission that is spectrally nigh-indistinguishable from spin-allowed state recombination. The existence of "dark exciton" states has been known since the early days of QD research[80], though the full extent of the underlying mechanisms is the subject of ongoing investigation.

For use in aqueous environments, hydrophobic QD surface coatings must be modified or replaced by ligands that can confer water-dispersibility to the QDs. Curiously, a variety of thiol ligands were found to have profound and drastically differing effects on different QD compositions[81] – the PL of bare core CdSe QDs (without a passivating ZnS shell layer) was strongly quenched by "solubilization" with a number of small thiol molecules, whereas the PL QY of CdTe QDs was enhanced[82]. This was attributed to the shifted positions of the valence band edges of each QD type relative to the redox potential of the thiol ligands – CdTe having a higher band edge position that prevents trapping of photogenerated holes at the surface by the ligands.

The photoluminescence of colloidal QDs is thus known to be highly sensitive to some aspects of their surroundings, particularly under illumination[83], dynamics that are further obfuscated in biological environments[84, 85, 86]. CdSe QDs are often modified with an epitaxial ZnS shell that is intended to passivate core surface traps associated with dangling bonds and/or ligands,

and to prevent photo-oxidation[87]. While ZnS shells have an overall beneficial effect on radiative recombination probability, their surface coverage is often irregular and they can introduce new trap states on the surface of or within the shell volume, or at the core/shell interface[88, 89], as well as significantly alter dynamics in physiological solutions – mechanisms that have since been investigated further[33]. Although monothiol ligands are fairly compact and provide dense surface coverage, small molecule adsorbates can access the QD surface, and may either help to passivate surface traps or introduce new ones. In particular, oxygen is known to be an important passivant of colloidal QDs, able to interact with surface Cd, Se or Te (forming Cd-O, SeO_2 or TeO_2, respectively)[90, 91, 92].

While luminescence quenching (or bleaching) due to photochemical instability is observed in organic fluorophores and QDs alike, photoinduced fluorescence enhancement (PFE) is a more unusual feature of QDs. Competitive quenching and PFE mechanisms can result in dramatic variability in the photoluminescence of QDs. The first reports focused on PFE appeared ca. 2000. Jones *et al*. investigated PFE of colloidal QD ensembles using steady-state PL and TCSPC measurements as well as transient absorption spectroscopy[83]. Trioctylphosphine oxide (TOPO)-capped CdSe/ZnS QDs in toluene or hexane were illuminated with above-band-gap light for four periods, each of 2.5 hour duration. During the initial illumination period, the PL QY of the QDs increased steadily. During subsequent illuminations, the QYs had declined somewhat compared to their values at the end of the prior illumination, but rapidly enhanced at the onset and over the course of 10+ minutes before resuming a gradual enhancement rate for the remainder of the illumination. Concomitant increases in the fluorescence lifetimes of the samples suggested the likely mechanism to be passivation of trap states, rather than simply an increased efficiency of radiative band-edge recombination. Addition of methanol to the colloidal QD solutions

dramatically changed the dynamics of PFE, with enhanced brightening ascribed to water molecules stabilizing surface-associated holes through oxygen coordination, and/or water/methanol increasing local dielectric screening in the vicinity of the QDs. PFE of QD ensembles was proposed to reflect a number of distinct phenomena potentially affecting single QDs: (1) QDs switching from "dark" to "bright" states, altering the actively luminescing proportion of the population; (2) differences in blinking dynamics, changing the distribution of "on/off" times of single QDs; or (3) chemical influences that affect the rate of radiative recombination (QY) during the "on" times. Dark states (distinct from off periods associated with blinking) can persist due to exciton annihilation in charged QDs.

PFE was also observed in separate studies of colloidal CdS/ZnS[93] and CdSeTe/ZnS[94] QDs at the ensemble and single-QD levels. The mechanisms of PFE described above were observed directly, including increased on times and PL QYs, as well as dark/bright state switching under illumination. Yuan *et al*. observed PFE of CdSeTe/ZnS ensembles in air and to a lesser degree in vacuum, accompanied by blue shifts in the emission peaks, using 5-minute increments of 480 nm illumination. Individual QDs on glass coverslips were imaged using 405 nm pulsed excitation from a confocal microscope, before and after 20 minutes of illumination at 480 nm. A number of QDs became brighter after illumination, while a smaller number became dark, or did not change from an initially-bright state. The "PFE QDs" exhibited relatively long on times, with distinct variations in the intensities observed during the on times. On-time intensities of PFE QDs, ranging between values larger and smaller than "true neutral" QDs, were attributed to neutral core/charged shell states.

A better understanding of the fundamental interactions of QDs with characteristic biological species could encourage more meaningful conclusions to be drawn. The influence of

these mechanisms may vary considerably between QDs prepared in different ways, and even between batches. QDs bioconjugated to redox-active dopamine provided a system to study the interplay between QDs, surface ligands, covalently-attached charge-transferring biomolecules, and extraneous factors such as antioxidants in aqueous, biologically-relevant solutions[23, 46, 95, 96]. The results of these investigations simultaneously shed light on fundamental QD photophysics and therapeutic potential, and have encouraged the development of further applications such as biosensors[97, 98].

1.6 Thesis overview

Chapter 1 provides background information relevant to the original QD-centric research in Chapters 2 & 3, which address photoenhancement of luminescence and photosensitization by colloidal thiol-stabilized CdSe/ZnS and CdTe QDs and QD-dopamine bioconjugates in aqueous environments. Chapter 4 introduces a new variety of NP, luminescent lanthanide-doped insulators, and provides background for the original research presented in Chapter 5, including novel synthesis of cerium fluoride and cerium-doped lanthanum fluoride NPs and investigation of mechanisms of photoluminescence and energy transfer to bound and unbound photosensitizer molecules. Chapter 6 presents a few of our latest results, along with proposed future lines of inquiry and conclusions regarding the work as a whole.

1.7 References

1. Lakowicz, J. R. *Principles of fluorescence spectroscopy*; Springer2007.
2. van der Meer, B. W. Förster Theory. In *FRET – Förster Resonance Energy Transfer*; Wiley-VCH Verlag GmbH & Co. KGaA, 2013, pp 23-62.
3. Shimomura, O.; Johnson, F. H.; Saiga, Y. Extraction, purification and properties of aequorin, a bioluminescent protein from the luminous hydromedusan, Aequorea. *J Cell Comp Physiol* **1962,** *59* (3), 223-39.
4. Heim, R.; Cubitt, A. B.; Tsien, R. Y. Improved green fluorescence. *Nature* **1995,** *373* (6516), 663-664.
5. Prasher, D. C.; Eckenrode, V. K.; Ward, W. W.; Prendergast, F. G.; Cormier, M. J. Primary structure of the Aequorea victoria green-fluorescent protein. *Gene* **1992,** *111* (2), 229-233.
6. Chalfie, M.; Tu, Y.; Euskirchen, G.; Ward, W.; Prasher, D. Green fluorescent protein as a marker for gene expression. *Science* **1994,** *263* (5148), 802-805.
7. Inouye, S.; Tsuji, F. I. Aequorea green fluorescent protein: Expression of the gene and fluorescence characteristics of the recombinant protein. *FEBS Letters* **1994,** *341* (2–3), 277-280.
8. Ormo, M.; Cubitt, A. B.; Kallio, K.; Gross, L. A.; Tsien, R. Y.; Remington, S. J. Crystal structure of the Aequorea victoria green fluorescent protein. *Science* **1996,** *273* (5280), 1392-5.
9. Yang, F.; Moss, L. G.; Phillips, G. N. The molecular structure of green fluorescent protein. *Nat Biotech* **1996,** *14* (10), 1246-1251.
10. Shaner, N. C.; Steinbach, P. A.; Tsien, R. Y. A guide to choosing fluorescent proteins. *Nat Meth* **2005,** *2* (12), 905-909.
11. Resch-Genger, U.; Grabolle, M.; Cavaliere-Jaricot, S.; Nitschke, R.; Nann, T. Quantum dots versus organic dyes as fluorescent labels. *Nat Meth* **2008,** *5* (9), 763-775.
12. Baker, S. N.; Baker, G. A. Luminescent carbon nanodots: emergent nanolights. *Angewandte Chemie* **2010,** *49* (38), 6726-44.
13. Shen, J.; Zhu, Y.; Yang, X.; Li, C. Graphene quantum dots: emergent nanolights for bioimaging, sensors, catalysis and photovoltaic devices. *Chemical Communications* **2012,** *48* (31), 3686-3699.
14. Sun, Y. P.; Zhou, B.; Lin, Y.; Wang, W.; Fernando, K. A.; Pathak, P.; Meziani, M. J.; Harruff, B. A.; Wang, X.; Wang, H.; Luo, P. G.; Yang, H.; Kose, M. E.; Chen, B.; Veca, L. M.; Xie, S. Y. Quantum-sized carbon dots for bright and colorful photoluminescence. *Journal of the American Chemical Society* **2006,** *128* (24), 7756-7.
15. Medintz, I. L.; Uyeda, H. T.; Goldman, E. R.; Mattoussi, H. Quantum dot bioconjugates for imaging, labelling and sensing. *Nat Mater* **2005,** *4* (6), 435-446.
16. Brunetti, V.; Chibli, H.; Fiammengo, R.; Galeone, A.; Malvindi, M. A.; Vecchio, G.; Cingolani, R.; Nadeau, J. L.; Pompa, P. P. InP/ZnS as a safer alternative to CdSe/ZnS core/shell quantum dots: in vitro and in vivo toxicity assessment. *Nanoscale* **2013,** *5* (1), 307-317.
17. Chibli, H.; Carlini, L.; Park, S.; Dimitrijevic, N. M.; Nadeau, J. L. Cytotoxicity of InP/ZnS quantum dots related to reactive oxygen species generation. *Nanoscale* **2011,** *3* (6), 2552-2559.
18. Nadeau, J. *Introduction to Experimental Biophysics: Biological Methods for Physical Scientists*; CRC Press2011.
19. Bawendi, M. G.; Steigerwald, M. L.; Brus, L. E. The quantum-mechanics of larger semiconductor clusters (quantum dots). *Annual Review of Physical Chemistry* **1990,** *41* (1), 477-496.

20. Yu, W. W.; Qu, L. H.; Guo, W. Z.; Peng, X. G. Experimental determination of the extinction coefficient of CdTe, CdSe, and CdS nanocrystals. *Chemistry of Materials* **2003,** *15* (14), 2854-2860.
21. Sreenivasan, V. K. A.; Zvyagin, A. V.; Goldys, E. M. Luminescent nanoparticles and their applications in the life sciences. *Journal of Physics: Condensed Matter* **2013,** *25* (19), 194101.
22. Nirmal, M.; Dabbousi, B. O.; Bawendi, M. G.; Macklin, J. J.; Trautman, J. K.; Harris, T. D.; Brus, L. E. Fluorescence intermittency in single cadmium selenide nanocrystals. *Nature* **1996,** *383* (6603), 802-804.
23. Khatchadourian, R.; Bachir, A.; Clarke, S. J.; Heyes, C. D.; Wiseman, P. W.; Nadeau, J. L. Fluorescence intensity and intermittency as tools for following dopamine bioconjugate processing in living cells. *Journal of biomedicine & biotechnology* **2007,** *2007*, 70145.
24. Chen, Y.; Vela, J.; Htoon, H.; Casson, J. L.; Werder, D. J.; Bussian, D. A.; Klimov, V. I.; Hollingsworth, J. A. "Giant" multishell CdSe nanocrystal quantum dots with suppressed blinking. *Journal of the American Chemical Society* **2008,** *130* (15), 5026-7.
25. Hohng, S.; Ha, T. Near-complete suppression of quantum dot blinking in ambient conditions. *Journal of the American Chemical Society* **2004,** *126* (5), 1324-5.
26. Lee, S. F.; Osborne, M. A. Brightening, blinking, bluing and bleaching in the life of a quantum dot: friend or foe? *Chemphyschem* **2009,** *10* (13), 2174-91.
27. Mahler, B.; Spinicelli, P.; Buil, S.; Quelin, X.; Hermier, J.-P.; Dubertret, B. Towards non-blinking colloidal quantum dots. *Nat Mater* **2008,** *7* (8), 659-664.
28. Rombach-Riegraf, V.; Oswald, P.; Bienert, R.; Petersen, J.; Domingo, M. P.; Pardo, J.; Gräber, P.; Galvez, E. M. Blinking effect and the use of quantum dots in single molecule spectroscopy. *Biochemical and Biophysical Research Communications* **2013,** *430* (1), 260-264.
29. Schmidt, R.; Krasselt, C.; Gohler, C.; von Borczyskowski, C. The fluorescence intermittency for quantum dots is not power-law distributed: a luminescence intensity resolved approach. *ACS Nano* **2014,** *8* (4), 3506-21.
30. Yao, J.; Larson, D. R.; Vishwasrao, H. D.; Zipfel, W. R.; Webb, W. W. Blinking and nonradiant dark fraction of water-soluble quantum dots in aqueous solution. *Proceedings of the National Academy of Sciences of the United States of America* **2005,** *102* (40), 14284-14289.
31. Bachir, A. I.; Durisic, N.; Hebert, B.; Grütter, P.; Wiseman, P. W. Characterization of blinking dynamics in quantum dot ensembles using image correlation spectroscopy. *Journal of Applied Physics* **2006,** *99* (6), -.
32. Durisic, N.; Godin, A. G.; Walters, D.; Grutter, P.; Wiseman, P. W.; Heyes, C. D. Probing the "dark" fraction of core-shell quantum dots by ensemble and single particle pH-dependent spectroscopy. *ACS Nano* **2011,** *5* (11), 9062-73.
33. Durisic, N.; Wiseman, P. W.; Grutter, P.; Heyes, C. D. A common mechanism underlies the dark fraction formation and fluorescence blinking of quantum dots. *ACS Nano* **2009,** *3* (5), 1167-75.
34. Galland, C.; Ghosh, Y.; Steinbrück, A.; Hollingsworth, J. A.; Htoon, H.; Klimov, V. I. Lifetime blinking in nonblinking nanocrystal quantum dots. *Nat Commun* **2012,** *3*, 908.
35. Galland, C.; Ghosh, Y.; Steinbruck, A.; Sykora, M.; Hollingsworth, J. A.; Klimov, V. I.; Htoon, H. Two types of luminescence blinking revealed by spectroelectrochemistry of single quantum dots. *Nature* **2011,** *479* (7372), 203-207.
36. Krauss, T. D.; Peterson, J. J. Quantum dots: A charge for blinking. *Nat Mater* **2012,** *11* (1), 14-16.

37. Georgin, M.; Carlini, L.; Cooper, D.; Bradforth, S. E.; Nadeau, J. L. Differential effects of β-mercaptoethanol on CdSe/ZnS and InP/ZnS quantum dots. *Physical Chemistry Chemical Physics* **2013,** *15* (25), 10418-10428.
38. Nadeau, J. L.; Carlini, L.; Suffern, D.; Ivanova, O.; Bradforth, S. E. Effects of β-mercaptoethanol on quantum dot emission evaluated from photoluminescence decays. *The Journal of Physical Chemistry C* **2012,** *116* (4), 2728-2739.
39. Yin, Y.; Alivisatos, A. P. Colloidal nanocrystal synthesis and the organic-inorganic interface. *Nature* **2005,** *437* (7059), 664-670.
40. Gaponik, N.; Talapin, D. V.; Rogach, A. L.; Hoppe, K.; Shevchenko, E. V.; Kornowski, A.; Eychmuller, A.; Weller, H. Thiol-capping of CdTe nanocrystals: An alternative to organometallic synthetic routes. *Journal of Physical Chemistry B* **2002,** *106* (29), 7177-7185.
41. Rogach, A. L.; Franzl, T.; Klar, T. A.; Feldmann, J.; Gaponik, N.; Lesnyak, V.; Shavel, A.; Eychmuller, A.; Rakovich, Y. P.; Donegan, J. F. Aqueous synthesis of thiol-capped CdTe nanocrystals: State-of-the-art. *Journal of Physical Chemistry C* **2007,** *111* (40), 14628-14637.
42. Rogach, A. L.; Kornowski, A.; Gao, M. Y.; Eychmuller, A.; Weller, H. Synthesis and characterization of a size series of extremely small thiol-stabilized CdSe nanocrystals. *Journal of Physical Chemistry B* **1999,** *103* (16), 3065-3069.
43. Zhang, Y.; Clapp, A. Overview of stabilizing ligands for biocompatible quantum dot nanocrystals. *Sensors (Basel, Switzerland)* **2011,** *11* (12), 11036-55.
44. Chan, W. C.; Nie, S. Quantum dot bioconjugates for ultrasensitive nonisotopic detection. *Science* **1998,** *281* (5385), 2016-8.
45. Aldana, J.; Wang, Y. A.; Peng, X. Photochemical instability of CdSe nanocrystals coated by hydrophilic thiols. *Journal of the American Chemical Society* **2001,** *123* (36), 8844-50.
46. Clarke, S. J.; Hollmann, C. A.; Zhang, Z.; Suffern, D.; Bradforth, S. E.; Dimitrijevic, N. M.; Minarik, W. G.; Nadeau, J. L. Photophysics of dopamine-modified quantum dots and effects on biological systems. *Nat Mater* **2006,** *5* (5), 409-417.
47. He, Y.; Yin, P.; Gong, H.; Peng, J.; Liu, S.; Fan, X.; Yan, S. Characterization of the interaction between mercaptoethylamine capped CdTe quantum dots with human serum albumin and its analytical application. *Sensors and Actuators B: Chemical* **2011,** *157* (1), 8-13.
48. Liu, W.; Choi, H. S.; Zimmer, J. P.; Tanaka, E.; Frangioni, J. V.; Bawendi, M. Compact cysteine-coated CdSe(ZnCdS) quantum dots for in vivo applications. *Journal of the American Chemical Society* **2007,** *129* (47), 14530-1.
49. Breus, V. V.; Heyes, C. D.; Tron, K.; Nienhaus, G. U. Zwitterionic biocompatible quantum dots for wide pH stability and weak nonspecific binding to cells. *ACS Nano* **2009,** *3* (9), 2573-80.
50. Breus, V. V.; Heyes, C. D.; Nienhaus, G. U. Quenching of CdSe−ZnS Core−Shell Quantum Dot Luminescence by Water-Soluble Thiolated Ligands. *The Journal of Physical Chemistry C* **2007,** *111* (50), 18589-18594.
51. Susumu, K.; Uyeda, H. T.; Medintz, I. L.; Pons, T.; Delehanty, J. B.; Mattoussi, H. Enhancing the stability and biological functionalities of quantum dots via compact multifunctional ligands. *Journal of the American Chemical Society* **2007,** *129* (45), 13987-96.
52. Uyeda, H. T.; Medintz, I. L.; Jaiswal, J. K.; Simon, S. M.; Mattoussi, H. Synthesis of compact multidentate ligands to prepare stable hydrophilic quantum dot fluorophores. *Journal of the American Chemical Society* **2005,** *127* (11), 3870-8.
53. Clapp, A. R.; Goldman, E. R.; Mattoussi, H. Capping of CdSe-ZnS quantum dots with DHLA and subsequent conjugation with proteins. *Nature protocols* **2006,** *1* (3), 1258-66.

54. Takeuchi, H.; Omogo, B.; Heyes, C. D. Are bidentate ligands really better than monodentate ligands for nanoparticles? *Nano Lett* **2013,** *13* (10), 4746-52.
55. Pellegrino, T.; Manna, L.; Kudera, S.; Liedl, T.; Koktysh, D.; Rogach, A. L.; Keller, S.; Radler, J.; Natile, G.; Parak, W. J. Hydrophobic nanocrystals coated with an amphiphilic polymer shell: A general route to water soluble nanocrystals. *Nano Letters* **2004,** *4* (4), 703-707.
56. Pinaud, F.; Michalet, X.; Bentolila, L. A.; Tsay, J. M.; Doose, S.; Li, J. J.; Iyer, G.; Weiss, S. Advances in fluorescence imaging with quantum dot bio-probes. *Biomaterials* **2006,** *27* (9), 1679-1687.
57. Zhu, M.-Q.; Chang, E.; Sun, J.; Drezek, R. A. Surface modification and functionalization of semiconductor quantum dots through reactive coating of silanes in toluene. *Journal of Materials Chemistry* **2007,** *17* (8), 800-805.
58. Soo Choi, H.; Liu, W.; Misra, P.; Tanaka, E.; Zimmer, J. P.; Itty Ipe, B.; Bawendi, M. G.; Frangioni, J. V. Renal clearance of quantum dots. *Nat Biotech* **2007,** *25* (10), 1165-1170.
59. Hsieh, J. M.; Ho, M. L.; Wu, P. W.; Chou, P. T.; Tsai, T. T.; Chi, Y. Iridium-complex modified CdSe/ZnS quantum dots; a conceptual design for bi-functionality toward imaging and photosensitization. *Chemical communications (Cambridge, England)* **2006,** (6), 615-7.
60. Tsay, J. M.; Trzoss, M.; Shi, L.; Kong, X.; Selke, M.; Jung, M. E.; Weiss, S. Singlet Oxygen Production by Peptide-Coated Quantum Dot−Photosensitizer Conjugates. *Journal of the American Chemical Society* **2007,** *129* (21), 6865-6871.
61. Charron, G.; Stuchinskaya, T.; Edwards, D. R.; Russell, D. A.; Nann, T. Insights into the Mechanism of Quantum Dot-Sensitized Singlet Oxygen Production for Photodynamic Therapy. *The Journal of Physical Chemistry C* **2012,** *116* (16), 9334-9342.
62. Medintz, I. L.; Stewart, M. H.; Trammell, S. A.; Susumu, K.; Delehanty, J. B.; Mei, B. C.; Melinger, J. S.; Blanco-Canosa, J. B.; Dawson, P. E.; Mattoussi, H. Quantum-dot/dopamine bioconjugates function as redox coupled assemblies for in vitro and intracellular pH sensing. *Nat Mater* **2010,** *9* (8), 676-684.
63. Cai, W.; Chen, X. Preparation of peptide-conjugated quantum dots for tumor vasculature-targeted imaging. *Nature protocols* **2008,** *3* (1), 89-96.
64. Kloepfer, J. A.; Mielke, R. E.; Wong, M. S.; Nealson, K. H.; Stucky, G.; Nadeau, J. L. Quantum dots as strain- and metabolism-specific microbiological labels. *Applied and Environmental Microbiology* **2003,** *69* (7), 4205-4213.
65. Fernandez-Arguelles, M. T.; Costa-Fernandez, J. M.; Pereiro, R.; Sanz-Medel, A. Simple bio-conjugation of polymer-coated quantum dots with antibodies for fluorescence-based immunoassays. *Analyst* **2008,** *133* (4), 444-447.
66. Sperling, R. A.; Parak, W. J. Surface modification, functionalization and bioconjugation of colloidal inorganic nanoparticles. *Philosophical transactions. Series A, Mathematical, physical, and engineering sciences* **2010,** *368* (1915), 1333-83.
67. Alivisatos, A. P.; Gu, W.; Larabell, C. Quantum dots as cellular probes. *Annu Rev Biomed Eng* **2005,** *7* (1), 55-76.
68. Smith, A. M.; Gao, X.; Nie, S. Quantum dot nanocrystals for in vivo molecular and cellular imaging. *Photochem Photobiol* **2004,** *80* (3), 377-85.
69. Gao, X.; Cui, Y.; Levenson, R. M.; Chung, L. W. K.; Nie, S. In vivo cancer targeting and imaging with semiconductor quantum dots. *Nat Biotech* **2004,** *22* (8), 969-976.
70. Cho, K.; Wang, X.; Nie, S.; Chen, Z. G.; Shin, D. M. Therapeutic nanoparticles for drug delivery in cancer. *Clinical cancer research : an official journal of the American Association for Cancer Research* **2008,** *14* (5), 1310-6.

71. Nie, S.; Xing, Y.; Kim, G. J.; Simons, J. W. Nanotechnology applications in cancer. *Annu Rev Biomed Eng* **2007,** *9* (1), 257-88.
72. Smith, A. M.; Duan, H.; Mohs, A. M.; Nie, S. Bioconjugated quantum dots for in vivo molecular and cellular imaging. *Advanced Drug Delivery Reviews* **2008,** *60* (11), 1226-1240.
73. Klostranec, J. M.; Chan, W. C. W. Quantum dots in biological and biomedical research: Recent progress and present challenges. *Advanced Materials* **2006,** *18* (15), 1953-1964.
74. Parak, W. J.; Pellegrino, T.; Plank, C. Labelling of cells with quantum dots. *Nanotechnology* **2005,** *16* (2), R9-R25.
75. Jamieson, T.; Bakhshi, R.; Petrova, D.; Pocock, R.; Imani, M.; Seifalian, A. M. Biological applications of quantum dots. *Biomaterials* **2007,** *28* (31), 4717-4732.
76. Juzenas, P.; Chen, W.; Sun, Y.-P.; Coelho, M. A. N.; Generalov, R.; Generalova, N.; Christensen, I. L. Quantum dots and nanoparticles for photodynamic and radiation therapies of cancer. *Advanced Drug Delivery Reviews* **2008,** *60* (15), 1600-1614.
77. Derfus, A. M.; Chan, W. C. W.; Bhatia, S. N. Intracellular delivery of quantum dots for live cell labeling and organelle tracking. *Advanced Materials* **2004,** *16* (12), 961-+.
78. Brus, L. Zero-dimensional "excitons" in semiconductor clusters. *Quantum Electronics, IEEE Journal of* **1986,** *22* (9), 1909-1914.
79. Underwood, D. F.; Kippeny, T.; Rosenthal, S. J. Ultrafast carrier dynamics in CdSe nanocrystals determined by femtosecond fluorescence upconversion spectroscopy. *The Journal of Physical Chemistry B* **2001,** *105* (2), 436-443.
80. Nirmal, M.; Norris, D. J.; Kuno, M.; Bawendi, M. G.; Efros, A. L.; Rosen, M. Observation of the "dark exciton" in Cdse quantum dots. *Physical Review Letters* **1995,** *75* (20), 3728-3731.
81. Wuister, S. F.; Donega, C.; Meijerink, A. Influence of Thiol Capping on the Exciton Luminescence and Decay Kinetics of CdTe and CdSe Quantum Dots. *Journal of Physical Chemistry B* **2004,** *108* 17393-17397.
82. Rajh, T.; Micic, O. I.; Nozik, A. J. Synthesis and characterization of surface-modified colloidal cadmium telluride quantum dots. *The Journal of Physical Chemistry* **1993,** *97* (46), 11999-12003.
83. Jones, M.; Nedeljkovic, J.; Ellingson, R. J.; Nozik, A. J.; Rumbles, G. Photoenhancement of luminescence in colloidal CdSe quantum dot solutions. *Journal of Physical Chemistry B* **2003,** *107* (41), 11346-11352.
84. Sun, Y. H.; Liu, Y. S.; Vernier, P. T.; Liang, C. H.; Chong, S. Y.; Marcu, L.; Gundersen, M. A. Photostability and pH sensitivity of CdSe/ZnSe/ZnS quantum dots in living cells. *Nanotechnology* **2006,** *17* (17), 4469.
85. Ma, J.; Chen, J.-Y.; Zhang, Y.; Wang, P.-N.; Guo, J.; Yang, W.-L.; Wang, C.-C. Photochemical instability of thiol-capped CdTe quantum dots in aqueous solution and living cells: process and mechanism. *The Journal of Physical Chemistry B* **2007,** *111* (41), 12012-12016.
86. Zhang, Y.; He, J.; Wang, P. N.; Chen, J. Y.; Lu, Z. J.; Lu, D. R.; Guo, J.; Wang, C. C.; Yang, W. L. Time-dependent photoluminescence blue shift of the quantum dots in living cells: effect of oxidation by singlet oxygen. *Journal of the American Chemical Society* **2006,** *128* (41), 13396-401.
87. van Sark, W. G. J. H. M.; Frederix, P. L. T. M.; Bol, A. A.; Gerritsen, H. C.; Meijerink, A. Blueing, Bleaching, and Blinking of Single CdSe/ZnS Quantum Dots. *ChemPhysChem* **2002,** *3* (10), 871-879.
88. Chen, X.; Lou, Y.; Samia, A. C.; Burda, C. Coherency Strain Effects on the Optical Response of Core/Shell Heteronanostructures. *Nano Letters* **2003,** *3* (6), 799-803.

89. Cretí, A.; Anni, M.; Rossi, M. Z.; Lanzani, G.; Leo, G.; Della Sala, F.; Manna, L.; Lomascolo, M. Ultrafast carrier dynamics in core and core/shell CdSe quantum rods: Role of the surface and interface defects. *Physical Review B* **2005,** *72* (12), 125346.
90. Dabbousi, B. O.; Rodriguez-Viejo, J.; Mikulec, F. V.; Heine, J. R.; Mattoussi, H.; Ober, R.; Jensen, K. F.; Bawendi, M. G. (CdSe)ZnS Core−Shell Quantum Dots: Synthesis and Characterization of a Size Series of Highly Luminescent Nanocrystallites. *The Journal of Physical Chemistry B* **1997,** *101* (46), 9463-9475.
91. Hines, D. A.; Becker, M. A.; Kamat, P. V. Photoinduced surface oxidation and its effect on the exciton dynamics of CdSe quantum dots. *Journal of Physical Chemistry C* **2012,** *116* (24), 13452-13457.
92. Lobo, A.; Borchert, H.; Talapin, D. V.; Weller, H.; Möller, T. Surface oxidation of CdTe nanocrystals—A high resolution core-level photoelectron spectroscopy study. *Colloids and Surfaces A: Physicochemical and Engineering Aspects* **2006,** *286* (1–3), 1-7.
93. Tsay, J. M.; Doose, S.; Pinaud, F.; Weiss, S. Enhancing the photoluminescence of peptide-coated nanocrystals with shell composition and UV irradiation. *J Phys Chem B* **2005,** *109* (5), 1669-74.
94. Yuan, C. T.; Chou, W. C.; Chuu, D. S.; Chen, Y. N.; Lin, C. A.; Chang, W. H. Photoinduced fluorescence enhancement in colloidal CdSeTe/ZnS core/shell quantum dots. *Applied Physics Letters* **2008,** *92* (18), 183108.
95. Clarke, S.; Koshy, S.; Zhang, J.; Cohen, N.; Nadeau, J. Power and wavelength dependence of photoenhancement in (CdSe) ZnS-dopamine in aqueous solution and live cells. *Zeitschrift fur Physikalische Chemie* **2008,** *222* (5), 851-864.
96. Clarke, S. J.; Hollmann, C. A.; Aldaye, F. A.; Nadeau, J. L. Effect of ligand density on the spectral, physical, and biological characteristics of CdSe/ZnS quantum dots. *Bioconjug Chem* **2008,** *19* (2), 562-8.
97. Ji, X.; Palui, G.; Avellini, T.; Na, H. B.; Yi, C.; Knappenberger Jr, K. L.; Mattoussi, H. On the pH-dependent quenching of quantum dot photoluminescence by redox active dopamine. *Journal of the American Chemical Society* **2012,** *134* (13), 6006-6017.
98. Medintz, I. L.; Stewart, M. H.; Trammell, S. A.; Susumu, K.; Delehanty, J. B.; Mei, B. C.; Melinger, J. S.; Blanco-Canosa, J. B.; Dawson, P. E.; Mattoussi, H. Quantum-dot/dopamine bioconjugates function as redox coupled assemblies for in vitro and intracellular pH sensing. *Nature materials* **2010,** *9* (8), 676-684.

Chapter 2

Photoenhancement of lifetimes in CdSe/ZnS and CdTe quantum dot-dopamine conjugates

Abstract

The response of water-soluble, mercaptocarboxylic acid-capped fluorescent semiconductor nanoparticles, or quantum dots (QDs), to extended visible-light irradiation is variable and poorly described. Here we use time-resolved spectroscopy to investigate the photoluminescence intensities and lifetimes of CdSe/ZnS and CdTe QDs as a function of blue light illumination. Conjugates of the particles to the electron donor dopamine were also investigated, and the effect of the antioxidant beta-mercaptoethanol was explored. Both types of QD showed signs of direct electron transfer to the conjugate, but enhancement was much more pronounced in CdSe/ZnS. A model of the two different types of enhancement is proposed.

Adapted from:

Cooper, D. R., Suffern, D., Carlini, L., Clarke, S. J., Parbhoo, R., Bradforth, S. E., & Nadeau, J. L. (2009). Photoenhancement of lifetimes in CdSe/ZnS and CdTe quantum dot-dopamine conjugates. *Physical Chemistry Chemical Physics*, *11*(21), 4298-4310.

2. Photoenhancement of lifetimes in CdSe/ZnS and CdTe quantum dot-dopamine conjugates

2.1 Introduction

Fluorescent semiconductor nanoparticles, or quantum dots (QDs), possess attractive optical properties that have encouraged their use as biological probes in recent years. Several applications have emerged that employ QD energy or electron transfer for probing biological systems[1, 2, 3]. However, it has proven difficult to use QDs as biosensors because of instability in QD emission with environment and time. In particular, photobrightening, or photoinduced fluorescence enhancement (PFE), of QDs has been observed under many different conditions, including inside cells[4], but remains controversial. A variety of models have been proposed to explain the observed increase in emissivity with light exposure: adsorption of water molecules or reactive oxygen species may act to passivate surface states[5]; charge migration may lead to an enhanced "on" state[6]; or rearrangement of surface ligands may passivate traps[7]. If illumination is sufficiently powerful or prolonged, thiol-stabilized CdSe QDs may lose their quenching thiols and develop a layer of surface oxides, leading to brightening[8]. Yet other studies suggest that PFE is more readily observed in thin films than colloidal solutions because it removes some of the quenching due to inter-dot coupling[9].

Variations in QD preparations, experimental conditions, and differences in types of samples required for different experimental techniques account for some of these discrepancies. PFE depends strongly on illumination power, wavelength, and time[10]. In films, there are influences of film thickness and substrate[11]. However, despite the presence of ambiguous and contradictory results, some certainties have emerged in recent years. It has been shown using cyclic voltammetry that fluorescence enhancement can result from electron injection into CdSe/CdS/ZnS QDs and

interaction of the resulting unpaired exciton electron with water molecules. The same does not apply to hole injection, which leads to irreversible quenching[12].

Reliable chemical electron injection remains elusive, however, especially in complex solutions. While it is true that reduction of QDs by chemical electron donors leads to immediate quenching[13], later enhancement may result due to interaction with water and other molecules[12].

Dopamine (DA) is a small molecule neurotransmitter that can act as an electron donor to QDs. It is easy to oxidize when adsorbed to an electron acceptor[14], with redox potentials that vary with buffer conditions but which are always thermodynamically favorable for oxidation by QDs (Fig. 2.1). Oxidation of DA leads to the formation of dopamine quinones and reactive oxygen species (ROS) such as superoxide and hydrogen peroxide[15].We have previously characterized CdSe/ZnS QD-DA conjugates by a variety of methods. EPR spectroscopy demonstrated the formation of DA^+ radicals in these conjugates after illumination[1]. We have also quantified steady-state photoenhancement of these conjugates in thin films, occurring over the course of seconds to minutes. The extent and nature of the photoenhancement was found to be decisively dependent upon illumination power (photoenhancement being entirely absent at powers less than ~1 mW), and dependent also upon the number of DA molecules conjugated to the QD surface[16].

In this study, we use TCSPC to investigate the photophysics of QDs and QD-dopamine conjugates in dilute aqueous solutions as a function of visible-light irradiation. The illumination power was comparable to that used in the steady-state experiments[16]. We looked at a time scale much shorter than that of most studies, which usually examine PFE over many hours to days. The sensitivity of our system allowed us to measure fluorescence lifetimes in one-minute intervals, giving insight into rapid mechanisms of PFE that have not been previously described. Both CdSe/ZnS and CdTe QDs were investigated, and were found to exhibit very different behavior.

CdTe lifetimes were initially strongly quenched by DA but enhanced under light; CdSe/ZnS lifetimes showed enhancement only. Reduction of dopamine radicals by beta-mercaptoethanol (BME) nearly eliminated PFE with CdSe/ZnS but not with CdTe. In the absence of oxygen, both CdSe/ZnS and CdTe were quenched by DA conjugation and PFE was completely prevented.

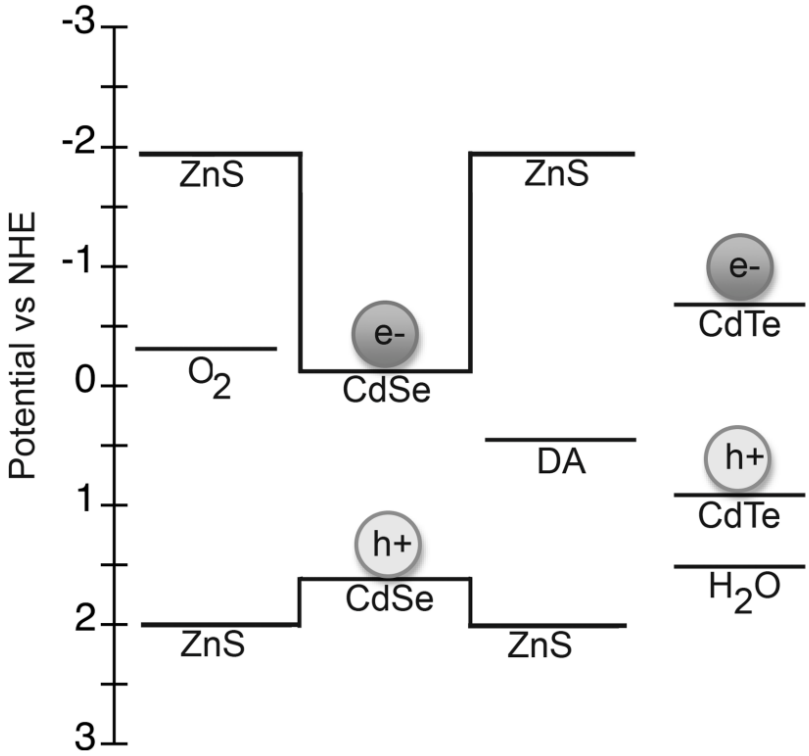

Figure 2.1 Relative energy levels of the valence bands and conduction bands of relevant semiconductors in aqueous solutions, dopamine (DA) in phosphate buffer, and water and oxygen. Values for the semiconductors are taken from published values obtained by cyclic voltammetry for nanoparticles comparable in size to the ones we used in this study[17, 18, 19].

2.2 Experimental section

2.2.1 Chemicals

Unless otherwise specified, all chemicals were purchased from Sigma-Aldrich Canada, Oakville, ON and used as received.

2.2.2 QD synthesis and solubilization

CdSe/ZnS core-shell QDs were synthesized with 2 to 3 monolayers of ZnS using a method based on the noncoordinating solvent 1-octadecene (ODE) [20]. CdTe QDs were synthesized by a recently developed procedure involving the nucleation of the particles in the presence of Cd^0 [21]. Briefly, 0.026 g (0.20 mmol) of CdO and 0.179 g (0.63 mmol) oleic acid (OA) were added to a three-neck flask containing 10 mL of ODE. This mixture was degassed for 5 minutes and heated under a nitrogen (N_2) atmosphere to 220 °C until the solution became colorless. In a separate vessel, the tellurium precursor trioctylphosphine telluride (TOPTe) was prepared by mixing 0.01 g (0.08 mmol) of Te with 0.415 g (1.12 mmol) trioctylphosphine (TOP) and 2 mL ODE under N_2 into a sealed vial. This mixture was vigorously stirred until solution became light yellow. Next, the temperature of the CdO-ODE mixture was further increased to 310 °C. Formation of a grey Cd^0 precipitate was evident after prolonged heating (10-20 min) of the reaction mixture at 310 °C. Immediately after formation of Cd^0, the TOPTe precursor was rapidly injected. The temperature was allowed to drop and stabilized at 270 °C for the growth of the nanoparticles. Aliquots of the reaction mixture were withdrawn at various time points and injected into cold toluene to quench further growth.

CdSe/ZnS QDs were functionalized with 3-mercaptopropionic acid (MPA) by standard methods. 200-500 µL of hydrophobic QDs was suspended in a mixture of 2 mL chloroform, 5 mL methanol and 50 µL MPA. The pH was adjusted to ~9-10 with tetramethylammonium hydroxide

(TMAH) and the mixture was incubated at room temperature in the dark for 16-24 hours. To isolate the MPA-functionalized QDs from excess thiol in the reaction solution, a large excess of ethyl acetate was added and the solution was centrifuged for 5 min at 10000g. The supernatant was discarded and the precipitated QDs were resuspended in distilled water or buffer as required. CdTe QDs were functionalized with MPA using a biphasic approach[22]. 400 µL of toluene, 500 µL of 200 mM phosphate buffered saline (PBS) (pH 9) and 1 µL of MPA were added to 100 µL of concentrated hydrophobic QDs. Following vigorous mixing, the QDs moved from the organic phase to the aqueous phase, which was extracted using a pipette. The CdTe QDs were isolated from excess thiol by several cycles of concentration and dilution using a filter with a 10 kDa cutoff (Vivaspin).

Concentrations of solubilized QDs were estimated from UV-Visible absorbance spectra using published methods[23]. Spectra were taken on a Varian Cary 50 UV-Visible spectrometer.

2.2.3 Conjugation to dopamine

Conjugation of QDs to DA was performed using a method of 1-ethyl-3-(3-dimethylaminopropyl)-carbodiimide hydrochloride (EDC)-mediated coupling that was previously determined to result in a highly reproducible number of conjugated molecules per QD[24]. Briefly, for CdSe/ZnS QDs, 500 equivalents of dopamine and 500 ("low") or 1500 ("high") equivalents of EDC were added to 1 µM QDs in PBS. Similarly, conjugation of CdTe QDs to DA was performed by adding 500 ("low") or 1000 ("high") equivalents of DA and 1500 equivalents of EDC to 1 µM QDs in PBS. The mixtures were reacted for 30-60 minutes at room temperature and cleaned from excess DA and side products using gel filtration columns (Sephadex G25, Harvard Apparatus). For the QD-DA+BME sample, a duplicate "High DA" sample was prepared as above, except that 1 mM BME was added just before measurement. Similarly, for the QD+BME only samples, 1 mM BME was

added just before measurement. After measurement, emission spectra were taken. Samples were then concentrated by filtration and UV-Vis spectra measured.

2.2.4 Preparation of deaerated samples

In order to determine the dependence of the results on oxygen, deaerated samples were prepared under a nitrogen atmosphere. 500 mL of PBS and 50 μL of concentrated QD solution were placed into at AtmosBag glove bag (Sigma) that was continuously flushed with N_2 gas; the PBS solution was bubbled with N_2 gas for 60-90 min. Dopamine and EDC powders were then introduced into the bag and the samples were prepared as above. The deaerated samples were placed into a measurement cuvette before removal from the bag, flushed with N_2, tightly capped and removed just before measurement.

2.2.5 TCSPC

Emission lifetimes were recorded using the TCSPC technique using the apparatus described previously[25]. Briefly, samples were excited with laser pulses provided by the frequency-doubled output of a Ti:Sapphire regenerative amplifier operating at a 250 kHz repetition rate, giving a peak pulse excitation wavelength of 400 nm. The bandwidth was about 3 nm at full width at half maximum (FWHM). The temporal width of the pulses was approximately 100 fs. Laser pulses were focused into the sample using a 15 cm focal length lens, with a peak pulse intensity at the sample of 1×10^7 W/cm^2 after attenuation of the laser light with neutral density filters placed before the focusing lens. Emission was collected at the emission peak of the QD conjugate at magic angle with respect to the 400 nm vertical excitation laser polarization and focused into a monochromator with a 10 cm focal length secondary lens. Both optics had a diameter of 1 inch, and the focal length of the secondary lens was chosen based on an *f* number of 3.9 for the monochromator. The monochromator was a CVI CMSP112 double spectrograph with a 1/8 m total

pathlength in negative dispersive mode with 600 grove/mm grating. Typically the slit widths were 0.6-1.2 mm, and based on a monochromator dispersion of 16 nm/mm, provided 10-20 nm resolution. The PMT was mounted on the exit slit. The PMT was a Hamamatsu RU3809 micro-channel plate detector powered by a variable high voltage power supply. The usual operating voltage was –3.0 kV to maximize the time resolution of the detector.

Signals were amplified and then recorded with a Becker and Hickl SPC-630 photon counting board. A small portion of the excitation beam was directed into a fast photodiode to provide a reference signal. In order to hold excitation power and sample concentrations constant, the monochromator slit width was changed to obtain discriminated count rates between ~500 and 10,000 per second or below 0.04 of the laser repetition rate to avoid pulse pileup. The instrument response is ~25 ps. Concentration of QD solutions was held to < 100 nM to prevent scattering. Controls containing dopamine alone, EDC alone, and dopamine and EDC showed no fluorescence in our set-up.

Steady-state spectra were recorded on a Fluorolog-3 (Jobin Yvon) spectrometer.

2.2.6 Data analysis

The instrument response function (IRF) was determined from scatter off a solution of dilute coffee creamer. It was deconvolved from the signal and fit using the software FluoFit 4.0 (PicoQuant GmbH, Berlin). Goodness-of-fit data and residuals were used to gauge fit results; a $\chi^2 \leq 1$ and random distribution of residuals around the x-axis were necessary for a fit to be considered accurate. A control solution of fluorescein in 0.001 N NaOH was used to ensure that the correct single-exponential value of 4.16 ns was reproduced[26]. Fits to lifetime-vs.-time curves were done using Prism 5.0 for Macintosh (GraphPad Software, San Diego, CA). Model comparisons were performed and goodness-of-fit measured by residuals and R^2 values. Confidence intervals for

parameters A, A_1, τ, τ_1, β and β_1 were typically less than ±5% of the fit values, while for A_1 and τ_2, less than ±20% was typical, though for some smaller values (such as with CdSe/ZnS alone) they exceeded ±50%. Steady-state fluorescence at peak was estimated from the irradiated solutions as the integral under the raw (unnormalized) decay curves, calculated using Prism.

2.3 Results

2.3.1 Samples and power dependence

All experiments in air were performed on ten samples, abbreviated as follows: CdSe/ZnS QDs alone ("CdSe/ZnS" or "QD only"); CdSe/ZnS+BME ("CdSe/ZnS-BME"); CdSe/ZnS conjugated to high levels of dopamine ("CdSe/ZnS-High DA"); CdSe/ZnS conjugated to low levels of dopamine ("CdSe/ZnS-Low DA"); CdSe/ZnS conjugated to high levels of dopamine with BME ("CdSe/ZnS-DA-BME"); CdTe alone ("CdTe" or "QD only"); CdTe alone with BME ("CdTe-BME"); CdTe conjugated to high levels of dopamine ("CdTe-High DA"); CdTe conjugated to low levels of dopamine ("CdTe-Low DA"); CdTe conjugated to high levels of dopamine with BME ("CdTe-DA-BME"). Deaerated samples were CdSe/ZnS, CdSe/ZnS-High DA, CdTe, and CdTe-High DA.

Preliminary tests indicated that changes in lifetime were not seen at 20 or 220 μW irradiation with any of our CdSe/ZnS samples for up to 1 hr (not shown). At 2.4 mW, the lifetime changes in CdSe/ZnS alone were minimal, but the DA conjugates showed substantial changes. Thus all experiments reported here were performed with 2.4 mW laser illumination. This corresponded to an intensity at the sample of 1×10^7 W/cm^2 or a fluence of 1×10^{-6} J/cm^2.

2.3.2 Steady-state and integrated photoluminescence

Absorbance spectra taken before and after the irradiation showed that the CdSe/ZnS QDs had an exciton peak absorbance at 585 nm that was almost unaffected by the 20 min of TCSPC illumination (Fig. 2.2A). DA conjugation essentially eliminated this peak, consistent with electron transfer [27] (Fig. 2.2B). This was somewhat prevented with BME (Fig. 2.2C, D). The CdTe QDs had an exciton peak at 600 nm that was somewhat flattened by illumination, suggesting oxidation[28] (Fig. 2.2E). Conjugation of DA didn't completely eliminate the peak until after illumination, although electronic coupling was indicated by the appearance of a new peak at ~490 nm (Fig. 2.2F). BME did not prevent the changes associated with illumination (Fig. 2.2G, H).

Steady-state emission spectra taken before and after TCSPC showed that while photoluminescence (PL) intensity changed with irradiation, peak position remained constant (not shown; 595 nm emission peak for CdSe/ZnS and 610 nm for CdTe). We thus chose to analyze the integrated time-resolved fluorescence as a measure of steady-state, as it allowed us to compare the steady-state and lifetime values for the same samples under the same conditions. These values may thus be directly compared with the lifetimes.

The integrated PL of CdSe/ZnS QDs with high or low DA was slightly lower than that of the samples without DA at the start of irradiation, but increased rapidly for 5-6 min. The addition of BME had a slight enhancement effect as well, but the combination of DA conjugation and the presence of BME led to an overall reduction in PL with irradiation (Fig. 2.3A). When normalized to their starting values, it could be observed that the PL of CdSe/ZnS QDs with high and low DA photoenhanced much more than any other samples (Fig. 2.3B). CdSe/ZnS QDs alone enhanced slightly for 2-3 min, then decayed throughout the rest of the recording. When BME was present, the PL of the samples increased slightly and very slowly. For CdSe/ZnS QDs with DA-BME, the

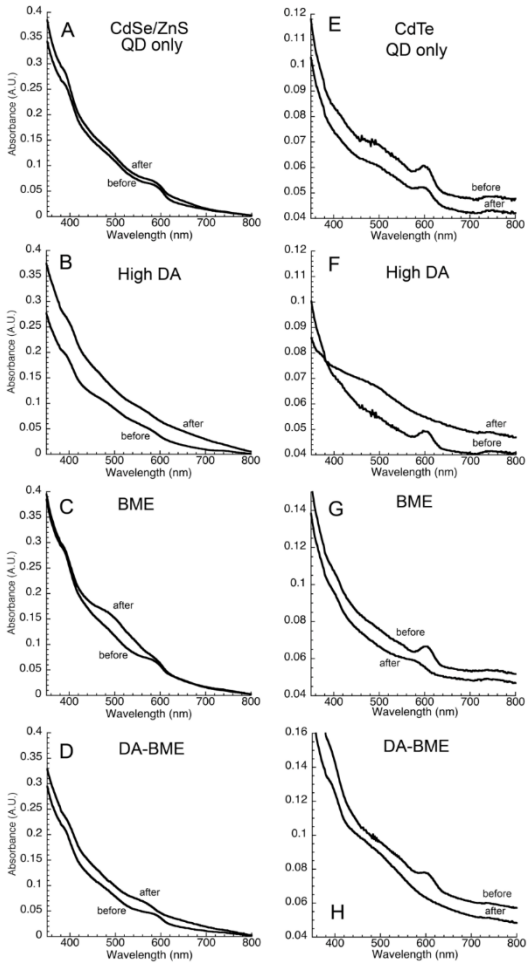

Figure 2.2 UV-Vis absorbance spectra for QDs and conjugates before and after 20 min of illumination. (A) CdSe/ZnS QDs alone. (B) QD-high DA. (C) QD-BME. (D) QD-DA-BME. (E) CdTe QDs alone. (B) QD-high DA. (C) QD-BME. (D) QD-DA-BME.

PL enhanced quickly for several minutes and declined significantly thereafter (Fig. 2.3B). These samples never attained the level of enhancement seen with the CdSe/ZnS-High DA and Low DA without BME. It was also useful to compare the integrated PL of the CdSe/ZnS QDs in the absence and presence of DA; the best fit to this data was obtained by calculating I_0/I, where I_0 was the

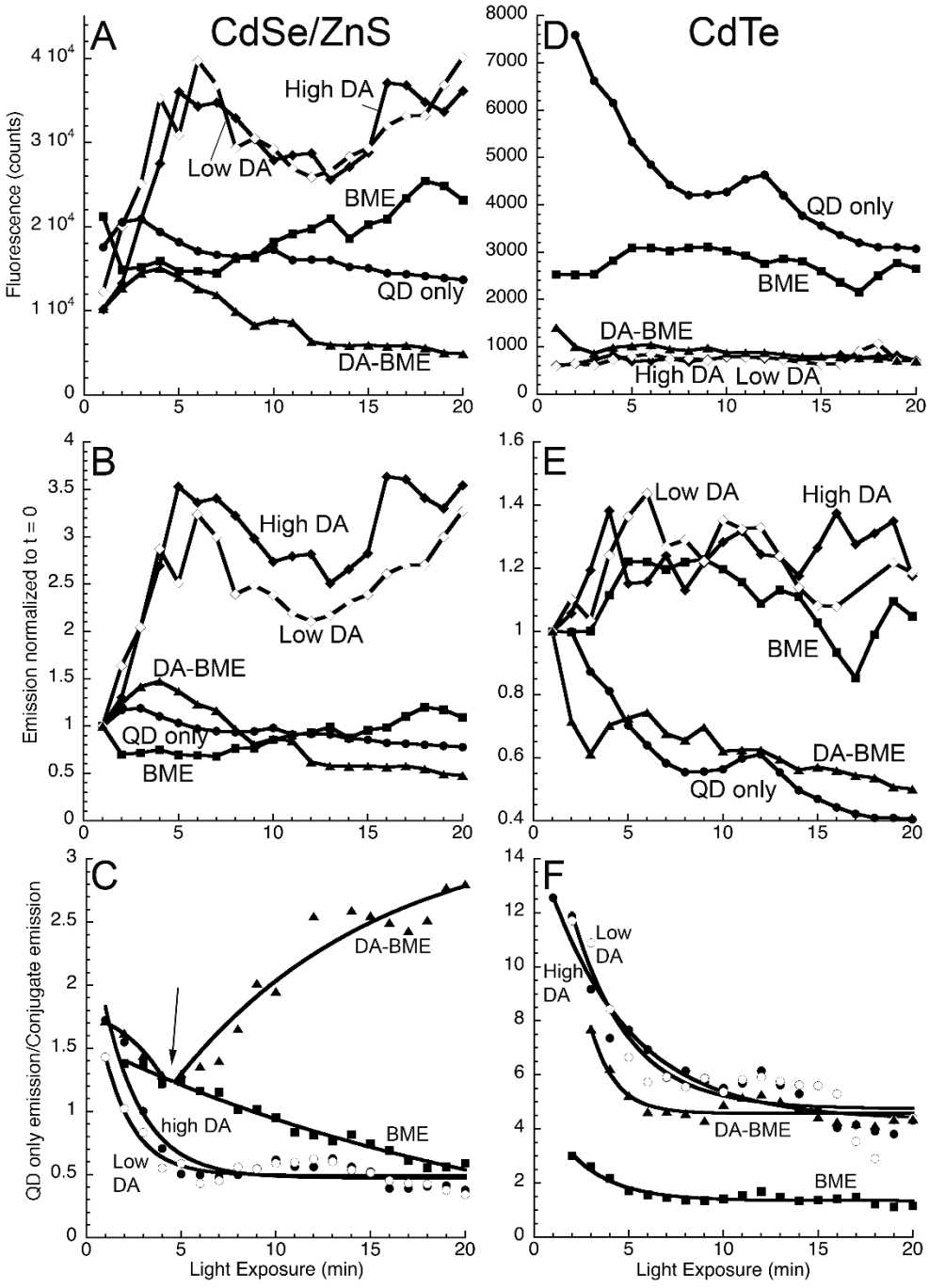

Figure 2.3 Integrated photoluminescence for irradiated samples, corresponding to steady-state emission at peak. The lines are guides for the eye except in panels C, F. Shown are QD only (●), QD-BME (■), QD-low DA (◊), QD-high DA (♦), and QD-DA-BME (▲). (A) Total integrated fluorescence for CdSe/ZnS. (B) CdSe/ZnS fluorescence normalized to its initial value. (C)

CdSe/ZnS fluorescence for conjugates divided by that of CdSe/ZnS alone at each given time point. The symbols are data points, and the lines are fits to Eq. 2.1 for QD-BME (■) (a = -0.23, b = 1.78, c = .042; R^2 = 0.99), QD-low DA (❍)(a = 0.49, b = 1.79, c = .63; R^2 = 0.94), QD-high DA (●)(a = 0.47, b = 2.23, c = .49; R^2 = 0.96), and QD-high-DA-BME (▲). DA-BME required 2 fits: for t ≤ 4 min, a = 1.89, b = -.126, c = -.40; R^2 = 0.99; for t > 4 min, a = 3.26, b = -3.16, c = .094; R^2 = 0.94. The arrow indicates the inflection point. (D) Total integrated fluorescence for CdTe. (E) CdSe/ZnS fluorescence normalized to its initial value. (F) CdTe fluorescence for conjugates divided by that of CdTe alone at each given time point, with the lines indicating exponential fits. Shown are QD-BME (■)(a = 1.34, b = 4.13, c = .043; R^2 = 0.96), QD-low DA (❍)(a = 4.74, b = 14.26, c = 0.34; R^2 = 0.93), QD-high DA (●)(a = 4.33, b = 10.44, c = .23; R^2 = 0.97), and QD-high-DA-BME (▲)(a = 4.57, b = 32.6, c = .77; R^2 = 0.92).

CdSe/ZnS QD-only PL at each time point and I was the value of the samples with DA coverage at the same time point (Fig. 2.3C). The ratio I_0/I is typically used for Stern-Volmer analysis of quenching phenomena. The reduced level of fluctuation seen in this ratio suggested that the observed variations were a reproducible feature of all of the QD preparations, thus not a result of the conjugate. Relative to CdSe/ZnS QDs alone, the effect of DA was initial quenching of the PL, followed by a rapid enhancement. BME treatment caused a gradual enhancement of the PL, while the presence of both DA and BME lead to quenching (Fig. 2.3C).

CdTe total emission decayed sharply with time but was held stable with BME; total emission was weak in DA conjugates even over the irradiation period (Fig. 2.3D). When normalized to start values, it was seen that QDs only and DA-BME conjugates declined with time, while all the others remained relatively stable, with moderate fluctuations (Fig. 2.3E). When

normalized to QDs alone as above, it was seen that all of the conjugates and preparations were quenched, the dopamine conjugates very strongly and the BME preparation only slightly. In all cases, light exposure decreased the quenching (Fig. 2.3F). Irradiation of CdTe conjugates led to loss of solubility and precipitation.

The values relative to QDs alone could be fit to exponential curves

$$\frac{I_0}{I} = a + b\exp(-ct) \tag{2.1}$$

where *a, b*, and *c* were fit parameters with values given in the figure captions. The other values fluctuated too much for a reasonable fit.

2.3.3 One-minute lifetime scans

The changes in total integrated photoluminescence were reflected in changes in lifetime. For CdSe/ZnS, QD-High DA and Low DA began with a small but measurable enhancement over QD alone and lifetimes continued to lengthen over the irradiation period (Fig. 2.4A). QDs alone in the presence of BME showed a faster lifetime than QDs alone, but this did not change visibly with light exposure. The lifetimes of CdSe/ZnS-DA-BME, however, did change significantly: lifetimes began with a rapid decay but developed a slow component upon irradiation (Fig. 2.4B).

CdTe QDs were different from CdSe/ZnS in several notable ways. The lifetimes of the QDs alone were much longer, and dopamine conjugation led to a striking reduction. Although the irradiated samples recovered, they never reached the point of the QDs alone (Fig. 2.4C). CdTe-BME showed a significantly faster lifetime than the QDs alone, with no appreciable changes upon irradiation. However, CdTe-DA conjugates enhanced in the presence of BME, nearly achieving the lifetimes of the CdTe-BME after 20 min (Fig. 2.4D).

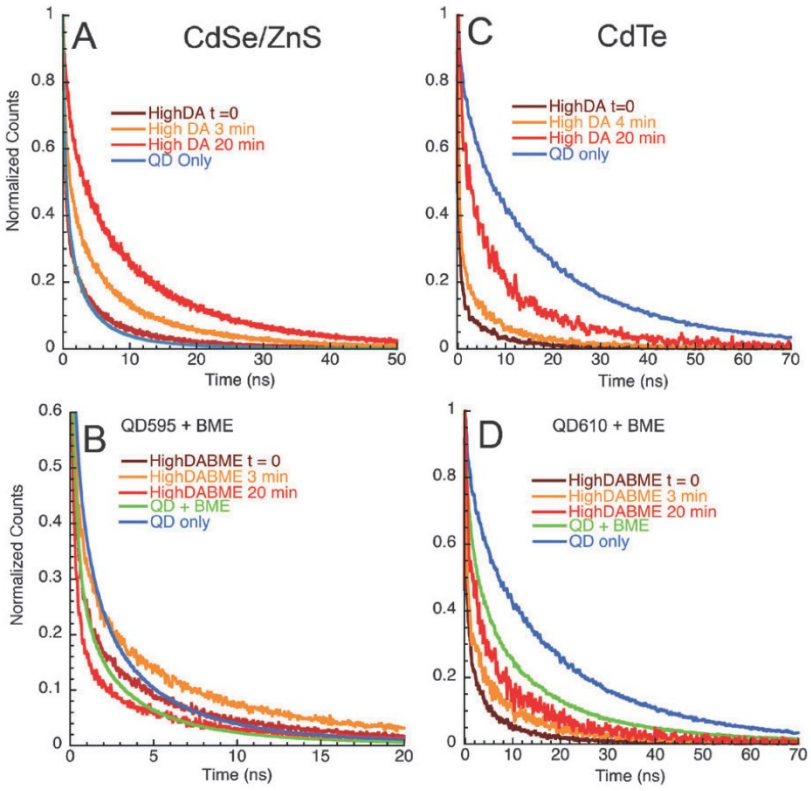

Figure 2.4 Lifetime traces from QD preparations exposed to 2.4 mW, 400 nm laser light in one-minute increments. The first scan is taken as $t = 0$. (A) CdSe/ZnS QD alone average over all 20 scans (blue), with QD-High DA at three time points shown for comparison. No perceptible changes were seen in the QDs alone. Low DA was similar to High DA and is not shown. (B) CdSe/ZnS with BME. Neither the QDs alone (blue) nor the QDs with BME (green) showed any perceptible lifetime changes, and the time-average is shown. With BME present, the High DA conjugate showed first a lifetime increase ($t = 3$ min, orange) followed by a decrease ($t = 20$ min, red) relative to the initial values ($t = 0$, maroon). (C) CdTe QDs, with QDs alone unchanging (blue) and changes seen in the High DA conjugate. (D) CdTe QDs with BME, showing stable values for QD-BME (green) and QDs alone shown for comparison (blue).

The latest irradiation times pictured (10 or 20 min) represented a plateau, with the last 4-5 scans overlapping (not shown). Thus, the graphs shown indicate the maximum photoenhancement in each case.

2.3.4 Stretched exponential fits to lifetimes

The fluorescence intensity I with time could be fit to a stretched exponential function

$$I = A\ \exp(-[t/\tau\ ]^{\beta}) \tag{2.2}$$

where τ represents a stretched exponential with a stretching factor β. This model has shown to provide better estimates of average lifetimes than a multiexponential model, with the average lifetime given by

$$\langle\tau\rangle = \frac{\tau}{\beta}\Gamma\left(\frac{1}{\beta}\right) \tag{2.3}$$

where Γ is the gamma function. Stretched exponentials are commonly used for QDs as they provide a good estimate of average lifetime, along with an evaluation of the heterogeneity of the sample; for homogeneous samples, β will tend towards 1[29]. In principle inverse Laplace transforms may be used to extract multiple exponentials from a stretched exponential fit; however, in practice this is poorly defined as it is extremely sensitive to the quality of the underlying fit. This model was able to provide a good qualitative view of the changes associated with light exposure in these conjugates. For CdSe/ZnS, a single stretched exponential was insufficient to fit the early times, and an additional fast lifetime τ' was added as has been done previously for similar QDs[30]:

$$I = A\exp(-[t/\tau]^{\beta}) + A'\exp(-t/\tau') \tag{2.4}$$

CdTe QDs did not require this factor. In both cases, the stretched exponential provided better fits than a sum of three exponentials. QDs alone of both types showed minimal changes with

irradiation, but in the presence of dopamine and/or BME the changes were substantial (Table 2.1, Fig. 2.5) (Full fits and goodness-of-fit parameters are given in Appendix A).

The average lifetimes were plotted vs. time to determine the magnitude and time course of the changes. For CdSe/ZnS, the particles alone showed no photoenhancement under these conditions, but rather a slight decrease in lifetime with irradiation. BME had a small effect, namely to slightly enhance lifetimes after > 10 min of irradiation, protecting against the decrease seen with the particles alone. In contrast, QD-dopamine showed a large exponential enhancement of lifetime, with no difference between the low and high dopamine conjugates. In the presence of DA and BME, the initial response was comparable to that of DA, with the lifetimes then decaying back almost to QD-alone baseline (Fig. 2.5A). When normalized to $t = 0$, the same effects were apparent, but the enhancement effect of BME at later times became more apparent (Fig. 2.5B). When QD lifetimes were divided by conjugate lifetimes, it could be seen that BME was a quencher at early times, but its curve approached that of QDs alone by the end of the irradiation period. Both High DA and Low DA enhanced equally. The mixture of DA-BME began by following the DA curve, then turned around and approached the BME curve after ~5 min (Fig. 2.5C).

For CdTe, average lifetimes were significantly shortened by BME, but neither QDs alone nor QD-BME changed significantly with 20 min of irradiation (Fig. 2.5D). Dopamine resulted in a slow exponential enhancement to a plateau lifetime four times faster than that with QDs alone. Low DA showed a similar pattern to high DA but at a reduced level at all time points. DA-BME made the effect occur more rapidly but resulted in the same plateau value (Fig. 2.5D). Normalization to $t = 0$ (Fig. 2.5E) or division of QD-only values by conjugate values (Fig. 2.5F) made the strong dependence upon DA concentration more marked.

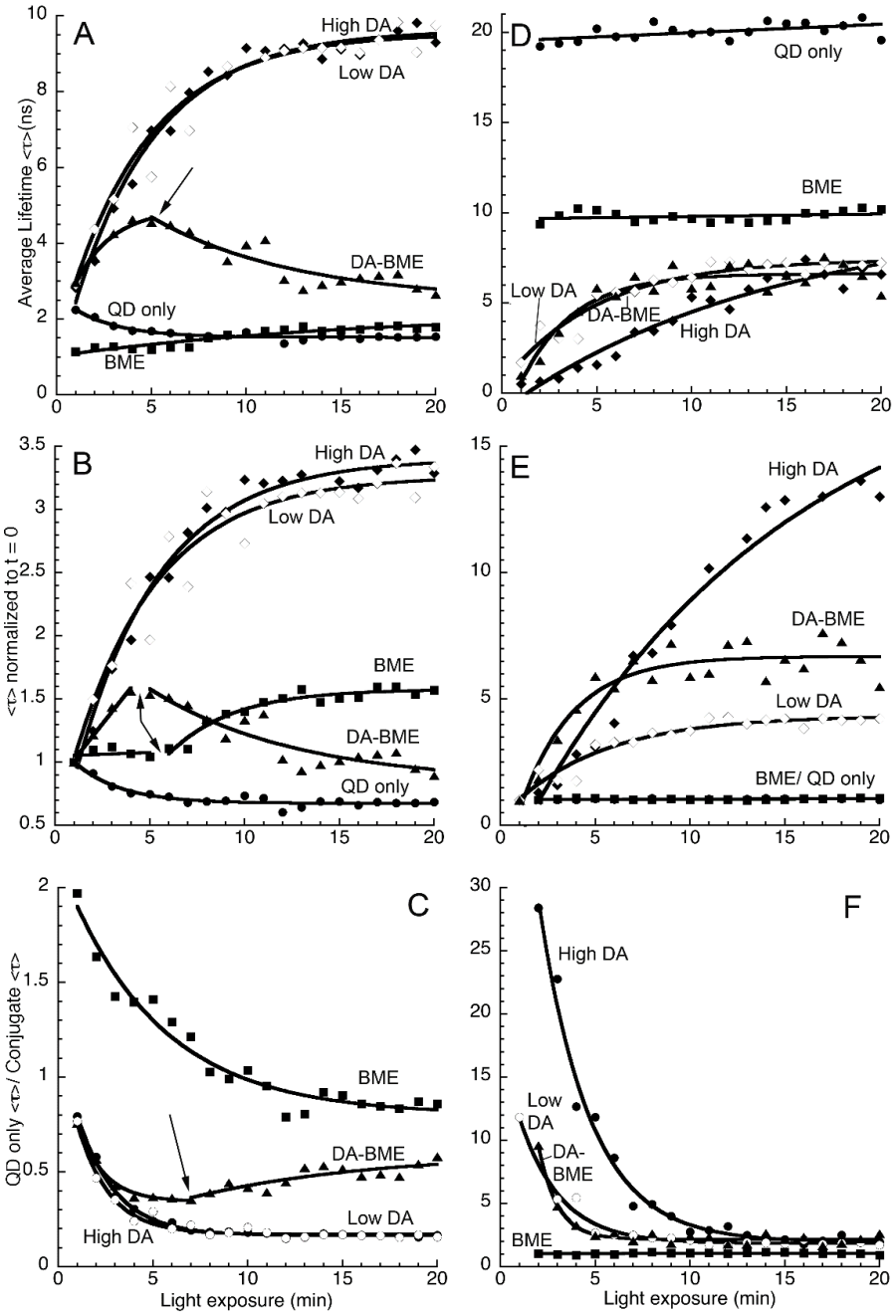

Figure 2.5 Average (slow) lifetimes vs. light exposure for two types of QDs with and without dopamine at the highest concentration and/or BME. The symbols are data points, and the lines are fits to exponentials or to straight lines (fits given in Table 2.2). Shown are QD only (●), QD-BME (■), QD-low DA (◊), QD-high DA (♦), and QD-high-DA-BME (▲). (A) CdSe/ZnS core-shell. The low DA curve overlaps the high DA curve although it is slightly noisier (Table 2.2). The curve

for DA-BME was fit to a rising exponential at early times ($t \leq 5$ min) and a falling exponential for $t > 5$ min; the arrow indicates the inflection point. (B) CdSe/ZnS normalized to initial values. From this graph the enhancement effect of DA relative to QDs alone can be appreciated, and the inflection point indicates the shift of DA-BME from rising to falling. The curve for BME only was flat and began its exponential rise at the point indicated by the arrow. (C) Lifetimes of CdSe/ZnS QDs only divided by those of conjugates. The curves for high DA (●) and low DA (❍ overlap almost perfectly, whereas those of BME (■) and DA-BME (▲) are distinct. (D) Average lifetimes for CdTe and conjugates. (E) CdTe and conjugates normalized to $t = 0$. The curves for BME only and QD only overlap. Note the large difference between high DA (♦) and low DA (◊). (F) CdTe QD only lifetimes divided by those of conjugates. Note the difference between High DA (●) and low DA (❍; the latter is similar to DA-BME (▲).

All of the lifetime vs. time curves could be fit to Eq. 2.1 and parameters are given in Table 2.2.

The fast time constants were also altered by DA for CdSe/ZnS. DA led to an increase in the fast time constant and to large fluctuations in this constant with time of irradiation; these were not seen with QDs alone or with BME (Fig. 2.6A). In the presence of both DA and BME, the fast constant rose to the level of the case with DA, then fell below that of BME, without major fluctuations (Fig. 2.6B). The percentage of the amplitude represented by the fast component showed a slow increase in all cases except when dopamine was present (Fig. 2.6C).

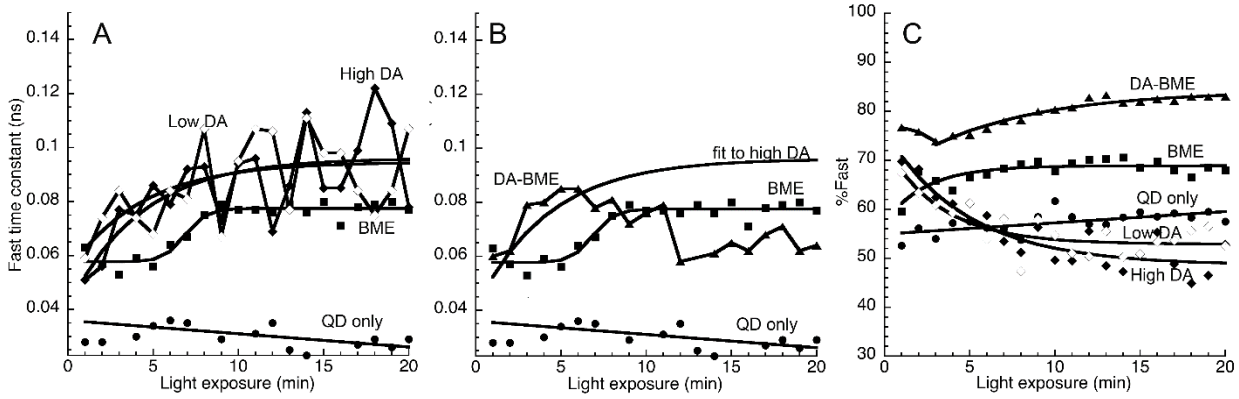

Figure 2.6 Fast time constants and percentage of amplitude represented by the fast component for CdSe/ZnS QDs with and without dopamine and/or BME. The lines are fits to Eq. 2.1 unless stated otherwise. (A) Fast time constant for QD only (●), QD-BME (■), QD-high DA (♦), and QD-low DA (◊). Approximate fits to High and Low DA are shown (see Table 2.2); a line is also drawn between successive points to illustrate the observed fluctuations. (B) DA-BME (▲) is shown separately for ease of visualization with respect to QD only(●), QD-BME (■), and the fit to high DA (line). (C) Percent fast for QD only (●), QD-BME (■), QD-high DA (♦), QD-DA (◊), and QD-DA-BME (▲).

2.3.5 Effects of oxygen removal

In the absence of oxygen, CdSe/ZnS QDs alone had lifetimes approximately one-half those of the aerated sample. A slight reduction in lifetime occurred over the irradiation period. CdSe/ZnS-DA was almost completely quenched, with lifetimes more than five-fold smaller than the QDs alone (Fig. 2.7A, B). The dopamine conjugates fit best to a single stretched exponential (Table 2.1). PFE was completely abolished (Fig. 2.7B, Table 2.1, Table 2.2). Absorbance spectra showed loss of the exciton peak with no changes upon irradiation (not shown).

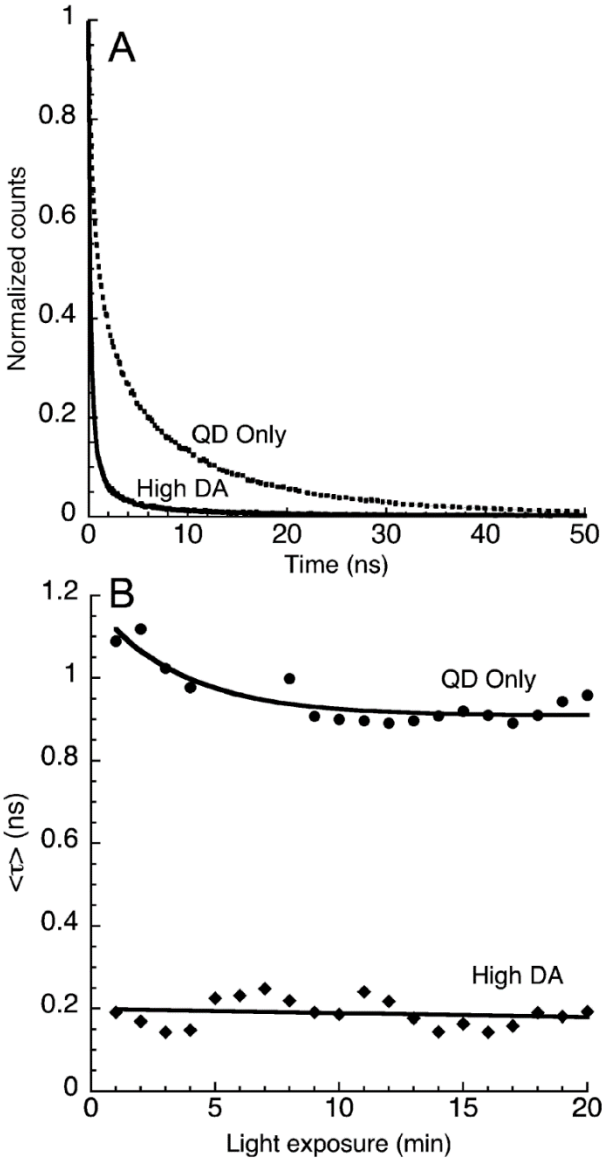

Figure 2.7 Lifetime traces and fits for deaerated samples. Fit values are given in Tables 2.1 and 2.2. (A) Average of 20 one-minute scans for CdSe/ZnS only and QD-high DA. The scans overlapped completely for high DA and shifted only slightly for QD only. (B) Average lifetimes for QD only (●) and QD-high DA (♦) vs. time; the lines are best fits to Eq 2.1.

For CdTe, DA conjugation in the absence of oxygen led to profound quenching, so that even at our largest slit width the signal was too weak to obtain lifetime values. 20 min of laser light exposure did not reverse this quenching (not shown).

2.4 Discussion

We report the first time-resolved study of photobrightening of QDs conjugated to an electron donor. Many previous studies have shown PFE in unconjugated QDs[6, 10, 11, 31, 32], and other studies have confirmed that chemical electron injection quenches QD fluorescence[13, 33]. However, the photo-induced changes in these quenched QDs have so far only been reported in a cyclic voltammetry study involving direct electron injection[12]. Our findings are consistent with those of that study, which found that quenching due to electron injection could be removed by light exposure in the presence of oxygen, in a manner dependent upon illumination power.

We had previously confirmed such power dependence in steady-state spectra of QD-dopamine, and found here that no changes in lifetime were observed at illumination powers < 2 mW[16]. This suggests that this is a true photoenhancement effect and not simply an artefact of passivation.

Rather than being exposed to a high concentration of DA molecules, the QDs were conjugated to a limited number of them (approximately 200/particle). This led to a photoenhancement effect that lasted 5-10 min before reaching a plateau. The different behaviors of the different types of QDs suggest quite different models for the effects seen here.

2.4.1 CdSe/ZnS

In the absence of oxygen, CdSe/ZnS is quenched by dopamine conjugation and the quenching is not reversed by light. This implies that DA can transfer an electron to the QD, leading to a

negatively charged "off" state. It is possible for such a state to be permanently non-radiative if the surface-trapped electron interacts with photogenerated holes in a non-radiative pathway (Fig. 2.8A).

The off state is extremely sensitive to environmental conditions, namely oxygen. This highly suggests that the electron is not in the conduction band of the CdSe core, which is well passivated by the ZnS shell. We thus postulate that the electron from the DA is in a trap state on the surface of the ZnS. In this case, several things can happen in the presence of oxygen, even in the dark (Fig. 2.8B, C). DA autoxidizes readily, especially in the presence of metal ions, leading to the formation of reactive oxygen species. These reactive species can bind to the QD surface and passivate trap states by raising their energy level above that of the CdSe band edge. In these experiments, the QD-DA conjugate had longer lifetimes than the QDs alone even before irradiation when oxygen was present, suggesting that some degree of passivation had occurred already. We expect that the degree of passivation seen in the dark will be highly variable among QD batches and colors, being related to surface defect states. In steady-state experiments, we have consistently seen great variability in the amount of quenching caused by DA conjugation[1].

The slight enhancement at time 0 is quickly overwhelmed by photo-induced lifetime changes. Electrons in deep trap states can only be removed by photoexcitation and recombination with a hole; thus, deep trap states will remain until the particle has generated enough excitons to remove them. Each time the particle is excited, ligands such as water and reactive oxygen species bind to the charged QD by electrostatic interactions and compete for the trap sites. The more tightly these ligands bind and the more they raise the energy level of the trap states, the more complete is the passivation and thus the brighter the QD. Once all the trap states are passivated, there is no place for the photogenerated electron to go except into the $1S_e$ exciton level. At this point, the

lifetime decay should be described as a single exponential with a lifetime of tens of ns, which is the band-edge lifetime[34].

It is believed that several thousand excitons are needed to fully passivate a QD surface by photoexcitation and ligand rearrangement[12]. The photoenhancement that we see here is not entirely complete, since the QDs never show a complete loss of the fast component, simply a reduction (Fig. 2.6). However, the dopamine-dependent PFE we see is limited by the amount of DA on the particle. Once all the DA molecules are oxidized, the mechanism in Figure 2.8 can no longer take place. The degree in reduction in the fast component was less in low-DA conjugates than in those with high DA.

In the presence of the antioxidant BME, PFE is only seen for the first 4 min of irradiation, and is followed by a decrease in lifetimes. This observation supports the oxidative model. BME can reduce dopamine quinones and free radicals, preventing the generation of ROS (Fig. 2.8D). Further irradiation causes the passivating agents to desorb, returning the lifetime values to near those of QDs alone. It is also possible for BME molecules to replace the solubilizing thiols on the QD; however, because QD-BME and QDs alone show similar lifetimes, this was difficult to ascertain from these experiments.

Oscillations were seen in lifetime values of CdSe/ZnS-DA, particularly in the fast component. Previous studies have observed fluorescence oscillations in QD solutions, which were dependent upon salt concentration and temperature and had a period of ~ 8 min[35]. These were attributed to interaction with ions in the solution. Our oscillations occurred on a faster time scale, but are consistent with the same explanation. Since passivation of traps requires electrostatic binding, any alteration of QD charge or ionizability will affect PFE.

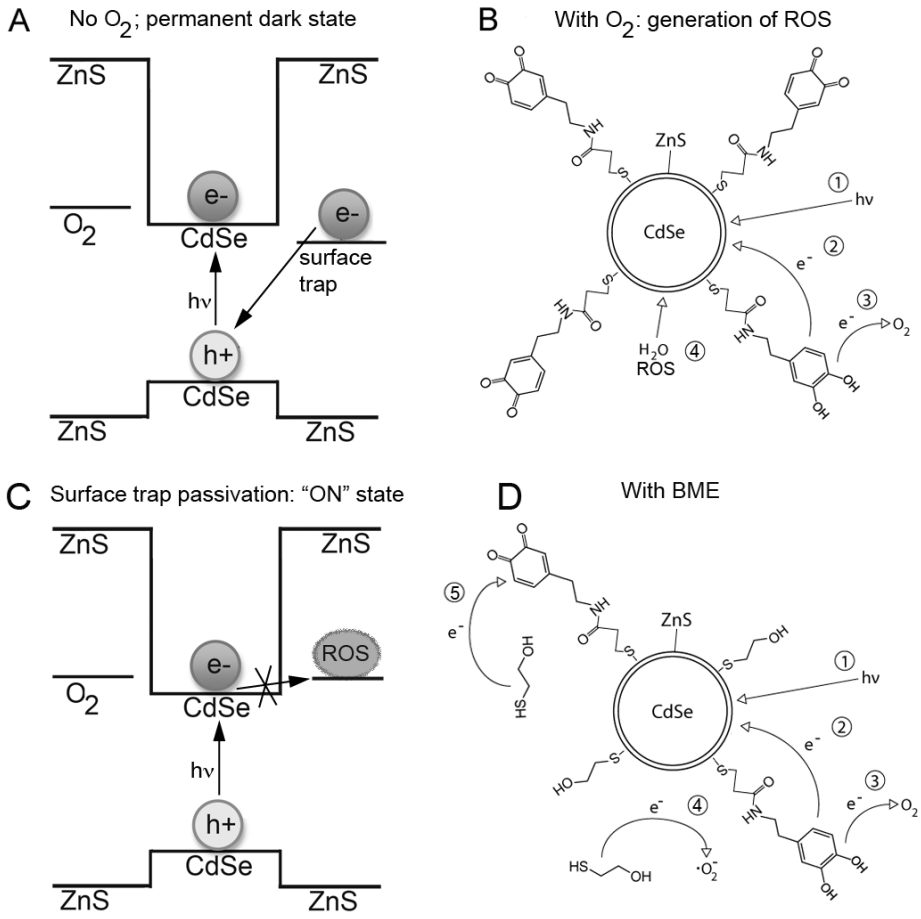

Figure 2.8 Proposed mechanisms of PFE in CdSe/ZnS. (A) In the absence of oxygen, the DA transfers an electron to a trap state on the surface of the ZnS shell. This state has a high cross-section for recombination with photogenerated holes, so that a photogenerated exciton is likely to recombine non-radiatively, creating a dark state. (B) In the presence of oxygen, a photogenerated exciton (1) leads to electron transfer (2) as before. However, the oxidized dopamine can interact with molecular oxygen and lead to ROS generation (3); these species and water can bind to the QD surface (4) with varying degrees of affinity. Once all the dopamines are oxidized, the process ends, leading to a plateau in the effect. (C) Mechanism of passivation by water and ROS. A ligand that raises the energy level of the trap state above the CdSe band edge passivates the trap completely. One that raises it somewhat, but not above the band edge, passivates it partially. Water

binds traps weakly and can be removed during photoexcitation; other ligands bind more tightly. (D) In the presence of BME, any ROS (4) or oxidized dopamine (5) produced will probably be scavenged before they interact with the QD, greatly reducing the PFE effect. BME molecules can also bind directly to the surface of the QD, displacing the dopamine (6).

2.4.2 CdTe

An important difference between CdTe and CdSe is that CdTe is enhanced by thiol ligands such as MPA, whereas CdSe is quenched. Thiol-capped CdTe QDs show long lifetimes which may approach single exponentials[36]. Correspondingly, we observe that the CdTe QDs only have the longest lifetimes of any of the samples, and that any changes to the MPA cap reduce lifetimes. Dopamine quenches the particle PL and lifetimes almost completely. This suggests that direct electron transfer is occurring between the conjugate and the particles (Fig. 2.9A). As the conjugates are irradiated, the quenching is reduced to a certain point; enhancement plateaus after ~10 min for low DA and ~20 min for high DA. These changes are accompanied by loss of solubility, suggesting that what is being observed in this case is cap decay. CdTe is unstable to irradiation, even more so under oxidizing conditions, with loss of surface capping groups and aggregation[37]. The departure of the surface groups leads to loss of the quencher and thus relative brightening, but never brightening to the extent of the original particles because of the creation of surface defects and because the enhancement effect of the MPA is being lost (Fig. 2.9B). This model is supported by the observation that high DA conjugates enhance more slowly than low DA conjugates: with high DA, more capping groups must be lost to eliminate the quenching effect.

In the presence of BME, there is a degree of enhancement followed by a plateau, without loss of solubility. We thus conclude that the BME molecules are binding to the QD upon loss of

the surface cap, which eliminates the quenching caused by DA but results in a shorter lifetime than that of QDs alone (Fig. 2.9C).

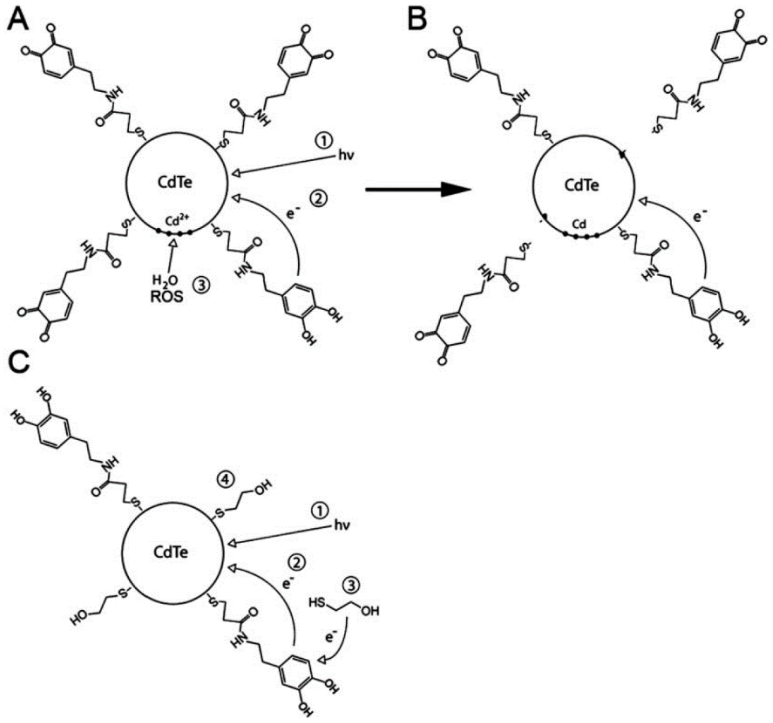

Figure 2.9 Proposed mechanisms of PFE in CdTe. (A) Dopamine can transfer an electron to CdTe (1, 2) leading to ROS (3) which leads to formation of disulfide bonds between capping groups and cap decay. (B) Upon prolonged illumination in the presence of oxygen and oxidative species, nearly all the solubilizing groups detach from the QD, leaving behind surface defects. The final product is poorly soluble and less fluorescent than the original QDs because the enhancement effect of the MPA has been lost. (C) In the presence of BME, electron transfer can occur as before (1, 2) except that the dopamine is re-reduced after electron transfer (3). In addition, BME molecules can replace surface ligands, leading to a lower number of DA molecules/QD without loss of solubility (4).

2.5 Conclusions

Chemical injection of electrons into QDs can lead to quenching followed by photoinduced enhancement that is dependent upon the presence of oxygen. This is consistent with what was seen in cyclic voltammetry experiments[12]. Future studies will relate the mechanisms elucidated here to blinking statistics and femtosecond absorption results and will explore quantitative variations in oxygen saturation.

It is expected that results will vary according to QD size (and thus position of the band edges), shell thickness, and number of surface defect states. This could possibly be used as a principle to design biosensors for anoxic environments, which is important for several applications. In particular, photodynamic therapy targeted to cells is highly sensitive to microenvironment, especially oxygen concentration, limiting its effectiveness in solid tumors such as lung cancer that have a large hypoxic component[38, 39].

Table 2.1 Lifetimes from fits to stretched exponential or stretched exponential plus fast component ; [% fast] indicates the ratio of amplitudes: 100[A'/(A+A')]. "Before" and "After" indicate before or after 20 min of 400 nm irradiation at 2.4 mW. $\langle\tau\rangle$ is calculated from Eq (2.2); for all fit parameters and goodness-of-fit results, see Appendix A. *Taken at maximum, which occurred at < 20 min irradiation.

Sample	**$\langle\tau\rangle$ (ns)**	**τ' (ns) [% fast]**
QD595 CdSe/ZnS Before	2.2	0.028 [53]
QD595 CdSe/ZnS After	1.5	0.028 [58]

QD595+ BME Before	1.2	0.057 [64]
QD595+ BME After	1.8	0.078 [68]
QD595-DA Before	2.8	0.051 [70]
QD595-DA After	9.3	0.10 [48]
QD595-DA+ BME Before	2.9	0.061 [77]
QD595-DA+ BME After	4.6*	0.081[83] *
QD-595 CdSe/ZnS Deaerated Before	1.1	0.16 [48]
QD-595 CdSe/ZnS Deaerated After	0.9	0.24 [41]
QD-595-DA Deaerated Before	0.16	0 [0]
QD-595-DA Deaerated After	0.16	0 [0]
QD610 CdTe Before	19.3	0 [0]
QD610 CdTe After	19.5	0 [0]
QD610+ BME Before	9.6	0 [0]
QD610+ BME After	10.2	0 [0]
QD610-DA Before	0.5	0 [0]
QD610-DA After	6.7	0 [0]
QD610-DA+ BME Before	1.0	0 [0]

QD610-DA+ BME After	7.1*	0 [0]

Table 2.2 Fits of lifetimes (raw and normalized) vs. time of irradiation to exponentials ($y = a + be^{-cx}$). When $c = 0$, the fit is a straight line of the form $y = a + bx$.

Sample	***a***	***b***	***c***	R^2
CdSe/ZnS only	1.52	1.12	0.40	0.96
Normalized to t = 0	0.68	0.50	0.40	0.96
CdSe/ZnS+BME	2.20	-1.18	0.06	0.94
Normalized to t= 0 (t > 4 min)	1.58	-2.96	0.29	0.96
Relative to QD only	0.80	1.34	0.20	0.98
CdSe/ZnS-HighDA	9.62	-9.03	0.23	0.99
Normalized to t= 0	3.40	-3.20	0.23	0.99
Relative to QD only	0.16	1.05	0.50	0.99
CdSe/ZnS-LowDA	9.53	-8.22	0.23	0.96
Normalized to t= 0	3.27	-2.82	0.23	0.96
Relative to QD only	0.17	1.05	0.59	0.99
CdSe/ZnS-High DA + BME (t > 4 min)	2.48	4.22	0.13	0.90
Normalized to t= 0 (t > 4 min)	1.22	-0.93	0.09	0.88

Relative to QD only (t < 7 min)	0.34	0.87	0.74	0.99
Relative to QD only (t > 7 min)	0.60	-0.49	0.10	0.90
CdSe/ZnS only deaerated	0.90	0.28	0.29	
CdSe/ZnS-HighDA deaerated	0.19	-0.001	0	
CdTe Only	19.51	0.047	0	0.99
Normalized to t = 0	1.01	0.002	0	0.99
CdTe+BME	9.65	0.014	0	0.99
Normalized to t= 0	1.02	0.002	0	0.99
Relative to QD only	1.02	0.002	0	0.99
CdTe+High DA	9.76	-10.7	0.07	0.97
Normalized to t= 0	19.2	-21.1	0.07	0.97
Relative to QD only	1.95	57.4	0.37	0.99
CdTe+Low DA	7.43	-6.92	0.20	0.96
Normalized to t= 0	4.34	-4.05	0.20	0.96
Relative to QD only	1.84	15.9	0.47	0.99
CdTe+High DA +BME	6.62	-8.67	0.36	0.94
Normalized to t= 0	6.69	-8.76	0.36	0.94
Relative to QD only	2.17	54.6	1.00	0.98

2.6 Acknowledgements

JLN, DRC and LC thank the CIHR Nanomedicine and Regenerative Medicine Seed Grant, the NSERC Individual Discovery program, and the US EPA. Work at USC is supported by the US National Science Foundation (CHE-0617060).

2.7 References

1. Clarke, S. J.; Hollmann, C. A.; Zhang, Z.; Suffern, D.; Bradforth, S. E.; Dimitrijevic, N. M.; Minarik, W. G.; Nadeau, J. L. Photophysics of dopamine-modified quantum dots and effects on biological systems. *Nat Mater* **2006**.
2. Sandros, M. G.; Shete, V.; Benson, D. E. Selective, reversible, reagentless maltose biosensing with core-shell semiconducting nanoparticles. *Analyst* **2006,** *131* (2), 229-235.
3. Zayats, M.; Willner, I. Photoelectrochemical and optical applications of semiconductor quantum dots for bioanalysis. In *Biosensing for the 21st Century*, 2008; Vol. 109, pp 255-283.
4. Zhang, Y.; He, J.; Wang, P. N.; Chen, J. Y.; Lu, Z. J.; Lu, D. R.; Guo, J.; Wang, C. C.; Yang, W. L. Time-dependent photoluminescence blue shift of the quantum dots in living cells: Effect of oxidation by singlet oxygen. *Journal of the American Chemical Society* **2006,** *128* (41), 13396-13401.
5. Oda, M.; Tsukamoto, J.; Hasegawa, A.; Iwami, N.; Nishiura, K.; Hagiwara, I.; Ando, N.; Horiuchi, H.; Tani, T. Photobrightening of CdSe/ZnS/TOPO nanocrystals. *Journal of Luminescence* **2007,** *122*, 762-765.
6. Yuan, C. T.; Chou, W. C.; Chuu, D. S.; Chen, Y. N.; Lin, C. A.; Chang, W. H. Photoinduced fluorescence enhancement in colloidal CdSeTe/ZnS core/shell quantum dots. *Applied Physics Letters* **2008,** *92* (18), 183108.
7. Jones, M.; Nedeljkovic, J.; Ellingson, R. J.; Nozik, A. J.; Rumbles, G. Photoenhancement of luminescence in colloidal CdSe quantum dot solutions. *Journal of Physical Chemistry B* **2003,** *107* (41), 11346-11352.
8. Aldana, J.; Wang, Y. A.; Peng, X. G. Photochemical instability of CdSe nanocrystals coated by hydrophilic thiols. *Journal of the American Chemical Society* **2001,** *123* (36), 8844-8850.
9. Cordero, S. R.; Carson, P. J.; Estabrook, R. A.; Strouse, G. F.; Buratto, S. K. Photo-activated luminescence of CdSe quantum dot monolayers. *Journal of Physical Chemistry B* **2000,** *104* (51), 12137-12142.
10. Uematsu, T.; Maenosono, S.; Yamaguchi, Y. Photoinduced fluorescence enhancement in mono- and multilayer films of CdSe/ZnS quantum dots: Dependence on intensity and wavelength of excitation light. *Journal of Physical Chemistry B* **2005,** *109* (18), 8613-8618.
11. Uematsu, T.; Maenosono, S.; Yamaguchi, Y. Photoinduced fluorescence enhancement in CdSe/ZnS quantum dot monolayers: Influence of substrate. *Applied Physics Letters* **2006,** *89* (3), 031910.
12. Gooding, A. K.; Gomez, D. E.; Mulvaney, P. The effects of electron and hole injection on the photoluminescence of CdSe/CdS/ZnS nanocrystal monolayers. *Acs Nano* **2008,** *2* (4), 669-676.
13. Shim, M.; Wang, C.; Guyot-Sionnest, P. Charge-tunable optical properties in colloidal semiconductor quantum dots. *Journal of Physical Chemistry B* **2001,** *195*, 2369-2373.

14. Xu, G.; Iwasaki, Y.; Niwa, O. Selective electrochemical response of dopamine against 3,4-dihydroxyphenylacetic acid at bare indium-tin oxide electrode. *Chemistry Letters* **2005,** *34* (8), 1120-1121.
15. Akagawa, M.; Ishii, Y.; Ishii, T.; Shibata, T.; Yotsu-Yamashita, M.; Suyama, K.; Uchida, K. Metal-catalyzed oxidation of protein-bound dopamine. *Biochemistry* **2006,** *45* (50), 15120-8.
16. Clarke, S.; Koshy, S.; Zhang, J.; Cohen, N.; Nadeau, J. Power and wavelength dependence of photoenhancement in (CdSe)ZnS-dopamine in aqueous solution and live cells. *Zeitschrift Fur Physikalische Chemie-International Journal of Research in Physical Chemistry & Chemical Physics* **2008,** *222* (5-6), 851-863.
17. Nozik, A. J.; Memming, R. Physical chemistry of semiconductor-liquid interfaces. *Journal of Physical Chemistry* **1996,** *100* (31), 13061-13078.
18. Jasieniak, J.; Pacifico, J.; Signorini, R.; Chiasera, A.; Ferrari, M.; Martucci, A.; Mulvaney, P. Luminescence and amplified stimulated emission in CdSe-ZnS-nanocrystal-doped TiO_2 and ZrO_2 waveguides. *Advanced Functional Materials* **2007,** *17* (10), 1654-1662.
19. Moeno, S.; Idowu, M.; Nyokong, T. Spontaneous charge transfer between zinc tetramethyl-tetra-2,3-pyridinoporphyrazine and CdTe and ZnS quantum dots. *Inorganica Chimica Acta* **2008,** *361* (9-10), 2950-2956.
20. Asokan, S.; Krueger, K. M.; Alkhawaldeh, A.; Carreon, A. R.; Mu, Z. Z.; Colvin, V. L.; Mantzaris, N. V.; Wong, M. S. The use of heat transfer fluids in the synthesis of high-quality CdSe quantum dots, core/shell quantum dots, and quantum rods. *Nanotechnology* **2005,** *16* (10), 2000-2011.
21. Kloper, V.; Osovsky, R.; Kolny-Olesiak, J.; Sashchiuk, A.; Lifshitz, E. The Growth of Colloidal Cadmium Telluride Nanocrystal Quantum Dots in the Presence of Cd^0 Nanoparticles. *J. Phys. Chem. C* **2007,** *111* (28), 10336-10341.
22. Liu, W.; Choi, H. S.; Zimmer, J. P.; Tanaka, E.; Frangioni, J. V.; Bawendi, M. Compact cysteine-coated CdSe(ZnCdS) quantum dots for in vivo applications. *J Am Chem Soc* **2007,** *129* (47), 14530-1.
23. Yu, W. W.; Qu, L. H.; Guo, W. Z.; Peng, X. G. Experimental determination of the extinction coefficient of CdTe, CdSe, and CdS nanocrystals. *Chemistry of Materials* **2003,** *15* (14), 2854-2860.
24. Clarke, S. J.; Hollmann, C. A.; Aldaye, F. A.; Nadeau, J. L. Effect of ligand density on the spectral, physical, and biological characteristics of CdSe/ZnS quantum dots. *Bioconjug Chem* **2008,** *19* (2), 562-8.
25. Kloepfer, J. A.; Bradforth, S.; Nadeau, J. L. Photo-physical properties of biologically compatible CdSe quantum dot structures. *Journal of Physical Chemistry B* **2005,** *109*, 9996-10003.
26. Magde, D.; Wong, R.; Seybold, P. G. Fluorescence quantum yields and their relation to lifetimes of rhodamine 6G and fluorescein in nine solvents: improved absolute standards for quantum yields. *Photochem Photobiol* **2002,** *75* (4), 327-34.
27. Shim, M.; Guyot-Sionnest, P. n-type colloidal semiconductor nanocrystals. *Nature* **2000,** *407* (6807), 981-3.
28. Kloepfer, J. A.; Mielke, R. E.; Wong, M. S.; Nealson, K. H.; Stucky, G.; Nadeau, J. L. Quantum dots as strain- and metabolism-specific microbiological labels. *Appl Environ Microbiol* **2003,** *69* (7), 4205-13.
29. van Driel, A. F.; Nikolaev, I. S.; Vergeer, P.; Lodahl, P.; Vanmaekelbergh, D.; Vos, W. L. Statistical analysis of time-resolved emission from ensembles of semiconductor quantum dots: Interpretation of exponential decay models. *Physical Review B* **2007,** *75* (3), 8.

30. Oneil, M.; Marohn, J.; McLendon, G. Dynamics of electron-hole pair recombination in semiconductor clusters. *Journal of Physical Chemistry* **1990,** *94* (10), 4356-4363.
31. Bakalova, R.; Zhelev, Z.; Jose, R.; Nagase, T.; Ohba, H.; Ishikawa, M.; Baba, Y. Role of free cadmium and selenium ions in the potential mechanism for the enhancement of photoluminescence of CdSe quantum dots under ultraviolet irradiation. *Journal of nanoscience and nanotechnology* **2005,** *5* (6), 887-894.
32. Zhelev, Z.; Jose, R.; Nagase, T.; Ohba, H.; Bakalova, R.; Ishikawa, M.; Baba, Y. Enhancement of the photoluminescence of CdSe quantum dots during long-term UV-irradiation: privilege or fault in life science research? *Journal of photochemistry and photobiology. B, Biology* **2004,** *75* (1-2), 99-105.
33. Wang, C.; Shim, M.; Guyot-Sionnest, P. Electrochromic nanocrystal quantum dots. *Science* **2001,** *291* (5512), 2390-2.
34. Gong, H. M.; Zhou, Z. K.; Song, H.; Hao, Z. H.; Han, J. B.; Zhai, Y. Y.; Xiao, S.; Wang, Q. Q. The influence of surface trapping and dark states on the fluorescence emission efficiency and lifetime of CdSe and CdSe/ZnS quantum dots. *J Fluoresc* **2007,** *17* (6), 715-20.
35. Maenosono, S.; Eiha, N.; Yamaguchi, Y. Nonlinear time-series analysis of photoinduced fluorescence oscillation in a water dispersion of colloidal quantum dots. *Journal of Physical Chemistry B* **2003,** *107* (12), 2645-2650.
36. Wuister, S. F.; Donega, C.; Meijerink, A. Influence of Thiol Capping on the Exciton Luminescence and Decay Kinetics of CdTe and CdSe Quantum Dots. *Journal of Physical Chemistry B* **2004,** *108* 17393-17397.

37. Ma, J.; Chen, J. Y.; Zhang, Y.; Wang, P. N.; Guo, J.; Yang, W. L.; Wang, C. C. Photochemical instability of thiol-capped CdTe quantum dots in aqueous solution and living cells: process and mechanism. *J Phys Chem B* **2007,** *111* (41), 12012-6.
38. Juarranz, A.; Jaen, P.; Sanz-Rodriguez, F.; Cuevas, J.; Gonzalez, S. Photodynamic therapy of cancer. Basic principles and applications. *Clinical & Translational Oncology* **2008,** *10* (3), 148-154.
39. Chen, B.; Pogue, B. W.; Zhou, X. D.; O'Hara, J. A.; Solban, N.; Demidenko, E.; Hoopes, P. J.; Hasan, T. Effect of tumor host microenvironment on photodynamic therapy in a rat prostate tumor model. *Clinical Cancer Research* **2005,** *11* (2), 720-727.

Chapter 3

Photosensitization of CdSe/ZnS QDs and reliability of assays for reactive oxygen species production

Abstract

CdSe/ZnS quantum dots (QDs) conjugated to biomolecules that can act as electron donors are said to be "photosensitized": that is, they are able to oxidize or reduce molecules whose redox potential lies inside their band edges, in particular molecular oxygen and water. This leads to the formation of reactive oxygen species (ROS) and phototoxicity. In this work, we quantify the generation of different forms of ROS from as-synthesized QDs in toluene; water-solubilized, unconjugated QDs; QDs conjugated to the neurotransmitter dopamine; and dopamine alone. Results of indirect fluorescent ROS assays, both in solution and inside cells, are compared with those of spin-trap electron paramagnetic resonance spectroscopy (EPR). The effect of these particles on the metabolism of mammalian cells is shown to be dependent upon light exposure and proportional to the amount of ROS generated.

Adapted from:

Cooper, D. R., Dimitrijevic, N. M., & Nadeau, J. L. (2010). Photosensitization of CdSe/ZnS QDs and reliability of assays for reactive oxygen species production. *Nanoscale*, *2*(1), 114-121.

3. Photosensitization of CdSe/ZnS QDs and reliability of assays for reactive oxygen species production

3.1 Introduction

A photosensitizer (or photocatalyst) is any substance that upon absorption of light (ultraviolet, visible, or infrared) is able to transfer energy to another molecule; when the final acceptor molecule is water or oxygen, this leads to the generation of reactive oxygen species (ROS) which are lethal to bacteria, fungi, and mammalian cells. The use of photosensitizers to kill bacteria is highly effective and has been investigated since the middle of the nineteenth century, notably by Paul Ehrlich. The field was largely forgotten with the discovery of antibiotics, but has recently attracted increasing interest due to the emergence of antibiotic-resistant pathogens. Due to their high absorption and emission yields, most photosensitizers are organic dye molecules. Common dyes such as methylene blue, acridine orange, and toluidine blue serve as non-specific bacterial stains as well as light-activated microbicides[1]. However, most dyes are photochemically unstable and may not be able absorb light in the desired wavelength range. Since 99% of the energy output from the sun is in the visible range, it is desirable for photosensitizers for sunlight-mediated disinfection to absorb visible light. For medical applications, absorbance in the near infrared range is desirable, as these wavelengths penetrate more deeply into tissues than visible light[2].

The photocatalytic properties of semiconductor nanoparticles have been recognized for at least a decade as an important tool for environmental or therapeutic applications[3, 4]. Nanoparticles are more photostable than dyes, the procedures for their synthesis are simpler, and their absorbance properties can be adjusted by varying particle material and size. TiO_2 and ZnS particles have been made into solar cells; Ag and TiO_2 have been used as microbicides in anti-microbial clothing[5] and protocols for drinking-water purification[6].

Fluorescent semiconductor quantum dots (QDs) have also been explored for these applications, although results in the literature have been contradictory. Some studies find significant ROS production from QDs, and others find none[7]. Cytotoxicity is often ascribed to "singlet oxygen" without a clear demonstration of the mechanism. Part of the problem is that QDs of different compositions (CdTe, CdSe, CdSe/ZnS) have been compared across studies when they each have very different photophysics. Another issue is that certain ROS reporter dyes may be directly oxidized by nanoparticles, thus leading to a positive signal even when no ROS is present. A recent study found that fluorescent reporters that create a signal when oxidized gave false positive ROS results with fullerenes[8]. Only reporters that required reduction to generate the signal were reliable, notably the XTT assay. However, the same group found that despite their lack of ROS production, fullerenes were able to cause toxicity to bacterial cells by directly oxidizing membrane proteins[9]. Thus, observation of oxidative toxicity to cells does not necessarily imply ROS production.

Another issue is that there are many different mechanisms for ROS production and several different forms of ROS. Free radicals may be generated from photoexcited nanoparticles by either the *reductive pathway* (involving the electron transferring to an acceptor, A) or the *oxidative pathway* (involving the hole transferring to a donor, D) (Fig. 3.1A):

$$A + e^-_{CB} \rightarrow A^{\bullet -}$$

$$D + h^+_{VB} \rightarrow D^{\bullet +} \qquad (3.1)$$

If the radicals formed interact with water or oxygen, ROS can result. However, the radicals might also recombine rapidly, such as in the "electron shuttling" seen with quinones[10], for example by the process

$$A + e^-_{CB} \rightarrow A^{\bullet -}$$

$$A^{\bullet -} + h^+_{VB} \rightarrow A \quad (3.2)$$

In this case, no ROS is produced and the presence of the radicals, which may have femtosecond lifetimes, is difficult to detect.

Can CdSe/ZnS QDs make ROS? The energy of a CdSe electron is very close to the redox potential of molecular oxygen (Fig. 3.1B), making direct formation of large amounts of singlet oxygen unlikely. CdSe holes are highly oxidizing, but considerably less so than those of TiO_2, and might also be prevented from interacting by the ZnS shell. The formation of hydroxyl radicals directly is thus doubtful, but it could occur through an indirect mechanism, such as the photolysis of peroxide. In the presence of an electron-donating molecule such as dopamine (DA), however, the hole is expected to oxidize the DA, forming a semiquinone radical that can generate singlet oxygen:

$$DA + h^+_{VB} \rightarrow D^{\bullet +} \text{ (semiquinone)}$$

$$D^{\bullet +} + O_2 \rightarrow O_2^{\bullet -} + \text{DA-quinone} \quad (3.3)$$

The formation of singlet oxygen during autooxidation of dopamine and other catecholamines was reported earlier[11] and most probably involves semiquinone radicals, as fully chemically oxidized dopamine does not produce singlet oxygen.

At the same time, scavenging of holes by dopamine represses charge recombination, allowing for the increase yield of superoxide, and consequent formation of singlet oxygen[12]:

$$O_2 + e^-_{CB} \rightarrow O_2^{\bullet -}$$

$$O_2^- + H^+ \leftrightarrow HO_2, \text{ pK} = 4.8 \quad (3.4)$$

$$2HO_2 \text{ (or } 2O_2^-) \rightarrow H_2O_2 \text{ (or } O_2) + {}^1O_2$$

Thus, attachment of dopamine to QDs (via conjugation of amine groups) can result in superoxide/singlet oxygen formation both in reduction and oxidation processes.

The goal of this work was three-fold. The first aim was to use spin-trap EPR to distinguish between oxidative and reductive ROS production, and to compare these processes with QDs in organic solvent, water, and with dopamine conjugation. We found that QDs in toluene produced no substantial ROS. Solubilized, MPA-capped QDs produced oxidizing species but no significant singlet oxygen; the opposite was true of QD-dopamine.

The second aim was to compare and contrast these results with those obtained from fluorescent ROS reporters both in solution and in cultured mammalian cells, using several different types of reporter (sodium terephthalate; 2,3-bis-(2-methoxy-4-nitro-5-sulfophenyl)-2H-tetrazolium-5-carboxanilide, or XTT; 5-(and-6)-chloromethyl-2',7'-dichlorodihydrofluorescein diacetate, acetyl ester, or CM-H_2DCFDA; and Singlet Oxygen Sensor Green). The tests in solution confirmed the EPR results and suggested that these reporter dyes do not show false-positive results with QDs. However, CM-H_2DCFDA with cells was unreliable, possibly due to cap decay of QDs outside cells which then interacted with the dye. Finally, we measured the metabolic effects of these conjugates on cells in order to determine the correlation between cellular ROS and metabolic inhibition. For this, we used the colorimetric 3-(4,5-dimethylthiazol-2-yl)-2,5-diphenyltetrazolium bromide (MTT) assay. This assay is a standard measure of cell proliferation, and has been used in many studies involving QDs[13]. Here we found that a certain threshold concentration of QD-DA and a significant degree of light exposure were both necessary to observe metabolic inhibition in these cells. QDs alone showed very little toxicity, suggesting that the oxidative processes were not sufficient to cause cell death.

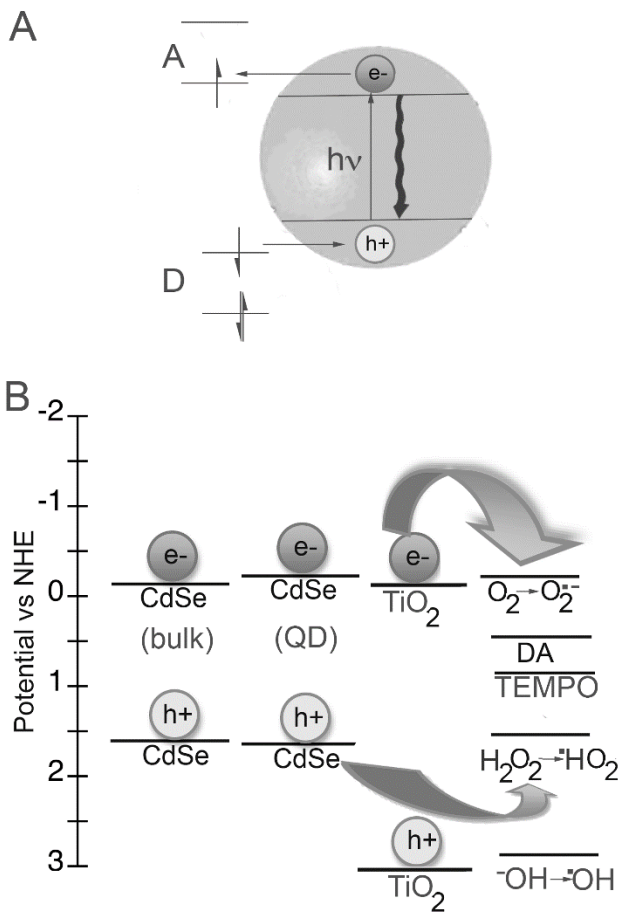

Figure 3.1 Mechanisms and energy levels involved in QD redox processes. (A) When a nanoparticle is excited by light more energetic than the band gap (*hv*), an electron-hole pair (exciton) is formed. The electron may interact with an acceptor A, and/or the hole with a donor D. It is important to note that the electron wave function penetrates significantly into the surrounding solution whereas that of the hole does not. The donors must thus be strongly adsorbed to the nanoparticle for reaction to occur. (B) Approximate energy levels (*vs.* NHE) in aqueous solution for bulk CdSe (band gap 1.7 eV) and a yellow CdSe QD (band gap 2.1 eV as measured from absorbance peak). TiO2 is shown for comparison, as are the energies of the molecules appropriate to this study: dopamine (DA), TEMPO, oxygen, peroxide, and hydroxylate ions.

3.2 Methods and materials

3.2.1 QD synthesis and characterization

Chemicals were purchased from Sigma-Aldrich Canada (Oakville, ON). CdSe/ZnS QDs were synthesized using a method adapted from the literature[14] based on the noncoordinating solvent 1-octadecene (ODE). Briefly, 0.026 g of cadmium oxide (CdO) and 1 mL oleic acid (OA) were added to a three-neck flask containing 10 mL of ODE. This mixed was degassed and heated under N_2 gas to 260 °C. The mixed turned colorless around 150 °C. The selenium (Se) precursor was prepared by mixing 0.01 g of Se with 0.5 mL trioctylphosphine (TOP) under inert atmosphere and sonicating until the solution became transparent. The zinc sulfide (ZnS) precursor was prepared as follows: 0.5 mL of TOP was combined with 0.2 mL bis(trimethylsilyl) sulfide ($(TMS)_2S$) and 0.3 mL dimethylzinc ($Zn(CH_3)_2$) under an inert atmosphere and diluted to 5 mL with ODE. Once the CdO/OA/ODE mixture reached 260 °C, the heat was turned off, and the Se precursor was injected rapidly using a needled syringe. The ZnS precursor was injected over a time course of 5 min during the desired stage of QD growth. Afterwards, the temperature was allowed to drop to 100 °C and it was maintained at this temperature for several hours. The QDs were purified from the reaction side products by precipitation with acetone, anhydrous ethanol and chloroform, and resuspended in toluene. MPA was used to replace the OA surfactant by a thiol-exchange reaction. 200 µL of concentrated QDs (optical density > 5) in toluene were added to 2 mL chloroform and 5 mL of methanol. 50 µL MPA was added and the pH was adjusted to ~9-10 with tetramethylammonium hydroxide pentahydrate (TMAH). This solution was left at room temperature in the dark for 24 h. The thiol-modified QDs were separated from excess MPA ligand by precipitation and washing with ethyl acetate. The QDs were dried at room temperature under air and resuspended in distilled H_2O (Millipore). Absorbance spectra were measured on a

SpectraMax Plus plate reader, and emission spectra on a SpectraMax Gemini (Molecular Devices, Sunnyvale, CA).

3.2.2 Conjugation to dopamine

Dopamine was coupled to the QDs by a 1-ethyl-3-(3-dimethylaminopropyl)-carbodiimide hydrochloride (EDC)-mediated reaction. QDs in H_2O were dialyzed (membrane cutoff 10 kDa) against PBS for 1 h and diluted to a final concentration of 1 μM. EDC and DA hydrochloride were added to the reaction mixture at a ratio of 1500 : 500 : 1 QD. The mixture was reacted for 30 min under gentle shaking and purified from excess side products by precipitation with THF and resuspension in PBS. The level of DA binding was quantified using the fluorescent indicator *o*-phthaldialdehyde as described[15]. For EPR studies, the conjugates were not purified or tested with *o*-phthaldialdehyde, but used immediately after preparation.

3.2.3 EPR spectroscopy

EPR spectra were collected on a Bruker Elexys E580 spectrometer at room temperature, with a power of 66.32 mW and a modulation amplitude of 1.0 gauss. Illumination was with a 300 W Xe lamp (ILC Inc.) using a cutoff filter of 400 nm longpass, intensity ~100 mW/cm^2. The changes in spin-trap concentration over time were determined by measuring EPR spectra at certain time intervals, while solutions were under continuous illumination. Typically, the accumulation of a single spectrum (sweep time) was 42 s in all experiments. The concentration of radicals was determined after double integration of spectra, and normalized to the 10 μM (2,2,6,6-tetramethylpiperidin-1-yl)oxy (TEMPO) radical. The *g* tensor values were calibrated for homogeneity and accuracy by comparing to a coal standard (g = 2.00285 ± 0.00005). The concentration of 2,2,6,6-tetramethylpiperidine (TMP) was 0.1 M for all solutions; the concentration of TEMPO was varied, for conjugated QDs it was 33 μM. All solutions were in air.

Some samples were bubbled with oxygen (and sealed), leading to a subsaturated solution of O_2. Controls for QD-dopamine included DA alone and DA + EDC at the same concentrations as used for conjugation.

3.2.4 ROS assays in solution

All fluorescent assays were read in a 96-well black plate (Corning) in a Gemini EM plate reader (Molecular Devices). Colorimetric assays were read in a clear 96-well plate on a SpectraMax UV-Vis spectrometer (Molecular Devices). For all assays, QD concentrations ranged from 0.1–1 μM. Duplicate samples were prepared for each condition, one to be blue light-exposed and the other aged under room oxygen but not light-exposed. The unexposed side of the plate was screened with aluminium foil. The lamp for exposure was a custom 96-LED lamp made of 2.5 mW, 440 nm LEDs arranged in the format of a 96-well plate to ensure uniform irradiation to each well. The generation of singlet oxygen was assayed using 1 μM Singlet Oxygen Sensor Green (SOS Green) (Invitrogen) with excitation at 504 nm and emission at 514–600 nm. The generation of hydroxyl radicals was measured with sodium terephthalate following published methods[16]. Briefly, QDs were mixed with disodium terephthalate (1 mM) (Sigma Aldrich) and irradiated. Aliquots of the reaction mixture were withdrawn at 10 min time intervals, treated with 0.5 volumes of 1 M NaOH and monitored by fluorescence emission with excitation at 300 nm. The colorimetric formation of XTT formazan was used to measure $HO_2^{\bullet}/O_2^{-}$ generation[17]. The generated radicals reduce the tetrazolium dye XTT (sodium salt, Sigma Aldrich), which was added to the QDs at 1 mM. After the indicated period of irradiation, absorbance was measured at 470 nm.

3.2.5 Incubation of QDs with cells and ROS generation/MTT assay

Experiments with cell lines were performed using PC12 cells stably transfected with human D2 dopamine receptors (gift of Stuart Sealfon, Mount Sinai School of Medicine; selectable marker

G418). Cells were maintained in high glucose Dulbecco's Modified Eagle's Medium (DMEM) (Invitrogen Canada, Burlington, ON) supplemented with 10% fetal bovine serum, 5% horse serum, 0.2 mM glutamine, 100 U mL^{-1} penicillin, 100 μg mL^{-1} streptomycin and 500 μg mL^{-1} G418 in a 5% CO_2 atmosphere at 37°C. For passage, cells were rinsed first with phosphate-buffered saline (PBS) and then with Hank's balanced salt solution containing 0.05% trypsin and 0.02% EDTA, incubated for 2 min at room temperature, and resuspended in supplemented DMEM. Cells were passaged onto glass bottom dishes (MatTek, Ashland, MA) or 96-well plates (Fisher Scientific) the day before use at 50-80% confluency. Just prior to labeling, growth medium was removed by two washes in sterile PBS, and then replaced with 1 mL serum-free medium without phenol red (OptiMem, Invitrogen). In preliminary studies, incubation times were varied between 15 min and 2 h, and it was found that some uptake of unconjugated QDs could occur at longer time scales. Thus, all data presented show cells incubated for 2 h unless stated otherwise, to permit possible identification of ROS generated in cells from unconjugated QDs. Unconjugated QDs or QD-dopamine conjugates were applied directly into serum-free medium at a concentration of ~5-10 nM particles. For co-labeling with Lysotracker Red or MitoTracker Orange (Invitrogen), dye was added to cells at a concentration of 1 μM at least 30 min before the end of the QD incubation. All cells were washed several times with sterile PBS after labeling and live cells were imaged in PBS.

ROS generation inside cells was quantified using CM-H_2DCFDA (Invitrogen). After incubation with QDs, cells were washed with PBS, and the medium replaced with PBS containing 10 μM dye. After incubation for 30 min, cells were once again rinsed in PBS and the fluorescence spectrum taken with excitation at 485 nm. The wells were then irradiated in 10-min intervals using a hand-held UV lamp at wavelength of 365 nm for varying time periods (approximate emission power, 2.5 mW) (UVP, Upland, CA). Wells not to be irradiated were shielded with aluminium

foil. Controls included cells with no dye; dye with no cells; cells with dopamine without QDs; and cells with dopamine with QDs but not conjugated.

The protocol for the MTT colorimetric assay followed published methods[18]. PC12 cells were plated into 96-well plates at 50-80% confluency 1-2 days preceding the assay. CdSe/ZnS-dopamine conjugates with varying concentrations were prepared in serum-free, phenol-red-free medium, and 200 μL of the conjugates was added to each well and incubated for 30-60 min. After washing with PBS, 200 μL PBS was added to each well and the wells were irradiated as described for the ROS assay. The PBS was then replaced with complete medium and the cells were further incubated for 18-24 hours. 12.5 μL of a 5 mg mL^{-1} MTT solution in PBS was added to each well and incubated for 4 h. The resulting crystals were dissolved in dimethyl sulfoxide (200 μL in each well) and absorbance measured at 570 nm.

For Hg-lamp exposure studies of single cells, cells were examined and imaged with an Olympus IX-71 inverted microscope and a Nuance multispectral imaging system, which provides spectral data from 420-720 nm in 10 nm steps (CRI Instruments, Cambridge, MA). The objective lens was a Nikon PlanFluor 100× (N.A. = 1.30). Illumination was through a Quantum Dot filter cube set (excitation = 380-460 nm, dichroic = 475 nm, emission = 500 LP) or a DAPI filter cube set (excitation = 350/50 nm, dichroic = 400 nm, emission = 420 LP) (Chroma Technologies, Rockingham, VT). Confocal imaging was performed on a Zeiss 510 LSM with a PlanApo 100× oil objective. QDs were excited with an Ar ion laser 488 nm line. LysoTracker Red and MitoTracker Orange were excited with a HeNe laser (543 nm line). Cells labeled with > 1 probe were examined for channel bleed-through before imaging.

3.3 Results

3.3.1 QD characterization

In this study we used yellow-emitting CdSe/ZnS QDs (QD590, emission peak 595 ± 20 nm) for all experiments. This wavelength allowed for easy distinction from cellular autofluorescence, organelle dyes, and ROS indicators. Dopamine altered the optical properties of the particles, primarily by fluorescence quenching (Fig. 3.2A). The conjugation of dopamine molecules was confirmed by gel electrophoresis[19] (Fig. 3.2B) and quantified by spectroscopy. When bound by their primary amino group to functional groups on the QD surface, dopamine has neutral charge. Therefore, the effect of binding is a reduction in the net surface charge of the particles. In gel electrophoresis, QD-dopamine migrates towards the positive electrode at a slower rate than the unmodified QD control indicating successful conjugation of these ligands. It was necessary to optimize the coupling reactions in order to modify only a portion of the surface. MPA-coated QDs are charge-stabilized and complete loss of charge results in particles that are unstable in solution. Not surprisingly, QDs saturated with dopamine remained in the loading well during gel electrophoresis, indicating macroscopic aggregation (not shown).

3.3.2 EPR spectroscopy

The EPR spin-probe TEMPO is a stable free radical that can be oxidized by holes, OH radicals, or any other oxidative species, that have a redox potential ≥ +0.75 V vs. normal hydrogen electrode (NHE) (refer again to Fig. 3.1B). Thus the disappearance of TEMPO radical EPR spectra upon irradiation indicates photogenerated oxidative species. We found significant decay of TEMPO signals only upon illumination of QD-MPA, but not for QD-DA or QDs in toluene (Fig. 3.3A, B).

The TMP method measures the formation of singlet oxygen or superoxide anion using EPR-silent TMP. The reaction of non-paramagnetic species TMP with singlet oxygen/superoxide

yields formation of a stable, EPR-sensitive radical adduct (nitroxide-type radical). In this case it is thus the formation of the radical rather than its disappearance which is measured, and the kinetics of formation can give a clue to the mechanisms. We found significant TMP-radical signals only with QD-DA, which increased when the solution was bubbled with oxygen (Fig. 3.3C, D).

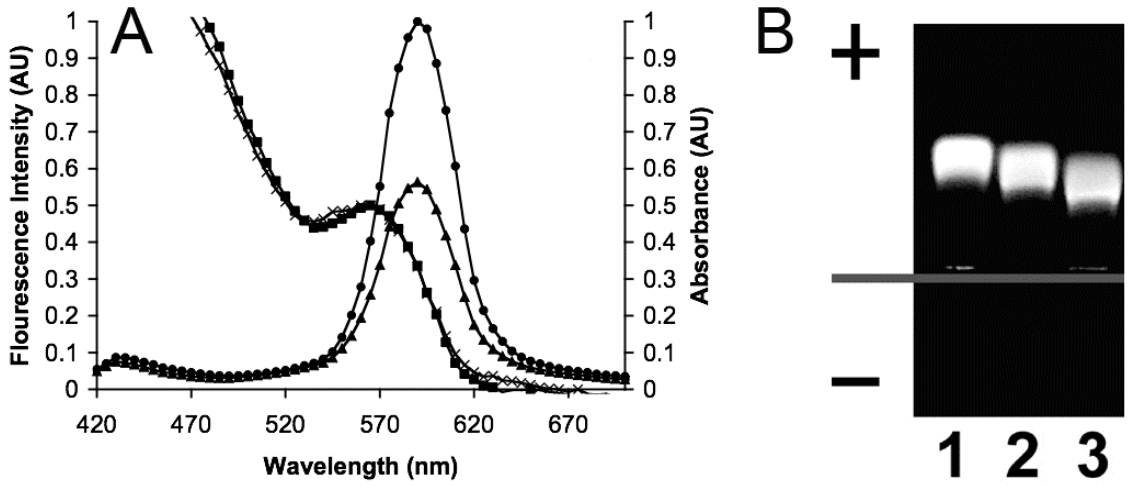

Figure 3.2 Optical and electrophoretic properties of QDs in this study. (A) Absorbance and normalized fluorescence intensity for QDs before and after conjugation to dopamine. The absorbance spectra are nearly identical between the QDs alone (■) and the conjugate (×). The emission spectra indicate partial quenching of the conjugate (▲) relative to the QDs alone (●). (B) Confirmation of conjugation reactions by gel electrophoresis. Lane l: solubilized QDs alone; lane 2: QD-DA (*ca.* 62 ligands/particle) lane 3: QD-DA (*ca.* 140 ligands/particle). The sample corresponding to lane 3 was used for cell-labeling and toxicity experiments. The gray line indicates the sample loading position on the gel.

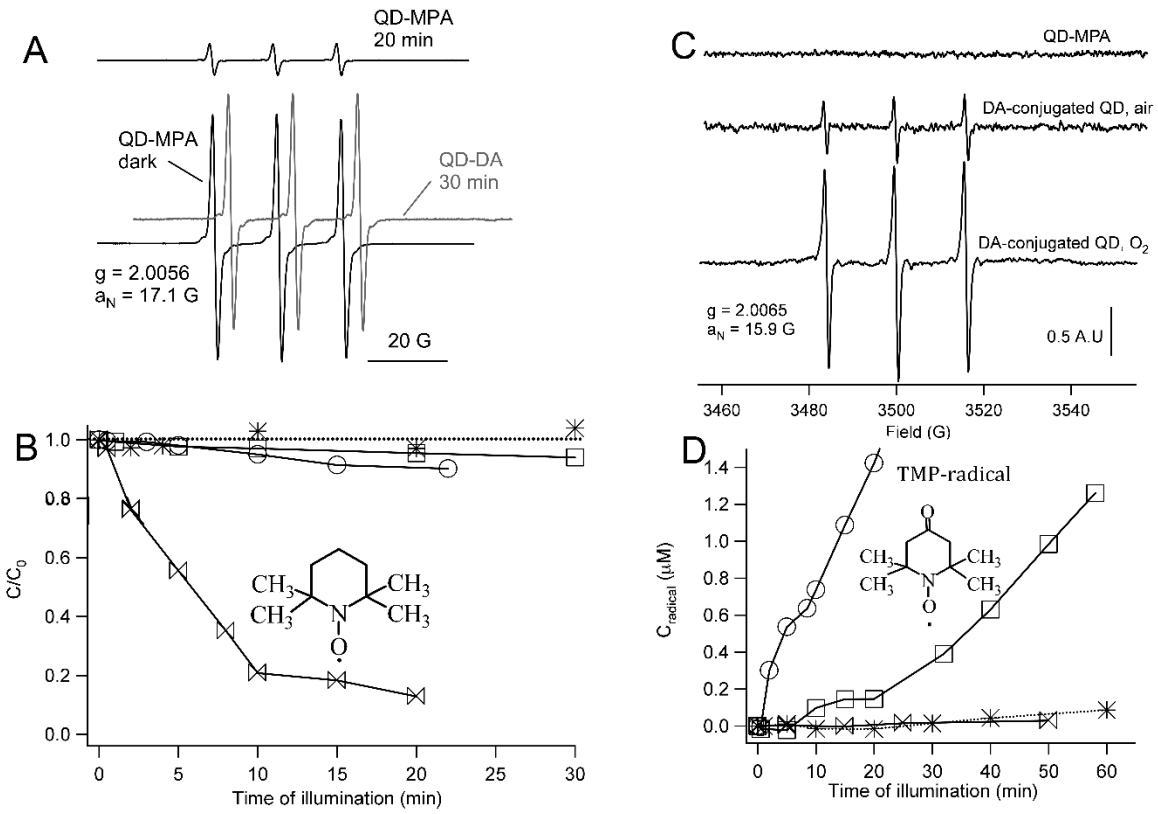

Figure 3.3 EPR spectroscopy using TMP and TEMPO radicals as spin traps. (A) The spectra of TEMPO radicals showing initial intensity of QD-MPA *vs.* substantial decay at 20 min. The QD-DA signal remained essentially constant with time (gray line, the spectrum is shifted for better visibility). (B) Decay of TEMPO radical relative concentrations with time of illumination showing QD-MPA (bowties), QD-DA (squares), DA alone (stars), and hydrophobic QDs in toluene (circles). Only QD-MPA shows a significant effect. (C) Spectra of TMP-radicals formed upon 60 minutes of illumination. The QD-MPA does not show any formation of TMP-radical, while QD-DA showed a significant effect, which increases with oxygen. (D) Concentration of formed TMP-radical *vs.* irradiation time for QD-MPA (stars), DA only (bowties), and QD-DA in air (squares) *vs.* bubbled with oxygen (circles).

3.3.3 ROS assays in solution

Singlet oxygen sensor green (SOSG) has been reported to be highly specific for $^1O_2$, and to respond very little to hydroxyl radicals or peroxide[16]. As in our previous work, we found a significant signal from SOSG with QD-DA, but not with dopamine alone, QD-MPA, or the dye alone (Fig. 3.4A). Correspondingly, the hydroxyl radical sensor sodium terephthalate showed a signal only with QD-MPA (Fig. 3.4B).

XTT is unique in that it must be reduced, rather than oxidized, to yield a signal. Thus direct oxidation by the nanoparticles will not yield a false positive[8]. It is also more quantitative than the fluorimetric assays. XTT is sensitive to perhydroxyl and superoxide radicals, and thus might be expected to give a signal both with QD-MPA and QD-DA. This is indeed what we found, although the kinetics of the reactions differed. QDs alone showed a rapid increase in signal with a plateau after approximately 20 min of irradiation; QD-DA showed a more gradual increase throughout the irradiation period. With 100 nM QDs, the final amount of radical produced was very similar after the 60 min period (6.6 μM for QD-DA *vs.* 6.4 μM for QD-MPA, using the published extinction coefficients). However, with 200 nM QDs, the final values were 8.0 μM for QD-DA and 10.5 μM for QD-MPA (Fig. 3.4C).

3.3.4 Generation of ROS in PC12 cells with D2 dopamine receptors

QD-dopamine and unmodified QDs both showed substantial uptake by our dopamine-receptor-bearing PC12 cells after 30-120 min of exposure to 10 nM concentrations (Fig. 3.5A-C).

One striking feature of QD-dopamine that we have previously reported is photoenhancement of internalized QDs, especially those associated with mitochondria[20]. Fluorescence in lysosomes faded rapidly, either due to the internal chemistry of these organelles or because light-induced rupture allowed lysosomal QDs to travel elsewhere in the cell (Fig. 3.5D).

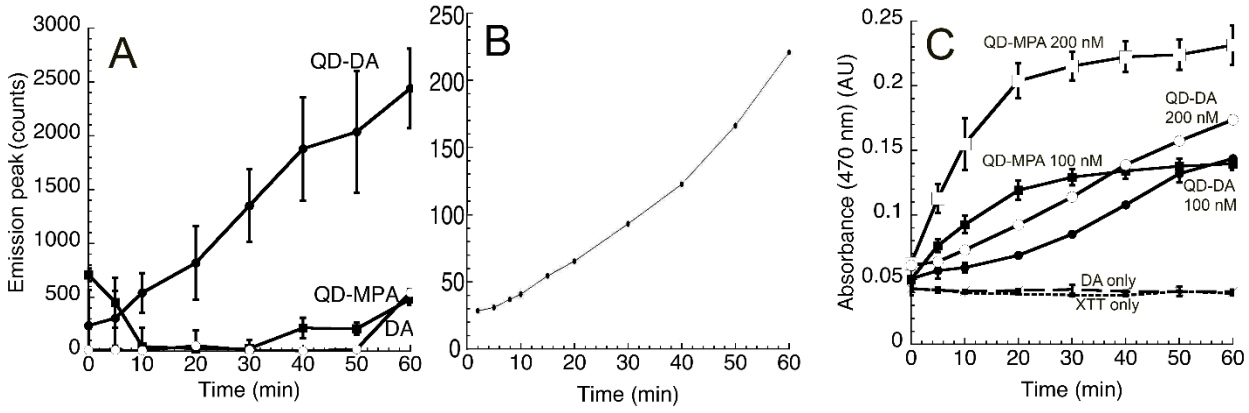

Figure 3.4 Fluorescent and colorimetric ROS assays in solution. All data points are averages of 3-5 experiments with error bars shown; when error bars do not appear, they are smaller than the symbols. (A) Singlet oxygen sensor green, peak at 530 nm. The signal from dye alone was subtracted. Shown are QD-DA and QD-MPA (at 100 nM), and DA alone (at 100 μM). (B) Sodium terephthalate peak at 435 nm from QD-MPA at 250 nM. (C) XTT. There was no signal from dye alone or DA alone. Two concentrations of QD-MPA and QD-DA are shown: 100 and 200 nM. Note the different kinetics with QD-MPA *vs.* QD-DA.

Labeling with specific dyes such as Lysotracker and Mitotracker enabled QD localization to these organelles to be identified and specific patterns to be identified. When QD-DA was present, mitochondrial-associated QD fluorescence increased with photoexposure, paralleling classic signs of mitochondrial toxicity such as rounding of the mitochondria within 30 s of confocal laser exposure (Fig. 3.5E).

In order to quantify intracellular ROS generation, we used CM-H_2DCFDA, which measures generation of ROS inside cells only. It must be modified twice in order to become fluorescent: first deacetylated by intracellular esterases, then oxidized[21]. Thus, this assay should

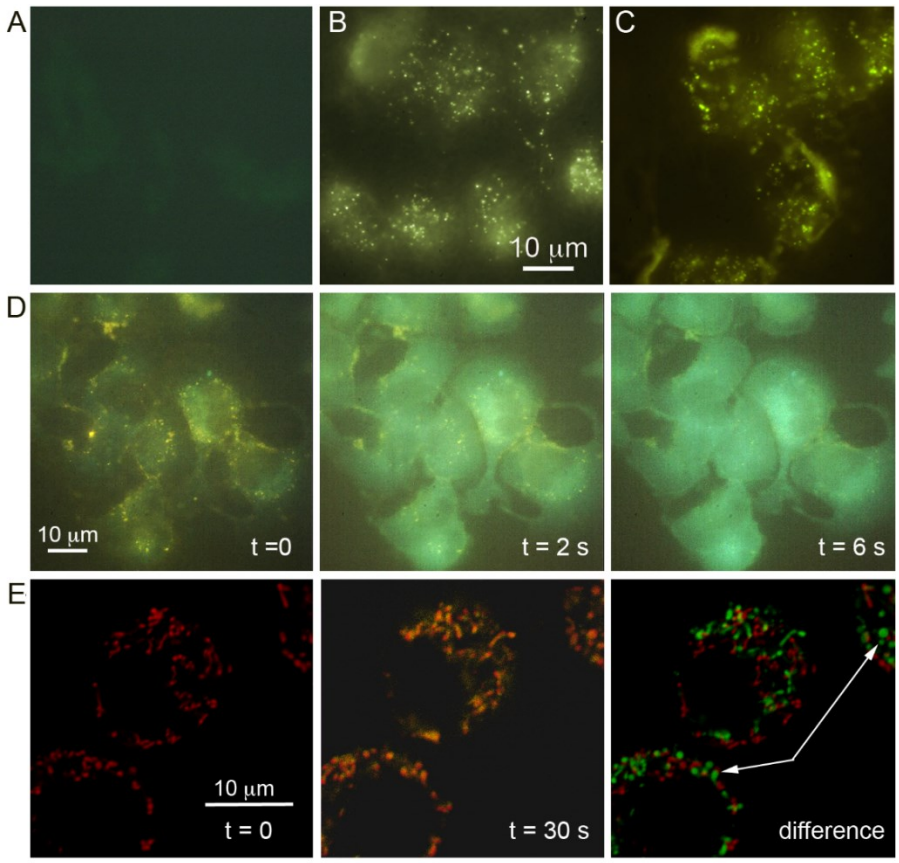

Figure 3.5 Uptake and processing of QDs and conjugates by PC12 cells. (A) PC12 cells alone under the Quantum Dot filter (see Methods). (B) Unmodified QD-MPA, 5 nM exposed for 2 h, showing an endosomal uptake pattern. (C) QD-DA, 5 nM for 1 hr, also showing intracellular vesicles consistent with endosomal uptake. (D) Photoenhancement of QD-DA under the DAPI filter. The photoenhancement of QD-DA has been studied in detail in reference [20]. Note vesicular labeling that travels throughout the cell during the course of a few seconds of high-power Hg lamp exposure. (E) Photoenhancement and mitochondrial toxicity with QD-DA under confocal laser illumination. From t = 0 to 30 s, a brightening of the QD fluorescence (yellow) is seen over the MitoTracker Dye (red). In the last panel, the QD fluorescence has been removed, and the difference in the MitoTracker signals from t = 0 and 30 s is shown, with green indicating the later time point. Note the significant rounding of mitochondria (arrows).

be a measure of relative QD uptake by the cells as well as of the capacity of the internalized QDs to generate ROS. When the dye was added after QD internalization, the results were sometimes consistent with ROS generation from QD-DA conjugates but little from QD-MPA or DA alone (Fig. 3.6A). However, we found that the QDs alone sometimes interacted with the dye, generating large signals external to the cells that could be rinsed away. In this case the QDs only gave greater signals than any of the conjugates (Fig. 3.6B). This occurred to different extents in different assays, perhaps reflecting the number of QDs that remained outside the cells when the dye was added. It had a poor correlation with concentration (note that the highest signal was seen with the lowest QD concentration used, 0.1 nM).

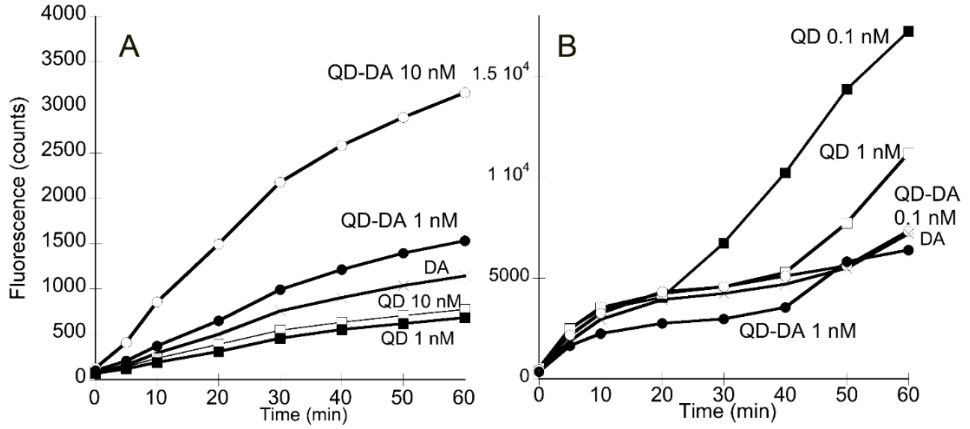

Figure 3.6 Variability of CM-H_2DCFDA assay in PC12 cells exposed to QDs for 30-60 minutes and irradiated in 10-minute increments. All values were consistent among triplicates done in the same experiment, with error bars smaller than symbols. (A) A "successful" assay. QD-DA shows a significant, time- and concentration-dependent signal. 100 μM dopamine alone shows a much smaller signal, and QD-MPA show a negligible signal. (B) An "erroneous" assay. Note the very different scale on the y-axis. Very large signals are seen with very low concentrations of QDs alone. Although QD-DA shows a signal comparable to that in (A), it is swamped by that of the QDs alone.

3.3.5 Effects of QDs on PC12 cell metabolism

Dopamine alone did not lead to any significant metabolic inhibition. Unconjugated QD-MPA showed a small (statistically insignificant) effect that was not measurably affected by irradiation. QD-dopamine was not significantly effective at concentrations below 10 nM or for irradiation times < 40 min. However, above these concentrations and exposure times, the effects on cells were marked, reducing metabolic activity to one-fifth of its original value (Fig. 3.7).

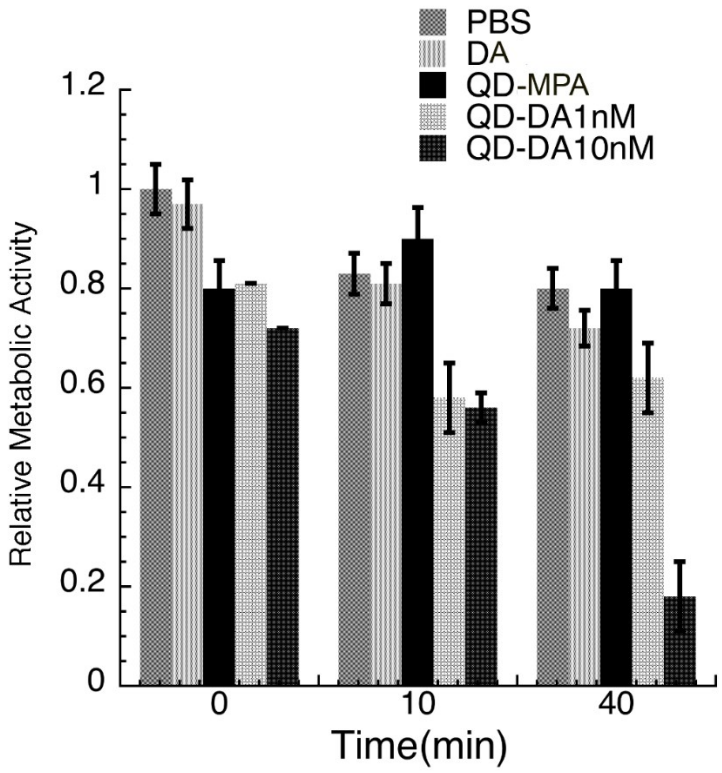

Figure 3.7 Effect of QDs and conjugates on cellular metabolism as measured by the MTT assay. All assays were performed 2-3 times on independent plates and error bars indicate SEM. Controls consisted of cells with mock application of PBS and with DA alone (100 μM). Although QD-MPA had a significant effect on cells without irradiation ($p < 0.05$), there was no significant difference between irradiated cells exposed to QDs or DA alone. A significant pattern of inhibition is not seen except in 10 nM QD-DA irradiated for 40 min or more ($p < 0.001$).

3.4 Discussion

The phototoxicity of nanoparticles, particularly quantum dots, has been known for some time. However, while core CdSe[22] and CdTe[13] are extremely efficient at ROS generation, it has been suggested that core-shell CdSe/ZnS does not produce significant ROS by itself[7, 23]. However, there is a large variation in shell thickness in different CdSe/ZnS preparations, and also a large difference in homemade *vs*. commercial QDs, both in shell synthesis methods and solubilization ligands. Recent reports also call into question the validity of fluorescent reporter assays for ROS when used with nanoparticles, since these reporter dyes might be directly oxidized, giving a false positive signal.

In this work we show that CdSe/ZnS QDs, unlike C_{60}, does indeed make reactive oxygen species, although negligible singlet oxygen. Results of spin-trapped EPR and fluorescent and colorimetric reporter dyes are consistent. The MPA-capped QDs generate perhydroxyl radicals or superoxide and hydroxyl radicals. Given the position of the band edges and the confinement of the holes, it is likely that the hydroxyl radicals arise from an indirect process such as a Fenton reaction. It is also likely that the superoxide interacts with the holes in a "shuttling" process, preventing its conversion to singlet oxygen.

When conjugated to dopamine, CdSe/ZnS produces significant singlet oxygen. This is likely due to the generated superoxide, formed most probably both in reduction and oxidation reaction processes, namely in reaction of photogenerated electrons or in reaction of positively-charged dopamine radicals with oxygen, respectively. As more oxygen is added to the solution, production of singlet oxygen increases.

QD-dopamine is taken up by dopamine-receptor-bearing PC12 cells. Unconjugated QDs are also endocytosed by these cells, so that a direct comparison of toxicity is possible. The one

note of caution seen in our assays was that we often saw large erroneous signals with the green CM-H_2DCFDA fluorescent ROS reporter dye. This was associated with aggregates of QD-MPA remaining outside the cells, so may represent photooxidized QDs that interact directly with the dye. Until this chemistry is worked out, ROS results using this dye will have to be treated with caution.

Cell toxicity corresponded best to levels of singlet oxygen generation. Very little toxicity was seen with QD-MPA, even upon blue light irradiation for 40 min. However, QD-dopamine led to visible effects on cells, particularly mitochondrial rounding, consistent with previous reports[24]. Effects on cell metabolism were apparent after 30-40 minutes of blue light irradiation. The inhibition seen was striking and important, reducing metabolic activity to 20% of baseline. Other nanoparticle-photosensitizer conjugates have reported reduction to 40% of baseline, which is considered sufficient for medical applications such as photodynamic therapy[18].

The most important implication of this work is that simple biomolecules attached to QDs may 'photosensitize' core-shell particles into formation of ROS, which otherwise are not produced by photoexcitation of QDs due to strong exciton interactions. This leads to cytotoxicity and mitochondrial dysfunction when the particles are taken up into cells, even though release of toxic metals such as Cd^{2+} does not occur[23]. It is not likely that this presents any particular environmental danger to complex organisms that may ingest the particles, as the wavelengths of light needed to excite CdSe (UV to blue) have very shallow penetration depths into tissue. However, skin exposure represents a possible hazard, and animal studies will be needed to indicate possible cytotoxic or mutagenic effects on skin. These photosensitized conjugates may also potentially be used as agents for photodynamic therapy (PDT) of superficial cancers such as skin cancer[25]. The hydrophilic

nature of the QD conjugates makes them ideal for uptake into inflamed tissues, often a barrier to successful PDT[26].

3.5 Acknowledgements

This research is funded by U.S. EPA—Science to Achieve Results (STAR) program Grant #R831712 and by the National Science and Engineering Research Council of Canada (NSERC) Individual Discovery and NanoInnovation Platform programs. SJC is supported by the Canadian Institutes of Health Research (CIHR) Nanomedicine Seed Grant. The EPR experiments were performed at Argonne under DOE BES Contract No. DE-AC02-06CH11357.

3.6 References

1. Wainwright, M. Photodynamic antimicrobial chemotherapy (PACT). *Journal of Antimicrobial Chemotherapy* **1998,** *42* (1), 13-28.
2. Soltesz, E. G.; Kim, S.; Laurence, R. G.; DeGrand, A. M.; Parungo, C. P.; Dor, D. M.; Cohn, L. H.; Bawendi, M. G.; Frangioni, J. V.; Mihaljevic, T. Intraoperative sentinel lymph node mapping of the lung using near-infrared fluorescent quantum dots. *Ann Thorac Surg* **2005,** *79* (1), 269-77; discussion 269-77.
3. Hagfeldt, A.; Gratzel, M. Light-induced redox reactions in nanocrystalline systems. *Chemical Reviews* **1995,** *95* (1), 49-68.
4. Hagfeldt, A.; Gratzel, M. Molecular photovoltaics. *Acc Chem Res* **2000,** *33* (5), 269-77.
5. Pohle, D.; Damm, C.; Neuhof, J.; Roesch, A.; Miinstedt, H. Antimicrobial properties of orthopaedic textiles after in-situ deposition of silver nanoparticles. *Polymers & polymer composites* **2007,** *15* (5), 357-363.
6. Sichel, C.; Blanco, J.; Malato, S.; Fernández-Ibáñez, P. Effects of experimental conditions on E. coli survival during solar photocatalytic water disinfection. *Journal of Photochemistry and Photobiology A: Chemistry* **2007,** *189* (2–3), 239-246.
7. Ipe, B. I.; Lehnig, M.; Niemeyer, C. M. On the generation of free radical species from quantum dots. *Small* **2005,** *1* (7), 706-9.
8. Lyon, D. Y.; Brunet, L.; Hinkal, G. W.; Wiesner, M. R.; Alvarez, P. J. Antibacterial activity of fullerene water suspensions (nC60) is not due to ROS-mediated damage. *Nano Lett* **2008,** *8* (5), 1539-43.
9. Hotze, E. M.; Labille, J.; Alvarez, P.; Wiesner, M. R. Mechanisms of photochemistry and reactive oxygen production by fullerene suspensions in water. *Environ Sci Technol* **2008,** *42* (11), 4175-80.
10. Burda, C.; Green, T. C.; Link, S.; El-Sayed, M. A. Electron shuttling across the interface of CdSe nanoparticles monitored by femtosecond laser spectroscopy. *Journal of Physical Chemistry B* **1999,** *103* (11), 1783-1788.

11. Lichszteld, K.; Michalska, T.; Kruk, I. Identification by Esr Spectroscopy and Spectrophotometry of Singlet Oxygen, Formed during Autoxidation of Catecholamines. *Zeitschrift Fur Physikalische Chemie-International Journal of Research in Physical Chemistry & Chemical Physics* **1992,** *175*, 117-122.
12. Khan, A. U. The discovery of the chemical evolution of singlet oxygen. Some current chemical, photochemical, and biological applications. *International Journal of Quantum Chemistry* **1991,** *39* (3), 251-267.
13. Choi, A.; Cho, S. J.; Desbarats, J.; Lovric, J.; Maysinger, D. Quantum dot-induced cell death involves Fas upregulation and lipid peroxidation in human neuroblastoma cells. *Journal of Nanobiotechnology* **2007,** *5* (1), 1.
14. Asokan, S.; Krueger, K. M.; Alkhawaldeh, A.; Carreon, A. R.; Mu, Z.; Colvin, V. L.; Mantzaris, N. V.; Wong, M. S. The use of heat transfer fluids in the synthesis of high-quality CdSe quantum dots, core/shell quantum dots, and quantum rods. *Nanotechnology* **2005,** *16* (10), 2000.
15. Clarke, S. J.; Hollmann, C. A.; Aldaye, F. A.; Nadeau, J. L. Effect of ligand density on the spectral, physical, and biological characteristics of CdSe/ZnS quantum dots. *Bioconjug Chem* **2008,** *19* (2), 562-8.
16. Flors, C.; Fryer, M. J.; Waring, J.; Reeder, B.; Bechtold, U.; Mullineaux, P. M.; Nonell, S.; Wilson, M. T.; Baker, N. R. Imaging the production of singlet oxygen in vivo using a new fluorescent sensor, Singlet Oxygen Sensor Green®. *Journal of Experimental Botany* **2006,** *57* (8), 1725-1734.
17. Able, A. J.; Guest, D. I.; Sutherland, M. W. Use of a New Tetrazolium-Based Assay to Study the Production of Superoxide Radicals by Tobacco Cell Cultures Challenged with Avirulent Zoospores ofPhytophthora parasitica varnicotianae. *Plant Physiology* **1998,** *117* (2), 491-499.
18. Wieder, M. E.; Hone, D. C.; Cook, M. J.; Handsley, M. M.; Gavrilovic, J.; Russell, D. A. Intracellular photodynamic therapy with photosensitizer-nanoparticle conjugates: cancer therapy using a 'Trojan horse'. *Photochemical & Photobiological Sciences* **2006,** *5* (8), 727-734.
19. Pons, T.; Uyeda, H. T.; Medintz, I. L.; Mattoussi, H. Hydrodynamic dimensions, electrophoretic mobility, and stability of hydrophilic quantum dots. *J Phys Chem B* **2006,** *110* (41), 20308-16.
20. Clarke, S.; Koshy, S.; Zhang, J.; Cohen, N.; Nadeau, J. Power and wavelength dependence of photoenhancement in (CdSe) ZnS-dopamine in aqueous solution and live cells. *Zeitschrift fur Physikalische Chemie* **2008,** *222* (5), 851-864.
21. www.probes.com. www.probes.com.
22. Chan, W.-H.; Shiao, N.-H.; Lu, P.-Z. CdSe quantum dots induce apoptosis in human neuroblastoma cells via mitochondrial-dependent pathways and inhibition of survival signals. *Toxicology Letters* **2006,** *167* (3), 191-200.
23. Clarke, S. J.; Hollmann, C. A.; Zhang, Z.; Suffern, D.; Bradforth, S. E.; Dimitrijevic, N. M.; Minarik, W. G.; Nadeau, J. L. Photophysics of dopamine-modified quantum dots and effects on biological systems. *Nat Mater* **2006,** *5* (5), 409-417.
24. Cho, S. J.; Maysinger, D.; Jain, M.; Roder, B.; Hackbarth, S.; Winnik, F. M. Long-term exposure to CdTe quantum dots causes functional impairments in live cells. *Langmuir* **2007,** *23* (4), 1974-80.
25. Karrer, S.; Szeimies, R. M.; Abels, C.; Landthaler, M. The use of photodynamic therapy for skin cancer. *Onkologie* **1998,** *21* (1), 20-27.

26. Calzavara-Pinton, P. G.; Venturini, M.; Sala, R. Photodynamic therapy: update 2006. Part 1: Photochemistry and photobiology. *Journal of the European Academy of Dermatology and Venereology : JEADV* **2007,** *21* (3), 293-302.

Chapter 4

Introduction to nanoscintillator-photosensitizer systems

4 Introduction to nanoscintillator-photosensitizer systems

4.1 Introduction

In 2006, Wei Chen and Jun Zhang, then researchers at Nomadics Inc., proposed a new approach to NP-based therapies aiming to combine and enhance the effects of radiation therapy and photodynamic therapy through the use of scintillating NPs conjugated to photosensitizer molecules[1]. This chapter will provide a description of the basic physical, chemical and biological principles of the proposed system and the current status of relevant investigations, as well as background information on synthesis and properties of scintillating NPs and of photosensitizer conjugate design considerations that will complement the work presented in the following chapters.

4.1.1 Radiation therapy

Radiation therapy (XRT) is a critical component of the modern approach to curative and adjuvant treatment of cancers. XRT controls the growth of cancerous cells by bombardment with ionizing radiation, causing DNA damage by direct ionization or through generation of free radicals by radiolysis of water or oxygen molecules. Sufficient damage to DNA in this fashion can arrest cell growth and prevent metastasis. The primary drawback is collateral damage: there is little distinction in absorption between healthy and malignant tissues, and thus doses must be limited in order to mitigate unwanted damage to the tumor surroundings. External beam radiotherapy (EBRT) utilizes X-ray beams produced by orthovoltage units, or linear accelerators that may be spatially oriented and shaped using multileaf collimators in order to maximize the specificity for the target. Distinct energy ranges are available for different EBRT targets: 40-100 kV (kilovoltage or “superficial” X-rays) for skin cancers or other exposed structures, 100-300 kV (orthovoltage) and 4-25 MV (megavoltage or “deep” X-rays) for sub-surface tumors. Techniques such as 3-

dimensional conformal and intensity-modulated radiation therapies have vastly improved the targeting capabilities of external beam therapy, but naturally there is still a strong desire to be able to further reduce the doses required for effective treatment. The SI derived unit for absorbed dose is the gray (Gy), equivalent to one joule of ionizing radiation energy deposited per kilogram of matter (1 Gy = 1 J/kg = 1 m^2/s^2).

Brachytherapy, or internal radiotherapy, utilizes a radioactive source to provide a steady dose of radiation in a small volume. It is typically used for cervical, prostate, breast and skin cancers. Radioactive sources include ^{125}I and ^{103}Pd, which produce γ rays of ~20-35 keV, ^{192}Ir (γ rays, 300-610 keV), ^{137}Cs (γ rays, 662 keV), ^{60}Co (γ rays, 1.17 & 1.33 MeV), ^{198}Au (γ rays, 410-1009 keV), ^{226}Ra (γ rays, 190-2430 keV) and ^{106}Ru which decays primarily through β^- emission at 3.54 MeV. Seeds of the listed materials can provide doses of up to 12 Gy/hour (high dose rate or HDR brachytherapy), though typical low dose rate (LDR) treatments amount to around 65 Gy over 5-6 days.

As oxygen is an important radiosensitizer[2], many solid tumors can become resistant to radiation as they outgrow their blood supply, leading to oxygen deficiency (hypoxia). The hypoxic state can confer a 2-3 fold increase in radiation resistance, and thus there is great interest in developing ways to sensitize the malignant tissue by enhancing effective radiation doses or by some complementary treatment. Radiotherapy and chemotherapy are often combined, but can have devastating results that greatly diminish quality of life. A number of synthetic radiosensitizers have been developed in recent years, including misonidazole, metronidazole, and the hypoxia-specific cytotoxin Tirapazamine.

Heavy elements are also potent radiosensitizers[3]. It has been demonstrated that platinum-containing DNA-crosslinking drugs such as Cisplatin can enhance the effects of ionizing radiation

through the "high Z effect," or what has come to be known as Auger therapy. Heavy elements have significantly higher photoelectric cross-sections than soft tissue for sub-MeV energies, approximated for "X-ray energies" by the equation[4, 5]

$$\sigma_{pe} \propto \frac{Z^n}{E^3} \tag{4.1}$$

where σ_{pe} is the cross-section, $E = h\nu$ is the photon energy, Z is the atomic number, and n varies between 4 and 5 depending on the value of E. The photoelectric effect dominates below the electron rest energy of 511 keV, beyond which inelastic Compton scattering becomes more prevalent. As the photon energy decreases, it is no longer potent enough to eject inner-shell electrons, producing the characteristic sawtooth pattern with K, L and M edge structures. When ionized by X-ray or γ ray energy, mid- to high-Z elements (roughly Br and up) can produce a cascade of low-energy Auger electrons that can locally enhance the effective radiation dose[3]. By extension, it is easy to imagine how dense inorganic NPs can also provide radiation dose enhancement. AuNPs have been under investigation for this purpose for several years[6, 7, 8, 9, 10, 11, 12], and shown considerable promise as radiosensitizers. Much of this work has been recently reviewed[13, 14]. Effective dose enhancement by high-Z NPs depends largely on the radiation energy, as will be discussed in Section 4.1.3.

4.1.2 Photodynamic therapy

Photodynamic therapy (PDT) is another promising tool for the treatment of cancers and other neoplastic diseases[15]. PDT involves the use of nontoxic 'photosensitizer' (PS) molecules such as porphyrins that can selectively damage tissue upon excitation by light. First observed around 1900 by Oscar Raab after exposing paramecium in solutions containing the dye acridine to varying amounts of light, interest in PDT has wavered throughout the years, though it has experienced a

resurgence in experimental activity over the last two decades. A number of PSs have been approved for a variety of clinical uses: porfimer sodium (the sodium salt of hematoporphyrin derivative, sold as Photofrin®) for instance is used to treat or relieve the symptoms of esophageal cancer and non-small cell lung cancer, while verteporfin (Visudyne) is used to treat "wet" macular degeneration through destruction of abnormal blood vessels.

Excited photosensitizers function by generating reactive oxygen species (ROS) through two mechanisms: Type I reactions involve charge transfer with a substrate, producing radicals of the PS and substrate. Typically this consists of oxidation of the substrate and reduction of the PS, which can react further to produce other oxygenated products. This may be destructive to the PS unless the extra electron is then transferred to dioxygen, producing the superoxide radical ($O_2^{\cdot -}$), in which case the PS is regenerated. Type II reactions result when a PS in the triplet state transfers energy to ground state molecular oxygen ($^3O_2$), converting it to highly-reactive singlet oxygen ($^1O_2$) along with regeneration of the ground state PS. The relative probability of each reaction type depends on a number of conditions including oxygen concentration and PS aggregation[16]. PDT-mediated cytotoxicity is thought to arise primarily from singlet oxygen generated in Type II reactions, favored for unaggregated PSs and at high oxygen concentrations. Because of the hypoxic nature of tumors, generation of singlet oxygen may become less efficient further from the blood vessels. As the lifetime of singlet oxygen is short (~3 μs in water), it has a short radius of action (tens to hundreds of nm) and is not expected to diffuse significantly on the scale of a cell.

The basic photophysical principle of singlet oxygen generation by a generic PS is shown in Figure 4.1. Macrocyclic molecules with conjugated double bond systems, when excited to singlet states, have a high probability of forming long-lived (μs) triplet states. Shown below is one path of PDT activity[15], consisting of the following processes: (i) excitation of an electron to the

second excited singlet state by absorption of light, (ii) nonradiative de-excitation to the first excited singlet state by internal conversion (ic), conserving spin, (iii) nonradiative transitioning to the first triplet state by intersystem crossing (isc), reversing the spin, (iv) energy transfer from the PS triplet state to ground state triplet oxygen, generating singlet oxygen and returning the PS to the ground state. Singlet oxygen can then be quenched in several ways: (i) phosphorescence, generating a photon with a wavelength of 1270 nm (0.98 eV), (ii) physical quenching involving no chemical changes but generating small amounts of heat (physical quenchers can either be biomolecules such as β-carotene or others like the azide molecule N_3^-, which is typically used in lab environments for this purpose), (iii) chemical quenching, describing most reactions with biomolecules. Singlet oxygen is electrophilic and will undergo oxidation reactions with electron-rich compounds such as those with double bonds. There are a number of distinct reaction types that may affect a wide variety of biomolecules, and have been described in detail elsewhere[17, 18].

$$\mathrm{PS(S_0)} \xrightarrow{h\nu} \mathrm{PS(S_2)} \xrightarrow{ic} \mathrm{PS(S_1)} \xrightarrow{isc} \mathrm{PS(T_1)}$$

$$\mathrm{PS(T_1)} + {}^3\mathrm{O_2} \longrightarrow \mathrm{PS(S_0)} + {}^1\mathrm{O_2} \tag{4.2}$$

$$\mathrm{Biomolecules} + {}^1\mathrm{O_2} \longrightarrow \mathrm{Products}$$

Currently, PDT is effectively limited to superficial applications or regions that are accessible by fiber optics, due to limitations of light penetration and drug delivery. The absorbance spectra for some basic PS structures are shown in Figure 4.2. Excitation to the first excited state ($S_0 \rightarrow S_1$) manifests as the peaks I-IV (known as Q-bands), and excitation to the second excited state ($S_0 \rightarrow S_2$) as the strong Soret band peaking around 400 nm. The dashed line gives a rough idea of how tissue transmittance varies from near-UV to near-IR: many organic molecules and proteins, in particular hemoglobin (which contains Fe-bound porphyrin), absorb light strongly in the UV and

visible range. Therefore, light of these wavelengths does not penetrate deeply into tissue, precluding direct excitation of PS molecules in the Soret band. For this reason, applications of PDT currently use red light: chlorins and bacteriochlorins have strong absorbance bands in the deep red, and related synthetic molecules such as phthalocyanine and naphthalocyanine even stronger still. Improvement of the absorbance of PS molecules in the NIR, the so-called optical or water window where tissue is most transparent (and therefore light has maximum penetration depth), is an active field of research.

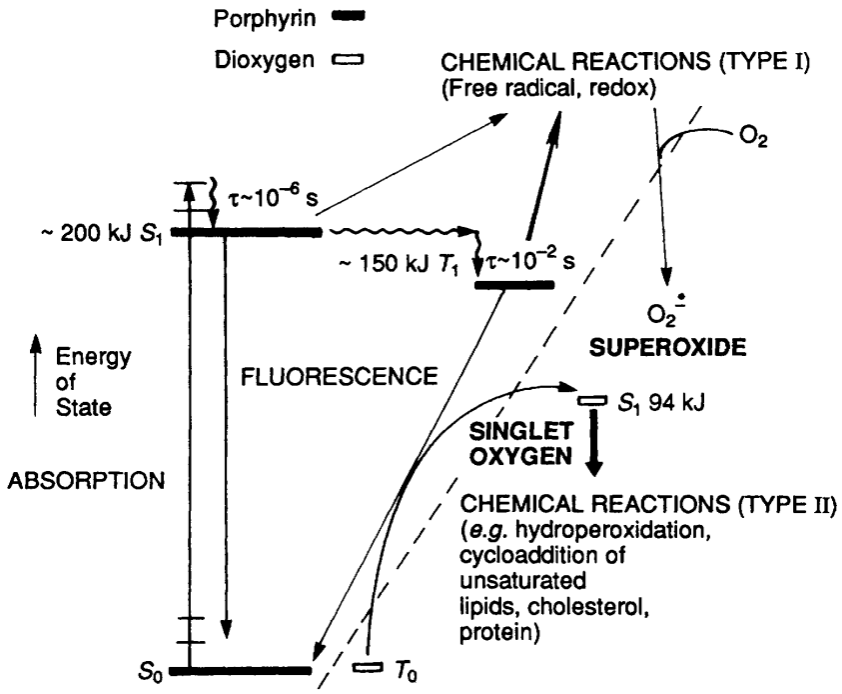

Figure 4.1 Jablonski diagram showing the processes involved in PDT. A photosensitizer in the ground state S_0, referred to as ^{1}PS, is excited by light to the first excited singlet state S_1, forming ^{1}PS*, where it can transfer charge to a substrate (Type I reaction) or undergo intersystem crossing to the first triplet state, forming ^{3}PS*, where it can react with ground state triplet oxygen to form singlet oxygen (Type II reaction). A number of reactions can then occur with photosensitized products. Reprinted with permission from reference [15].

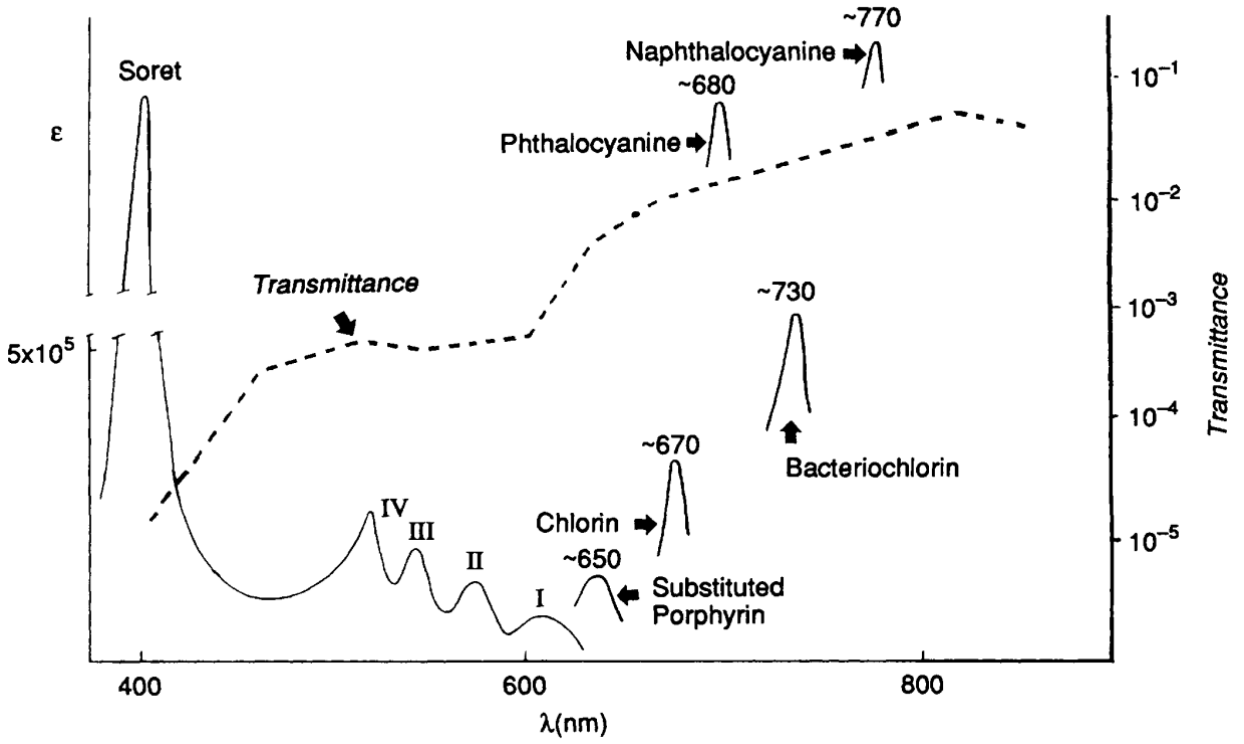

Figure 4.2 Schematic representation of the extinction coefficients of several generic PS types. Also shown is the approximate transmittance of human tissue in the same region. The bands I-IV, also known as Q-bands, are due to excitation to the first excited singlet state. The Soret band is due to excitation to the second excited singlet state, and is much stronger than the Q-bands for most basic PSs. Because tissue transmittance is low in the Soret band region, PDT typically uses red or near-infrared excitation light. Reprinted with permission from reference [15].

Issues related to drug delivery are perhaps best understood by considering the targets of PDT. PS-generated ROS can react with a myriad of biomolecules, though at the single cell level, there are particular subcellular structures that are most sensitive to this type of damage, including the nuclear envelope, mitochondria, endoplasmic reticulum and lysosomes. Interference with the proper functioning of the molecular machinery of these organelles can trigger apoptosis, or

programmed cell death. The primary trade-off with free PS molecules is that they are more likely to localize in these regions if they have some lipophilic character (in the absence of some other targeting), which encourages their association with phospholipid bilayers. Hydrophilic PS molecules that localize to the cytosol tend to be less effective, as many cytosolic components are more resilient to ROS-mediated damage. For instance, tetraphenylporphyrin tetrasulfonic acid (TPPS-4) has a better singlet oxygen yield than hematoporphyrin derivative (HPD), but lower efficacy *in vitro*, implicating its water solubility as a detriment to cytotoxicity[19]. An amphiphilic tetraphenylporphyrin derivative with two adjacent sulfonic acid groups (TPPS-2/A) was found to be more effective than TPPS-4 as well as a monosulfonic acid variant, a trisulfonic acid variant, and a variant with two opposing sulfonic acid groups (TPPS-2/O).

However, the situation *in vivo* is more complex, and PSs may be effective without entering the cancer cells themselves, through mechanisms such as collapse of tumor microvasculature. Some photosensitizers exhibit a degree of tumor targeting in their free forms, believed to arise from changes in ionization state due to the acidic pH of tumor microenvironments[20], leading to increased association with particular plasma constituents. Tumor-targeting PSs tend to associate with high- or low-density plasma lipoproteins (HDL/LDL), whereas those that do not exhibit targeting tend to associate with serum albumin, a globular protein that acts as a carrier for a number of small molecules[21, 22]. The distinction in efficacy between hydrophilic and hydrophobic PSs *in vivo* is certainly less clear than *in vitro*, and many of the more promising stand-alone PS variants in development have more complex asymmetric structures with less obvious physical mechanisms.

NPs in general can provide improved delivery and targeting options for conjugated PSs[23], while scintillating NPs may provide a route to efficiently excite conjugated PSs by bypassing issues of light penetration. Combined with radiotherapy dose enhancement, it is not difficult to see

how such a system may provide a synergistic approach and rout cancerous tissue through various insults, which is undoubtedly an attractive proposition.

4.1.3 Current status of nanoscintillator and photosensitizer conjugate investigations

Several varieties of doped and semiconductor NPs have been proposed to fill the role of the nanoscintillator. While scintillation has been demonstrated for CdSe/ZnS QDs[24], they have poor radiation hardness and degrade rapidly under γ ray exposure[25]. As the toxicity of these QDs is also primarily related to their chemical degradation, it seemed prudent to seek alternatives.

In 2009, Morgan *et al*. published a theoretical report detailing the conditions required for a nanoscintillator-photosensitizer conjugate system to produce therapeutically-relevant results, using physical parameters including NP uptake into cells, enhancement of radiation dose, scintillation light yields and energy transfer efficiencies[26]. These parameters were used to estimate the overall singlet oxygen yield of the NP-PS system with X-ray irradiation. As singlet oxygen is considered to be the primary effector of PDT, its production was taken to be indicative of the potential of conjugates to damage malignant tissue through PS activation. The study specifically cited cerium-doped lanthanum trifluoride ($LaF_3:Ce^{3+}$) as a potential nanoscintillator, in part due to its luminescence in the UV-blue (corresponding well to the Soret band of PSs) and in part due to the established techniques for its colloidal NP synthesis.

Published values of mass attenuation coefficients, available from the NIST database, allowed for calculation of the radiation absorbed by a given volume of NPs relative to an equal volume of tissue. Despite the considerable difference in relative absorption for sub-MeV radiation (up to several hundred-fold at peak, shown in Figure 4.3), only modest enhancements would be expected from this effect, as the NPs take up a small volume fraction in a realistic scenario. For a 5% cell volume fraction occupied by NPs, the increase in absorption becomes negligible above

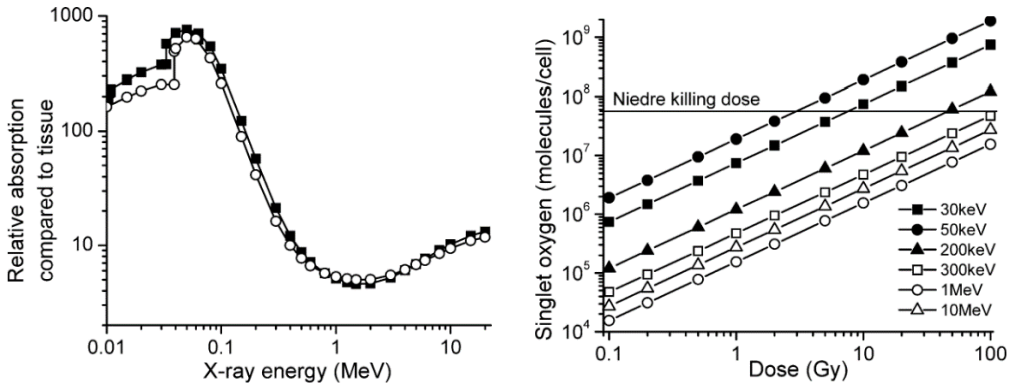

Figure 4.3 Calculated effectiveness of nanoscintillator-photosensitizers conjugates. Left: The relative absorption of X-rays of varying energy by LuI_3 (solid squares) and LaF_3 (open circles) compared to soft tissue. Right: The number of singlet oxygen molecules produced per cell by a hypothetical LaF_3: Ce^{3+} nanoscintillator-photosensitizer conjugate for different monoenergetic X-ray irradiations. Reprinted with permission from *Radiation Research*[26].

~300 keV. Overall singlet oxygen production Φ_{1O_2} was determined from the product of the scintillation yield φ_s, characteristic of the material and given in photons per MeV of absorbed radiation, the NP-PS energy transfer efficiency φ_{ET}, and the PS singlet oxygen yield φ_p. For an extremely generous value of $\varphi_s > 10^5$ photons/MeV (taken from bulk crystals of hygroscopic LuI_3:Ce^{3+}) and somewhat generous values of $\varphi_{ET} = 0.75$ and $\varphi_p = 0.89$, and using the relative X-ray absorption of the NPs, it was determined that to deliver the "Niedre killing dose" of singlet oxygen (reduction of a cell population to 1/*e* fraction, based on *in vitro* measurements of OCI-AML5 leukemia)[27, 28], only X-ray energies below ~200 keV (with peak efficiency ~50 keV) would be effective for reasonable total radiation doses. Though these results suggest that it will be difficult to produce a dramatic outcome with PDT effects alone, most of the parameters vary widely in practice and unexpected effects frequently arise in biological systems. For instance, PDT light

dose fractionation was shown to potentiate phototoxicity by enhancing PS uptake after initial damage to plasma membranes resulting in increased permeability[29]. Several additional mechanisms of interest will be described in Section 6.3.

The research group of Marek Osinski at the University of New Mexico has provided insightful investigations of the photoluminescence, scintillation and radiation dose enhancement of $Ce_xLa_{1-x}F_3$ NPs[30, 31, 32, 33]. The energy dependence of radiation dose enhancement was found to be similar to that reported by Morgan *et al*., predicting only modest enhancement factors without optimal energies and high concentrations of NPs[32].

Though there is a sizable body of work focused on radiosensitization by NPs alone and some with photosensitizers alone, only one non-QD nanoscintillator-PS conjugate system has been experimentally realized to the extent of demonstrating a measurable enhancement of X-ray irradiation in a cancer cell line. Scaffidi *et al*. modified commercially available Y_2O_3 NPs with 2-chloroethylphosphonic acid (2-CEP) ligands, which were used to form thioether linkages to fragments of the HIV-1 TAT cell-penetrating/nuclear targeting peptide bound to the PS psoralen[34]. Psoralen, used for "PUVA" therapy, is distinct from porphyrin-like PSs in that operates in a fashion more akin to a photoactivated version of a typical alkylating chemotherapeutic agent, first intercalating with DNA before generating covalent interstrand crosslinks upon absorption of UV radiation and inducing apoptosis in the affected cell. Hence, to maximize its therapeutic effect, psoralen must enter the cell nucleus through the nuclear membrane, a boundary that is generally impermeable to all but the smallest NPs. If psoralen dissociates from the NPs to enter the nucleus, the efficiency of energy transfer from the NPs will be severely diminished if not eliminated entirely. While this approach has the advantage of being able to function independently of oxygen, it is perhaps unsurprising that the enhancement was determined to be modest. Several suggestions

were extended to enhance the efficacy of the system, including better spectral overlap and light yield of the nanoscintillators.

4.2 Nanoscintillator properties and synthesis

The NPs investigated in this work are lanthanide trifluorides with the general core composition $Ce_xLa_{1-x}F_3$ where x = 0.1 or 1. Lanthanides will be abbreviated as Ln, and lanthanide-doped NPs will be generally referred to as LnNPs. Many insights into the $Ce_xLa_{1-x}F_3$ NPs have been gleaned from published work on other NP compositions (scintillating or not), including $NaLnF_4:Ln^{3+}$ (Ln = Y, Gd), $LnPO_4$ (Ln = La, Ce, Tb) and Ce^{3+}-doped $Y_3Al_5O_{12}$ (YAG), which will be discussed where appropriate. Some of the principal differences between QDs and LnNPs for biological applications are highlighted in reference [35].

Much of the pioneering work for lanthanide fluoride and phosphate NPs was conducted in the labs of Frank van Veggel, first at the University of Twente and then at the University of Victoria, including investigation of ligands for organic and aqueous synthesis, thermodynamics of NP formation, photophysics, colloidal stability and bioconjugation, as will be discussed in the following sections.

4.2.1 Physical properties

The physical properties of lanthanide-doped NPs vary considerably between different host compositions. Ionic lanthanide trifluoride crystals are characterized by optical transparency and low phonon energies, and exhibit good thermal, chemical and radiation stability. Properties listed here are for bulk crystals unless otherwise specified[36]. $Ce_xLa_{1-x}F_3$ crystallizes with the hexagonal tysonite structure, space group $P\bar{3}c1$ (D_{3d}^4), with lattice constants a = 7.13 Å and c = 7.29 Å. Because of their chemical similarity, La^{3+} and Ce^{3+} can be fully substituted for one another without altering the crystal structure, as has been demonstrated with NPs. As such, most properties of the

NPs are the same for x values ranging from 0 to 1 (LaF_3 to fully substituted CeF_3), with small variations in size and the notable exception of luminescence. The density of bulk $Ce_xLa_{1-x}F_3$ crystals varies from approximately 5.94 g/cm^3 for LaF_3 to 6.16 g/cm^3 for CeF_3 (compared to 4.81 g/cm^3 for bulk InP and 19.3 g/cm^3 for bulk Au) and is assumed to be similar for NPs. There is only one La^{3+}/Ce^{3+} site, with C_2 symmetry and 11 F^- ions in the first coordination sphere: nine at distances from 2.42 to 2.64 Å and two at 2.99 Å. The other La^{3+}/Ce^{3+} ions are at distances of ~4.10 Å (six ions), 4.35 Å (six ions), 5.99 Å (six ions), 6.29 Å (four ions), and 7.2 Å (six ions). $Ce_xLa_{1-x}F_3$ crystals are insulators with band gap energies of about 10.1-10.4 eV, and highest optical phonon energy ~466 cm^{-1} (57.8 meV).

Common approaches to synthesis of LaF_3:Ln^{3+} NPs (for more details, see Section 4.2.4) result in sizes ranging from ~3-30 nm in diameter with roughly spherical or hexagonal prism morphologies being typical. Ligand type and concentration are the primary determinants of NP size and morphology. Sizes can be further tuned by varying temperature, precursor types, concentrations and addition rates. Morphology is also somewhat dependent on the fluoride source, with ammonium fluoride producing "perforated" structures in some cases[37].

4.2.2 Optical properties & photoluminescence

Lanthanides are well known for the luminescence of their trivalent cations, which emit primarily through phosphorescence resulting from electronic transitions within the *4f* shell[38]. Because these transitions are "forbidden" by Laporte's parity selection rule (formally prohibiting electric dipole transitions between states that conserve parity), they have low absorption cross-sections and are typically sensitized by Ce^{3+} (for downconversion, with Tb^{3+} acceptor) or Yb^{3+} (for upconversion, with Tm^{3+}, Er^{3+}, and Ho^{3+} acceptors), though more complex combinations of lanthanides are certainly possible. The efficiency of both processes benefits from a low phonon energy host,

though is of increasing importance for lower energy transitions. In the case of upconverting NPs, hexagonal phase (β phase) $NaYF_4$ or isostructural $NaGdF_4$ are generally the preferred host materials.

The mechanism of cerium luminescence is distinct from other lanthanides. Neutral cerium has a $[Xe]4f^15d^16s^2$ electronic configuration; in solution or in solid hosts, the +3 or +4 oxidation states are the most common. Only the +3 state is luminescent, though the +4 state also has important implications that will be discussed in Chapter 6. In the +3 state, the 6*s* and 5*d* electrons are lost, leaving one optically active electron in the shielded 4*f* shell. Fluorescence ($\Delta S = 0$) arises from parity-allowed, high oscillator strength 4*f*–5*d* transitions. Because the 5*d* orbitals are external, these transitions are sensitive to the crystal field, and vary in energy across a substantial range depending on the host material[39]. Figure 4.4 illustrates the spin-orbit split $4f^1$ ($^2F_{5/2}$, $^2F_{7/2}$) states and crystal field splitting of the $5d^1$ ($^2D_{3/2}$, $^2D_{5/2}$) electronic configuration of Ce^{3+} in $(La,Ce)F_3$, along with the 5 distinct $4f \rightarrow 5d$ transitions. The 5*d* centroid of the free ion is positioned at 51,230 cm^{-1} (6.35 eV) relative to the $^2F_{5/2}$ ground state, and is shifted ε_c = 5580 cm^{-1} (0.69 eV) in the crystal matrix. The total crystal field splitting ε_{cfs} = 11386 cm^{-1} (1.41 eV)[40], putting the 5*d* levels at 4.98, 5.30, 5.69, 5.96 and 6.39 eV.

Because it is advantageous to be able to keep track of NPs visually in the lab environment and the Ce^{3+} emission does not have a substantial component in the visible range, NPs co-doped with a small amount of Tb^{3+} (5%) were also produced. Excitation of the Ce^{3+} sensitizes Tb^{3+}, producing sharp emission peaks at 492, 547, 587 & 623 nm at the expense of Ce^{3+} luminescence[41]. Example absorbance and PL spectra of $Ce_{0.1}La_{0.85}Tb_{0.05}F_3/LaF_3$ NPs are shown in Figure 4.5.

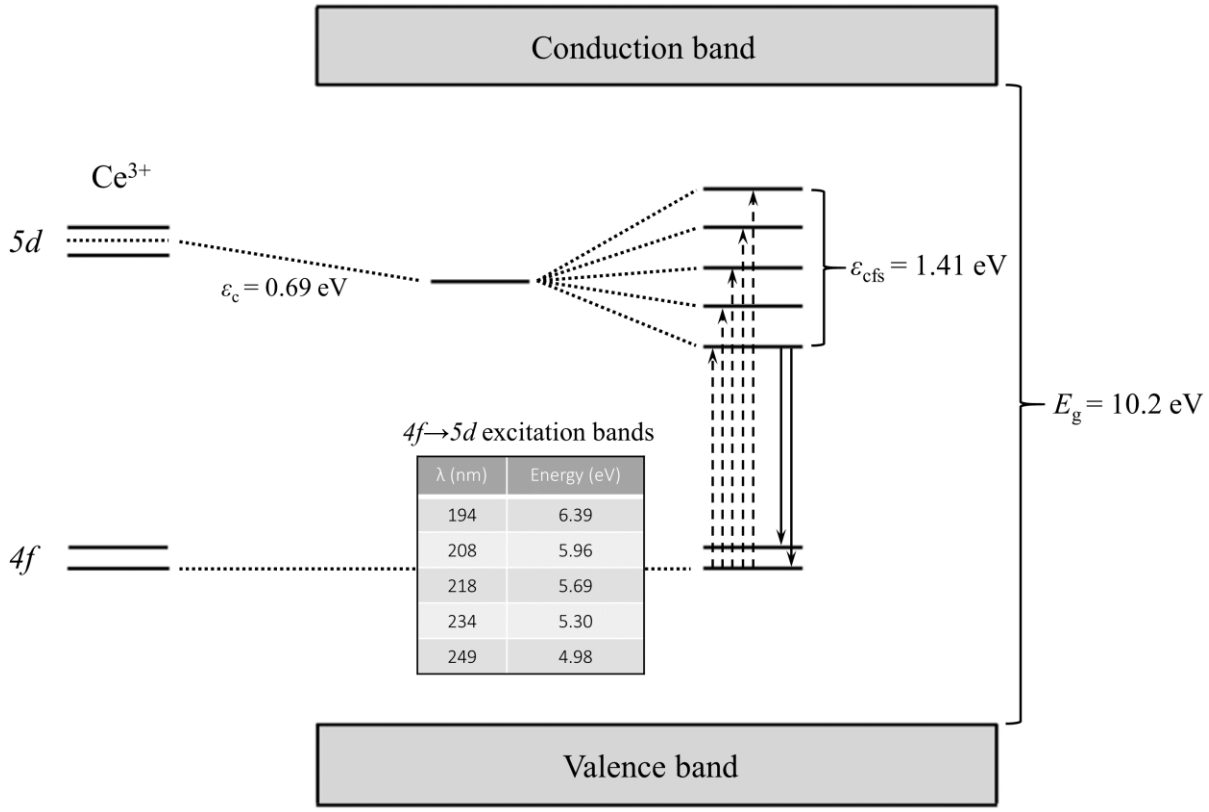

Figure 4.4 Centroid shift and crystal field splitting of the 5*d* levels of Ce^{3+} doped into LaF_3.

UV spectroscopy requires special consideration due to the high absorption of many organic compounds and solvents in this region. The absorbance spectra of several relevant compounds and materials are shown in Appendix B.

4.2.3 Scintillation

Scintillation is the process whereby a material, referred to as a scintillator, produces light upon interaction with ionizing radiation. Radioluminescence (RL) mechanisms of bulk $Ce_xLa_{1-x}F_3$ crystals were elucidated in the late 80s and early-to-mid 90s to evaluate their potential as candidates for radiation detection purposes[36, 42, 43, 44, 45, 46, 47]. Though the scintillation was found to be significantly faster than commonly used scintillators (BGO, CsI:Tl, NaI:Tl) on a per-photon

basis, the overall light output was found to be unexpectedly weak, with variable luminescence that is significantly dependent on the quality of the crystal and the presence of defects. This variability precluded their use as reliable detectors for the most part, at least compared to other options being developed concurrently, such as $PbWO_4$. Much of the most insightful work into scintillation mechanisms was done in the lab of Alexander Łempicki at Boston University in collaboration with scholars on leave from Nicolaus Copernicus University in Toruń, Poland.

The general process of scintillation occurs in three steps: first, conversion of absorbed ionizing radiation energy into electronic-lattice excitations (electron-hole pairs and/or excitons), followed by transfer of the excitation energy to the emitting ions and then luminescence. The overall scintillation efficiency is given by the product of the individual efficiencies:

$$\eta = \beta S Q, \ 0 \leq \eta, \beta, S, Q \leq 1 \tag{4.3}$$

where β, the efficiency of the conversion process, encompasses the fraction of absorbed energy lost to optical phonons, S is the efficiency of the transfer process, and Q is the luminescence quantum yield of the emitting center. The overall light output L (in photons/MeV) is given by:

$$L = n_{e-h}\eta = \frac{10^6}{2.3E_g}\beta S Q \tag{4.4}$$

where $n_{\text{e-h}}$ is the number of *e-h* pairs or excitons that are generated per MeV of absorbed radiation, discounting losses to optical phonons, and E_g is the band gap of the host (in eV). The factor of 2.3 is related to the derived minimum incident photon energy required to generate a single *e-h* pair[48], $\xi_{\text{min}} = 2.3E_g$, and so $n_{\text{e-h}} = E/2.3E_g$ where E is the energy of the incident photon, in this case 1 MeV = 10^6 eV.

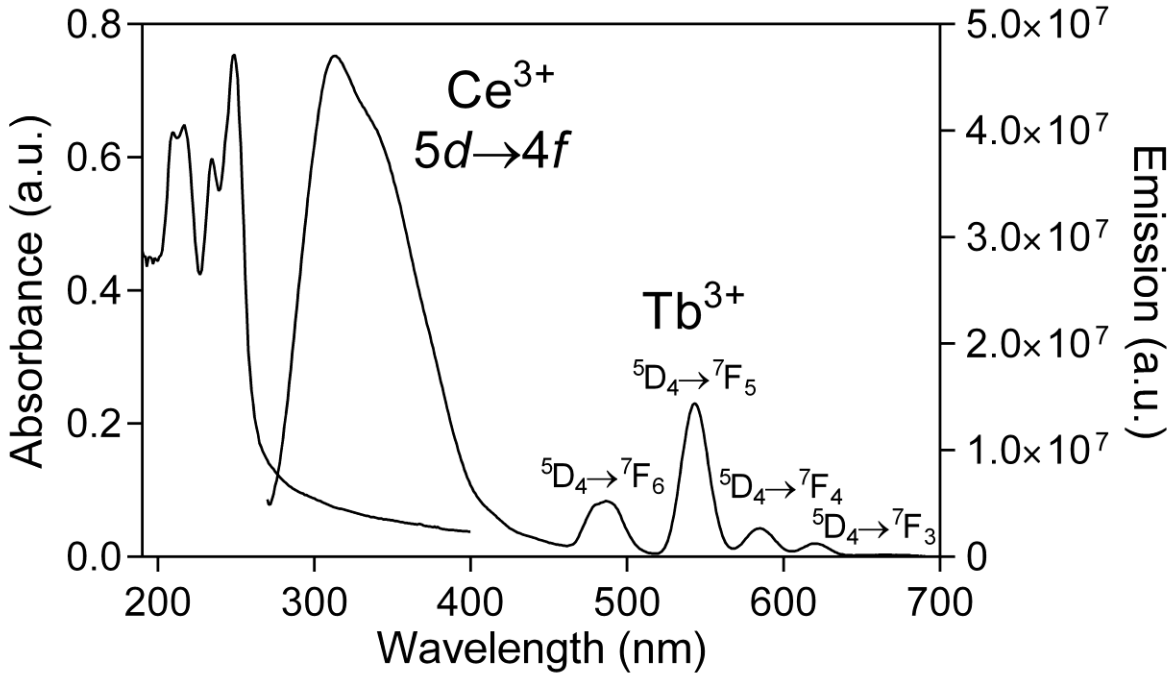

Figure 4.5 Absorbance and photoluminescence spectra of $Ce_{0.1}La_{0.85}Tb_{0.05}F_3/LaF_3$ NPs, synthesized using a hydrothermal technique with aminocaproic acid ligands. The strong absorbance in the 200-300 nm range is due to 4*f*→5*d* transitions of Ce^{3+}, which can fluoresce through 5*d*→4*f* recombination, or transfer energy to Tb^{3+}, which emits through phosphorescence, with the distinct narrow peaks characteristic of most luminescent lanthanides. The relevant electronic transitions are labeled. From original unpublished data.

Low phonon energy hosts such as LaF_3 tend toward higher values of β, while the transfer process *S* is relatively inefficient compared to pentaphosphate or orthophosphate hosts. The β and *S* mechanisms of $Ce_xLa_{1-x}F_3$ were determined to consist of three distinct processes that have different relative contributions depending on the value of *x*: (i) direct excitation of Ce^{3+} by X-rays or secondary electrons, (ii) ionization of Ce^{3+} followed by electron capture and formation of bound

excitons, or (iii) energy transfer to Ce^{3+} from lattice excitations of the bulk matrix. At lower concentrations of Ce^{3+}, up to $x \sim 0.5$, mechanism (iii) dominates the scintillation response. At higher Ce contents, mechanism (i) is predominant, accounting for a large fraction of the light output in CeF_3[36].

Intuitively, it is easy to imagine possible limitations for scintillation of NPs and energy transfer (ET) in PS conjugates. In ionic crystals, the diffusion length of *e-h* pairs may be up to 100 nm. If these account for a significant portion of the scintillation, the physical dimensions of the NP may limit the output by constraining the number of possible *e-h* pairs per excitation. Regarding conjugates, the short luminescence lifetime, while useful for detectors where speed is of the essence, may actually be a disadvantage for ET if non-ET processes outcompete ET.

Scintillation of NPs has recently been demonstrated, though RL of colloidal $Ce_xLa_{1-x}F_3$ in particular has not been thoroughly studied. Jacobsohn *et al*. have published RL spectra for powdered LaF_3:Eu (~4.4 nm), BaF_2:Ce (~10 nm) and CaF_2:Eu (~18 nm) NPs under excitation by a 40 kV Bullet X-ray tube and $CaF_2:Eu^{3+}$ excited by a 1 μCi ^{241}Am source (E_α = 5.5 MeV, E_γ = 60 keV)[49]. A number of reports have investigated the scintillation response of $Ce_xLa_{1-x}F_3$ nanocomposites, where small nanocrystals (~10 nm) are cast into oleic acid or polymer matrices with consistencies ranging from liquid to waxy. In initial studies by McKigney *et al*., nanocomposites exhibited photopeaks for ^{137}Cs, ^{241}Am and ^{57}Co irradiation[50, 51]. Most recently, a modest scintillation response (compared to a BC-400 polyvinyltoluene detector) has been shown for 25% NP-loaded composites exposed to several sources: ^{22}Na (3.22 μCi), ^{60}Co (3.78 μCi), ^{137}Cs (31.9 μCi), ^{241}Am (9.09 μCi), and ^{252}Cf (5.03 μCi)[52].

Scintillation also occurs in conjugated or aromatic organic molecules due to π-orbitals[53], the same characteristic of the electronic structure that gives rise to the strong absorption of photosensitizers.

4.2.4 Synthesis

As with semiconductor NPs, many variations have been developed to synthesize lanthanide-doped NPs in both organic and aqueous phases. In a similar manner, organic phase synthesis tends to provide greater reproducibility and better control over the size, shape and crystallinity of the NPs produced, while aqueous methods use milder conditions and less noxious reagents. Synthesis of LaF_3 NPs was first reported in 2001 by Dang *et al*., using the ligand ammonium di-*n*-octadecyldithiophosphate (ADDP) in a mixed ethanol/water phase[54]. As-synthesized ADDP-stabilized NPs are soluble in non-polar organic solvents such as chloroform and toluene. ADDP synthesis found regular use for a few years and has maintained some popularity for PL investigations of NPs[55]. In 2005, the van Veggel group published techniques for low-temperature hydrothermal synthesis of small (<10 nm diameter) NPs using citric acid[56] or phosphorylethanolamine (PEA)[57] ligands. NPs synthesized in this way were found to be highly water-dispersible, stable at concentrations of up to 50 mg/mL.

Many synthesis variations were investigated for this work, using different lanthanide and fluoride sources, ligands/stabilizers, temperatures, concentrations and precursor addition orders and rates. Lanthanides were provided as hydrated chloride or nitrate salts, fluorine from ammonium fluoride, sodium fluoride, or sodium/potassium tetrafluoroborate. Ligands/stabilizer types and concentrations were varied the most. A number were investigated alone and in combination, including the amino acids glycine and glutamic acid, neurotransmitter 4-aminobutanoic acid (aka γ-aminobutyric acid or GABA), “linear core amino acids” 6-

aminohexanoic acid (aka ε-aminocaproic acid or ACA, a lysine derivative) and 12-aminododecanoic acid, diethylene glycol, polyethylene glycol (PEG)-diamine, PEG (M_n = 600), folate, flavin mononucleotide (FMN) and citric acid. The primary criteria for evaluating NPs were colloidal stability, size and PL. Most subsequent work (including the entirety of the following two chapters) was conducted with NPs synthesized with ACA or citric acid, one of the most common choices for aqueous synthesis. ACA has recently been reported in synthesis protocols for other LnNPs[58], and was found to be less toxic than MPA or PEG coatings on upconverting nanoparticles (UCNPs)[59].

Similarly to other luminescent NPs, the addition of 'shell' layers that passivate the luminescent core can enhance the PL QY by reducing surface quenching effects[56, 60, 61], as well as slow the oxidation of Ce^{3+} to nonluminescent Ce^{4+}[62]. In most cases, lanthanide-doped NPs are shelled with the same material as the core but undoped, sometimes referred to as 'self-shelling.' As with the NP core synthesis, a number of approaches have been developed for the addition of shells. Li *et al*. produced citrate-stabilized CeF_3:Tb/LaF_3 NPs by sequential hydrosolvothermal treatment, first forming and purifying the NP cores before adding the reagents for the LaF_3 shell and treating a second time[63]. A common method for both aqueous and organic-based synthesis techniques is the alternate addition of the shell precursors in small amounts, ostensibly forming the shell layer by layer[55, 64]. In one instance, this method produced $Ce_{0.45}La_{0.4}F_3Tb_{0.15}$/$LaF_3$ NPs with ~10% greater QY than those made by adding each shell precursor sequentially after core formation, as well as by forming the cores in the presence of a stoichiometric excess of fluoride, followed by the addition of the shell lanthanum[65]. In 2009, Dong *et al*. definitively demonstrated that the addition of excess free Ln^{3+} ions to aqueous solutions containing already-formed lanthanide fluoride NPs could result in rapid cation exchange, the extent of which depended on the

relative sizes of the lanthanides used[66]. In an effort to circumvent this exchange during subsequent core/shell NP syntheses, shell precursors (lanthanum nitrate hexahydrate) were added to the core NPs in the presence of an excess of fluoride precursor (sodium fluoride), to limit the amount of free La^{3+} in solution[67]. Interestingly, while additional shell volume enhances the photoluminescence, it may initially increase the radioluminescence yield up to a certain thickness before decreasing it if the diffusion length of carriers is insufficient to produce efficient excitation of the emitting centers in the core[55].

4.2.5 Surface chemistry & stability

Surface chemistry is of critical importance for biomedical applications of NPs, as it not only affects luminescence, but dictates colloidal stability and tendency to aggregate, sensitivity to ionic strength, pH and solvent polarity, and potential for drug loading and bioconjugation. When NPs are applied to cells in culture or *in vivo*, surface charge, ligand bulk and degree of surface coverage determine where NPs accumulate and at what rate. Generally, the greater the charge, the more rapidly NPs are taken up by cells, but also reveals them as prime targets for scavenging by macrophages *in vivo*.

It is established that phosphate anions, an important biological species, have a high affinity for lanthanide cations, complicating the use of LnNPs in physiological media. Weaker ligands such as carboxylates and amines are easily displaced at relevant phosphate concentrations along with any ligand-bound molecules, compromising the colloidal stability of the NPs. Despite this apparent hindrance, the issue is infrequently mentioned, though it has been a salient point in a few recent reports. The incompatibility of phosphate with lanthanide fluoride NPs was first addressed in 2009 by Boyer *et al*., who exchanged oleate ligands on as-synthesized $NaYF_4$ NPs with monophosphate-PEGs of M_n = 750 and 2000[68]. The phosphate-PEG-coated NPs were found to be

stable in water at neutral and acidic pH, though they suffered from agglomeration at pH > 8 attributed to displacement of the ligands by OH^- groups. In 10 mM phosphate-buffered saline (PBS), the NPs were found to agglomerate and settle within minutes due to the strong association of phosphate anions with the NP surface. However, the NPs could be kept stable in PBS & growth medium at up to 10 mg/mL if some excess ligand remained in solution. Monophosphate/phosphonate-PEG coatings have also been investigated for Fe_3O_4 (magnetite) NPs[69], Y_2O_3 NPs[70] and CeO_2 NPs[71].

Cao *et al*. expanded on the work of Boyer *et al*. by investigating the effect of multivalent PEG-phosphonate ligands on the stability of 9-11 nm $NaLnF_4$ nanocrystals in PBS (137 mM NaCl, 2.7 mM KCl, 10 mM $Na_2HPO_4 \cdot H_2O$, 2 mM KH_2PO_4, pH 7.4) and 200 mM phosphate buffer[72]. The NPs were synthesized in an organic solvent with oleate ligands and transferred to aqueous phase after ligand exchange, wherein aggregation was assessed by DLS CONTIN in solutions of 1 mg/mL NPs. Monophosphate-PEG_{2000} was found to be insufficient at preventing aggregation in water adjusted to pH 3 by addition of HCl or to pH 9 by addition of NaOH, diphosphonate-PEG_{2000} was found to be suitable at pH 3 but not at pH 9, and tetraphosphonate-PEG_{2000} was able to entirely prevent aggregation in PBS and mostly prevent aggregation in 200 mM phosphate buffer. Somewhat conflicting results were reported shortly after by Hou *et al*., indicating long-term colloidal stability in PBS of 20 nm $NaGdF_4$ NPs similarly coated with maleimide-diphosphonate-PEG (n = 44), though the NP concentration was not clear[73].

In the meantime, the most common approaches to adapting LnNPs for use in physiological environments are similar to those used with QDs, including encapsulation of oleate-stabilized NPs with amphiphilic polymers[74, 75, 76] or silanization, the process of growing silica shells around the NPs[77]. Both techniques provide coatings that are more robust than typical ligands, at the cost of

adding significant bulk to the NPs, which can be detrimental to clearance *in vivo*. They also provide a means for drug loading or conjugation, the benefits and drawbacks of which will be discussed in Section 4.3.

We opted to seek out a compact ligand to exchange with ACA or CA that would maintain colloidal stability and provide an anchor for bioconjugation. Candidates included the small monophosphate ligands phosphorylethanolamine and phospho-DL-threonine (inspired by the success of *D*-penicillamine ligands used with QDs[78], which provide steric protection of the NP surface), polyacrylic acid, chitosan oligomers, though none were determined to provide adequate resistance to stability loss in physiological solutions.

Ultimately we turned to bisphosphonates, a class of tetraprotonic drugs characterized by two phosphate groups linked by a P-C-P backbone that are well-known to chelate metals with high affinity. They are primarily used for the treatment of osteoporosis and related diseases, but have found some use as NP ligands. Additionally, some bisphosphonates have been shown to have antineoplastic activity, which will be discussed in Section 6.3. Surface modification with etidronate (1-hydroxyethane 1,1-diphosphonic acid or HEDP) was shown to significantly improve the upconversion efficiency of $NaYF_4$:Yb^{3+},Er^{3+} in powder form or in aqueous colloidal solutions[79]. Alendronic acid ([4-amino-1-hydroxy-1-(hydroxy-oxido-phosphoryl)-butyl]phosphonic acid trihydrate) is a nitrogenous bisphosphonate with –OH and $–(CH_2)_3$-NH_2 side chains, and therefore a good candidate ligand to provide both a strong attachment to the NP surface and a free amine for bioconjugation. Thus far, it has been used elsewhere as a ligand for superparamagnetic γFe_2O_3 (maghemite) NPs, where it has been shown to provide a degree of stabilization in physiological solutions and a platform for bioconjugation of the fluorescent dye

rhodamine B for imaging[80], and/or PEG molecules for improved colloidal stability over a wide pH range.

4.3 Conjugate design and energy transfer

The choice of photosensitizer (PS) is not arbitrary, as there are a number of physical and chemical properties of the PS beyond singlet oxygen yield that will dictate the efficacy of the construct. Similarly, the approach to conjugation/PS loading is important, as will be discussed in the following sections. Many conventional photosensitizers are based on naturally-occurring porphin, chlorin and bacteriochlorin structures, comprised of highly conjugated heterocyclic macrocycles that exist in *free base* form or with metal cations coordinated at the ring center. The basic free base structures are shown in Figure 4.6. Porphin consists of four pyrrole subunits linked via four methine bridges, with 22 π electrons delocalized over the macrocycle, conferring intense absorption bands in the UV/visible range. Chlorins have a similar structure with one pyrrole replaced by a pyrroline subunit (20 π electrons), and bacteriochlorins/isobacteriochlorins contain two pyrroles and two pyrrolines (18 π electrons). Compounds such as hemes (Fe^{2+}-bound porphyrins) and chlorophylls (Mg^{2+}-bound porphyrins and chlorins) provide functionality to metalloproteins that serve many important biological roles. Hundreds of derivatives are commercially available covering many side chains and functionalities, as well as complexes with a number of divalent and trivalent *d*-block elements among others, including Mg^{2+}, Cr^{3+}, Mn^{3+}, $Fe^{2+/3+}$, $Co^{2+/3+}$, Ni^{2+}, Cu^{2+}, Zn^{2+}, Ga^{3+}, In^{3+}, Sn^{4+}, Al^{3+}, Si^{4+}, Mo^{5+}, Ru^{2+}, $Rh^{2+/3+}$, Pd^{2+}, Ag^{2+}, Er^{3+}, Yb^{3+}, Ir^{3+}, Pt^{2+}, Au^{3+} and $[VO]^{2+}$. Frontier Scientific alone has 492 distinct products in the "porphyrin" category. Generally, the free base form of a PS is a superior photosensitizer, but this is not strictly the case. Coordinated metal ions can improve the solubility and stability of a PS, typically at the expense of singlet oxygen yield.

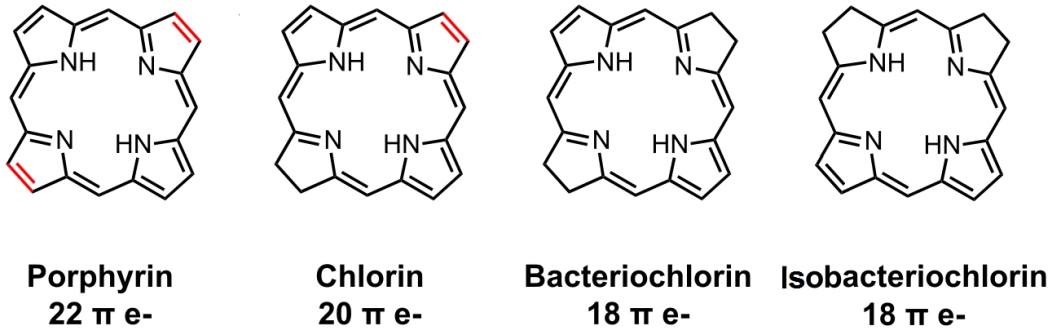

Figure 4.6 Basic structures of photosensitizer cores.

Though most of the aforementioned derivatives are characterized by strong Soret band absorption at ~400 nm due to π-π* transitions, properties such as extinction coefficient, triplet and singlet oxygen yield, photobleaching rate, solubility and aggregation are strongly influenced by side chain modifications and coordinated or proximal metal atoms. The available options are considerably narrowed by the requirement of functional groups for conjugation, and preference for low cost and available information regarding chemical and photosensitizing properties.

Chlorin e6 (Ce6), a second generation PS derived from the chlorophyll degradation product pheophorbide A, was determined to be the best option for proof of principle studies due to its low cost and desirable properties, which have in turn made it a popular choice for many experiments over the last two decades. The variant mono-L-aspartyl chlorin e6, also known as NPe6, LS11 or Talaporfin, which varies from Ce6 primarily in solubility, has been approved in Japan (as Laserphyrin) for PDT of lung cancer and has undergone multiple clinical trials in the US for the treatment of solid tumors as Aptocine/Litx™. Ce6 and its derivatives have been studied extensively as free molecules[81, 82, 83] and conjugated to or otherwise complexed with QDs[84, 85], Au

nanorods[86], UCNPs[87], "carbon dots"[88], carbon nanotubes (CNTs)[89], graphene oxide[90, 91] and polymer/protein structures[92, 93, 94, 95].

Before NP-Ce6 conjugates had been successfully prepared in our lab, NP-PS interactions were first evaluated using electrostatic complexes of ACA-stabilized NPs with the water-soluble PS deuteroporphyrin IX 2,4-disulfonic acid. The results of this investigation form the bulk of Chapter 5.

4.3.1 Drug loading & bioconjugation

Amphiphilic polymer encapsulation provides a convenient means to package lipophilic drugs by loading them into the hydrophobic layer surrounding NPs. This simple supramolecular approach allows for fairly high loading amounts and retention, but adds considerable bulk to the NPs and provides poor control over drug aggregation, orientation and nature of coupling to NPs. It was recently demonstrated with popular therapeutic agents by Wang *et al*., who encapsulated oleate-stabilized $NaYF_4$:Yb^{3+},Er^{3+} UCNPs with poly(maleic anhydride-alt-1-octadecene) (PMAO)-PEG amphiphilic copolymers[96]. Encapsulated NPs were mixed with the chemotherapeutic agent doxorubicin (dox) in PBS, and loading amounts up to 8% w/w were obtained after mixing overnight at pH 8. The release of the adsorbed dox was found to be pH-dependent, occurring faster under slightly acidic conditions where dox becomes protonated (pH 5). Ce6 dissolved in dimethyl sulfoxide (DMSO) was loaded in a similar fashion at up to 8.6% w/w, and slowly released under standard physiological conditions, reaching only ~10% released after 50 hours in PBS (pH 7.4). Production of singlet oxygen by UCNP-sensitized Ce6 excitation under 980 nm laser irradiation was notable, as reported indirectly by bleaching of *p*-nitrosodimethylaniline (RNO) in the presence of imidazole, and the system produced promising results for NP-assisted NIR PDT using 4T1 breast cancer cells *in vitro* and *in vivo*[87].

Given that the efficacy of free PS molecules *in vitro* is affected by their solubility, or more specifically, their amphiphilicity, we therefore supposed it may be beneficial to attach PSs in a way that would maximize their exposure to the solvent and surroundings, encouraging their association with other biomolecules in a similar way as the free molecules are known to do. One of the distinct advantages of using NPs as a drug delivery platform is the potential to impart additional targeting through size, charge, chemical and biological modifications, but we nonetheless aimed to begin with a simple system that could be modified in the future.

We sought to establish a system for bioconjugation of Ce6 or other molecules of interest that would satisfy a few basic requirements, revolving around compact ligands that would confer colloidal and chemical stability and prevent aggregation of NPs along with providing functional groups to allow covalent attachment of PSs as close as possible to the NP surface. Alendronate satisfies most of these criteria but results in NPs that are pH-sensitive, precipitating under neutral or basic conditions. Attachment of PEG groups to the free amines provides resistance to precipitation in PBS, as observed in our lab by modifying alendronate-coated NPs with methyl-PEG_4-NHS ester (mPEG-NHS). A cartoon illustrating the conjugation of Ce6 and $mPEG_4$ to alendronate-coated NPs is shown in Figure 4.7.

In addition to the affinity of the dual phosphonate groups for the lanthanide cations, the carbon linkage between them provides additional chemical stability over an oxygen linkage. The utility of bisphosphonates in preventing growth of calcium crystals partially stems from this increased stability relative to pyrophosphate, which is rapidly hydrolyzed *in vivo*.

Preparation of LnNP bioconjugates (employing covalent attachment) appears infrequently in the literature. The principles of bioconjugation are similar to those discussed for QDs, with the additional stability and solubility concerns mentioned in the preceding sections. Ligand-exchanged

and silicated LnNPs typically present primary amine functionalities which provide some additional versatility over carboxylate groups. Amines provide a number of conjugation routes, as shown in Figure 4.8. Diamente *et al*. prepared conjugates of PEA-stabilized Eu^{3+} and Ce^{3+}/Tb^{3+}-doped LaF_3 by reacting the free amine of the ligand with activated biotin-PEG or mPEG NHS esters, demonstrating a successful strategy for attachment of molecules through amide bond formation. The use of these conjugates was restricted to borate buffer. Biotin conjugates have also been prepared with CeF_3:Tb NPs silanized using TEOS/APTES[97, 98] and PEA-stabilized Ln^{3+}-doped zirconia[99].

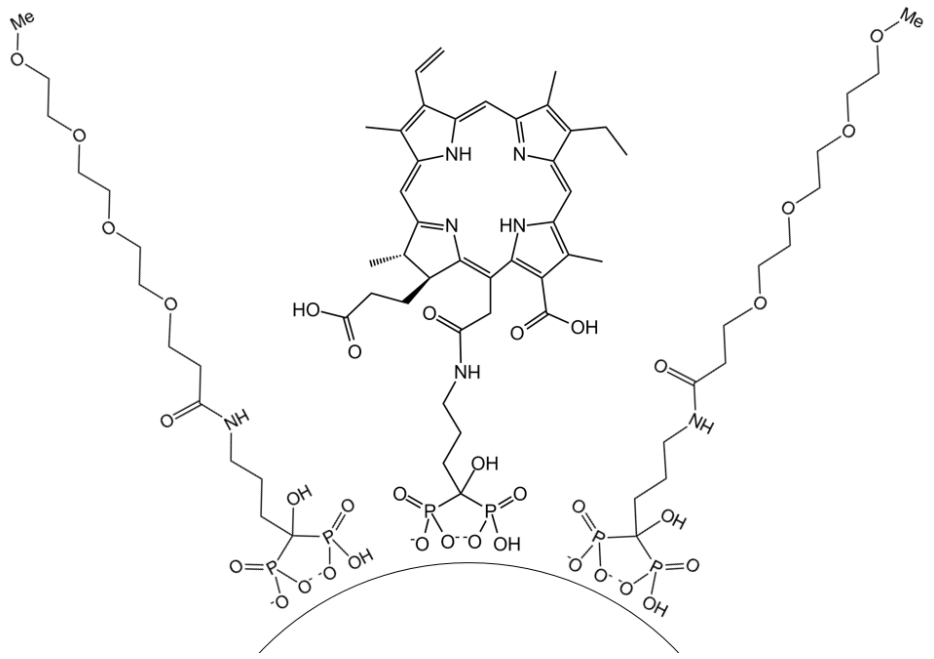

Figure 4.7 Cartoon depiction of Ce6 (center) and $mPEG_4$ (sides) conjugated to NPs. Amide bonds are formed with the free amine of alendronate, which is coordinated to the NP surface through bisphosphonate groups.

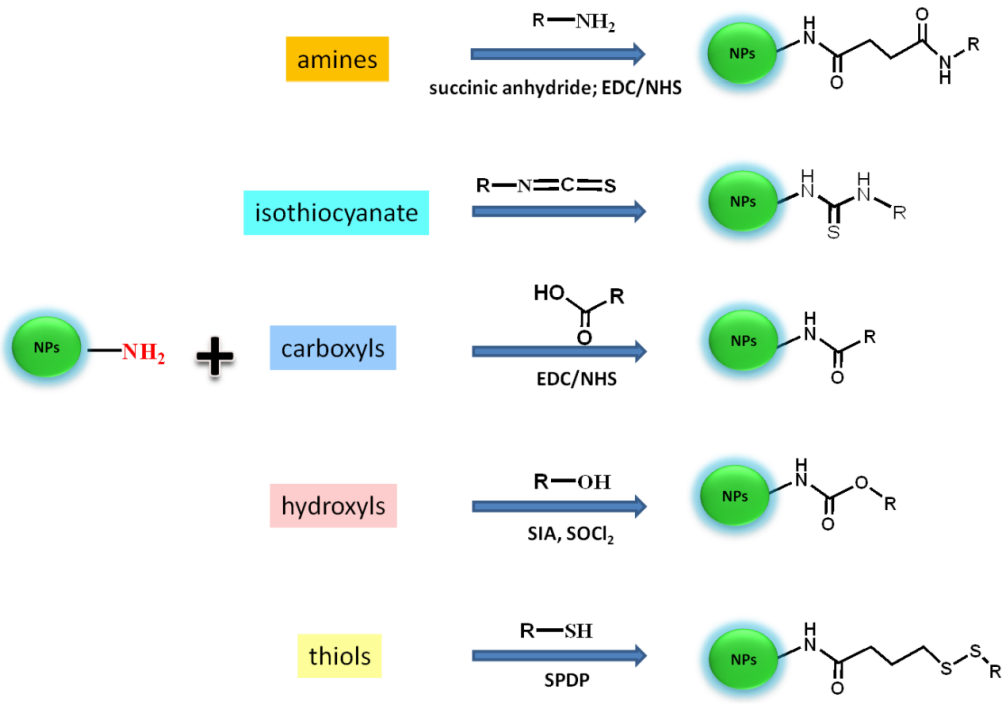

Figure 4.8 Bioconjugation routes for NPs presenting terminal amines. Molecules of interest, denoted as R, can be conjugated through a number of functionalities. Reprinted with permission from reference [100].

4.3.2 Energy transfer

Lanthanide energy and charge transfer (ET and CT) have been extensively studied for lanthanide chelates and organic dye pairs by Paul Selvin and others[101, 102], and more recently in LnNPs, though most efforts have focused on sensitization of 4*f*–4*f* luminescence by Ce^{3+}, Yb^{3+} or surface-associated organic molecules. The situation can quickly become rather complex with lanthanides whose luminescence involves the $4f^n$ configuration. In these cases, magnetic dipole transitions are allowed and may have intensity of the same order of magnitude as electric dipole transitions. Additionally, some induced dipole transitions are hypersensitive to the environment of the

lanthanide ion and apparently follow the selection rules of electric quadrupole transitions, leading them to be referred to as pseudo-quadrupolar transitions.

Reports involving cerium dopants as direct or indirect energy donors to organic molecules are few in number. Fortunately, Ce^{3+} luminescence is comparatively simple and can be adequately described by typical Förster resonance energy transfer (FRET) theory for non-radiative dipole-dipole coupling. FRET efficiency η between an energy donor and acceptor separated by a distance r_{da} is given by:

$$\eta = \frac{1}{1+(r_{da}/R_0)^6} \tag{4.5}$$

R_0 is referred to as the Förster distance and corresponds to the value of r_{da} at which $\eta = 0.5$, with a value that depends on the fluorescence QY of the donor (Q_d), the spectral overlap between the donor emission and acceptor absorbance (J) and the dipole orientation factor κ:

$$R_0^6 = \frac{9Q_d(ln10)\kappa^2 J}{128\pi^5 n^4 N_A} = 8.25 \times 10^{-25}(Q_d \kappa^2 n^{-4} J) \tag{4.6}$$

$$J = \int f_d(\lambda)\varepsilon_a(\lambda)\lambda^4 d\lambda \tag{4.7}$$

Alternatively, FRET efficiencies are often estimated by the change in steady-state or time-resolved luminescence of the donor in the presence of the acceptor:

$$\eta = 1 - \frac{\tau_{da}}{\tau_d} = 1 - \frac{f_{da}}{f_d} \tag{4.8}$$

In 2004, Wuister *et al*. investigated energy transfer between porous networks of interconnected 18 nm YAG:Ce^{3+} nanocrystals (NCs) and the amine-reactive fluorescent dye tetramethylrhodamine isothiocyanate (TRITC)[103]. Glycine was used to coat the NCs, bound to the surface through the carboxylate moieties and providing terminal amines for attachment of TRITC. ET for the

conjugate was demonstrated through strong emission of TRITC relative to NCs following selective excitation of the NCs, as well as the appearance of a fast initial decay of the time-resolved PL. The ET was estimated using Förster-Dexter theory, giving a "critical distance" (equivalent to R_0) of 7 nm, resulting in energy transfer rates of up to 10^8 s^{-1} for Ce^{3+} sites within 5 nm of the NC surface, supposed to be ~90% of the total Ce^{3+} given the NC size.

Di *et al*. investigated electrostatic complexes of $CePO_4$:Tb nanorods and Rhodamine B (RhB), which used Ce^{3+}-sensitized Tb^{3+} emission to excite RhB resulting in ET efficiency η up to 0.85 as determined by ratiometric luminescence analysis[104]. Evidence of ET was taken by the quenching of the NP steady-state luminescence and concomitant increase in RhB emission with increasing amounts of RhB. Time-resolved measurements of the $^5D_4 \rightarrow {}^7F_5$ transition of Tb^{3+} also exhibited quenching but did not quantitatively agree, reporting efficiencies lower than those determined by steady-state quenching ($\eta \sim 0.7$ at the highest quenching condition), a discrepancy that was not addressed. The non-negligible extinction coefficient of RhB at the excitation wavelength was not discussed.

In 2013, Kar *et al*. investigated electrostatic complexes of $LaPO_4$:Ce nanorods and the fluorescent dye coumarin 440 (C-440) using steady-state and time-resolved PL measurements[105]. The Stern-Volmer sphere of action static quenching model was applied to the steady-state quenching, and the ET efficiency estimated by the ratio of the Ce^{3+} fluorescence lifetimes, giving $\eta = 0.24$ for an estimated 1:47 nanorod:dye ratio. ET was corroborated by an increase of the fluorescence lifetime of the dye, excited at 280 nm, when complexed with the nanorods.

In the previous examples, the nanomaterials were not modified by shells. A recent report by Wang *et al*. used core/shell upconversion $NaYF_4$:Yb^{3+},Er^{3+}/$NaYF_4$ nanoparticles with the photosensitizer rose bengal (RB) to investigate the effect of shell thickness on ET efficiency, but

more importantly, on singlet oxygen production[106]. While additional undoped shell thickness enhances the luminescence efficiency substantially up to a point, it also increases the spatial separation between the emitting centers of the NP core and the ET acceptors near the shell surface. Indeed, an optimal shell thickness was determined for RB activation which did not coincide with the strongest upconversion luminescence or greatest ET efficiency – with unshelled NPs, the ET efficiency was greatest, as RB quenched a large amount of the relatively low luminescence output. As the shell thickness increased, the NP luminescence increased dramatically, and so while the same amount of RB quenched a smaller proportion of the total emission, it was still a substantially larger amount of energy absorbed and singlet oxygen produced. Beyond the optimal shell thickness, increases in NP luminescence did not outweigh the decline in ET efficiency due to the increased donor-acceptor distance.

4.4 References

1. Chen, W.; Zhang, J. Using nanoparticles to enable simultaneous radiation and photodynamic therapies for cancer treatment. *Journal of nanoscience and nanotechnology* **2006,** *6* (4), 1159-66.
2. Oronsky, B. T.; Knox, S. J.; Scicinski, J. Six degrees of separation: the oxygen effect in the development of radiosensitizers. *Translational oncology* **2011,** *4* (4), 189-98.
3. Kobayashi, K.; Usami, N.; Porcel, E.; Lacombe, S.; Le Sech, C. Enhancement of radiation effect by heavy elements. *Mutation Research/Reviews in Mutation Research* **2010,** *704* (1–3), 123-131.
4. Attix, F. H. Gamma- and X-Ray Interactions in Matter. In *Introduction to Radiological Physics and Radiation Dosimetry*; Wiley-VCH Verlag GmbH, 2007, pp 124-159.
5. Hubbell, J. H. Review of photon interaction cross section data in the medical and biological context. *Physics in medicine and biology* **1999,** *44* (1), R1.
6. McMahon, S. J.; Mendenhall, M. H.; Jain, S.; Currell, F. Radiotherapy in the presence of contrast agents: a general figure of merit and its application to gold nanoparticles. *Physics in medicine and biology* **2008,** *53* (20), 5635-51.
7. Brun, E.; Sanche, L.; Sicard-Roselli, C. Parameters governing gold nanoparticle X-ray radiosensitization of DNA in solution. *Colloids and surfaces. B, Biointerfaces* **2009,** *72* (1), 128-34.
8. Heuvel, F. V. d.; Jean-Pierre, L.; Nuyts, S. Beam energy considerations for gold nano-particle enhanced radiation treatment. *Physics in medicine and biology* **2010,** *55* (16), 4509.
9. Zhang, X. D.; Wu, D.; Shen, X.; Chen, J.; Sun, Y. M.; Liu, P. X.; Liang, X. J. Size-dependent radiosensitization of PEG-coated gold nanoparticles for cancer radiation therapy. *Biomaterials* **2012,** *33* (27), 6408-19.
10. Leung, M. K. K.; Chow, J. C. L.; Chithrani, B. D.; Lee, M. J. G.; Oms, B.; Jaffray, D. A. Irradiation of gold nanoparticles by x-rays: Monte Carlo simulation of dose enhancements and the spatial properties of the secondary electrons production. *Medical Physics* **2011,** *38* (2), 624-631.
11. Cho, S. H.; Jones, B. L.; Krishnan, S. The dosimetric feasibility of gold nanoparticle-aided radiation therapy (GNRT) via brachytherapy using low-energy gamma-/x-ray sources. *Physics in medicine and biology* **2009,** *54* (16), 4889-905.
12. Rahman, W. N.; Bishara, N.; Ackerly, T.; He, C. F.; Jackson, P.; Wong, C.; Davidson, R.; Geso, M. Enhancement of radiation effects by gold nanoparticles for superficial radiation therapy. *Nanomedicine: Nanotechnology, Biology and Medicine* **2009,** *5* (2), 136-142.
13. Jain, S.; Hirst, D. G.; O'Sullivan, J. M. Gold nanoparticles as novel agents for cancer therapy. *The British journal of radiology* **2012,** *85* (1010), 101-13.
14. Jelveh, S.; Chithrani, D. B. Gold nanostructures as a platform for combinational therapy in future cancer therapeutics. *Cancers* **2011,** *3* (1), 1081-1110.
15. Bonnett, R. Photosensitizers of the porphyrin and phthalocyanine series for photodynamic therapy. *Chemical Society reviews* **1995,** *24* (1), 19-33.
16. Grossweiner, L. I.; Patel, A. S.; Grossweiner, J. B. Type I and type II mechanisms in the photosensitized lysis of phosphatidylcholine liposomes by hematoporphyrin. *Photochem Photobiol* **1982,** *36* (2), 159-67.
17. Dougherty, T. J.; Gomer, C. J.; Henderson, B. W.; Jori, G.; Kessel, D.; Korbelik, M.; Moan, J.; Peng, Q. Photodynamic therapy. *Journal of the National Cancer Institute* **1998,** *90* (12), 889-905.

18. Kessel, D. Sites of photosensitization by derivatives of hematoporphyrin. *Photochem Photobiol* **1986,** *44* (4), 489-93.
19. Kessel, D.; Thompson, P.; Saatio, K.; Nantwi, K. D. Tumor localization and photosensitization by sulfonated derivatives of tetraphenylporphine. *Photochem Photobiol* **1987,** *45* (6), 787-90.
20. Vermathen, M.; Marzorati, M.; Vermathen, P.; Bigler, P. pH-dependent distribution of chlorin e6 derivatives across phospholipid bilayers probed by NMR spectroscopy. *Langmuir* **2010,** *26* (13), 11085-94.
21. Kessel, D. Proposed structure of the tumor-localizing fraction of HPD (hematoporphyrin derivative). *Photochem Photobiol* **1986,** *44* (2), 193-6.
22. Kessel, D. Porphyrin-lipoprotein association as a factor in porphyrin localization. *Cancer Letters* **1986,** *33* (2), 183-188.
23. Duncan, R.; Gaspar, R. Nanomedicine(s) under the microscope. *Mol Pharm* **2011,** *8* (6), 2101-41.
24. Letant, S. E.; Wang, T. F. Semiconductor quantum dot scintillation under gamma-ray irradiation. *Nano Lett* **2006,** *6* (12), 2877-80.
25. Withers, N. J.; Sankar, K.; Akins, B. A.; Memon, T. A.; Gu, T.; Gu, J.; Smolyakov, G. A.; Greenberg, M. R.; Boyle, T. J.; Osiński, M. Rapid degradation of CdSe⁄ZnS colloidal quantum dots exposed to gamma irradiation. *Applied Physics Letters* **2008,** *93* (17), -.
26. Morgan, N. Y.; Kramer-Marek, G.; Smith, P. D.; Camphausen, K.; Capala, J. Nanoscintillator conjugates as photodynamic therapy-based radiosensitizers: calculation of required physical parameters. *Radiat Res* **2009,** *171* (2), 236-44.
27. Niedre, M.; Patterson, M. S.; Wilson, B. C. Direct near-infrared luminescence detection of singlet oxygen generated by photodynamic therapy in cells in vitro and tissues in vivo. *Photochem Photobiol* **2002,** *75* (4), 382-91.
28. Niedre, M. J.; Secord, A. J.; Patterson, M. S.; Wilson, B. C. In vitro tests of the validity of singlet oxygen luminescence measurements as a dose metric in photodynamic therapy. *Cancer Research* **2003,** *63* (22), 7986-7994.
29. Berg, K.; Madslien, K.; Bommer, J. C.; Oftebro, R.; Winkelman, J. W.; Moan, J. Light induced relocalization of sulfonated meso-tetraphenylporphines in NHIK 3025 cells and effects of dose fractionation. *Photochem Photobiol* **1991,** *53* (2), 203-10.
30. Osinski, M.; Plumley, J.; Withers, N.; Akins, B.; Medina, G.; Rivera, A.; Smolyakov, G. In *Synthesis and characterization of lanthanide halide scintillating nanocrystals for gamma radiation detection*, Nanoscience and Nanotechnology (ICONN), 2010 International Conference on, 2010; IEEE, pp 189-192.
31. Sankar, K.; Plumley, J. B.; Akins, B. A.; Memon, T. A.; Withers, N. J.; Smolyakov, G. A.; Osinski, M. In *Synthesis and characterization of scintillating cerium-doped lanthanum fluoride nanocrystals*, SPIE BiOS: Biomedical Optics, 2009; International Society for Optics and Photonics, pp 718909-718909-12.
32. Withers, N. J.; Glazener, N. N.; Plumley, J. B.; Akins, B. A.; Rivera, A. C.; Cook, N. C.; Smolyakov, G. A.; Timmins, G. S.; Osiński, M. In *Locally increased mortality of gamma-irradiated cells in presence of lanthanide-halide nanoparticles*, 2011, pp 79090L-79090L-12.
33. Withers, N. J.; Plumley, J. B.; Triño, N. D.; Sankar, K.; Akins, B. A.; Rivera, A. C.; Smolyakov, G. A.; Timmins, G. S.; Osinski, M. In *Scintillating-nanoparticle-induced enhancement of absorbed radiation dose*, SPIE BiOS: Biomedical Optics, 2009; International Society for Optics and Photonics, pp 718917-718917-8.

34. Scaffidi, J. P.; Gregas, M. K.; Lauly, B.; Zhang, Y.; Vo-Dinh, T. Activity of psoralen-functionalized nanoscintillators against cancer cells upon X-ray excitation. *ACS Nano* **2011,** *5* (6), 4679-87.
35. Bouzigues, C.; Gacoin, T.; Alexandrou, A. Biological applications of rare-earth based nanoparticles. *ACS Nano* **2011,** *5* (11), 8488-505.
36. Wojtowicz, A. J.; Balcerzyk, M.; Berman, E.; Lempicki, A. Optical spectroscopy and scintillation mechanisms of $Ce_xLa_{1-x}F_3$. *Physical Review B* **1994,** *49* (21), 14880-14895.
37. Liu, Y.; Zhao, Y.; Luo, H.; Wu, Z.; Zhang, Z. Hydrothermal synthesis of CeF_3 nanocrystals and characterization. *J Nanopart Res* **2011,** *13* (5), 2041-2047.
38. Bünzli, J.-C. G.; Eliseeva, S. V. Basics of Lanthanide Photophysics. *Lanthanide Luminescence* **2010,** *7*, 1-45.
39. Dorenbos, P. The 5d level positions of the trivalent lanthanides in inorganic compounds. *Journal of Luminescence* **2000,** *91* (3–4), 155-176.
40. Dorenbos, P. 5d-level energies of Ce^{3+} and the crystalline environment. I. Fluoride compounds. *Physical Review B* **2000,** *62* (23), 15640-15649.
41. Blasse, G.; Bril, A. Energy transfer in Tb^{3+}-activated cerium(III) compounds. *The Journal of Chemical Physics* **1969,** *51* (8), 3252-3254.
42. Lempicki, A.; Wojtowicz, A. J.; Berman, E. Fundamental limits of scintillator performance. *Nuclear Instruments and Methods in Physics Research Section A: Accelerators, Spectrometers, Detectors and Associated Equipment* **1993,** *333* (2–3), 304-311.
43. Moses, W. W.; Derenzo, S. E. Cerium fluoride, a new fast, heavy scintillator. *Nuclear Science, IEEE Transactions on* **1989,** *36* (1), 173-176.
44. Moses, W. W.; Derenzo, S. E. The scintillation properties of cerium-doped lanthanum fluoride. *Nuclear Instruments and Methods in Physics Research Section A: Accelerators, Spectrometers, Detectors and Associated Equipment* **1990,** *299* (1–3), 51-56.
45. Moses, W. W.; Derenzo, S. E.; Weber, M. J.; Ray-Chaudhuri, A. K.; Cerrina, F. Scintillation mechanisms in cerium fluoride. *Journal of Luminescence* **1994,** *59* (1–2), 89-100.
46. Rodnyi, P.; Melchakov, E.; Zakharov, N.; Munro, I.; Hopkirk, A. Fast luminescence of cerium doped lanthanum fluoride. *Journal of Luminescence* **1995,** *65* (2), 85-89.
47. Wojtowicz, A. J.; Berman, E.; Koepke, C.; Lempicki, A. Stoichiometric cerium compounds as scintillators. I. CeF_3. *Nuclear Science, IEEE Transactions on* **1992,** *39* (4), 494-501.
48. Robbins, D. J. On Predicting the Maximum Efficiency of Phosphor Systems Excited by Ionizing-Radiation. *Journal of the Electrochemical Society* **1980,** *127* (12), 2694-2702.
49. Jacobsohn, L. G.; Sprinkle, K. B.; Roberts, S. A.; Kucera, C. J.; James, T. L.; Yukihara, E. G.; Devol, T. A.; Ballato, J. Fluoride nanoscintillators. *Journal of Nanomaterials* **2011,** *2011*.
50. McKigney, E. A.; Del Sesto, R. E.; Jacobsohn, L. G.; Santi, P. A.; Muenchausen, R. E.; Ott, K. C.; Mark McCleskey, T.; Bennett, B. L.; Smith, J. F.; Wayne Cooke, D. Nanocomposite scintillators for radiation detection and nuclear spectroscopy. *Nuclear Instruments and Methods in Physics Research Section A: Accelerators, Spectrometers, Detectors and Associated Equipment* **2007,** *579* (1), 15-18.
51. McKigney, E. A.; Muenchausen, R. E.; Cooke, D. W.; Del Sesto, R. E.; Gilbertson, R. D.; Bacrania, M. K.; Bennett, B. L.; Jacobsohn, L. G.; McCleskey, T. M.; Ott, K. C.; Sitarz, S. C.; Smith, J. F.; Stange, S. In *LaF_3:Ce nanocomposite scintillator for gamma-ray detection*, 2007, pp 67061A-67061A-11.

52. Guss, P.; Guise, R.; Yuan, D.; Mukhopadhyay, S.; O'Brien, R.; Lowe, D.; Kang, Z.; Menkara, H.; Nagarkar, V. V. Lanthanum halide nanoparticle scintillators for nuclear radiation detection. *Journal of Applied Physics* **2013,** *113* (6), 064303-064303-6.
53. Brooks, F. D. Development of organic scintillators. *Nuclear Instruments and Methods 162* (1–3), 477-505.
54. Zhou, J.; Wu, Z.; Zhang, Z.; Liu, W.; Dang, H. Study on an antiwear and extreme pressure additive of surface coated LaF_3 nanoparticles in liquid paraffin. *Wear* **2001,** *249* (5–6), 333-337.
55. Jacobsohn, L. G.; Sprinkle, K. B.; Kucera, C. J.; James, T. L.; Roberts, S. A.; Qian, H.; Yukihara, E. G.; DeVol, T. A.; Ballato, J. Synthesis, luminescence and scintillation of rare earth doped lanthanum fluoride nanoparticles. *Optical Materials* **2010,** *33* (2), 136-140.
56. Sudarsan, V.; van Veggel, F. C. J. M.; Herring, R. A.; Raudsepp, M. Surface Eu^{3+} ions are different than "bulk" Eu^{3+} ions in crystalline doped LaF_3 nanoparticles. *Journal of Materials Chemistry* **2005,** *15* (13), 1332-1342.
57. Diamente, P. R.; Burke, R. D.; van Veggel, F. C. Bioconjugation of Ln^{3+}-doped LaF_3 nanoparticles to avidin. *Langmuir* **2006,** *22* (4), 1782-8.
58. Wong, H.-T.; Tsang, M.-K.; Chan, C.-F.; Wong, K.-L.; Fei, B.; Hao, J. In vitro cell imaging using multifunctional small sized $KGdF_4$:Yb^{3+},Er^{3+} upconverting nanoparticles synthesized by a one-pot solvothermal process. *Nanoscale* **2013,** *5* (8), 3465-3473.
59. Wang, Z. L.; Hao, J.; Chan, H. L.; Law, G. L.; Wong, W. T.; Wong, K. L.; Murphy, M. B.; Su, T.; Zhang, Z. H.; Zeng, S. Q. Simultaneous synthesis and functionalization of water-soluble up-conversion nanoparticles for in-vitro cell and nude mouse imaging. *Nanoscale* **2011,** *3* (5), 2175-81.
60. Kömpe, K.; Lehmann, O.; Haase, M. Spectroscopic distinction of surface and volume ions in cerium (III)-and terbium (III)-containing core and core/shell nanoparticles. *Chemistry of materials* **2006,** *18* (18), 4442-4446.
61. Wang, F.; Wang, J.; Liu, X. Direct evidence of a surface quenching effect on size-dependent luminescence of upconversion nanoparticles. *Angewandte Chemie* **2010,** *49* (41), 7456-60.
62. Boyer, J. C.; Gagnon, J.; Cuccia, L. A.; Capobianco, J. A. Synthesis, characterization, and spectroscopy of $NaGdF_4$: Ce^{3+}, Tb^{3+}/$NaYF_4$ core/shell nanoparticles. *Chemistry of Materials* **2007,** *19* (14), 3358-3360.
63. Li, C.; Liu, X.; Yang, P.; Zhang, C.; Lian, H.; Lin, J. LaF_3, CeF_3, CeF_3: Tb^{3+}, and CeF_3: Tb^{3+}@ LaF_3 (core-shell) nanoplates: Hydrothermal synthesis and luminescence properties. *The Journal of Physical Chemistry C* **2008,** *112* (8), 2904-2910.
64. Cui, X.; She, J.; Gao, C.; Cui, K.; Hou, C.; Wei, W.; Peng, B. Luminescent properties of Nd^{3+}-doped LaF_3 core/shell nanoparticles with enhanced near infrared (NIR) emission. *Chemical Physics Letters* **2010,** *494* (1), 60-63.
65. Stouwdam, J. W.; van Veggel, F. C. Improvement in the luminescence properties and processability of LaF_3/Ln and $LaPO_4$/Ln nanoparticles by surface modification. *Langmuir* **2004,** *20* (26), 11763-71.
66. Dong, C.; van Veggel, F. C. Cation exchange in lanthanide fluoride nanoparticles. *ACS Nano* **2009,** *3* (1), 123-30.
67. Cross, A. M.; May, P. S.; van Veggel, F. C. J. M.; Berry, M. T. Dipicolinate Sensitization of Europium Luminescence in Dispersible 5% Eu:LaF_3 Nanoparticles. *Journal of Physical Chemistry C* **2010,** *114* (35), 14740-14747.

68. Boyer, J. C.; Manseau, M. P.; Murray, J. I.; van Veggel, F. C. Surface modification of upconverting $NaYF_4$ nanoparticles with PEG-phosphate ligands for NIR (800 nm) biolabeling within the biological window. *Langmuir* **2010,** *26* (2), 1157-64.
69. Lu, C.; Bhatt, L. R.; Jun, H. Y.; Park, S. H.; Chai, K. Y. Carboxyl-polyethylene glycol-phosphoric acid: a ligand for highly stabilized iron oxide nanoparticles. *Journal of Materials Chemistry* **2012,** *22* (37), 19806-19811.
70. Traina, C. A.; Schwartz, J. Surface modification of Y_2O_3 nanoparticles. *Langmuir* **2007,** *23* (18), 9158-61.
71. Qi, L.; Fresnais, J.; Muller, P.; Theodoly, O.; Berret, J. F.; Chapel, J. P. Interfacial activity of phosphonated-PEG functionalized cerium oxide nanoparticles. *Langmuir* **2012,** *28* (31), 11448-56.
72. Cao, P.; Tong, L.; Hou, Y.; Zhao, G.; Guerin, G.; Winnik, M. A.; Nitz, M. Improving lanthanide nanocrystal colloidal stability in competitive aqueous buffer solutions using multivalent PEG-phosphonate ligands. *Langmuir* **2012,** *28* (35), 12861-70.
73. Hou, Y.; Qiao, R.; Fang, F.; Wang, X.; Dong, C.; Liu, K.; Liu, C.; Liu, Z.; Lei, H.; Wang, F.; Gao, M. $NaGdF_4$ nanoparticle-based molecular probes for magnetic resonance imaging of intraperitoneal tumor xenografts in vivo. *ACS Nano* **2013,** *7* (1), 330-8.
74. Jiang, G.; Pichaandi, J.; Johnson, N. J.; Burke, R. D.; van Veggel, F. C. An effective polymer cross-linking strategy to obtain stable dispersions of upconverting $NaYF_4$ nanoparticles in buffers and biological growth media for biolabeling applications. *Langmuir* **2012,** *28* (6), 3239-47.
75. Budijono, S. J.; Shan, J.; Yao, N.; Miura, Y.; Hoye, T.; Austin, R. H.; Ju, Y.; Prud'homme, R. K. Synthesis of stable block-copolymer-protected $NaYF_4$:Yb^{3+}, Er^{3+} up-converting phosphor nanoparticles. *Chemistry of Materials* **2010,** *22* (2), 311-318.
76. Budijono, S. J.; Russ, B.; Saad, W.; Adamson, D. H.; Prud'homme, R. K. Block copolymer surface coverage on nanoparticles. *Colloids and Surfaces A: Physicochemical and Engineering Aspects* **2010,** *360* (1–3), 105-110.
77. Ma, J.; Huang, P.; He, M.; Pan, L.; Zhou, Z.; Feng, L.; Gao, G.; Cui, D. Folic acid-conjugated LaF_3:Yb,Tm@SiO_2 nanoprobes for targeting dual-modality imaging of upconversion luminescence and X-ray computed tomography. *J Phys Chem B* **2012,** *116* (48), 14062-70.
78. Zhang, Y.; Clapp, A. Overview of Stabilizing Ligands for Biocompatible Quantum Dot Nanocrystals. *Sensors* **2011,** *11* (12), 11036-11055.
79. Schäfer, H.; Ptacek, P.; Kömpe, K.; Haase, M. Lanthanide-doped $NaYF_4$ nanocrystals in aqueous solution displaying strong upconversion emission. *Chemistry of Materials* **2007,** *19* (6), 1396-1400.
80. Benyettou, F.; Lalatonne, Y.; Chebbi, I.; Di Benedetto, M.; Serfaty, J. M.; Lecouvey, M.; Motte, L. A multimodal magnetic resonance imaging nanoplatform for cancer theranostics. *Physical chemistry chemical physics : PCCP* **2011,** *13* (21), 10020-7.
81. Moisenovich, M. M.; Ol'shevskaya, V. A.; Rokitskaya, T. I.; Ramonova, A. A.; Nikitina, R. G.; Savchenko, A. N.; Tatarskiy, V. V., Jr.; Kaplan, M. A.; Kalinin, V. N.; Kotova, E. A.; Uvarov, O. V.; Agapov, II; Antonenko, Y. N.; Shtil, A. A. Novel photosensitizers trigger rapid death of malignant human cells and rodent tumor transplants via lipid photodamage and membrane permeabilization. *PLoS One* **2010,** *5* (9), e12717.
82. Jinadasa, R. G.; Hu, X.; Vicente, M. G.; Smith, K. M. Syntheses and cellular investigations of 17(3)-, 15(2)-, and 13(1)-amino acid derivatives of chlorin e(6). *Journal of medicinal chemistry* **2011,** *54* (21), 7464-76.

83. Sheleg, S. V.; Zhavrid, E. A.; Khodina, T. V.; Kochubeev, G. A.; Istomin, Y. P.; Chalov, V. N.; Zhuravkin, I. N. Photodynamic therapy with chlorin e(6) for skin metastases of melanoma. *Photodermatology, photoimmunology & photomedicine* **2004,** *20* (1), 21-6.
84. Charron, G.; Stuchinskaya, T.; Edwards, D. R.; Russell, D. A.; Nann, T. Insights into the Mechanism of Quantum Dot-Sensitized Singlet Oxygen Production for Photodynamic Therapy. *Journal of Physical Chemistry C* **2012,** *116* (16), 9334-9342.
85. Tsay, J. M.; Trzoss, M.; Shi, L.; Kong, X.; Selke, M.; Jung, M. E.; Weiss, S. Singlet oxygen production by peptide-coated quantum dot-photosensitizer conjugates. *Journal of the American Chemical Society* **2007,** *129* (21), 6865-71.
86. Huang, X.; Tian, X. J.; Yang, W. L.; Ehrenberg, B.; Chen, J. Y. The conjugates of gold nanorods and chlorin e6 for enhancing the fluorescence detection and photodynamic therapy of cancers. *Physical chemistry chemical physics : PCCP* **2013,** *15* (38), 15727-33.
87. Wang, C.; Tao, H.; Cheng, L.; Liu, Z. Near-infrared light induced in vivo photodynamic therapy of cancer based on upconversion nanoparticles. *Biomaterials* **2011,** *32* (26), 6145-6154.
88. Huang, P.; Lin, J.; Wang, X.; Wang, Z.; Zhang, C.; He, M.; Wang, K.; Chen, F.; Li, Z.; Shen, G.; Cui, D.; Chen, X. Light-triggered theranostics based on photosensitizer-conjugated carbon dots for simultaneous enhanced-fluorescence imaging and photodynamic therapy. *Advanced materials (Deerfield Beach, Fla.)* **2012,** *24* (37), 5104-10.
89. Xiao, H.; Zhu, B.; Wang, D.; Pang, Y.; He, L.; Ma, X.; Wang, R.; Jin, C.; Chen, Y.; Zhu, X. Photodynamic effects of chlorin e6 attached to single wall carbon nanotubes through noncovalent interactions. *Carbon* **2012,** *50* (4), 1681-1689.
90. Cho, Y.; Choi, Y. Graphene oxide-photosensitizer conjugate as a redox-responsive theranostic agent. *Chemical Communications* **2012,** *48* (79), 9912-9914.
91. Miao, W.; Shim, G.; Lee, S.; Lee, S.; Choe, Y. S.; Oh, Y. K. Safety and tumor tissue accumulation of pegylated graphene oxide nanosheets for co-delivery of anticancer drug and photosensitizer. *Biomaterials* **2013,** *34* (13), 3402-10.
92. Yoon, H. Y.; Koo, H.; Choi, K. Y.; Lee, S. J.; Kim, K.; Kwon, I. C.; Leary, J. F.; Park, K.; Yuk, S. H.; Park, J. H.; Choi, K. Tumor-targeting hyaluronic acid nanoparticles for photodynamic imaging and therapy. *Biomaterials* **2012,** *33* (15), 3980-9.
93. Jeong, H.; Huh, M.; Lee, S. J.; Koo, H.; Kwon, I. C.; Jeong, S. Y.; Kim, K. Photosensitizer-conjugated human serum albumin nanoparticles for effective photodynamic therapy. *Theranostics* **2011,** *1*, 230-9.
94. Lim, C. K.; Shin, J.; Kwon, I. C.; Jeong, S. Y.; Kim, S. Iodinated photosensitizing chitosan: self-assembly into tumor-homing nanoparticles with enhanced singlet oxygen generation. *Bioconjug Chem* **2012,** *23* (5), 1022-8.
95. Isakau, H. A.; Parkhats, M. V.; Knyukshto, V. N.; Dzhagarov, B. M.; Petrov, E. P.; Petrov, P. T. Toward understanding the high PDT efficacy of chlorin e6-polyvinylpyrrolidone formulations: photophysical and molecular aspects of photosensitizer-polymer interaction in vitro. *Journal of photochemistry and photobiology. B, Biology* **2008,** *92* (3), 165-74.
96. Wang, C.; Cheng, L.; Liu, Z. Drug delivery with upconversion nanoparticles for multi-functional targeted cancer cell imaging and therapy. *Biomaterials* **2011,** *32* (4), 1110-1120.
97. Kong, D.; Yang, P.; Wang, Z.; Chai, P.; Huang, S.; Lian, H.; Lin, J. Mesoporous silica coated CeF_3:Tb^{3+} particles for drug release. *Journal of Nanomaterials* **2008,** *2008*, 1-7.
98. Kong, D. Y.; Wang, Z. L.; Lin, C. K.; Quan, Z. W.; Li, Y. Y.; Li, C. X.; Lin, J. Biofunctionalization of CeF_3:Tb^{3+} nanoparticles. *Nanotechnology* **2007,** *18* (7), 075601.

99. Liu, Y.; Zhou, S.; Tu, D.; Chen, Z.; Huang, M.; Zhu, H.; Ma, E.; Chen, X. Amine-functionalized lanthanide-doped zirconia nanoparticles: optical spectroscopy, time-resolved fluorescence resonance energy transfer biodetection, and targeted imaging. *Journal of the American Chemical Society* **2012,** *134* (36), 15083-90.
100. Naccache, R.; Rodríguez, E. M.; Bogdan, N.; Sanz-Rodríguez, F.; Cruz, M. d. C. I. d. l.; Fuente, Á. J. d. l.; Vetrone, F.; Jaque, D.; Solé, J. G.; Capobianco, J. A. High Resolution Fluorescence Imaging of Cancers Using Lanthanide Ion-Doped Upconverting Nanocrystals. *Cancers* **2012,** *4* (4), 1067-1105.
101. Selvin, P. R. Lanthanide-based resonance energy transfer. *Selected Topics in Quantum Electronics, IEEE Journal of* **1996,** *2* (4), 1077-1087.
102. Selvin, P. R. Principles and biophysical applications of lanthanide-based probes. *Annu Rev Biophys Biomol Struct* **2002,** *31* (1), 275-302.
103. Wuister, S. F.; de Mello Donega, C.; Meijerink, A. Efficient energy transfer between nanocrystalline YAG:Ce and TRITC. *Physical Chemistry Chemical Physics* **2004,** *6* (8), 1633-1636.
104. Di, W.; Li, J.; Shirahata, N.; Sakka, Y. An efficient and biocompatible fluorescence resonance energy transfer system based on lanthanide-doped nanoparticles. *Nanotechnology* **2010,** *21* (45), 455703.
105. Kar, A.; Kundu, A.; Bhattacharyya, S.; Mandal, S.; Patra, A. Lanthanide based resonance energy transfer (LRET) between Ce-doped $LaPO_4$ nanorods and coumarin 440 dye. *RSC Advances* **2013,** *3* (32), 13372-13380.
106. Wang, Y.; Liu, K.; Liu, X. M.; Dohnalova, K.; Gregorkiewicz, T.; Kong, X. G.; Aalders, M. C. G.; Buma, W. J.; Zhang, H. Critical Shell Thickness of Core/Shell Upconversion Luminescence Nanoplatform for FRET Application. *J Phys Chem Lett* **2011,** *2* (17), 2083-2088.

Chapter 5

Photoluminescence of cerium fluoride and cerium-doped lanthanum fluoride nanoparticles and investigation of energy transfer to photosensitizer molecules

Abstract

$Ce_xLa_{1-x}F_3$ nanoparticles have been proposed for use in nanoscintillator-photosensitizer systems, where excitation of nanoparticles by ionizing radiation would result in energy transfer to photosensitizer molecules, effectively combining the effects of radiotherapy and photodynamic therapy. Thus far, there have been few experimental investigations of such systems. This study reports novel synthesis methods for water-dispersible $Ce_{0.1}La_{0.9}F_3/LaF_3$ and CeF_3/LaF_3 core/shell nanoparticles and an investigation of energy transfer to photosensitizers. Unbound deuteroporphyrin IX 2,4-disulfonic acid was found to substantially quench the luminescence of large (>10 nm diameter) aminocaproic acid-stabilized nanoparticles at reasonable concentrations and loading amounts: up to 80% quenching at 6% w/w photosensitizer loading. Energy transfer was found to occur primarily through a cascade, with excitation of "regular" site Ce^{3+} at 252 nm relayed to photosensitizer molecules at the nanoparticle surface through intermediate "perturbed" Ce^{3+} sites. Smaller (<5 nm) citrate-stabilized nanoparticles were coated with the bisphosphonate alendronate, allowing covalent conjugation to chlorin e6 and resulting in static quenching of the nanoparticle luminescence: ~50% at ~0.44% w/w. These results provide insight into energy transfer mechanisms that may prove valuable for optimizing similar systems.

Adapted from:

Cooper, D. R., Kudinov, K., Tyagi, P., Hill, C. K., Bradforth, S. E., & Nadeau, J. L. (2014). Photoluminescence of cerium fluoride and cerium-doped lanthanum fluoride nanoparticles and investigation of energy transfer to photosensitizer molecules. *Physical Chemistry Chemical Physics*, *16*(24), 12441-12453.

5. Photoluminescence of cerium fluoride and cerium-doped lanthanum fluoride nanoparticles and investigation of energy transfer to photosensitizer molecules

5.1 Introduction

Inorganic nanoparticles (NPs) doped with lanthanides have emerged as a versatile collection of materials for a range of potential optical and medical applications. Robust luminescence, low toxicity, and chemical stability make them an appealing choice for bioprobes and theranostics. The use of NPs as a means of drug delivery is an extremely active field of research, and in addition to a range of chemotherapeutic agents, photosensitizer (PS) molecules have become a popular choice for coupling to luminescent NPs[1, 2, 3, 4, 5, 6, 7, 8]. Photodynamic therapy (PDT) takes advantage of selective activation of PS molecules, which have minimal innate toxicity but which can produce reactive oxygen species (ROS) upon absorption of light. Considerable efforts have gone toward the development of UCNPs that circumvent issues of tissue transparency by producing tunable visible/infrared emission upon near-infrared excitation, allowing for deeper imaging[9, 10, 11] and/or indirect PS activation[12, 13, 14, 15, 16] in the "water window." A relatively unexplored approach to deep-tissue activation is to use radioluminescent or scintillating NPs that emit tunable UV/visible light upon excitation by highly penetrating ionizing radiation. As radiotherapy is used widely in clinical settings, a nanoscintillator-photosensitizer system may provide a means to radiosensitize malignant tissues through high-Z enhancement[17, 18, 19] combined with therapeutic effects of photosensitizers[20, 21, 22, 23, 24, 25, 26].

$Ce_xLa_{1-x}F_3$ is a heavy scintillator that has been investigated as bulk single crystals[27, 28, 29, 30, 31, 32] and more recently at the nanoscale[33, 34]. LaF_3 is a good host for the luminescence of Ce^{3+} dopants due to its optical transparency, large band gap, and low phonon energy. Due to the chemical similarly between trivalent lanthanum and cerium, one can be fully substituted for the

other without significantly affecting the physical properties of the crystal. Ce^{3+} is distinct from other luminescent lanthanides because of parity-allowed 5*d*–4*f* transitions that are notably sensitive to the environment due to a lack of shielding by outer electrons. The luminescence of $Ce_xLa_{1-x}F_3$ spans the UVA & UVB into the UVC & blue, with the shape of the emission profile and luminescence yield depending on the dopant concentration and crystal quality. While the emission wavelengths are appropriate for exciting photosensitizers, most of which have strong absorbance bands in the UVA/blue, the mechanisms of nanoscintillator luminescence and energy transfer (ET) have yet to be thoroughly assessed. In particular, surface effects are of critical importance at the nanoscale, so particles of different sizes might display very different behavior[35, 36].

Two compositions of NPs were chosen for this study: $Ce_{0.1}La_{0.9}F_3$ and CeF_3. Despite the substantial difference in cerium content, the scintillation yields of bulk single crystals were found to be comparable: beyond 10% Ce^{3+} doping, increased radiation trapping resulted in only a modest increase in radioluminescence. Nanoparticles of both compositions were synthesized using hydrothermal techniques and modified by the addition of undoped LaF_3 shells to improve luminescence yields through surface site passivation, though it has been established that cation exchange during aqueous synthesis may lead to more complex gradient structures rather than well-defined core/shell structures[37, 38]. Water-dispersible, platelet-like NPs were synthesized with aminocaproic acid ligands and mixed with the photosensitizer deuteroporphyrin IX 2,4-disulfonic acid (DPIX-DS) to investigate mechanisms of energy transfer in electrostatic complexes.

A separate synthesis technique using citric acid ligands was employed to produce smaller, more spherical NPs, which were functionalized for bioconjugation through ligand exchange with alendronic acid, a bisphosphonate drug. Alendronate provides a strong association to the NP surface through bisphosphonate groups, as well as free amine functional groups for

bioconjugation. The photosensitizer chlorin e6 (Ce6) was conjugated to the alendronate-coated NPs through amide bond formation to investigate energy transfer with covalently bound PS molecules.

As a prelude to experiments using excitation by ionizing radiation, here we have investigated the NPs and photosensitizer complexes and conjugates through steady-state and time-resolved photoluminescence (PL) spectroscopy, in order to provide insight that may be valuable toward maximizing energy transfer between luminescent Ce^{3+}-doped NPs and photosensitizers. We have determined that energy transfer to photosensitizers occurs efficiently through excitation of the NPs, with distinct populations of Ce^{3+} acting as energy relays.

5.2 Experimental section

5.2.1 Materials

Lanthanum(III) chloride heptahydrate (99.999%), cerium(III) chloride heptahydrate (99.999%), lanthanum(III) nitrate hexahydrate (99.999%), cerium(III) nitrate hexahydrate (99%, 1-2% La), 6-aminocaproic acid (≥99%) and citric acid (ACS, ≥99.5%) were purchased from Sigma-Aldrich and used without modification. Ammonium hydroxide (ACS) was purchased from ACP Chemicals Inc. Photosensitizers deuteroporphyrin IX 2,4-disulfonic acid dihydrochloride and chlorin e6 were purchased from Frontier Scientific. N-hydroxysuccinimide (>98%) and alendronate sodium trihydrate (97%) were purchased from Alfa Aesar.

5.2.2 Synthesis of aminocaproic acid-stabilized $Ce_xLa_{1-x}F_3/LaF_3$ (x = 0.1 or 1) "core/shell" nanoparticles

Water-dispersible aminocaproic acid-stabilized NPs (ACA-NPs) were synthesized using a one-pot hydrothermal technique. NP cores were prepared by first dissolving 30 mmol (3.94 g) of aminocaproic acid (ACA) and 0.5 mmol of lanthanide chloride hydrates in 35 mL of water in a

250 mL three-neck flask: $Ce_{0.1}La_{0.9}F_3$ core precursor solution consisted of 0.45 mmol (167 mg) $LaCl_3 \cdot 7H_2O$ and 0.05 mmol (18.6 mg) $CeCl_3 \cdot 7H_2O$; CeF_3 core precursor solution consisted of 0.5 mmol (186.3 mg) $CeCl_3 \cdot 7H_2O$. Fluoride precursor solution was prepared by dissolving 1.5 mmol (63 mg) NaF in 2 mL water and purging with N_2 gas for several minutes. The lanthanide precursor solution was stirred and purged with N_2 gas for an hour at room temperature and then heated to 75 °C, at which point the fluoride precursor solution was rapidly injected. The solution was stirred at 75 °C for 2 hours before addition of the shell.

For the addition of undoped LaF_3 shells, lanthanum and fluoride precursor solutions were prepared and alternately added dropwise in 10 fractions each over ~20 minutes. Lanthanum precursor solutions contained 0.5 mmol (186 mg) $LaCl_3 \cdot 7H_2O$ in 2 mL water, and fluoride precursor solutions contained 1.5 mmol (63 mg) NaF in 2 mL water. After addition, the core/shell NP solution was stirred at 75 °C for 2 hours, then allowed to cool to room temperature.

To remove excess reagents, the NPs were precipitated by the addition of ~360 mL of ethanol followed by centrifugation at 8,000 × g for 8 minutes. The NPs were collected as a translucent pellet, resuspended in ~10 mL of water, then filtered through a two-stage Millex 0.45/1.0 μm PVDF/APFB syringe filter. Stock solutions containing ~20-30 mg/mL of NPs appeared transparent.

5.2.3 Non-covalent association of deuteroporphyrin IX 2,4-disulfonic acid with ACA-NPs

Deuteroporphyrin IX 2,4-disulfonic acid dihydrochloride (DPIX-DS) was dissolved at 1 mg/mL in water and diluted into aqueous NP solutions at 1-12% w/w of the NPs to be investigated. No pH correction was done. NP-PS samples were diluted ten-fold for steady-state PL and TCSPC measurements to avoid inner-filter effects.

5.2.4 Synthesis of citrate-stabilized $Ce_{0.1}La_{0.9}F_3/LaF_3$ "core/shell" nanoparticles

Water-dispersible citrate-stabilized NPs (CA-NPs) were synthesized using a slightly modified hydrothermal method developed elsewhere[39, 40]. First, 10.4 mmol (2 g) of citric acid was dissolved in 35 mL water and partially neutralized with 28% NH_4OH to pH 5-6, then the solution was heated to 75 °C with stirring. Lanthanide precursor solutions were prepared by dissolving 1.33 mmol lanthanide nitrate hydrates in 2 mL methanol: $Ce_{0.1}La_{0.9}F_3$ core precursor solution consisted of 1.197 mmol (518.3 mg) $La(NO_3)_3{\cdot}6H_2O$ and 0.133 mmol (57.8 mg) $Ce(NO_3)_3{\cdot}6H_2O$. Fluoride precursor solution was prepared by dissolving 8.38 mmol (352 mg) NaF in 10 mL water. The lanthanide solution was then added to the heated citric acid solution dropwise, followed by the addition of the fluoride solution dropwise. The solution was stirred at 75 °C for 2 hours before addition of the shell.

For the addition of undoped LaF_3 shells, a solution of 1.33 mmol (576 mg) $La(NO_3)_3{\cdot}6H_2O$ was prepared and added dropwise. The NP solution was stirred at 75 °C for an additional 2 hours, then allowed to cool to room temperature.

To remove excess reagents, the NPs were precipitated by the addition of ~50 mL of ethanol followed by centrifugation at 4,000 RPM for 3 minutes. The white NP pellets were washed with 95% ethanol followed by centrifugation at 4,000 RPM for 3 minutes. The previous step was repeated, then the NP pellet was resuspended in ~25 mL of water and filtered through a two-stage Millex 0.45/1.0 μm PVDF/APFB syringe filter. Stock solutions containing ~20-30 mg/mL of NPs appeared transparent.

5.2.5 Ligand exchange of CA-NPs with alendronate and conjugation to chlorin e6

Citrate-stabilized NPs were coated with alendronate by ligand exchange in water. 100 mg of alendronate sodium trihydrate was dissolved in 30 mL water and 100 mg NPs (~4 mL) were added

under stirring. The solution was heated at 60 °C and stirred for 2 hours, becoming turbid after several minutes. NPs were pelleted by centrifugation at 12,000 × g for 15 minutes and the supernatant discarded. The pale blue glassy NP pellet was first redissolved in ~4 mL 0.1 M HCl then precipitated by the addition of ~40 mL ethanol and centrifugation at 12,000 × g for 15 minutes. The previous step was repeated, and the pellet of alendronate-stabilized NPs (ALE-NPs) was then dissolved in ~4 mL water.

Chlorin e6 (Ce6) conjugates were prepared by first dissolving 2 mg Ce6 in 4 mL DMSO, followed by the addition of 1 mL of 50 mM (~5.8 mg) N-hydroxysuccinimide (NHS) in DMSO and 6.2 μL of *N,N′*-diisopropylcarbodiimide (DIC), then were stirred for 30 minutes. 1 mL (~20 mg) of ALE-NPs was added quickly under heavy stirring. The reaction vial was protected from light and stirred for 18-20 hours. Conjugates were isolated from excess reagents and DMSO by addition of ~40 mL ethanol and NaCl to 10 mM (typically 90 μL of 5 M NaCl in water), followed by centrifugation at 12,000 × g for 15 minutes. The glassy green pellet was redissolved in ~2 mL of 0.1 M HCl and precipitated by the addition of ~30 mL ethanol and centrifugation at 12,000 × g for 15 minutes. The previous step was repeated, then the NP-PS pellet was dissolved in ~1 mL water.

5.2.6 Characterization of NPs

NP size, morphology and crystallinity were evaluated from high resolution transmission electron microscopy (HR-TEM) and selected area electron diffraction (SAED) images acquired with a Philips CM200 TEM operating at 200 kV. Samples were prepared by drop casting 5 μL of a diluted NP solution onto a grid and air-drying overnight.

The mass concentrations of the NPs were determined by drying several mL of the as-synthesized NP stock solutions under vacuum with a rotary evaporator. Mass extinction coefficients were then determined by measuring the absorbance of successive dilutions of the NPs in water and fitting the A_{250} values to a line. The values include the ligand mass contributions.

5.2.7 Time-resolved and steady-state photoluminescence

Photoluminescence decays were obtained by the TCSPC technique. 800 nm laser pulses (~70 fs) out of a Coherent RegA 9050 Ti/sapphire regenerative amplifier operating at 250 kHz repetition rate were coupled into an optical parametric amplifier (OPA) (Coherent 9450) which produced 504 nm light with an average power of ~30 mW. The OPA output was directed through a fused silica prism pair for pulse compression prior to a type I BBO doubling crystal. The resulting 252 nm output passed through a calcium-fluoride prism pair compressor primarily to spectrally clean the 252 nm pulses. The 252 nm beam was gently focused into the sample with a large focal spot diameter of 0.785 mm. The excitation power was ~2.4 mW, with peak pulse intensities at the sample of 1×10^7 W/cm^2 with 5-50 $\times 10^{-6}$ J/cm^2 fluence after attenuation of the 252 nm excitation beam with neutral density filters placed before the focusing lens. The luminescence was collected with a 3.5 cm focal length lens placed perpendicular to the excitation beam and the collimated luminescence focused into a monochromator with a 10 cm focal length lens. The monochromator was a CVI CMSP112 double spectrograph with a 1/8 m total path length in negative dispersive mode with a pair of 600 groove/mm gratings (overall f number 3.9). The slit widths were 1.2 mm and based on a monochromator dispersion of 14 nm/mm, provided 10 nm resolution. A Hamamatsu RU3809 microchannel-plate photomultiplier was mounted on the monochromator exit slit. A Becker and Hickl SPC-630 photon counting board was used to record the time-resolved emission. The reference signal was provided by a portion of the excitation beam sent to a fast

photodiode. To ensure good statistics, count rates were held at <1% of the laser repetition rate to avoid pulse pile up. Typical acquisition times were 10 minutes for a single scan. Lifetime decays of NPs were measured at 285 nm, 300 nm, 330 nm and 380 nm.

The instrument response function (IRF) was determined from scatter off a solution of dilute coffee creamer. The full width at half-maximum of the IRF was 37 ps. IRF reconvolution, multiexponential decay fits and intensity-weighted average lifetime calculations were performed using FluoFit 4.0 (PicoQuant, Berlin). Goodness-of-fit data and residuals were used to gauge fit results; a χ^2 between 0.9-1.1 and random distribution of residuals around the x-axis were necessary for a fit to be considered accurate. Lifetime decay contributions were weighted by fractional intensity. Negative amplitude decays (representing the rise times) were included in the calculation of average lifetime values, but not for fractional decay intensities. Multi-exponential decay fits were of the form

$$I(t) = \int_{-\infty}^{t} IRF(t') \sum_{i=1}^{n} A_i e^{-\frac{t-t'}{\tau_i}} dt' \qquad (5.1)$$

where IRF(*t'*) is the instrument response function. UV−visible absorbance spectra were taken with a Varian Cary 50 spectrometer or Molecular Devices SpectraMax Plus 384. Steady-state emission spectra were recorded with either a Horiba FluoroLog-3 spectrofluorometer (5 nm excitation and emission slit widths and corrected for variations in lamp intensity, Figures 5.2 & 5.3), a Varian Cary Eclipse spectrophotometer (5 nm excitation and emission slit widths, Figures 5.7 & 5.10), or Molecular Devices SpectraMax i3 (QY measurements). Emission spectra in Figures 5.3c & d are shown in arbitrary units proportional to the original data in counts per second. All spectra were recorded in quartz cuvettes and were averaged from ten consecutive scans, with the exception of absorbance spectra in Figures 5.8 & 5.10, which were recorded in UV-transparent plastic

"UVettes." Fitting of steady-state PL spectra using Gaussian functions was done using the Matlab Curve Fitting Toolbox with no constraints on the parameters.

Relative NP PL quantum yields (Φ_{NP}) were determined using standard methods by comparison to L-tryptophan in water ($\Phi_s = 0.12$)[41] using the equation

$$\phi_{NP} = \phi_s \left(\frac{F_{NP}}{A_{NP}}\right)\left(\frac{A_s}{F_s}\right)\left(\frac{n_{NP}}{n_s}\right)^2 \quad (5.2)$$

where *F* is the integrated intensity (using 250 nm excitation), *A* is the absorbance at 250 nm, and *n* is index of refraction of the solvent. For each sample, the emission intensity was measured for six dilutions and fit to a line of A_{250} vs. integrated emission, giving the *F/A* values which were used to calculate the QY (Figure C1). The fits were not forced through the origin as the background fluorescence of the multi-well plates could not be entirely accounted for. All measurements were taken at room temperature.

5.3 Results

5.3.1 Characterization and photoluminescence of ACA-stabilized NPs and DPIX-DS complexes

TEM images of ACA-NPs revealed roughly hexagonal platelet morphology, as shown in Figure 5.1. For measurements and calculations, they were approximated as thin cylinders. $Ce_{0.1}La_{0.9}F_3/LaF_3$ NPs had an average diameter of 11.9 ± 3.5 nm (n = 208) and an average thickness of 3.2 ± 0.5 nm (n = 33). CeF_3/LaF_3 NPs were noticeably larger, with an average diameter of 16.4 ± 3.9 nm (n = 218) and an average thickness of 4.3 ± 0.7 nm (n = 40) – giving ~1.9 times the surface area and ~2.6 times the volume and molar mass compared to the $Ce_{0.1}La_{0.9}F_3/LaF_3$ NPs (details shown in Table C1).

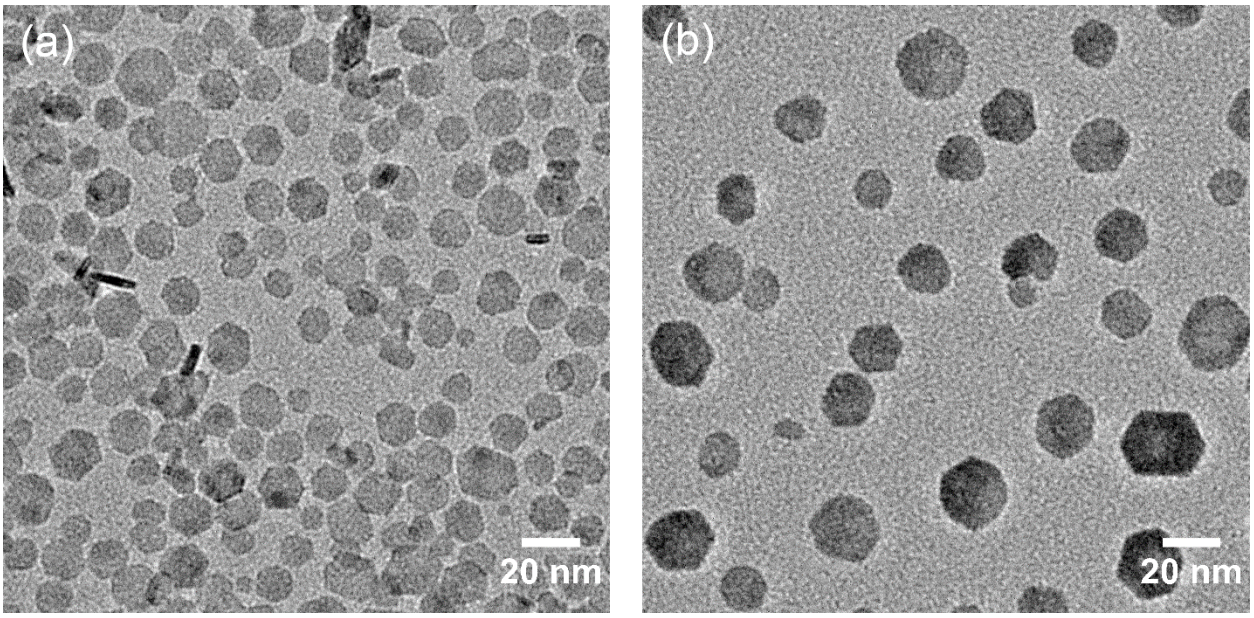

Figure 5.1 TEM images of ACA-stabilized $Ce_{0.1}La_{0.9}F_3/LaF_3$ (a) and CeF_3/LaF_3 (b) NPs.

Consistent with prior work in bulk and nanocrystals, primarily that of Wojtowicz *et al*. and Jacobsohn *et al*., the steady-state PL spectra of both NP compositions could be fit well by a sum of Gaussian functions (Figure 5.2a & b, Table 5.1). The three major components arise from the transitions from the lowest excited Ce^{3+} *5d* level to the spin-orbit split *4f* ground states $^2F_{5/2}$ (G_1) and $^2F_{7/2}$ (G_2), as well as a broad, lower energy band arising from Ce^{3+} residing in perturbed sites (G_3). Importantly, the reduced 5*d*–4*f* energy gap of Ce^{3+} in perturbed sites enables radiation trapping from regular sites by nonradiative transfer or re-absorption of emission. These "bulk-type" perturbations are believed to arise from crystallographic defects involving fluorine vacancies, likely Frenkel disorder. As each cation has 11 nearest F^- neighbors at distances from 2.421 Å to 2.999 Å, the degree of perturbation varies and results in an inhomogeneous broadening of energy levels. Ce^{3+} sites at or near the surface of the NPs that are incompletely passivated by the shell are further affected by asymmetry and local distortions in the crystal lattice[34], leading

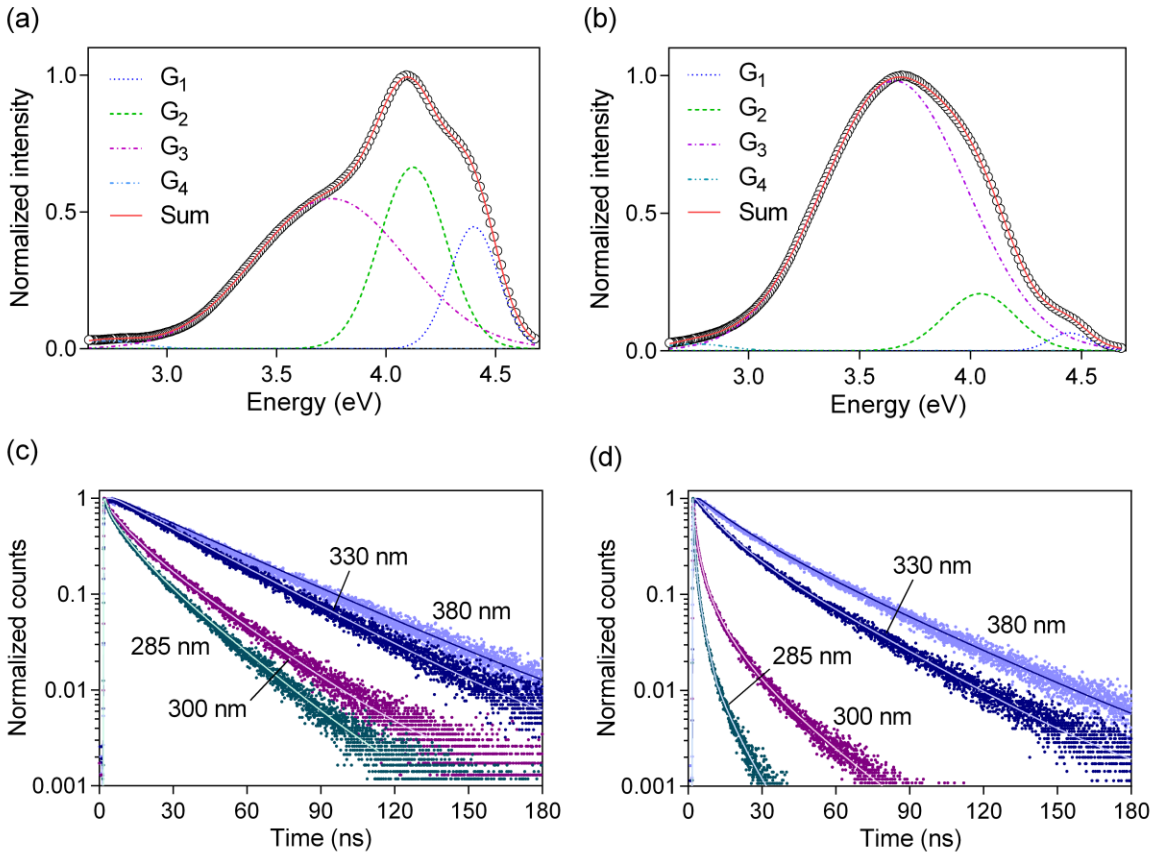

Figure 5.2 Photoluminescence of $Ce_xLa_{1-x}F_3/LaF_3$ NPs. (a,b) Steady-state emission spectra (black circles) and fits to Gaussian functions (sums shown as solid red lines) and (c,d) normalized PL lifetime decays and fits of ACA-stabilized (a,c) $Ce_{0.1}La_{0.9}F_3/LaF_3$ NPs at 50 µg/mL in water and (b,d) CeF_3/LaF_3 NPs at 10 µg/mL in water. With increased cerium concentration, there is a greater contribution of perturbed site emission, accompanied by a substantial reduction in the lifetimes of the emission measured at 285 nm (4.35 eV) and 300 nm (4.13 eV). Note similarities between 285 & 300 nm, and 330 (3.76 eV) & 380 nm (3.26 eV). The excitation wavelength was 252 nm (4.92 eV) for all data.

Table 5.1 Center positions of Gaussian fits of PL emission spectra shown in Figure 5.1a & b, and the relative contribution of the perturbed site band (G_3) to the total emission (A = area).

ACA-NP composition	μ_1 (eV)	μ_2 (eV)	μ_3 (eV)	μ_4 (eV)	A_3/A_{tot}	R^2
$Ce_{0.1}La_{0.9}F_3/LaF_3$	4.40	4.12	3.75	2.72	0.55	0.99
CeF_3/LaF_3	4.45	4.04	3.66	2.76	0.88	0.99

to additional bathochromic shift of the emission as well as luminescence quenching by high energy vibrations of water and organic ligands. The fourth low-amplitude, low-energy component, G_4, is believed to be associated with the surface sites. As-synthesized NPs were found to have fairly similar QY values: 0.17 for $Ce_{0.1}La_{0.9}F_3/LaF_3$ and 0.21 for CeF_3/LaF_3.

Excitation at 252 nm is primarily absorbed by regular site Ce^{3+} ions followed by energy transfer from regular site donors to perturbed site acceptors at a rate $W = \alpha/r^6$, where α is a transfer rate constant and r is the distance between any two such sites. For nearest neighbors in bulk crystals (r = 4.1 Å), the rate has been calculated to be 1.56×10^9 s^{-1}, roughly 1-1.5 orders of magnitude faster than the radiative rate[31]. Between sites of the same type (regular-regular and perturbed-perturbed), the transfer rates are expected to be significantly slower than the radiative rates, on the order of 10^5 s^{-1}. Even at 10% Ce^{3+} doping in NPs (where r is greater, provided uniform distribution of dopants), the efficiency of this transfer resulted in more than half of the steady-state emission arising from perturbed sites (A_3/A_{tot} in Table 5.1), increasing to ~88% for CeF_3/LaF_3 NPs. Indeed, the prominence of perturbed site emission has been reported in LaF_3 NPs (synthesized with ammonium di-*n*-octadecyldithiophosphate ligands in water) at Ce^{3+} doping as low as 1.3%[34].

To investigate NP-PS interactions, water-soluble DPIX-DS was added to NPs in water at 1-12% w/w and mixed briefly. DPIX-DS was chosen for its water-solubility (due to degree and symmetry of negative charge from carboxylic acid and sulfonic acid groups, also encouraging association with the positively-charged NPs). Like many PS molecules, DPIX-DS tends to aggregate, forming non-fluorescent dimers above certain concentrations in aqueous solution[42], which we have corroborated by observing a change in absorbance character of free DPIX-DS in solution at ~5 μg/mL (Figure C2). All PL measurements were taken with DPIX-DS at <5 μg/mL, in the monomeric regime. Absorbance measurements of the ACA-NPs alone and with added DPIX-DS are shown in Figure 5.3a & b. Note the absorption of the NPs shown here (primarily at $\lambda < 260$ nm) is due to Ce^{3+}, and so CeF_3/LaF_3 NPs of a given size absorb ~10X as strongly as $Ce_{0.1}La_{0.9}F_3/LaF_3$ NPs of the same size.

Addition of DPIX-DS to the NPs quenched the steady-state PL of the NPs in a concentration-dependent fashion. The spectra are shown in Figure 5.3c & d. The distinct peaks of the emission components can be easily resolved by eye starting at 6% w/w DPIX-DS for both NP types, and a bathochromic shift is apparent in the CeF_3/LaF_3 peak (roughly corresponding to the perturbed band peak), from 336 nm in the absence of DPIX-DS to 352 nm at 12% w/w DPIX-DS. The quenching efficiency $\eta = 1 - I/I_0$ is shown in Figure 5.4, where I and I_0 are the integrated intensities in the presence and absence of PS respectively. The quenching showed a similar trend with both types of NP and exceeded 80% for both types at 6% w/w DPIX-DS. It is not immediately apparent that this should be the case, considering the different sizes and Ce^{3+} concentrations of the NP types, and the NP concentration difference between the samples. For a given % w/w of DPIX-

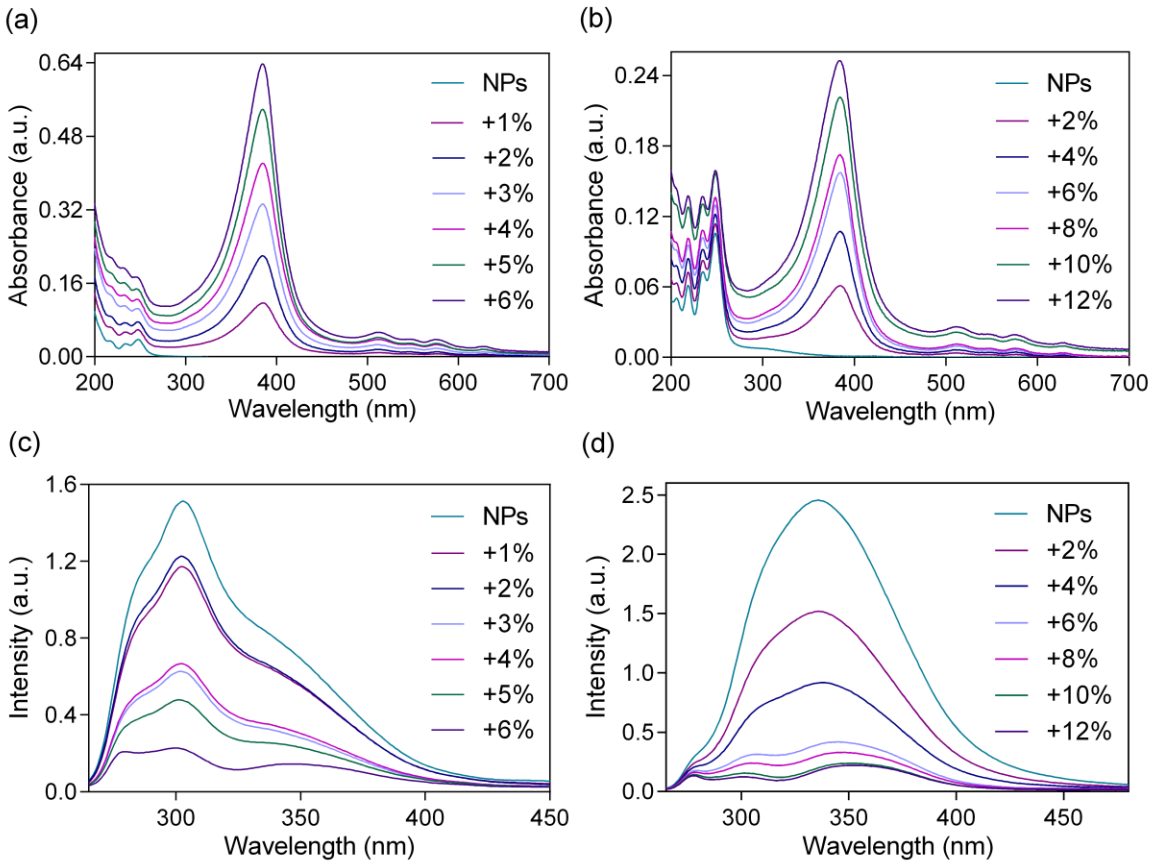

Figure 5.3 Quenching of NP photoluminescence by photosensitizers. Absorbance (a,b) and emission (c,d) spectra (excited at 252 nm) of ACA-stabilized (a,c) $Ce_{0.1}La_{0.9}F_3/LaF_3$ nanoparticles (500 µg/mL for absorbance and 50 µg/mL for emission) in water and (b,d) CeF_3/LaF_3 nanoparticles (100 µg/mL for absorbance and 10 µg/mL for emission) in water with increasing amounts of DPIX-DS, shown as % w/w.

DS, there were ~40% more DPIX-DS molecules per square nanometer of NP surface for CeF_3/LaF_3 NPs (for instance, 2% w/w was equivalent to ~0.10 molecules/nm^2 with $Ce_{0.1}La_{0.9}F_3/LaF_3$ and ~0.14 molecules/nm^2 with CeF_3/LaF_3). Details are shown in Table C2. Compared to radioexcitation, where a high degree of cerium concentration-dependent self-

quenching is expected, photoexcitation of NPs alone did not result in Ce^{3+} concentration-dependent luminescence quenching (as evidenced by the PL QY values of the NPs), and so the CeF_3/LaF_3 NPs effectively presented many more Ce^{3+} donors per NP (and per surface area) than the $Ce_{0.1}La_{0.9}F_3/LaF_3$ NPs. This became particularly apparent through Stern-Volmer fits of I_0/I values as a function of the absolute DPIX-DS concentrations (shown in Figure C3) which gave markedly different results for each NP type: quenching of $Ce_{0.1}La_{0.9}F_3/LaF_3$ NPs with 1-5% w/w DPIX-DS was best fit by a linear equation of the form

$$\frac{I_0}{I} = 1 + K_{SV}[PS] \tag{5.3}$$

where [PS] is the molar concentration of DPIX-DS, giving the dynamic quenching constant $K_{SV} = 0.52 \times 10^6\ M^{-1}$. Quenching of CeF_3/LaF_3 NPs, with DPIX-DS at 2-12% w/w, was best fit by a modification of the model incorporating an additional quenching factor to account for the non-linear behavior, of the form

$$\frac{I_0}{I} = (1 + K_{SV}[PS])e^{(K_q[PS])} \tag{5.4}$$

where K_q is a constant proportional to the volume of the static "quenching sphere" of the NPs[43]. The fit gave $K_{SV} = 3.38 \times 10^6\ M^{-1}$ and $K_q = 0.31 \times 10^6\ M^{-1}$. The K_q parameter is the product of N_A and the quenching volume V_q, leading to V_q = ~0.5 attoliters, or a sphere of ~50 nm radius. It is apparent from the fit values that the CeF_3/LaF_3 NPs were more efficiently quenched by DPIX-DS, which is unsurprising given the difference in Ce^{3+} content. It is important to note that the pronounced difference in quenching between NP types is not expected to extend to the case of radioexcitation, where each of the NP compositions is expected to be similar in terms of excitation and scintillation output for a given NP size.

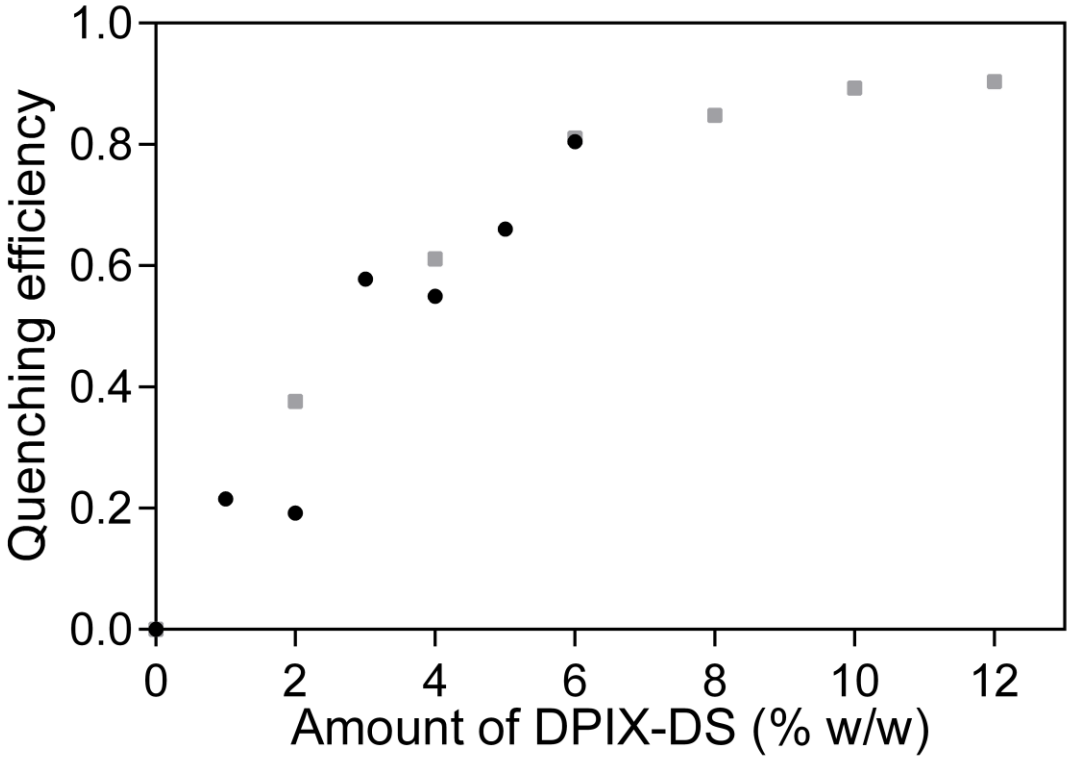

Figure 5.4 Ce^{3+} PL quenching with increasing amounts of DPIX-DS for ACA-stabilized $Ce_{0.1}La_{0.9}F_3/LaF_3$ (circles) and CeF_3/LaF_3 (squares).

The steady-state fits and NP-PS absorbance data were evaluated to determine informative wavelengths for time-resolved measurements: 285 nm (near the peak of the $^2D_{3/2} \rightarrow {}^2F_{5/2}$ emission), 300 nm (near the peak of the $^2D_{3/2} \rightarrow {}^2F_{7/2}$ emission), 330 nm (near the peak of the perturbed site band), and 380 nm (near the peak of the PS absorbance). With the exception of some 285 nm lifetime decays, each measurement could be fit to a sum of up to four exponential decay functions, depending on the detection wavelength and amount of added PS. Fits were chosen to give a self-

consistent description of the system. 300 & 330 nm were taken to be the most representative measurements and will be the focus of the analysis.

PL lifetime decays of NPs alone were found to be consistent with the physical model of direct excitation of regular sites followed by radiation trapping by perturbed sites: fits of measurements made at 300 nm contained major components suggesting regular and perturbed site emission, whereas those made at 330 & 380 nm (entirely within the perturbed site band) contained longer-lived components with rising edges (shown in Figure 5.2c). Assignment of the components was fairly intuitive for $Ce_{0.1}La_{0.9}F_3/LaF_3$ NPs: 300 nm data was dominated by two decays, 8.13 ns (20%) ascribed to regular sites & 26.8 ns (79%) from perturbed sites; 330 & 380 nm were each fit by mono-exponential decays of 32.5 ns & 38.8 ns respectively. Interpretation of the CeF_3/LaF_3 decays (shown in Figure 5.2d) was less straightforward. At 300 nm, an adequate fit required four exponentials: 0.34 ns (9.4%), 1.83 ns (27%), 6.36 ns (35%), and 19.1 ns (29%). The steady-state fits suggest this measurement contains primarily perturbed site emission with some regular site contribution. The four exponential fit is likely a semi-arbitrary discretization of Ce^{3+} populations based on the degree of surface quenching, similar to what has been seen in Ce^{3+}–doped YAG[44], as well as $LaPO_4$ and LaF_3 NPs doped with a variety of trivalent lanthanides[45]. Two exponentials were required to fit 330 & 380 nm data, likely a simpler distinction between the "interior" perturbed population (with lifetimes close to those found with $Ce_{0.1}La_{0.9}F_3/LaF_3$ NPs) and the "surface" perturbed population (with shorter lifetimes). In addition to the prominent decays, both types of NPs displayed one or two weak, fast components (mostly <2 ns) that become increasingly apparent at all measured wavelengths coincident with the quenching of the other components by the addition of DPIX-DS. Full TCSPC fit results are provided in Table C3. The average PL

lifetimes of ACA-NPs alone measured at different Ce^{3+} emission wavelengths are shown in Table 5.2.

Addition of DPIX-DS resulted in quenching of PL lifetimes measured at 300 & 330 nm, likely reflecting energy transfer from the perturbed sites to DPIX-DS (more favorable than from regular sites due to greater spectral overlap and association with the NP surface), and resultant quenching of the regular sites by repopulation of the quenched perturbed sites. This is shown for 0, 2, 4 & 6% w/w DPIX-DS in Figure 5.5a & b and Table C3. The rising edge associated with the build-up of perturbed site excited states is no longer discernable at ≥3% w/w DPIX-DS, and the 330 nm lifetime decays begin to resemble those at 300 nm (shown in Figure 5.5c & d). These changes are consistent with an energy transfer cascade of the form regular Ce^{3+}→perturbed Ce^{3+}→PS, as illustrated in Figure 5.6. Fits of perturbed site PL decays required additional exponentials with increasing PS concentrations. For $Ce_{0.1}La_{0.9}F_3/LaF_3$ NPs, splitting of the mono-exponential decay of the bare NPs reflects a distinction between sites close enough to the surface to act as the most effective donors, and those in the NP interior. For CeF_3/LaF_3 NPs, the longest lifetime component at 300 nm disappears as the perturbed site band recedes.

Table 5.2 Average PL lifetimes for the ACA-NPs at different Ce^{3+} emission wavelengths. See Table C3 for additional details.

ACA-NP composition	**τ_{ave} (ns) at 300 nm**	**τ_{ave} (ns) at 330 nm**	**τ_{ave} (ns) at 380 nm**
$Ce_{0.1}La_{0.9}F_3/LaF_3$	20.3	32.5	38.8
CeF_3/LaF_3	8.3	24.0	31.8

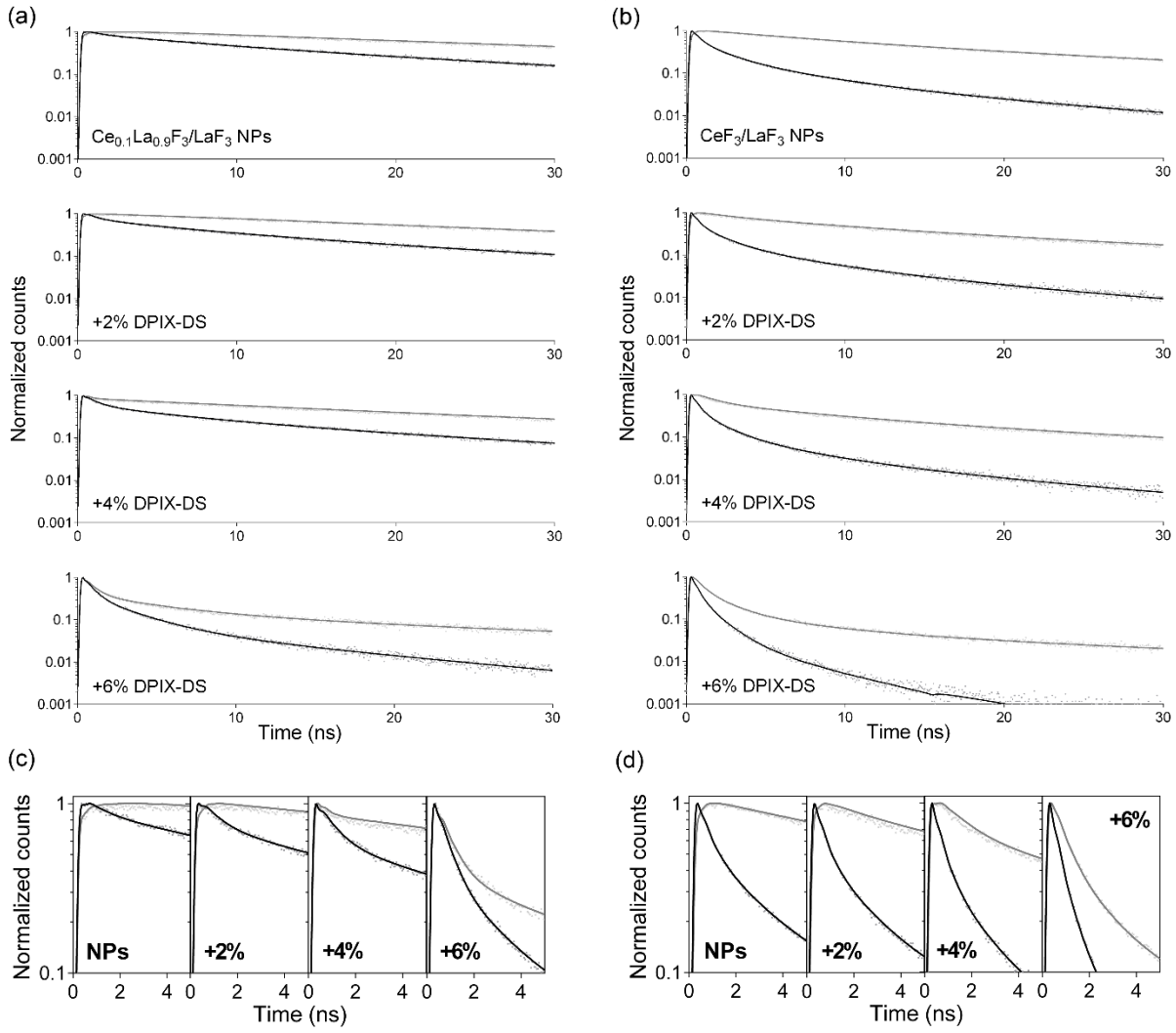

Figure 5.5 Time-resolved Ce^{3+} PL quenching and fits at 300 (dark traces) & 330 nm (light traces) for ACA-stabilized (a, c) $Ce_{0.1}La_{0.9}F_3/LaF_3$ and (b, d) CeF_3/LaF_3 with 0, 2, 4 & 6% w/w DPIX-DS. Panels c & d show magnified sections of the traces in a & b, exhibiting the effect on 330 nm lifetimes at short times.

Interestingly, average lifetimes measured at 380 nm increased gradually with addition of DPIX-DS. Lifetimes of CeF_3/LaF_3 at 330 nm also increased above 6% w/w. We noted that the 380 nm fits consisted of one component that was quenched as expected, and another that increased to

42.7 ns (for $Ce_{0.1}La_{0.9}F_3/LaF_3$) and 44.5 ns (for CeF_3/LaF_3), lifetimes similar to those found in some bulk CeF_3 crystals. Based on an observed loss of colloidal stability at high PS loading, this may be due to aggregation of NPs, leading to increased reabsorption of higher-energy emission and increasing the apparent lifetime of the low-energy population. This is consistent with the bathochromic shift of the CeF_3/LaF_3 emission. Internal conversion rates from $S_n \rightarrow S_1$ in excited DPIX-DS are likely sufficiently fast to preclude PS→perturbed site back-transfer.

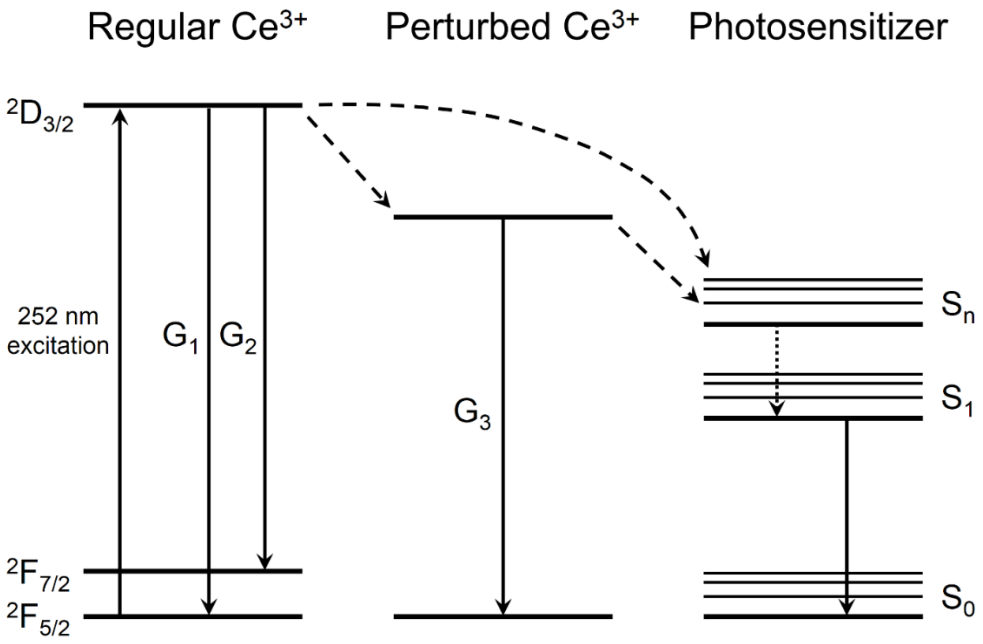

Figure 5.6 Simplified Jablonski diagram illustrating the primary processes investigated in this work. Absorption/excitation and fluorescence are shown as solid lines, energy transfer routes shown as dashed lines, and internal conversion and vibrational relaxation of the PS combined as the dotted line. Nonradiative relaxation and quenching, as well as photosensitizer triplet states and intersystem crossing were omitted for simplicity.

5.3.2 Characterization and photoluminescence of CA- and ALE-NPs and chlorin e6 conjugates

TEM images of CA- and ALE-NPs are shown in Figure 5.7. The images are consistent with previous studies that confirm that the particles are roughly spherical with a diameter of ~4 nm[39]. SAED confirms the small size of the NPs and the preservation of crystallinity after the ligand exchange process.

The general approach to alendronate ligand exchange and chlorin e6 (Ce6) conjugation is shown in Figure 5.8, with full details found in the Experimental Section. After isolation of alendronate-exchanged NPs, the citrate absorbance peak around 210 nm disappeared (Figure C4). The presence of alendronate on the NPs was corroborated by EDX spectra showing the phosphorus K_α line around 2 keV (Figure C5). Colloidal stability of the ALE-NPs was found to be sensitive to small changes in the ionic strength and pH of the solution, with precipitation resulting from an increase of either.

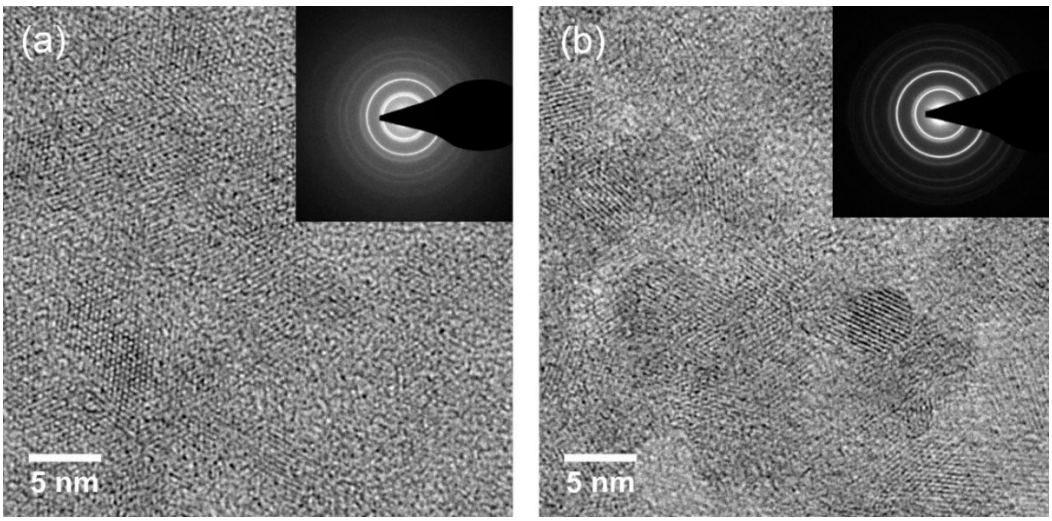

Figure 5.7 TEM and SAED images of $Ce_{0.1}La_{0.9}F_3/LaF_3$ NPs (a) as-synthesized (coated with citrate) and (b) after ligand exchange with alendronate.

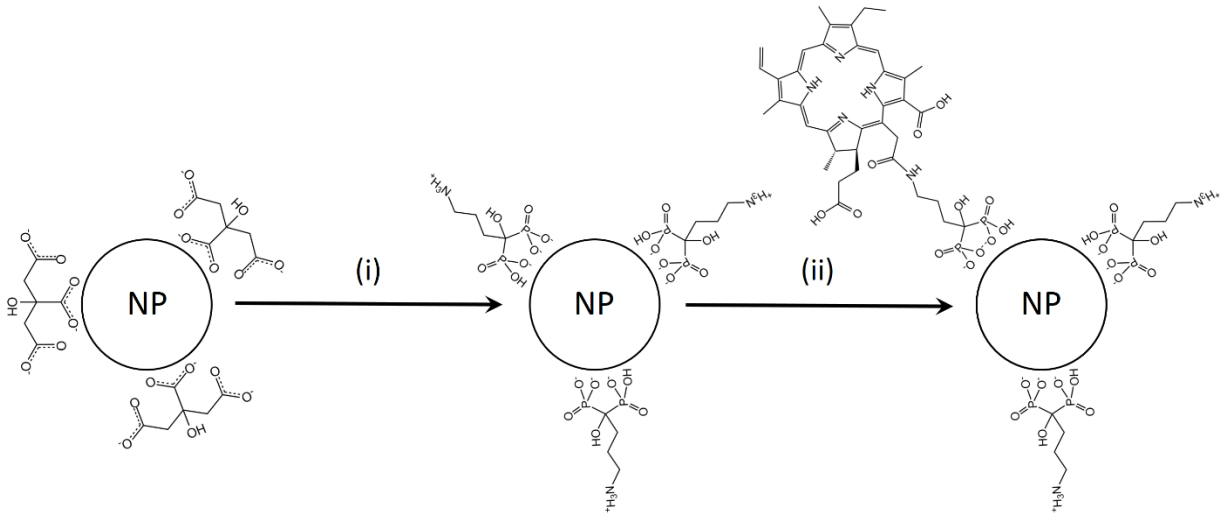

Figure 5.8 Preparation of NP-Ce6 conjugates. Reaction (i) represents ligand exchange, where the citrate ligands of the as-synthesized NPs are displaced by alendronate after stirring and heating for 2 hours in water. Reaction (ii) represents bioconjugation of chlorin e6, where chlorin e6 is covalently attached to the alendronate ligand through amide bond formation mediated by NHS & DIC, in a solution of primarily DMSO.

As-synthesized citrate-stabilized $Ce_{0.1}La_{0.9}F_3/LaF_3$ NPs were found to have a QY of 0.06. Steady-state PL spectra could be fit to a sum of four Gaussian functions as with ACA-NPs, though with significant differences in their positions and amplitudes, as shown in Figure 5.9a. In particular, the $^2D_{3/2} \rightarrow {}^2F_{7/2}$ (G_2) component was found to be considerably weaker, whereas the contribution of the G_4 component increased, likely due to the larger proportion of surface sites in the smaller NPs. As the surface sites are shifted to lower energies, it is likely that the G_2 component is quenched relative to G_1 because of increased energy transfer to the surface sites. PL lifetime fits (Figure 5.9c) required additional exponentials compared to ACA-NPs and average lifetimes were

somewhat shorter: 16.9 ns at 300 nm, 28.4 ns at 330 nm and 37.6 ns at 380 nm. These effects can also be attributed to the increased prominence of the surface sites and surface quenching. Ligand exchange with alendronate caused additional changes to the steady-state PL spectrum as shown in Figure 5.9b, notably a further hypsochromic shift and increase of the contribution of the G_4 component, along with a decrease of the spin-orbit splitting between G_1 and G_2 to 0.18 eV. Center positions are given in Table C4. Alendronate-modified NPs also had an increased apparent QY of 0.13, though the average PL lifetimes were not substantially different from the CA-NPs (Figure 5.9d). This result suggests that citric acid ligands act as static quenchers and that alendronate enhances passivation of the surface. Full TCSPC fits of CA-NPs and ALE-NPs are shown in Table 5.3.

Conjugation of Ce6 to ALE-NPs was accomplished through amide bond formation mediated by the coupling reagents NHS and DIC. Figure 5.10 shows absorbance measurements for ALE-NPs alone and ALE-NP-Ce6 conjugates, as well as a control reaction conducted without the coupling reagents NHS and DIC. The control sample retained a small amount of Ce6 after washing, suggesting that some may be free in solution or associated with the NPs non-covalently. In the conjugate sample, the Ce6 absorbance peaks located at 403 nm (Soret band), 525 & 641 nm (Q bands) are consistent with those reported previously for free Ce6 in PBS at pH <6[46]. The Ce6 concentrations were determined by comparing the absorbance values at the Q_x (0,0) peak (~640 nm) to a standard curve determined for free Ce6 in PBS pH ~3. The ε_{250} values of the conjugates were estimated to be ~10% greater than the ALE-NPs alone, an increase consistent with what would be expected by comparing the ε_{250} and ε_{400} values of Ce6 alone. The loading of Ce6 was ~0.44% w/w of the ALE-NPs, corresponding to ~1 Ce6 molecule/NP (calculations found in Appendix C). The control sample contained roughly 1/10 the amount of Ce6, ~0.04% w/w.

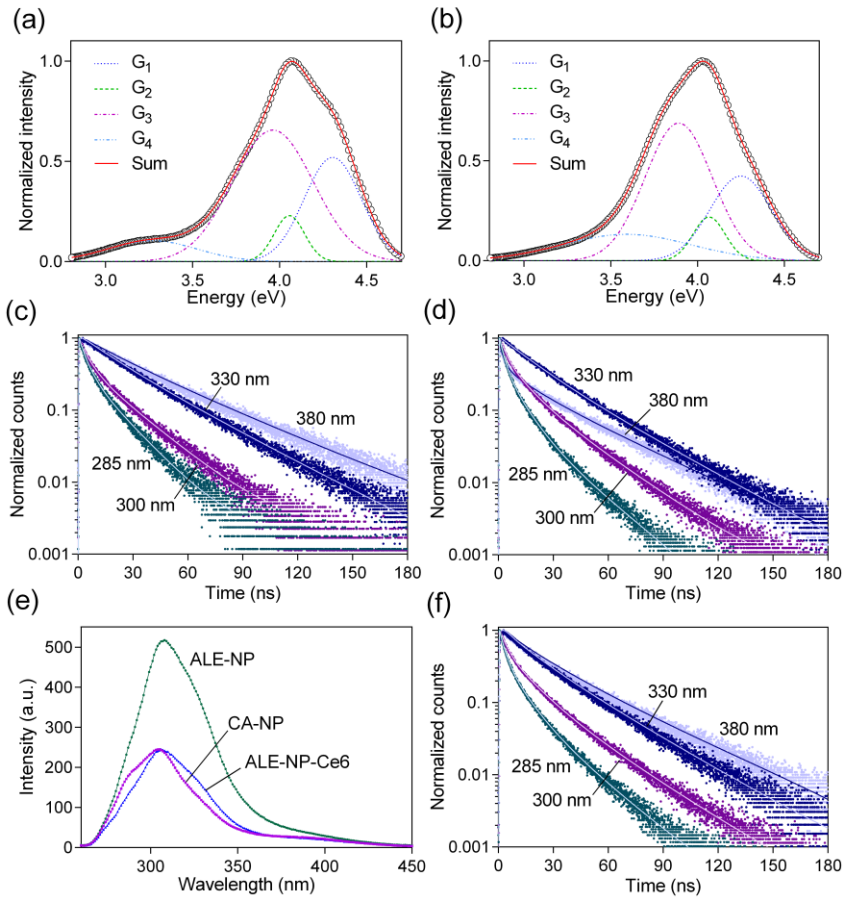

Figure 5.9 Photoluminescence of CA and ALE-NPs and Ce6 conjugates. (a,b) Steady-state emission spectra (black circles) and Gaussian fits (sum shown as solid red line) and (c,d) normalized PL lifetime decays and fits of (a,c) citrate-stabilized and (b,d) alendronate-stabilized $Ce_{0.1}La_{0.9}F_3/LaF_3$ NPs at 50 µg/mL in water. (e) Comparison of steady-state emission spectra of CA $Ce_{0.1}La_{0.9}F_3/LaF_3$ NPs, ALE-NPs and ALE-NP-Ce6 conjugates each at 50 µg/mL in water, using 252 nm excitation. Alendronate ligand exchange with alendronate altered the shape of the spectrum and increased the QY of the NPs approximately two-fold. Conjugation to Ce6 reduced the emission intensity by approximately half. (f) Normalized PL lifetime decays and fits of ALE-NP-Ce6 conjugates at 50 µg/mL in water. The average PL lifetimes did not change substantially compared to ALE-NPs (see Table 5.3 as well).

Table 5.3 Multiexponential fits of time-resolved PL measurements of citrate- and alendronate-stabilized $Ce_{0.1}La_{0.9}F_3/LaF_3$ NPs and Ce6 conjugates. Components with negative amplitudes were omitted. The "Conjugated Ce6 emission" measurements refer to emission at 660 nm from Ce6 that has been conjugated to ALE-NPs using excitation at either 252 nm or 400 nm, labeled accordingly. Confidence intervals for lifetimes greater than a few ns were typically less than ±5% of the fit value and less than ±1% for lifetimes greater than ~25 ns. For shorter lifetimes, confidence intervals were larger, up to ±50%.

CA $Ce_{0.1}La_{0.9}F_3/LaF_3$	I_1 (%)	τ_1 (ns)	I_2 (%)	τ_2 (ns)	I_3 (%)	τ_3 (ns)	I_4 (%)	τ_4 (ns)	$\langle\tau\rangle$ (ns)	χ^2
300 nm	—	—	1.2	0.32	22.5	5.2	76.3	20.7	16.9	1.0
330 nm	—	—	0.7	0.7	26.8	18	72.5	32.4	28.4	1.0
380 nm	—	—	—	—	38.2	24.4	61.8	45.6	37.6	0.99

ALE $Ce_{0.1}La_{0.9}F_3/LaF_3$	I_1 (%)	τ_1 (ns)	I_2 (%)	τ_2 (ns)	I_3 (%)	τ_3 (ns)	I_4 (%)	τ_4 (ns)	$\langle\tau\rangle$ (ns)	χ^2
300 nm	1	0.12	11.4	3	32.3	9.8	55.3	24.6	17.1	1.0
330 nm	—	—	—	—	19.5	13.3	80.5	28.9	26	1.0
380 nm	1.4	0.22	7.3	2.1	14.7	12.4	76.6	35.5	29.2	0.96

ALE-NP-Ce6 conjugate	I_1 (%)	τ_1 (ns)	I_2 (%)	τ_2 (ns)	I_3 (%)	τ_3 (ns)	I_4 (%)	τ_4 (ns)	$\langle\tau\rangle$ (ns)	χ^2
300 nm	1	0.13	13	3.4	36.2	11.4	49.8	25.8	17.4	1.0
330 nm	—	—	5.7	2.3	29	15.1	65.2	30.1	25.5	0.95

380 nm	—	—	5.2	4.7	62.5	24.1	32.3	54.2	33.6	1.0

Conjugated Ce6 emission	I_1 (%)	τ_1 (ns)	I_2 (%)	τ_2 (ns)	I_3 (%)	τ_3 (ns)	I_4 (%)	τ_4 (ns)	$\langle\tau\rangle$ (ns)	χ^2
252 nm ex / 660 nm em	—	—	—	—	66.4	4.7	33.6	14.9	8.3	0.98
400 nm ex / 660 nm em	—	—	—	—	13	1.5	87	3.6	3.3	0.95

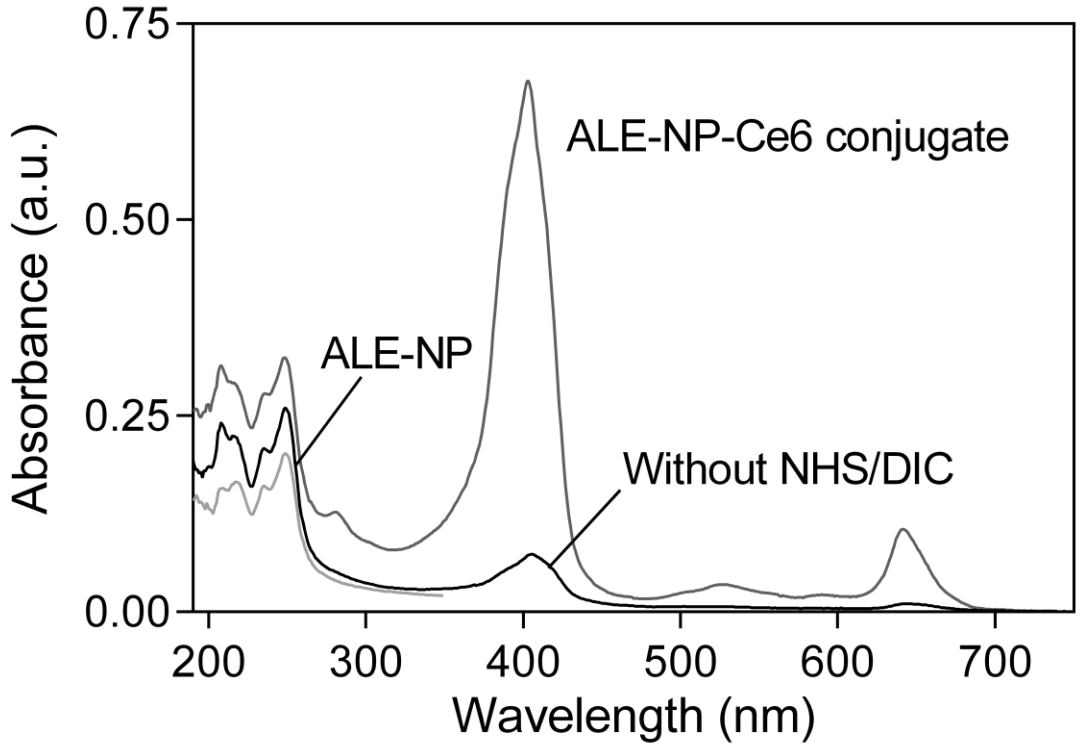

Figure 5.10 Absorbance spectra of alendronate-stabilized $Ce_{0.1}La_{0.9}F_3/LaF_3$ NPs (ALE-NPs), ALE-NPs conjugated to Ce6 (ALE-NP-Ce6) and a control conjugation reaction without NHS & DIC. Note: samples were at different NP concentrations.

The steady-state PL of NPs in the Ce6 conjugate sample was quenched with an efficiency $\eta = 0.52$ compared to an equal mass concentration of ALE-NPs alone, as shown in Figure 5.9e. A control reaction was conducted without Ce6 to confirm the PL quenching was not due to reactions with the DMSO or the coupling reagents. The NP PL lifetimes were not significantly altered, in distinct contrast to the substantial steady-state quenching. They are shown in Figure 5.9f with fit details in Table 5.3.

The PL lifetimes of Ce6 in the conjugate samples provided additional evidence of energy transfer, through comparison of different excitation wavelengths: 400 nm light was used to excite Ce6 independently of the NPs, providing the "native" lifetimes in the absence of energy transfer from Ce^{3+}; 252 nm light was used to excite both Ce^{3+} and Ce6, with the lifetimes reflecting both direct excitation as well as energy transfer from Ce^{3+}. As shown in Figure 5.11 and Table 5.3, Ce6 PL lifetimes (measured at 660 nm, near the Ce6 emission peak) increased noticeably when the conjugates were excited at 252 nm versus 400 nm, from around 3.3 ns to 8.3 ns, suggesting that energy transfer from Ce^{3+} extends the excited state lifetime of the conjugated Ce6.

5.4 Discussion and conclusions

We have conducted a photophysical investigation of cerium and cerium-doped lanthanum fluoride nanoparticle-photosensitizer systems using newly described NP compositions designed to be of biologically relevant sizes and surface chemistries. A recent investigation of singlet oxygen production in theoretical nanoscintillator-photosensitizer systems suggested that careful optimization of excitation energies and NP-PS energy transfer efficiencies will be necessary to achieve a therapeutically relevant effect[21], though there have been relatively few experimental investigations of such systems. In particular, though cerium-doped LaF_3 is explicitly mentioned, it has not been hitherto established whether these NPs are effective as energy donors. They are

potentially disadvantageous due to fluorescence lifetimes that are short compared to the long-lived phosphorescence of other luminescent lanthanides, but have favorable UV/blue emission that overlaps the strong Soret band shared by most porphyrin and chlorin-derived photosensitizers, and may additionally damage cells directly[47, 48, 49]. Our results suggest that both compositions of NPs studied are potentially efficient energy donors to PDT agents, though there are several considerations that should be taken into account to guide future work.

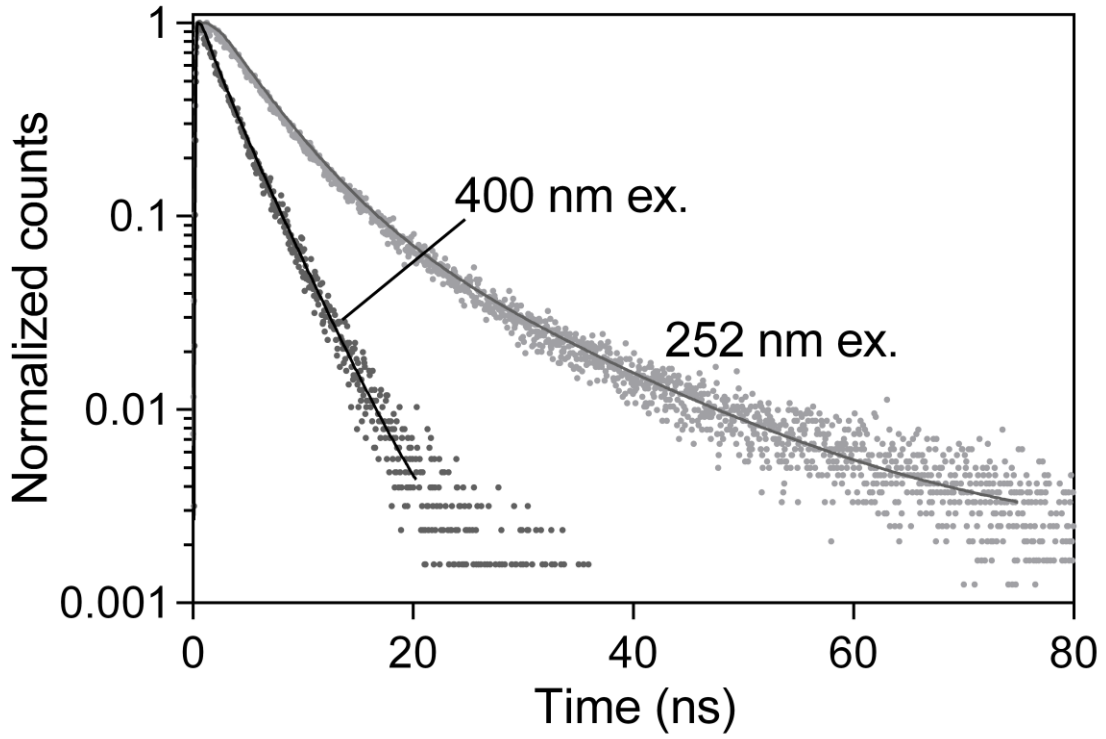

Figure 5.11 Lifetime decays and fits of chlorin e6 emission (measured at 660 nm) when conjugated to alendronate-stabilized $Ce_{0.1}La_{0.9}F_3/LaF_3$ NPs. Excitation at 252 nm (direct excitation of Ce^{3+} and Ce6) resulted in longer lifetimes than direct excitation of Ce6 alone at 400 nm, suggestive of energy transfer from Ce^{3+} to Ce6 upon Ce^{3+} excitation.

While energy transfer efficiency is typically estimated by the extent of quenching of steady-state and/or time-resolved donor luminescence in the presence of an acceptor, there are caveats for using these measures with our system. Because DPIX-DS, Ce6 and other PSs also absorb strongly at 252 nm, being excited directly and competitively with the Ce^{3+} absorption, changes in steady-state PL should not be assumed to be entirely due to increasing energy transfer when varying PS loading, especially in the case of $Ce_{0.1}La_{0.9}F_3/LaF_3$ NPs where DPIX-DS absorbs significantly more than the Ce^{3+}. It is perhaps more informative to consider the excitation spectrum of DPIX-DS when added to NPs, as shown in Figure 5.12 for CeF_3/LaF_3 NPs with 2% w/w DPIX-DS. Though direct excitation of DPIX-DS in the Soret band is certainly more efficient, the Ce^{3+} excitation peaks appear distinctly, providing additional evidence of energy transfer. Time-resolved measurements provided further insight into energy transfer mechanisms, but are complicated by overlapping components that are quenched to different degrees. Energy transfer from NPs to DPIX-DS molecules was found to take place primarily in an indirect multi-step manner via the intermediate perturbed Ce^{3+} sites, which may have implications for NP preparation techniques (particularly regarding the crystallinity of the NPs) as well as energy transfer through scintillation.

The degree of PS loading with ALE-NP-Ce6 conjugates was much lower compared to the amounts investigated with DPIX-DS and ACA-NPs. The ~50% decrease in PL from NPs covalently bound to as few as 1 PS molecule on average, combined with little discernible effect on the time-resolved fluorescence curves (Figure 5.9d-f), is best explained by static quenching due to the formation of ground-state complexes. This implies energy transfer that occurs at a rate faster than 20 ps, consistent with the very short separation. Poisson statistics suggest that there are roughly equal populations of unconjugated NPs (with the same PL lifetimes exhibited by ALE-NPs) and conjugated NPs with excited state lifetimes shorter than the TCSPC instrument response.

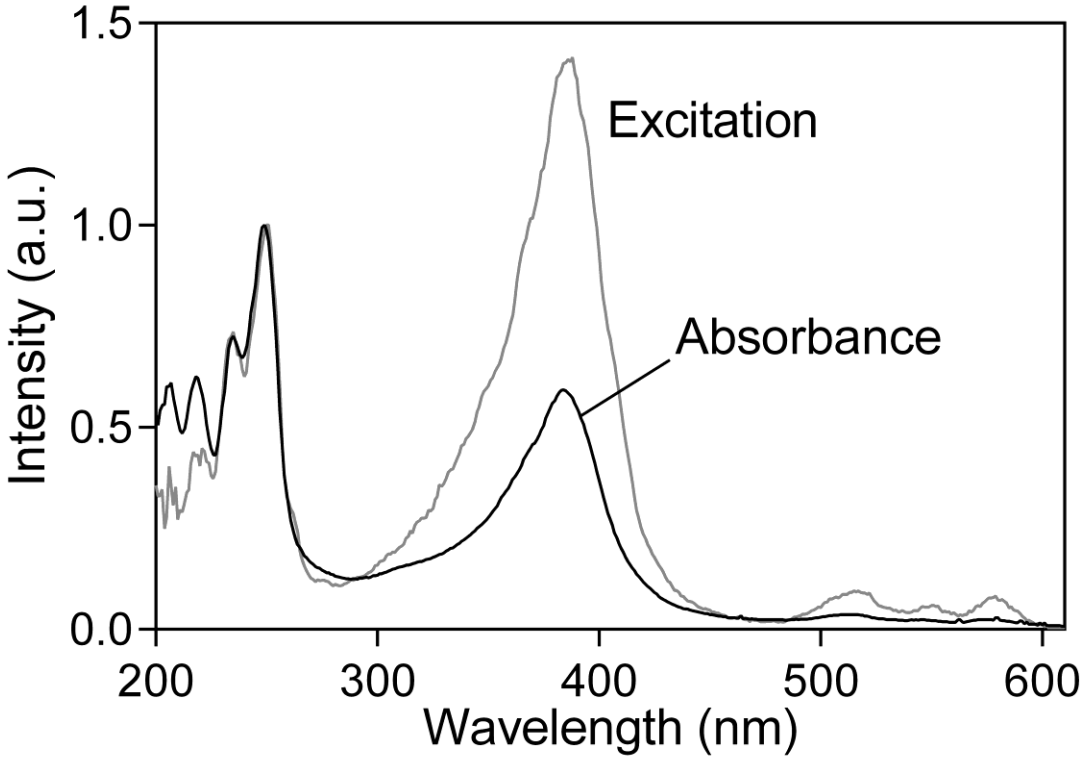

Figure 5.12 Absorbance of ACA-stabilized CeF_3/LaF_3 NPs with 2% DPIX-DS and excitation spectrum of DPIX-DS (emission at 635 nm) of the same sample, normalized to the Ce^{3+} peaks at 250 nm. While direct excitation of DPIX-DS is more efficient, the distinct Ce^{3+} peaks in the excitation spectrum support NP-PS energy transfer.

The role of surface effects, such as those due to ligands and passivation through shelling, are important considerations for the purposes of optimizing NP-PS energy transfer. As shown in Figure C7, the Ce^{3+} emission components vary considerably between NP preparations. While a lack of passivation tends to dramatically reduce the luminescence yield of surface sites, their proximity to surface-bound PS and spectral overlaps are favorable. Addition of undoped LaF_3

shells can improve the luminescence yield at the expense of increased donor-acceptor separation and hypsochromic shift of the perturbed site band. An optimal shell thickness for energy transfer was indeed determined recently in a UCNP-PS system[50]. In that case, using Yb^{3+}-sensitized Er^{3+} upconversion, the quenching of donor luminescence lifetimes was found to be a better reflection of PS activation than steady-state emission quenching, diverging most in the region of highest efficiency. Though the efficiency of transfer with unshelled NPs was high, the singlet oxygen generation was far lower than with any of the shelled NPs due to their relatively low luminescence yield.

The approach to attaching/associating photosensitizer molecules with NPs also plays an important role in energy transfer and the effectiveness of the system. Electrostatic association of DPIX-DS with ACA-NPs, evidenced by a compromise in the colloidal stability of the complexes at PS amounts >6% w/w, has proven valuable for initial experiments, but is insufficient for preserving complexes under harsher conditions. Common approaches to preparing lanthanide-based NPs for use in physiological environments include polymer encapsulation and hydrophobic interactions, allowing for reasonable drug loading capacities of up to 8% w/w[16]. In these systems, drugs (photosensitizers or otherwise) are typically intercalated within the NP coating by virtue of their lipophilic nature. Though these methods allow for relatively easy loading, covalent attachment may be preferable in order to maximize energy transfer, reduce bulk and control orientation and exposure of PS molecules. While alendronate provides an anchor for bioconjugation of PS molecules in close proximity to the NP surface, the colloidal stability of the NPs under physiological conditions remains problematic. Further modifications to the NP coating are under investigation, such as conjugation of mPEG molecules that may improve the stability and biocompatibility of the NPs.

Relative efficiencies will be sufficient to guide *in vitro* experiments. They can be evaluated through measurements of singlet oxygen production, the hallmark encompassing the overall effectiveness of the PS "activation." While singlet oxygen production is predicted to be the primary measure of biological efficacy in nanoscintillator-photosensitizer systems, unexpected synergies (or anti-synergies) also regularly arise when experiments are performed with living cells. For instance, cerium oxide NPs have been shown to have both radiosensitizing and radioprotective effects by virtue of the redox activity of cerium, with a significant dependence on pH and redox state of cerium, degree of surface exposure and energy of incident radiation[51, 52, 53, 54]. Additionally, localization of photosensitizers within a cell, which determines the likely targets of generated singlet oxygen, is an important factor.

As the intention is to use the conjugates with ionizing radiation, it is ultimately the radioluminescence behavior of the NPs that is most pertinent. Wojtowicz *et al.* observed no substantial differences between the luminescence spectra of Ce-doped LaF_3 bulk crystals using optical excitation at 250 nm versus γ and β radiation from a Ru/Rh source, but this excitation independence has not been firmly established in NPs. Scintillation of cerium-doped LaF_3 NPs has only been demonstrated for nanocomposites where the NPs are embedded at high loading volumes into oleic acid or polymer hosts[55, 56, 57], materials that facilitate the scintillation of the NPs. Scintillation of colloidal NPs will be the subject of a future report from our groups.

5.5 Acknowledgements

We acknowledge Prof. Charles McKenna (USC) for the suggestion and gift of the alendronate reagent, Dr. Pooja Tyagi (McGill) for assistance with the Stern-Volmer analysis and Dr. David Liu and Dr. Hicham Chibli (McGill) for assistance with TEM imaging. DRC acknowledges support from the Systems Biology Training Program. SEB and KK acknowledge support from the

Ming Hsieh Institute for Research on Engineering-Medicine for Cancer at the University of Southern California. JLN acknowledges the MDEIE PSR-SIIRI-562 and NSERC Individual Discovery RGPIN 312970-2013.

5.5 References

1. Bechet, D.; Couleaud, P.; Frochot, C.; Viriot, M. L.; Guillemin, F.; Barberi-Heyob, M. Nanoparticles as vehicles for delivery of photodynamic therapy agents. *Trends Biotechnol* **2008,** *26* (11), 612-21.
2. Charron, G.; Stuchinskaya, T.; Edwards, D. R.; Russell, D. A.; Nann, T. Insights into the mechanism of quantum dot-sensitized singlet oxygen production for photodynamic therapy. *Journal of Physical Chemistry C* **2012,** *116* (16), 9334-9342.
3. Chatterjee, D. K.; Fong, L. S.; Zhang, Y. Nanoparticles in photodynamic therapy: An emerging paradigm. *Advanced Drug Delivery Reviews* **2008,** *60* (15), 1627-1637.
4. Samia, A. C.; Chen, X.; Burda, C. Semiconductor quantum dots for photodynamic therapy. *Journal of the American Chemical Society* **2003,** *125* (51), 15736-7.
5. Wilson, B. C.; Patterson, M. S. The physics, biophysics and technology of photodynamic therapy. *Physics in medicine and biology* **2008,** *53* (9), R61-109.
6. Zenkevich, E. I.; Sagun, E. I.; Knyukshto, V. N.; Stasheuski, A. S.; Galievsky, V. A.; Stupak, A. P.; Blaudeck, T.; von Borczyskowski, C. Quantitative analysis of singlet oxygen ($^1O_2$) generation via energy transfer in nanocomposites based on semiconductor quantum dots and porphyrin ligands. *The Journal of Physical Chemistry C* **2011,** *115* (44), 21535-21545.
7. Fowley, C.; Nomikou, N.; McHale, A. P.; McCarron, P. A.; McCaughan, B.; Callan, J. F. Water soluble quantum dots as hydrophilic carriers and two-photon excited energy donors in photodynamic therapy. *Journal of Materials Chemistry* **2012,** *22* (13), 6456-6462.
8. Lim, C.-K.; Heo, J.; Shin, S.; Jeong, K.; Seo, Y. H.; Jang, W.-D.; Park, C. R.; Park, S. Y.; Kim, S.; Kwon, I. C. Nanophotosensitizers toward advanced photodynamic therapy of Cancer. *Cancer letters* **2013,** *334* (2), 176-187.
9. van Veggel, F. C. J. M.; Dong, C.; Johnson, N. J. J.; Pichaandi, J. Ln^{3+}-doped nanoparticles for upconversion and magnetic resonance imaging: some critical notes on recent progress and some aspects to be considered. *Nanoscale* **2012,** *4* (23), 7309-7321.
10. Wang, M.; Abbineni, G.; Clevenger, A.; Mao, C.; Xu, S. Upconversion nanoparticles: synthesis, surface modification and biological applications. *Nanomedicine : nanotechnology, biology, and medicine* **2011,** *7* (6), 710-729.
11. Naccache, R.; Rodríguez, E. M.; Bogdan, N.; Sanz-Rodríguez, F.; Cruz, M. d. C. I. d. l.; Fuente, Á. J. d. l.; Vetrone, F.; Jaque, D.; Solé, J. G.; Capobianco, J. A. High resolution fluorescence imaging of cancers using lanthanide ion-doped upconverting nanocrystals. *Cancers* **2012,** *4* (4), 1067-1105.
12. Chatterjee, D. K.; Gnanasammandhan, M. K.; Zhang, Y. Small upconverting fluorescent nanoparticles for biomedical applications. *Small* **2010,** *6* (24), 2781-95.
13. Qiao, X.-F.; Zhou, J.-C.; Xiao, J.-W.; Wang, Y.-F.; Sun, L.-D.; Yan, C.-H. Triple-functional core-shell structured upconversion luminescent nanoparticles covalently grafted with photosensitizer for luminescent, magnetic resonance imaging and photodynamic therapy in vitro. *Nanoscale* **2012,** *4* (15), 4611-4623.

14. Zhou, A.; Wei, Y.; Wu, B.; Chen, Q.; Xing, D. Pyropheophorbide A and c(RGDyK) comodified chitosan-wrapped upconversion nanoparticle for targeted near-infrared photodynamic therapy. *Mol Pharm* **2012,** *9* (6), 1580-9.
15. Liu, K.; Liu, X.; Zeng, Q.; Zhang, Y.; Tu, L.; Liu, T.; Kong, X.; Wang, Y.; Cao, F.; Lambrechts, S. A.; Aalders, M. C.; Zhang, H. Covalently assembled NIR nanoplatform for simultaneous fluorescence imaging and photodynamic therapy of cancer cells. *ACS Nano* **2012,** *6* (5), 4054-62.
16. Wang, C.; Tao, H.; Cheng, L.; Liu, Z. Near-infrared light induced in vivo photodynamic therapy of cancer based on upconversion nanoparticles. *Biomaterials* **2011,** *32* (26), 6145-6154.
17. Kobayashi, K.; Usami, N.; Porcel, E.; Lacombe, S.; Le Sech, C. Enhancement of radiation effect by heavy elements. *Mutation research* **2010,** *704* (1-3), 123-31.
18. Carter, J. D.; Cheng, N. N.; Qu, Y.; Suarez, G. D.; Guo, T. Nanoscale energy deposition by X-ray absorbing nanostructures. *J Phys Chem B* **2007,** *111* (40), 11622-5.
19. McMahon, S. J.; Hyland, W. B.; Muir, M. F.; Coulter, J. A.; Jain, S.; Butterworth, K. T.; Schettino, G.; Dickson, G. R.; Hounsell, A. R.; O'Sullivan, J. M.; Prise, K. M.; Hirst, D. G.; Currell, F. J. Biological consequences of nanoscale energy deposition near irradiated heavy atom nanoparticles. *Scientific reports* **2011,** *1*, 18.
20. Juzenas, P.; Chen, W.; Sun, Y.-P.; Coelho, M. A. N.; Generalov, R.; Generalova, N.; Christensen, I. L. Quantum dots and nanoparticles for photodynamic and radiation therapies of cancer. *Advanced Drug Delivery Reviews* **2008,** *60* (15), 1600-1614.
21. Morgan, N. Y.; Kramer-Marek, G.; Smith, P. D.; Camphausen, K.; Capala, J. Nanoscintillator conjugates as photodynamic therapy-based radiosensitizers: calculation of required physical parameters. *Radiat Res* **2009,** *171* (2), 236-44.
22. Luksiene, Z.; Juzenas, P.; Moan, J. Radiosensitization of tumours by porphyrins. *Cancer letters* **2006,** *235* (1), 40-47.
23. Luksiene, Z.; Labeikyte, D.; Juodka, B.; Moan, J. Mechanism of radiosensitization by porphyrins. *Journal of environmental pathology, toxicology and oncology : official organ of the International Society for Environmental Toxicology and Cancer* **2006,** *25* (1-2), 293-306.
24. Takahashi, J.; Misawa, M. Characterization of reactive oxygen species generated by protoporphyrin IX under X-ray irradiation. *Radiation Physics and Chemistry* **2009,** *78* (11), 889-898.
25. Wang, L.; Yang, W.; Read, P.; Larner, J.; Sheng, K. Tumor cell apoptosis induced by nanoparticle conjugate in combination with radiation therapy. *Nanotechnology* **2010,** *21* (47), 475103.
26. Scaffidi, J. P.; Gregas, M. K.; Lauly, B.; Zhang, Y.; Vo-Dinh, T. Activity of psoralen-functionalized nanoscintillators against cancer cells upon X-ray excitation. *ACS Nano* **2011,** *5* (6), 4679-87.
27. Lempicki, A.; Wojtowicz, A. J.; Berman, E. Fundamental limits of scintillator performance. *Nuclear Instruments and Methods in Physics Research Section A: Accelerators, Spectrometers, Detectors and Associated Equipment* **1993,** *333* (2–3), 304-311.
28. Moses, W. W.; Derenzo, S. E. Cerium fluoride, a new fast, heavy scintillator. *Nuclear Science, IEEE Transactions on* **1989,** *36* (1), 173-176.
29. Moses, W. W.; Derenzo, S. E. The scintillation properties of cerium-doped lanthanum fluoride. *Nuclear Instruments and Methods in Physics Research Section A: Accelerators, Spectrometers, Detectors and Associated Equipment* **1990,** *299* (1–3), 51-56.

30. Moses, W. W.; Derenzo, S. E.; Weber, M. J.; Ray-Chaudhuri, A. K.; Cerrina, F. Scintillation mechanisms in cerium fluoride. *Journal of Luminescence* **1994,** *59* (1–2), 89-100.
31. Wojtowicz, A. J.; Balcerzyk, M.; Berman, E.; Lempicki, A. Optical spectroscopy and scintillation mechanisms of $Ce_xLa_{1-x}F_3$. *Physical Review B* **1994,** *49* (21), 14880-14895.
32. Dorenbos, P. 5d-level energies of Ce^{3+} and the crystalline environment. I. Fluoride compounds. *Physical Review B* **2000,** *62* (23), 15640-15649.
33. Jacobsohn, L. G.; Sprinkle, K. B.; Roberts, S. A.; Kucera, C. J.; James, T. L.; Yukihara, E. G.; Devol, T. A.; Ballato, J. Fluoride nanoscintillators. *Journal of Nanomaterials* **2011,** *2011*.
34. Jacobsohn, L. G.; Toncelli, A.; Sprinkle, K. B.; Kucera, C. J.; Ballato, J. Spectral engineering of LaF_3:Ce^{3+} nanoparticles: The role of Ce^{3+} in surface sites. *Journal of Applied Physics* **2012,** *111* (7).
35. Kömpe, K.; Lehmann, O.; Haase, M. Spectroscopic distinction of surface and volume ions in cerium(III)- and terbium(III)-containing core and core/shell nanoparticles. *Chemistry of Materials* **2006,** *18* (18), 4442-4446.
36. Sudarsan, V.; van Veggel, F. C. J. M.; Herring, R. A.; Raudsepp, M. Surface Eu^{3+} ions are different than "bulk" Eu^{3+} ions in crystalline doped LaF3 nanoparticles. *Journal of Materials Chemistry* **2005,** *15* (13), 1332-1342.
37. Dong, C.; van Veggel, F. C. Cation exchange in lanthanide fluoride nanoparticles. *ACS Nano* **2009,** *3* (1), 123-30.
38. Dong, C.; Pichaandi, J.; Regier, T.; van Veggel, F. C. J. M. The unexpected structures of "core-shell" and "alloy" LnF_3 nanoparticles as examined by variable energy X-ray photo-electron spectroscopy. *Nanoscale* **2011,** *3* (8), 3376-3384.
39. Cross, A. M.; May, P. S.; van Veggel, F. C. J. M.; Berry, M. T. Dipicolinate sensitization of europium luminescence in dispersible 5% Eu:LaF_3 nanoparticles. *Journal of Physical Chemistry C* **2010,** *114* (35), 14740-14747.
40. Dong, C.; Raudsepp, M.; van Veggel, F. C. J. M. Kinetically determined crystal structures of undoped and La^{3+}-doped LnF_3. *The Journal of Physical Chemistry C* **2009,** *113* (1), 472-478.
41. Brouwer, A. Standards for photoluminescence quantum yield measurements in solution (IUPAC Technical Report). *Pure and Applied Chemistry* **2011,** *83* (12), 2213-2228.
42. Dairou, J.; Vever-Bizet, C.; Brault, D. Self-association of disulfonated deuteroporphyrin and its esters in aqueous solution and photosensitized production of singlet oxygen by the dimers. *Photochemistry and Photobiology* **2002,** *75* (3), 229-236.
43. Valeur, B. *Molecular fluorescence : principles and applications*; Wiley-VCH: Weinheim; New York, 2002.
44. Tian, L. J.; Sun, Y. J.; Yu, Y.; Kong, X. G.; Zhang, H. Surface effect of nano-phosphors studied by time-resolved spectroscopy of Ce^{3+}. *Chemical Physics Letters* **2008,** *452* (1–3), 188-192.
45. Stouwdam, J. W.; Hebbink, G. A.; Huskens, J.; van Veggel, F. C. J. M. Lanthanide-doped nanoparticles with excellent luminescent properties in organic media. *Chemistry of Materials* **2003,** *15* (24), 4604-4616.
46. Čunderlíková, B.; Gangeskar, L.; Moan, J. Acid–base properties of chlorin e6: relation to cellular uptake. *Journal of Photochemistry and Photobiology B: Biology* **1999,** *53* (1–3), 81-90.
47. Baumler, W.; Regensburger, J.; Knak, A.; Felgentrager, A.; Maisch, T. UVA and endogenous photosensitizers--the detection of singlet oxygen by its luminescence. *Photochemical & photobiological sciences : Official journal of the European Photochemistry Association and the European Society for Photobiology* **2012,** *11* (1), 107-17.

48. Besaratinia, A.; Yoon, J. I.; Schroeder, C.; Bradforth, S. E.; Cockburn, M.; Pfeifer, G. P. Wavelength dependence of ultraviolet radiation-induced DNA damage as determined by laser irradiation suggests that cyclobutane pyrimidine dimers are the principal DNA lesions produced by terrestrial sunlight. *FASEB journal : official publication of the Federation of American Societies for Experimental Biology* **2011,** *25* (9), 3079-91.
49. Cadet, J.; Mouret, S.; Ravanat, J. L.; Douki, T. Photoinduced damage to cellular DNA: direct and photosensitized reactions. *Photochem Photobiol* **2012,** *88* (5), 1048-65.
50. Wang, Y.; Liu, K.; Liu, X. M.; Dohnalova, K.; Gregorkiewicz, T.; Kong, X. G.; Aalders, M. C. G.; Buma, W. J.; Zhang, H. Critical shell thickness of core/shell upconversion luminescence nanoplatform for FRET application. *J Phys Chem Lett* **2011,** *2* (17), 2083-2088.
51. Briggs, A.; Corde, S.; Oktaria, S.; Brown, R.; Rosenfeld, A.; Lerch, M.; Konstantinov, K.; Tehei, M. Cerium oxide nanoparticles: influence of the high-Z component revealed on radioresistant 9L cell survival under X-ray irradiation. *Nanomedicine : nanotechnology, biology, and medicine* **2013,** *9* (7), 1098-1105.
52. Renu, G.; Rani, V. V. D.; Nair, S. V.; Subramanian, K. R. V.; Lakshmanan, V.-K. Development of cerium oxide nanoparticles and its cytotoxicity in prostate cancer cells. *Advanced Science Letters* **2012,** *6* (1), 17-25.
53. Wason, M. S.; Colon, J.; Das, S.; Seal, S.; Turkson, J.; Zhao, J.; Baker, C. H. Sensitization of pancreatic cancer cells to radiation by cerium oxide nanoparticle-induced ROS production. *Nanomedicine : nanotechnology, biology, and medicine* **2013,** *9* (4), 558-569.
54. Wason, M. S.; Zhao, J. Cerium oxide nanoparticles: potential applications for cancer and other diseases. *American journal of translational research* **2013,** *5* (2), 126-31.
55. Guss, P.; Guise, R.; Yuan, D.; Mukhopadhyay, S.; O'Brien, R.; Lowe, D.; Kang, Z.; Menkara, H.; Nagarkar, V. V. Lanthanum halide nanoparticle scintillators for nuclear radiation detection. *Journal of Applied Physics* **2013,** *113* (6), 064303-064303-6.
56. McKigney, E. A.; Del Sesto, R. E.; Jacobsohn, L. G.; Santi, P. A.; Muenchausen, R. E.; Ott, K. C.; Mark McCleskey, T.; Bennett, B. L.; Smith, J. F.; Wayne Cooke, D. Nanocomposite scintillators for radiation detection and nuclear spectroscopy. *Nuclear Instruments and Methods in Physics Research Section A: Accelerators, Spectrometers, Detectors and Associated Equipment* **2007,** *579* (1), 15-18.
57. McKigney, E. A.; Muenchausen, R. E.; Cooke, D. W.; Del Sesto, R. E.; Gilbertson, R. D.; Bacrania, M. K.; Bennett, B. L.; Jacobsohn, L. G.; McCleskey, T. M.; Ott, K. C.; Sitarz, S. C.; Smith, J. F.; Stange, S. In *LaF_3:Ce nanocomposite scintillator for gamma-ray detection*, 2007, pp 67061A-67061A-11.

Chapter 6

Preliminary radiation results, conclusions and future directions

6. Preliminary radiation results, conclusions and future directions

6.1 Introduction

We have also conducted preliminary experiments with $Ce_xLa_{1-x}F_3$ NPs in combination with ionizing radiation sources, toward evaluating their scintillation properties as well as their potential to enhance radiation doses when applied to cancer cell lines *in vitro*.

Establishing scintillation yields of colloidal $Ce_xLa_{1-x}F_3$ NPs is a top priority, as in the recent literature the yields often tend to be erroneously assumed to be comparable to those of bulk materials. Our collaborators at the University of Southern California have developed a system for sensitive scintillation measurements using a PMT spectrometer combined with a Precision X-ray X-RAD 320ix "biological irradiator," which will be detailed in an upcoming publication. Figure 6.1 shows a preliminary scintillation measurement of a concentrated solution of ACA-stabilized $Ce_{0.1}La_{0.9}F_3/LaF_3$ NPs in water, excited by 250 kVp X-rays hardened with a 2 mm Al filter.

6.2 Colony forming assays

The effects of radiation and dose enhancement by drugs or other treatment of cells *in vitro* are routinely quantified by clonogenic assays (also known as colony forming assays or CFAs)[1]. The basic protocol involves exposure of a population of cells in asynchronous growth phase to a compound of interest (in our case "bare" NPs, NP-PS conjugates or unconjugated PS) in advance of radiation treatment. The cells are incubated with the compound for a set amount of time before excess compound (remaining in solution, not taken up by or adherent to cells) is removed by washing and fresh growth media is added. The cell cultures are then exposed to a given dose of radiation before being replated at a low density in culture dishes. Because the effects of radiation exposure don't fully manifest until cells begin to divide, the reproductive potential of a relatively small amount of isolated cells (representative of the entire population) can be evaluated by their

ability to form colonies (comprised of 50+ cells) after a certain amount of time (dependent on the growth rate). The result is a survival curve as a function of ionizing radiation dose that can be analyzed further to determine dose enhancement relative to control conditions. With radiation alone, different cell types show considerable differences in radiation resistance[2].

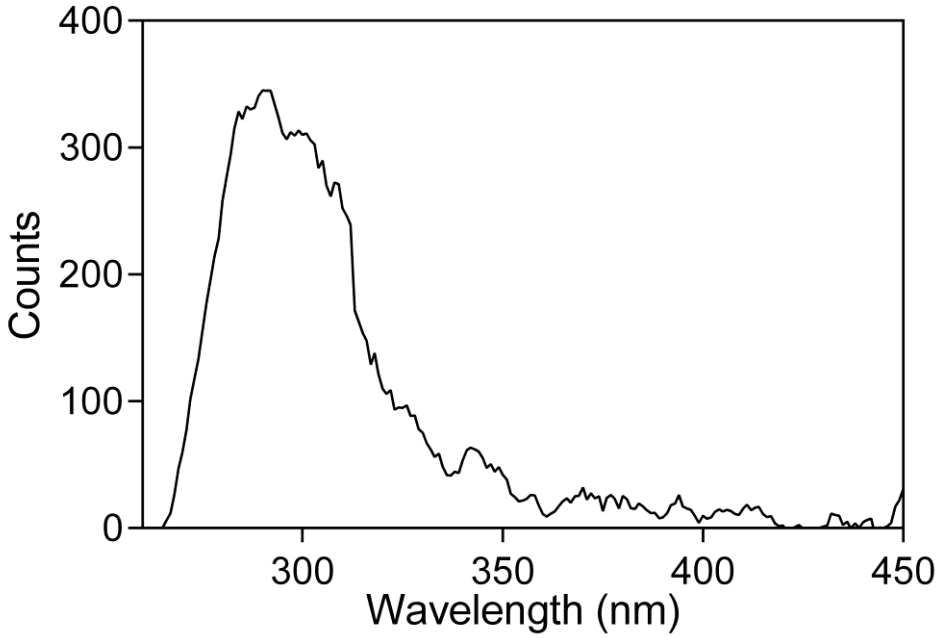

Figure 6.1 Scintillation spectrum of ACA-stabilized $Ce_{0.1}La_{0.9}F_3/LaF_3$ NPs in water.

Preliminary CFAs have been conducted with three cancer cell lines: B16, a murine melanoma, MeWo, a human melanoma, and LNCaP, a human prostate cell line. For experiments with NPs alone, high concentrations were added to cells as it was expected that they would provide a modest enhancement if any. The use of high concentrations was found to have adverse effects on the cells through mechanisms unrelated to those under investigation – particularly, that the pH of the growth media was affected by addition of citrate-stabilized NPs, presumably resulting from

detachment of the citrate ligands which then buffered the solution at an acidic pH that is harmful to the cells. Additionally, some cells were found to detach from the culture surface after incubation with low concentrations of NPs.

In an effort to avoid pH issues arising from citrate ligands, NPs were first incubated with growth media (containing fetal bovine serum) in the absence of cells. This was to allow the formation of a protein corona around the NPs, which could then be isolated from any displaced citrate before applying to the cells. Protein-NP interactions and protein corona formation are topics of principal importance for biological applications of NPs[2, 3, 4, 5, 6, 7, 8]. In this case, we did not attempt to quantify either protein adsorption or citrate displacement, but the adverse pH effects were absent when the pre-incubated NPs were applied to cells. Results of CFAs for B16 and MeWo cell lines treated with 2.6 mg/mL of citrate-stabilized $Ce_{0.1}La_{0.9}F_3/LaF_3$ NPs pre-incubated with serum-containing media are shown in Figure 6.2. These preliminary results were surprising, as the NPs alone were not expected to have a substantial dose enhancement effect at the concentration used. Possible explanations for this enhancement are discussed in the following sections.

6.3 Additional mechanisms of action

Though initial discussions of nanoscintillator-photosensitizer systems have focused almost entirely on radiation dose enhancement by NPs and therapeutic effects of PDT, there are a number of other mechanisms for our particular system that warrant mention in light of our preliminary CFA data.

6.3.1 Cerium redox activity

Besides its use in phosphors and detector applications, cerium is well-known for its high redox activity; for instance, cerium oxide is used industrially as a catalytic converter and hydrocarbon catalyst. Like other lanthanides, cerium is a strong reducing agent, but it is the Ce^{3+}/Ce^{4+} cycle that

is of particular interest. This cycle has been studied primarily in cerium oxides, which readily convert between CeO_2/Ce_2O_3 due to the high oxygen conductivity of the lattice arising from oxygen vacancies. NPs provide a distinct edge for taking advantage of these properties due to their high surface to volume ratio, exposing a substantial fraction of the total cerium content to the environment[9].

Cerium oxide NPs, also known as nanoceria or CONPs, have shown intriguing results when applied to healthy or cancerous cells with or without radiation treatment[10, 11, 12]. Cytotoxicity of CONPs alone was found to be variable and dependent on cell type, pH, NP concentration and aggregation, time of incubation, etc. In blood monocytes, they were determined to induce apoptosis through autophagy and mitochrondrial damage[13], whereas in separate studies using leukocytes[14] and cardiac progenitor cells[15], they were determined to protect against oxidative damage and apoptosis by mimicking the activity of two important antioxidant enzymes, superoxide dismutase and catalase. These enzymes are responsible for scavenging superoxide and hydrogen peroxide, respectively, protecting the cell contents from oxidative stress. CONPs are therefore believed to act as autoregenerative redox agents, having important implications for innate or induced production of reactive oxygen species (ROS).

Celardo *et al*. sought to elucidate a more precise mechanism of CONP antioxidant activity. By doping the NPs with Sm^{3+} (reducing the Ce^{3+}/Ce^{4+} ratio without otherwise altering the NPs significantly), they were able to differentiate between the effects of Ce^{3+}/Ce^{4+} cycling and oxygen vacancies, finding that increasing levels of Sm^{3+} progressively decreased the antioxidant and protective effects of the CONPs[14].

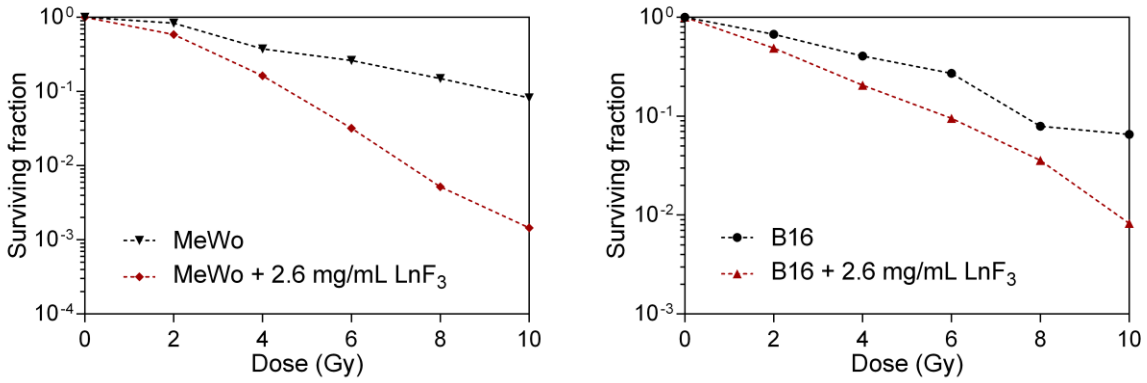

Figure 6.2 CFA results for MeWo and B16 cells treated with citrate-stabilized $Ce_{0.1}La_{0.9}F_3/LaF_3$ NPs that were pre-incubated with serum-containing media prior to X-ray treatment.

Particularly interesting effects were observed when cells were treated with CONPs in combination with X-ray irradiation. Wason *et al*. determined that in the acidic intracellular environment of pancreatic cancer cells, CONPs preferentially convert superoxide radicals into hydrogen peroxide over the conversion of hydrogen peroxide into water, resulting in an accumulation of hydrogen peroxide that is particularly damaging in combination with X-ray irradiation[16]. This radiosensitization effect was marked in comparison to "normal" pancreatic cells, where the CONPs actually provided a degree of radioprotection. A proposed model for hydrogen peroxide dismutation[10] is shown in Figure 6.3.

Briggs *et al*. investigated the dependence on X-ray energies for radiosensitization/radioprotection of rat gliosarcoma cells by CONPs, finding substantial differences between equivalent absorbed doses of 10 MV and 150 kVp X-rays[17]. Radioprotection by CONPs was found to be significant for 10 MV X-ray exposure (energies typical of external

beam radiotherapy) versus 150 kVp X-rays, which caused a degree of radiosensitization, attributed to the production of low-energy secondary electrons by the more prominent photoelectric effect.

Biomolecules may also be affected by CONPs. Kuchma *et al*. reported that CONPs are able to cleave phosphate ester bonds in a manner that is dependent on the availability of Ce^{3+} sites[18]. This phosphatase mimetic activity was found to affect *p*-nitrophenylphosphate, a constituent of ELISA assays, as well as O-phospho-L-tyrosine and adenosine triphosphate (ATP), important biological molecules. Though the CONPs were found to bind plasmid DNA, no hydrolysis products were detected.

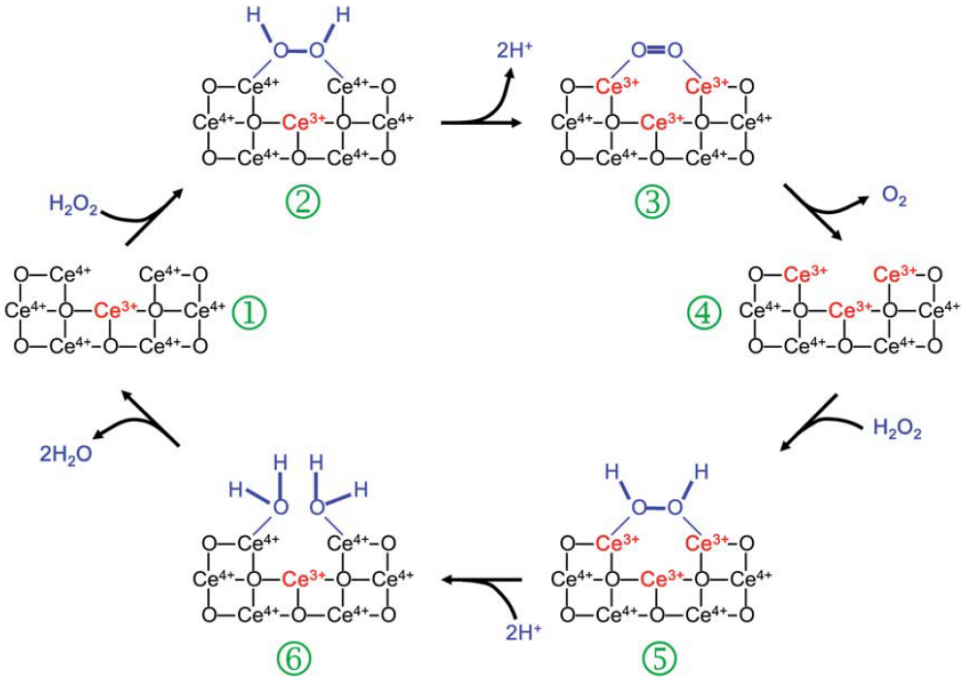

Figure 6.3 A proposed model for the dismutation of hydrogen peroxide at the nanoceria surface. Reprinted with permission from reference [10].

6.3.2 Biological effects of UV

It has long been established that UV radiation is able to do significant damage to living organisms, despite being primarily non-ionizing (the exception being "extreme UV" with energies above 10 eV, or 124 nm). Lower energies of UV are generally categorized as long-wavelength UVA (λ = 320-400 nm, ~3.10-3.87 eV), mid-wavelength UVB (λ = 280-320 nm, ~3.87-4.43 eV) and short-wavelength UVC (λ < 280 nm, >4.43 eV), all of which have been shown to induce distinct photochemical reactions that may produce similar end results to biological targets as ionizing radiation. We are most familiar with the long-term effects of chronic low-level exposure to the UV components of terrestrial solar radiation (comprised of 95% UVA and 5% UVB), making it somewhat difficult to imagine intuitively the possible effects of putting a UV source in contact with or inside of a cell. As the luminescence of $Ce_xLa_{1-x}F_3$ NPs spans the UVA-UVC from roughly 260-450 nm, it seems within the realm of possibility that they may be capable of damaging cells through their scintillation alone, though it was not expected to be a major contributing factor to their efficacy.

Most solar UV is absorbed by the Earth's atmosphere, with UVC contributing to the generation of ozone by photolysis of dioxygen. The accumulated stratospheric ozone provides the most significant protection against solar UV, filtering out the remainder of the UVC and the majority of the UVB, from ~200-315 nm. The relatively small amount of remaining unfiltered UV (~32 W/m^2 at zenith, roughly 3% of total solar irradiance at ground level) is the major contributor to the development of skin cancer, which caused ~80,000 deaths in 2010.

This potential for harm arises by a number of mechanisms. Until somewhat recently, it was generally believed that UVC & UVB were considerably more dangerous than UVA owing to their ability to cause direct DNA damage[19]. UVC is routinely referred to as "germicidal" due to its

ability to drastically diminish the viability of viruses, bacteria and other microorganisms. This is often exploited in laboratory settings to sterilize surfaces, accomplished by prolonged exposure to the 253.7 nm emission line from low-pressure mercury arc lamps in fused quartz housings. It is also used increasingly to disinfect water supplies and forced air systems. The primary mechanism is believed to be formation of pyrimidine dimers, so-called "molecular lesions" between thymine or cytosine bases in DNA that inhibit replication of the genetic material. Besaratinia *et al*. examined the wavelength dependence of UV-induced DNA damage from ~260-350 nm, finding the range of 260-305 nm effective at producing cyclobutane pyrimidine dimers in genomic DNA of mouse embryonic fibroblasts[20].

Vermeulen *et al*. recently investigated the bactericidal effect of several different wavelengths on a clinical strain of *Escherichia coli*, determining 265 & 275 nm were more effective than 250 nm at achieving 100% mortality[21]. As the wavelengths were increased, exponentially larger light doses were required to achieve the same effect. It was also demonstrated that there are many types of covalent bonds in biomolecules that can be broken by photons, with 265 nm (4.68 eV) capable of disrupting nearly all of them, including P-O bonds that are essential to the backbone structure of nucleic acids, and O-H and N-H bonds that are involved in the hydrogen bonding that preserves the tertiary structure of proteins and nucleic acids.

In addition to direct DNA or bond damage by higher energy UV, UVA has been increasingly implicated in causing deleterious effects through indirect damage by production of free radicals or ROS. A number of biomolecules can function as endogenous photosensitizers, through similar mechanisms as those discussed in prior chapters. The group of Wolfgang Baümler at the University of Regensburg monitored singlet oxygen production by some of these molecules through direct detection of singlet oxygen luminescence at 1270 nm after excitation by 355 nm

pulses from an Nd:YAG laser. By comparison to sulfonated perinaphthenone, the quantum yields of singlet oxygen were determined to be 0.54 ± 0.07 for riboflavin, 0.51 ± 0.07 for flavin mononucleotide (FMN) and 0.07 ± 0.02 for flavin adenine dinucleotide (FAD)[22]. The biomolecules β-nicotinamide adenine dinucleotide (NAD), β-nicotinamide adenine dinucleotide phosphate (NADP), urocanic acid and cholesterol did not produce an appreciable signal. Interestingly, these values suggest that on a per molecule basis, riboflavin and FMN are better at producing singlet oxygen in aerated solution than HPD ($\varphi = 0.35$). The same group also observed singlet oxygen luminescence directly from human skin *in vivo* under 355 nm excitation[23]. Most recently, they have demonstrated singlet oxygen generation by polyunsaturated fatty acids exposed to monochromatic UVB at 308 nm (near the peak of $Ce_{0.1}La_{0.9}F_3$ emission), with yields of 0.1-0.15[24]. This photosensitization was deemed to operate differently than Type II mechanisms described previously. In a biological context (such as lipid membranes), generation of ROS can initiate a lipid peroxidation chain reaction due to increased UVA absorption of the oxidized products and amplification of singlet oxygen generation[25].

The case of melanoma is particularly interesting because of the presence of melanin. In humans, melanin production is triggered by exposure to UV, and it functions to protect the skin and underlying structures from further UV damage by strongly absorbing UV and visible light and dissipating it as heat with >99.9% efficiency[26, 27]. Curiously, eumelanin, the most common variety, as well as pheomelanin, have been controversially implicated in the development of melanoma, seemingly in contradiction to its photoprotective role[28]. The presence of melanin was not found to inhibit singlet oxygen production by Ce6[29].

6.3.3 Antineoplastic activity of alendronate

Alendronate and other bisphosphonates (BPs) exhibit antitumoral and antimetastatic properties[30, 31, 32]. The primary mechanism of this activity of nitrogenous bisphosphonates (N-BPs) is believed to be disruption of the metabolic mevalonate pathway[33, 34], though other mevalonate-independent mechanisms are also under investigation[35].

Alendronate in particular has been shown to decrease the growth of PC-3 human prostate cell tumors in mice, as well as inhibiting metastasis to prostate-draining lymph nodes[36]. These results were attributed to interference with angiogenesis and induction of apoptosis, results that have also been observed elsewhere[37]. Other N-BPs were shown to inhibit the cell cycle in human melanoma cell lines[38]. Whether anticancer activity of BPs would be preserved when they are bound to NPs is unknown.

6.4 Conclusions and future directions

Luminescent nanoparticles show great promise for a wide range of applications, and new, more specialized varieties are being developed on a regular basis. Their use for biological applications continues to be complicated by numerous and variable interactions with physiological environments, but significant progress has been made in the last decade toward understanding the underlying mechanisms.

Using time-resolved fluorescence spectroscopy with CdSe/ZnS and CdTe QDs and conjugates to the electron donor dopamine (DA), we have helped elucidate the mechanisms and dynamics of photoinduced QD luminescence enhancement, including the roles of oxygen, surface traps and stabilizing thiols. In the absence of oxygen, electron donation from DA upon exciton formation in the QD led to irreversible quenching of the negatively-charged QDs. In the presence of oxygen, DA produced reactive oxygen species (ROS) that oxidized and passivated the QD

surface traps, leading to photoenhancement. Addition of the antioxidant β-mercaptoethanol (BME) resulted in efficient scavenging of ROS, preventing substantial photoenhancement. CdTe QDs, with luminescence enhanced by stabilizing thiol ligands, were highly quenched by electron donation from DA, a result of cap decay and creation of new unpassivated surface traps. BME was able to replace displaced thiol ligands, but was unable to significantly prevent quenching by DA. A follow-up investigation of CdSe/ZnS QDs and QD-DA conjugates compared the production of different types of ROS using electron paramagnetic resonance (EPR) measurements and a variety of ROS-specific chemical assays. Additionally, QD-DA conjugates were applied to PC12 mammalian pheochromocytoma cells, and their effects on cell metabolism were evaluated, showing the QD-DA conjugates significantly photosensitized the cells relative to QDs alone or DA alone. These results have important implications for biological imaging, biosensor design, and possible photosensitization applications. While Cd-containing QDs remain valuable as *in vitro* and *in vivo* fluorescent probes as well as for many other purposes, their biomedical applications will likely be limited to research environments. New compositions of QDs have increased biocompatibility, and many alternatives are under scrutiny, including luminescent lanthanide-based NPs.

We consequently established methods of synthesizing lanthanide NPs and began investigations of their photoluminescence and conjugation for therapeutic purposes. We have confirmed the occurrence of strong Ce^{3+}-Ce^{3+} energy transfer in $Ce_{0.1}La_{0.9}F_3/LaF_3$ and CeF_3/LaF_3 NPs, and established its role in an energy transfer cascade from the NPs to photosensitizer molecules. The efficiency of transfer was found to be high for reasonable loading amounts of unbound water-soluble photosensitizers, as well as to relatively small amounts of a different variety of covalently bound photosensitizer. We also established alendronate as a surface ligand

that has been thus-far unexploited for this variety of NPs and will provide a basis for further bioconjugation, including stabilizing the NPs and enabling targeting. Beyond investigating the topics discussed earlier in the chapter, there are a number of approaches that may be explored toward optimizing energy transfer and overall effectiveness of a nanoscintillator-photosensitizer system.

For our experiments, the composition $Ce_xLa_{1-x}F_3$ was chosen for the ease of its synthesis in nanoparticle form; in fact, many other Ce^{3+}-doped host materials are superior bulk scintillators in terms of light yield. Though most are water-soluble, precluding ease of preparation and use in aqueous solutions, other candidates have been successfully adapted to the nanoscale. Nanoparticles of lutetium pyrosilicate (β-$Lu_2Si_2O_7$)[39], $BaAl_2B_2O_7$[40], $Sr_2B_2O_5$[41], Sr_2LiSiO_4F[42] and $SrMgSi_2O_6$[43] doped with Ce^{3+} and/or Tb^{3+} have recently been synthesized through high temperature sol-gel routes and possess optical properties that would be superior for excitation of porphyrin-like photosensitizers in the Soret band, though their scintillation potential has not been established. Others such as yttrium gadolinium aluminate ($(Y_{1-x}Gd_x)_3Al_5O_{12}$) NPs doped with Ce^{3+} have emission spectra that can span roughly 500-800 nm[44].

Similarly, chlorin e6 serves as a good proof-of-principle, but may not be the optimal choice of photosensitizer. Many of the more effective porphyrin-like variants have been commercialized, some for the treatment of specific cancer types. Mono-L-aspartyl chlorin e6 (also known as MACE, NPe6 or LS11) is a simple chlorin e6 derivative with improved solubility properties that is approved for PDT of early lung cancer[45]. The modified ring structures of Verteporfin (a benzoporphyrin derivative) and Padoporfin (Pd-bacteriopheophorbide, also known as Tookad or WST09, currently undergoing clinical trials for prostate cancer treatment) broaden their absorbance spectra in the UV, possibly providing better spectral overlap with the NP emission as

well as any biochemical or pharmacological advantages. The structure of the aforementioned molecules is shown in Figure 6.4.

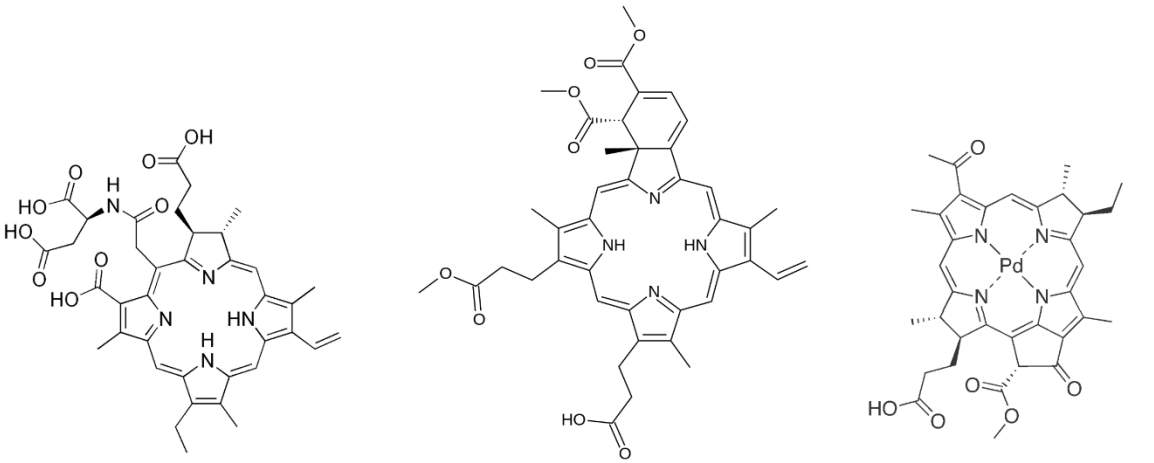

Figure 6.4 Approved photosensitizers currently being used for PDT that are candidates for bioconjugation.

6.5 References

1. Franken, N. A.; Rodermond, H. M.; Stap, J.; Haveman, J.; van Bree, C. Clonogenic assay of cells in vitro. *Nature protocols* **2006,** *1* (5), 2315-9.
2. Pajonk, F.; Vlashi, E.; McBride, W. H. Radiation resistance of cancer stem cells: the 4 R's of radiobiology revisited. *Stem cells (Dayton, Ohio)* **2010,** *28* (4), 639-48.
3. Lundqvist, M.; Stigler, J.; Elia, G.; Lynch, I.; Cedervall, T.; Dawson, K. A. Nanoparticle size and surface properties determine the protein corona with possible implications for biological impacts. *Proceedings of the National Academy of Sciences* **2008,** *105* (38), 14265-14270.
4. Casals, E.; Pfaller, T.; Duschl, A.; Oostingh, G. J.; Puntes, V. Time evolution of the nanoparticle protein corona. *ACS Nano* **2010,** *4* (7), 3623-32.
5. Barran-Berdon, A. L.; Pozzi, D.; Caracciolo, G.; Capriotti, A. L.; Caruso, G.; Cavaliere, C.; Riccioli, A.; Palchetti, S.; Lagana, A. Time evolution of nanoparticle-protein corona in human plasma: relevance for targeted drug delivery. *Langmuir* **2013,** *29* (21), 6485-94.
6. Lundqvist, M. Nanoparticles: Tracking protein corona over time. *Nat Nano* **2013,** *8* (10), 701-702.
7. Mirshafiee, V.; Mahmoudi, M.; Lou, K.; Cheng, J.; Kraft, M. L. Protein corona significantly reduces active targeting yield. *Chemical Communications* **2013,** *49* (25), 2557-2559.
8. Lynch, I.; Dawson, K. A. Protein-nanoparticle interactions. *Nano Today* **2008,** *3* (1–2), 40-47.
9. Sayle, T. X.; Molinari, M.; Das, S.; Bhatta, U. M.; Mobus, G.; Parker, S. C.; Seal, S.; Sayle, D. C. Environment-mediated structure, surface redox activity and reactivity of ceria nanoparticles. *Nanoscale* **2013,** *5* (13), 6063-73.
10. Celardo, I.; Pedersen, J. Z.; Traversa, E.; Ghibelli, L. Pharmacological potential of cerium oxide nanoparticles. *Nanoscale* **2011,** *3* (4), 1411-1420.
11. Celardo, I.; Traversa, E.; Ghibelli, L. Cerium oxide nanoparticles: a promise for applications in therapy. *Journal of experimental therapeutics & oncology* **2011,** *9* (1), 47-51.
12. Wason, M. S.; Zhao, J. Cerium oxide nanoparticles: potential applications for cancer and other diseases. *American journal of translational research* **2013,** *5* (2), 126-31.
13. Hussain, S.; Al-Nsour, F.; Rice, A. B.; Marshburn, J.; Yingling, B.; Ji, Z.; Zink, J. I.; Walker, N. J.; Garantziotis, S. Cerium dioxide nanoparticles induce apoptosis and autophagy in human peripheral blood monocytes. *ACS Nano* **2012,** *6* (7), 5820-9.
14. Celardo, I.; De Nicola, M.; Mandoli, C.; Pedersen, J. Z.; Traversa, E.; Ghibelli, L. Ce(3)+ ions determine redox-dependent anti-apoptotic effect of cerium oxide nanoparticles. *ACS Nano* **2011,** *5* (6), 4537-49.
15. Pagliari, F.; Mandoli, C.; Forte, G.; Magnani, E.; Pagliari, S.; Nardone, G.; Licoccia, S.; Minieri, M.; Di Nardo, P.; Traversa, E. Cerium oxide nanoparticles protect cardiac progenitor cells from oxidative stress. *ACS Nano* **2012,** *6* (5), 3767-75.
16. Wason, M. S.; Colon, J.; Das, S.; Seal, S.; Turkson, J.; Zhao, J.; Baker, C. H. Sensitization of pancreatic cancer cells to radiation by cerium oxide nanoparticle-induced ROS production. *Nanomedicine: Nanotechnology, Biology and Medicine* **2013,** *9* (4), 558-569.
17. Briggs, A.; Corde, S.; Oktaria, S.; Brown, R.; Rosenfeld, A.; Lerch, M.; Konstantinov, K.; Tehei, M. Cerium oxide nanoparticles: influence of the high-Z component revealed on radioresistant 9L cell survival under X-ray irradiation. *Nanomedicine* **2013,** *9* (7), 1098-105.
18. Kuchma, M. H.; Komanski, C. B.; Colon, J.; Teblum, A.; Masunov, A. E.; Alvarado, B.; Babu, S.; Seal, S.; Summy, J.; Baker, C. H. Phosphate ester hydrolysis of biologically relevant

molecules by cerium oxide nanoparticles. *Nanomedicine: Nanotechnology, Biology and Medicine* **2010,** *6* (6), 738-744.
19. Pfeifer, G. P.; Besaratinia, A. UV wavelength-dependent DNA damage and human non-melanoma and melanoma skin cancer. *Photochemical & Photobiological Sciences* **2012,** *11* (1), 90-97.
20. Besaratinia, A.; Yoon, J. I.; Schroeder, C.; Bradforth, S. E.; Cockburn, M.; Pfeifer, G. P. Wavelength dependence of ultraviolet radiation-induced DNA damage as determined by laser irradiation suggests that cyclobutane pyrimidine dimers are the principal DNA lesions produced by terrestrial sunlight. *FASEB journal : official publication of the Federation of American Societies for Experimental Biology* **2011,** *25* (9), 3079-91.
21. Vermeulen, N.; Keeler, W. J.; Nandakumar, K.; Leung, K. T. The bactericidal effect of ultraviolet and visible light on Escherichia coli. *Biotechnology and Bioengineering* **2008,** *99* (3), 550-556.
22. Baier, J.; Maisch, T.; Maier, M.; Engel, E.; Landthaler, M.; Baumler, W. Singlet oxygen generation by UVA light exposure of endogenous photosensitizers. *Biophys J* **2006,** *91* (4), 1452-9.
23. Baier, J.; Maisch, T.; Maier, M.; Landthaler, M.; Baumler, W. Direct detection of singlet oxygen generated by UVA irradiation in human cells and skin. *J Invest Dermatol* **2007,** *127* (6), 1498-506.
24. Regensburger, J.; Knak, A.; Maisch, T.; Landthaler, M.; Bäumler, W. Fatty acids and vitamins generate singlet oxygen under UVB irradiation. *Experimental Dermatology* **2012,** *21* (2), 135-139.
25. Baier, J.; Maisch, T.; Regensburger, J.; Pöllmann, C.; Bäumler, W. Optical detection of singlet oxygen produced by fatty acids and phospholipids under ultraviolet A irradiation. *BIOMEDO* **2008,** *13* (4), 044029-044029-7.
26. Brenner, M.; Hearing, V. J. The protective role of melanin against UV damage in human skin. *Photochemistry and photobiology* **2008,** *84* (3), 539-549.
27. Meredith, P.; Riesz, J. Radiative relaxation quantum yields for synthetic eumelanin. *Photochemistry and Photobiology* **2007,** *79* (2), 211-216.
28. Schmitz, S.; Thomas, P. D.; Allen, T. M.; Poznansky, M. J.; Jimbow, K. Dual role of melanins and melanin precursors as photoprotective and phototoxic agents: inhibition of ultraviolet radiation-induced lipid peroxidation. *Photochem Photobiol* **1995,** *61* (6), 650-5.
29. Parkhots, M. V.; Lapina, V. A.; Butorina, D. N.; Sobchuk, A. N.; Lepeshkevich, S. V.; Petrov, P. T.; Krasnovskii, A. A., Jr.; Dzhagarov, B. M. Spectral and photochemical characteristics of the photosensitizers chlorin e 6 and photolon in the presence of melanin. *Optics and Spectroscopy* **2005,** *98* (3), 374-382.
30. Clézardin, P. Bisphosphonates' antitumor activity: An unravelled side of a multifaceted drug class. *Bone* **2011,** *48* (1), 71-79.
31. Green, J. R. Antitumor effects of bisphosphonates. *Cancer* **2003,** *97* (S3), 840-847.
32. Muller, S.; Migianu, E.; Lecouvey, M.; Kraemer, M.; Oudar, O. Alendronate inhibits proliferation and invasion of human epidermoid carcinoma cells in vitro. *Anticancer Res* **2005,** *25* (4), 2655-60.
33. Fournier, P. G.; Stresing, V.; Ebetino, F. H.; Clezardin, P. How do bisphosphonates inhibit bone metastasis in vivo? *Neoplasia (New York, N.Y.)* **2010,** *12* (7), 571-8.

34. Virtanen, S. S.; Vaananen, H. K.; Harkonen, P. L.; Lakkakorpi, P. T. Alendronate inhibits invasion of PC-3 prostate cancer cells by affecting the mevalonate pathway. *Cancer Res* **2002,** *62* (9), 2708-14.
35. Tatsuda, Y.; Iguchi, K.; Usui, S.; Suzui, M.; Hirano, K. Protein kinase C is inhibited by bisphosphonates in prostate cancer PC-3 cells. *European journal of pharmacology* **2010,** *627* (1-3), 348-53.
36. Tuomela, J.; Valta, M.; Vaananen, K.; Harkonen, P. Alendronate decreases orthotopic PC-3 prostate tumor growth and metastasis to prostate-draining lymph nodes in nude mice. *BMC Cancer* **2008,** *8* (1), 81.
37. Stresing, V.; Fournier, P. G.; Bellahcène, A.; Benzaïd, I.; Mönkkönen, H.; Colombel, M.; Ebetino, F. H.; Castronovo, V.; Clézardin, P. Nitrogen-containing bisphosphonates can inhibit angiogenesis in vivo without the involvement of farnesyl pyrophosphate synthase. *Bone* **2011,** *48* (2), 259-266.
38. Forsea, A. M.; Muller, C.; Riebeling, C.; Orfanos, C. E.; Geilen, C. C. Nitrogen-containing bisphosphonates inhibit cell cycle progression in human melanoma cells. *Br J Cancer* **2004,** *91* (4), 803-810.
39. Li, Y.; You, B.; Zhang, W.; Yin, M. Luminescent properties of β-$Lu_2Si_2O_7$:RE^{3+} (RE=Ce, Tb) nanoparticles by sol-gel method. *Journal of Rare Earths* **2008,** *26* (3), 455-458.
40. Sun, J.; Sun, Y.; Lai, J.; Xia, Z.; Du, H. Luminescence properties and energy transfer investigations of $BaAl_2B_2O_7$:Ce^{3+},Tb^{3+} phosphors. *Journal of Luminescence* **2012,** *132* (11), 3048-3052.
41. Sun, J.; Lai, J.; Zhu, J.; Xia, Z.; Du, H. Luminescence properties and energy transfer investigations of $Sr_2B_2O_5$:Ce^{3+},Tb^{3+} phosphors. *Ceramics International* **2012,** *38* (7), 5341-5345.
42. Zhang, X.; Seo, H. J. Photoluminescence properties of Ce^{3+}, Mn^{2+} co-doped Sr_2LiSiO_4F phosphor. *Physica B: Condensed Matter* **2010,** *405* (10), 2436-2439.
43. Fu, X.; Fang, L.; Niu, S.; Zhang, H. Luminescence properties and energy transfer investigations of $SrMgSi_2O_6$:Ce,Tb phosphors. *Journal of Luminescence* **2013,** *142* (0), 163-166.
44. Uysal Satilmis, S.; Ege, A.; Ayvacikli, M.; Khatab, A.; Ekdal, E.; Popovici, E. J.; Henini, M.; Can, N. Luminescence characterization of cerium doped yttrium gadolinium aluminate phosphors. *Optical Materials* **2012,** *34* (11), 1921-1925.
45. O'Connor, A. E.; Gallagher, W. M.; Byrne, A. T. Porphyrin and nonporphyrin photosensitizers in oncology: preclinical and clinical advances in photodynamic therapy. *Photochem Photobiol* **2009,** *85* (5), 1053-74.

APPENDIX A

Supplementary information for Chapter 2

CdSeZnS	A_1	τ_1 (ns)	β	A_2	τ_2 (ns)	bgrnd (cnts)	χ^2
0	7341.5	1.151	0.507	8134.9	0.028	2.8	0.942
1	9361.6	0.997	0.493	11970.3	0.028	2.9	0.981
2	10569.3	0.849	0.482	12406.3	0.046	3.4	1.074
3	10496.4	0.761	0.473	14028	0.03	3	1.118
4	9873.8	0.764	0.476	13356.4	0.034	2.8	1.042
5	9562.8	0.729	0.472	12273.4	0.036	2.8	1.035
6	9936.1	0.651	0.461	12616.8	0.035	2.6	1.037
7	9650.7	0.67	0.465	11210.6	0.043	2.5	1.095
8	9688.7	0.674	0.464	13626.8	0.029	2.6	1.024
9	9601.3	0.726	0.468	15428.5	0.001	3.1	1.007
10	9086	0.709	0.469	12761.3	0.031	2.7	1.029
11	9505.7	0.653	0.49	12597.8	0.035	2.7	0.973
12	10146.9	0.574	0.447	13379.9	0.025	1.8	1.033
13	8982.9	0.661	0.462	12589.9	0.023	2.3	0.974
14	8880.8	0.662	0.462	13004.8	0.022	2.4	0.99
15	8931.8	0.61	0.454	12590.9	0.017	1.9	0.982
16	8439.8	0.664	0.464	12233	0.027	2.4	1.046
17	8421.8	0.647	0.461	11776.2	0.029	2.3	1.033
18	8322.6	0.648	0.461	12202.6	0.026	2.2	0.983
19	8089.6	0.664	0.464	10933.2	0.029	2.2	0.961
CdSeZnS-BME	A_1	τ_1 (ns)	β	A_2	τ_2 (ns)	bgrnd (cnts)	χ^2
0	15877.4	0.489	0.463	23359.6	0.063	5	1.163
1	9909.9	0.52	0.456	20725.1	0.057	3.4	1.132
2	10130.4	0.576	0.474	19439.6	0.053	3.2	1.173
3	11096	0.545	0.473	19618	0.059	3.8	1.168
4	10322.5	0.504	0.46	20510.6	0.056	3.2	1.15
5	9654.9	0.542	0.463	19699.5	0.064	3.7	1.084
6	9390.1	0.511	0.451	20228.6	0.067	3.1	1.215
7	8918.6	0.679	0.474	20059.8	0.075	4.1	1.166
8	8519.8	0.735	0.482	19661.8	0.079	4.5	1.198
9	9570.7	0.72	0.474	20158.8	0.077	4.2	1.347
10	9545.8	0.788	0.483	21657.6	0.077	4.7	1.214
11	9639.5	0.81	0.485	22676.2	0.076	5	1.235
12	9809.9	0.875	0.493	23099.9	0.079	5.9	1.243
13	9219.5	0.787	0.483	22068.8	0.076	4.9	1.271
14	9950.6	0.8	0.482	21610.2	0.08	5	1.207
15	10281.9	0.794	0.479	23631.9	0.071	4.9	1.168
16	10996.6	0.844	0.481	23356.5	0.078	5.1	1.245
17	12029.8	0.835	0.478	23899.8	0.079	5.8	1.279

18	11284.9	0.836	0.488	24602.5	0.08	6.6	1.223
19	11069.4	0.824	0.479	23419.8	0.077	5.4	1.256
CdSeZnS-HighDA	A_1	τ_1 (ns)	β	A_2	τ_2 (ns)	bgrnd (cnts)	χ^2
0	3275.8	1.253	0.47	7561.7	0.051	0.7	0.906
1	3485.8	1.738	0.496	7481.1	0.056	0.9	0.852
2	4030	2.823	0.542	6697	0.077	0.7	0.909
3	4742.4	3.432	0.568	7452.7	0.075	1.1	0.906
4	5000.6	4.755	0.612	6829.6	0.086	1.4	0.972
5	4784.7	4.728	0.61	6800.2	0.079	1.2	1
6	4255.4	5.734	0.64	4884.9	0.092	1.3	0.988
7	3773.2	6.295	0.655	3948	0.093	1.3	0.94
8	3518.5	6.188	0.651	4534.9	0.073	1.1	0.947
9	2981.8	6.975	0.675	2934.1	0.094	1.3	0.923
10	3072	6.842	0.668	3006	0.096	1.3	0.949
11	3075.7	6.907	0.67	3838.2	0.069	1.2	0.944
12	2702.6	7.03	0.672	2540.7	0.086	1.1	0.918
13	2989.6	6.605	0.661	2679.7	0.113	1.2	0.941
14	3090.2	6.887	0.669	3191.7	0.085	1.4	0.941
15	4032.8	6.742	0.666	4984.1	0.085	2	0.942
16	3839.6	7.133	0.674	3661.7	0.099	1.9	0.967
17	3548.2	7.366	0.679	2889.5	0.122	1.9	1.003
18	3352.1	7.62	0.687	2908.8	0.109	2	1.006
19	3804.6	6.99	0.666	4261.4	0.078	1.8	0.965
CdSeZnS-LowDA	A_1	τ_1 (ns)	β	A_2	τ_2 (ns)	bgrnd (cnts)	χ^2
0	3834.5	1.339	0.478	7928.4	0.059	1.1	0.87
1	4350.1	2.399	0.527	7515.6	0.074	1	0.919
2	4661.3	3.041	0.551	7243.4	0.084	1	1.005
3	4867.3	4.773	0.608	7082.1	0.074	1	0.982
4	5195.6	3.561	0.57	8203.7	0.068	0.9	1.048
5	4785.9	5.876	0.642	5560.3	0.084	1.4	0.977
6	5137.2	4.687	0.605	7108.8	0.081	1.2	1.084
7	3149.8	6.879	0.664	2831.1	0.107	1	0.947
8	3459.2	6.355	0.651	4757.3	0.067	1	0.984
9	3588.8	5.714	0.638	4327.7	0.095	1.2	0.99
10	2962.7	6.639	0.661	3081.6	0.107	1.3	0.947
11	2800.2	6.829	0.667	2843.5	0.106	1.5	0.947
12	2858.7	6.864	0.665	3566.7	0.077	1.2	1.012
13	3035.8	6.856	0.664	3071.7	0.111	1.4	0.904
14	3139.5	6.846	0.662	3251.9	0.098	1.4	0.99
15	3477.2	6.723	0.661	3977.6	0.098	1.9	0.977
16	3477	7.075	0.669	4022.4	0.084	2	0.935
17	3319.3	7.596	0.684	4155.9	0.075	2.2	1.032
18	3986.7	6.697	0.657	5172.5	0.084	2.3	0.986
19	4029.9	7.486	0.68	4452.7	0.107	3	0.995

CdSeZnS-DA-BME	A_1	τ_1 (ns)	β	A_2	τ_2 (ns)	bgrnd (cnts)	χ^2
0	3007.6	1.272	0.463	9876.5	0.06	1.6	0.888
1	3142.1	1.73	0.489	9847.7	0.062	1.6	0.86
2	3080.2	2.25	0.516	8676.1	0.079	1.7	0.957
3	2980.3	2.56	0.53	8953.5	0.08	1.6	1.06
4	2786.1	2.457	0.522	8441.2	0.085	1.7	0.904
5	2515.6	2.391	0.518	8153	0.085	1.5	0.917
6	2468.7	2.203	0.506	8744	0.078	1.4	0.936
7	2198.1	1.942	0.494	7876.7	0.081	1.3	1.015
8	2002.6	1.595	0.474	7976.8	0.072	1.4	0.954
9	1948.4	1.913	0.491	7939.7	0.076	1.2	0.943
10	1841.3	2.023	0.497	7734.8	0.079	1.2	0.88
11	1738	1.19	0.444	8363.5	0.058	1.2	0.98
12	1787.5	0.993	0.428	8912.1	0.045	1	0.854
13	1685.8	1.085	0.435	7503.1	0.061	1	0.899
14	1634.3	1.18	0.445	7436.5	0.065	1.1	0.894
15	1562.6	1.232	0.447	7373	0.062	0.9	0.925
16	1567.3	1.248	0.446	7204.2	0.068	0.7	0.949
17	1450.9	1.329	0.456	7082	0.071	0.9	0.908
18	1465.6	1.021	0.43	7132.1	0.062	0.8	0.915
19	1487	0.924	0.423	7251.5	0.064	0.9	0.912

CdTe	A	τ (ns)	β	bgrnd (dec)	χ^2
0	963.3	17.568	0.842	0.3	1.847
1	410.7	17.8608	0.853	0.4	0.773
2	383.3	17.9096	0.85	0.3	0.762
3	324.3	18.8856	0.874	0.4	0.795
4	289.3	18.2512	0.857	0.3	0.782
5	263.5	18.1048	0.849	0.3	0.711
6	246.1	19.3736	0.884	0.4	0.704
7	257.1	18.788	0.871	0.3	0.708
8	261.5	18.544	0.867	0.3	0.736
9	271.2	18.6416	0.868	0.3	0.717
10	275.7	17.9096	0.848	0.3	0.742
11	247.8	18.4952	0.857	0.3	0.726
12	220.4	19.3736	0.881	0.3	0.731
13	206.4	19.276	0.883	0.3	0.739
14	200.6	19.3248	0.884	0.3	0.749
15	187.3	18.7392	0.871	0.3	0.75
16	177.7	19.1296	0.881	0.3	0.673
17	186.6	19.6664	0.889	0.3	0.67
18	180	17.9096	0.844	0.2	0.684

CdTe-BME	A	τ (ns)	β	bgrnd (dec)	χ^2
0	324.3	6.602	0.628	0.1	0.701
1	323.5	6.952	0.629	0.1	0.73
2	316.7	7.443	0.646	0.1	0.728
3	359	7.345	0.644	0.1	0.682
4	386.5	7.137	0.639	0.1	0.873
5	411.4	6.467	0.611	0	0.781
6	400.7	6.694	0.623	0.1	0.699
7	413.7	7.087	0.643	0.2	0.794
8	426.8	6.8	0.628	0.1	0.728
9	402	6.648	0.627	0.2	0.775
10	389.8	6.809	0.629	0.1	0.744
11	360.4	6.471	0.614	0	0.754
12	381.1	6.71	0.626	0.2	0.683
13	368.6	6.549	0.612	-0.1	0.742
14	337.1	7.145	0.637	0.2	0.732
15	300.5	7.059	0.634	0.2	0.622
16	264.4	7.229	0.637	0.2	0.664
17	311.6	7.208	0.626	0	0.762
18	345.5	7.2	0.63	0	0.792
CdTe-HighDA	A	τ (ns)	β	bgrnd (dec)	χ^2
0	1156	0.009	0.22	-1.5	0.766
1	1179.2	0.015	0.228	-1.5	0.738
2	1187.1	0.014	0.219	-2.2	0.979
3	733.9	0.105	0.277	-1.4	0.786
4	550	0.165	0.298	-1.2	0.887
5	412.8	0.303	0.323	-1.2	0.805
6	283.3	1.053	0.404	-0.8	0.743
7	223.3	1.163	0.417	-0.4	0.723
8	230.1	1.491	0.434	-0.9	0.862
9	185.4	3.22	0.561	-0.1	0.831
10	186.1	2.954	0.541	-0.1	0.841
11	200.1	2.097	0.474	-0.7	0.898
12	149.5	3.932	0.613	0.3	0.684
13	133.4	4.503	0.629	0.2	0.74
14	134.5	4.32	0.598	-0.1	0.83
15	137.1	5.846	0.699	0.5	0.662
16	132.4	4.32	0.593	0	0.761
17	163.4	3.645	0.576	0.2	0.75
18	127.6	4.754	0.616	0	0.8
19	121.4	4.394	0.601	0.1	0.702

CdTe-LowDA	A	τ (ns)	β	bgrnd (dec)	χ^2
0	359.7	0.246	0.321	-0.7	0.749
1	199.8	1.531	0.452	-0.4	0.771
2	227.9	0.966	0.407	-0.6	0.784
3	272.1	0.994	0.414	-0.5	0.83
4	185.9	3.596	0.596	0.3	0.747
5	167.5	3.304	0.55	0	0.711
6	147.3	3.631	0.585	0.2	0.72
7	145.2	3.953	0.577	0	0.741
8	128	3.958	0.585	0.1	0.833
9	135.3	4.29	0.603	0.2	0.62
10	125.3	5.053	0.62	0.2	0.697
11	116.4	5.104	0.624	0.2	0.722
12	119.3	4.778	0.622	0.3	0.68
13	103.2	5.148	0.642	0.3	0.667
14	96.3	5.559	0.681	0.4	0.728
15	102.2	4.334	0.596	0.2	0.73
16	156.9	5.382	0.66	0.4	0.65
17	160.1	4.566	0.584	0.1	0.728
18	108	4.79	0.606	0.2	0.725
19	14.3	4.972	0.616	0.1	0.733
CdTe-HighDA-BME	A	τ (ns)	β	bgrnd (dec)	χ^2
0	1459.8	0.099	0.295	-1.2	0.925
1	661.2	0.199	0.301	-1.6	0.823
2	339.7	1.192	0.426	-0.6	0.842
3	289.4	2.23	0.495	-0.2	0.842
4	252.6	3.489	0.556	-0.2	0.818
5	244.8	2.893	0.52	-0.3	0.843
6	198.8	4.431	0.613	0.2	0.76
7	191.8	3.35	0.549	-0.1	0.743
8	190.9	5.086	0.635	0.1	0.781
9	181.2	3.18	0.525	-0.3	0.751
10	174.3	3.427	0.542	-0.1	0.688
11	150	4.946	0.623	0.2	0.759
12	153.8	5.103	0.629	0.1	0.812
13	165.3	3.071	0.523	-0.4	0.805
14	147.9	4.295	0.596	0.1	0.704
15	143.6	3.724	0.56	-0.1	0.79
16	128.6	5.786	0.678	0.3	0.725
17	141.7	5.26	0.649	0.2	0.684
18	136.4	4.278	0.594	-0.1	0.879
19	151.1	2.817	0.51	-0.4	0.805

APPENDIX B

Considerations for UV spectroscopy

Spectroscopic measurements in the ultraviolet (UV) region are complicated by the absorption of light by many species in this region. Typical spectrophotometers can measure UV wavelengths ≥ 190 nm – shorter wavelengths are referred to as vacuum UV since molecular oxygen and water vapor in air absorb them strongly, and thus vacuum is required for accurate measurements.

Most σ-bonded, π-bonded and lone pair electronic transitions of simple unconjugated organic chromophores occur between 150-190 nm, so do not interfere with our routine measurements. Notable exceptions include ligands and some solvents. Acetone is a solvent commonly used for precipitating and cleaning nanoparticles. Dimethyl sulfoxide (DMSO) is routinely used for making stock solutions of photosensitizer and other hydrophobic drugs, and to encourage efficient bioconjugation reactions. Ethanol is preferred due its relative transparency throughout the UV-visible range. Figure B1 shows the absorbance spectra of a plastic UVette, absolute ethanol, and 0.002% v/v solutions of DMSO and H_2O_2.

Common organic ligands may also possess significant UV absorption. Those containing carboxylic acid or carboxylate groups, R-COOH or $R\text{-}COO^-$, such as citric acid and 6-aminocaproic acid, absorb near 210 nm due to $n \rightarrow \pi^*$ transitions. Absorbance spectra of citric acid, 6-aminocaproic acid and alendronic acid dissolved in water are shown in Figure B2.

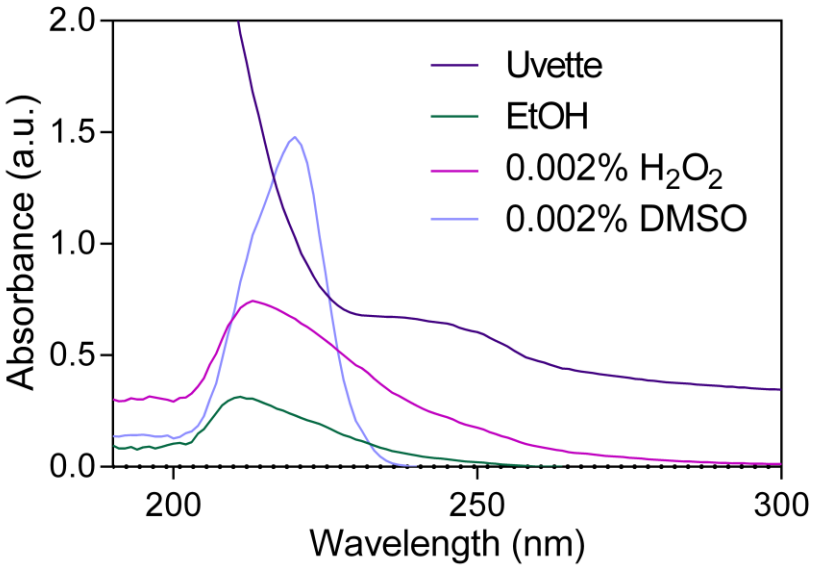

Figure B1 Absorbance spectra of a water-filled plastic UVette and selected solvents/species.

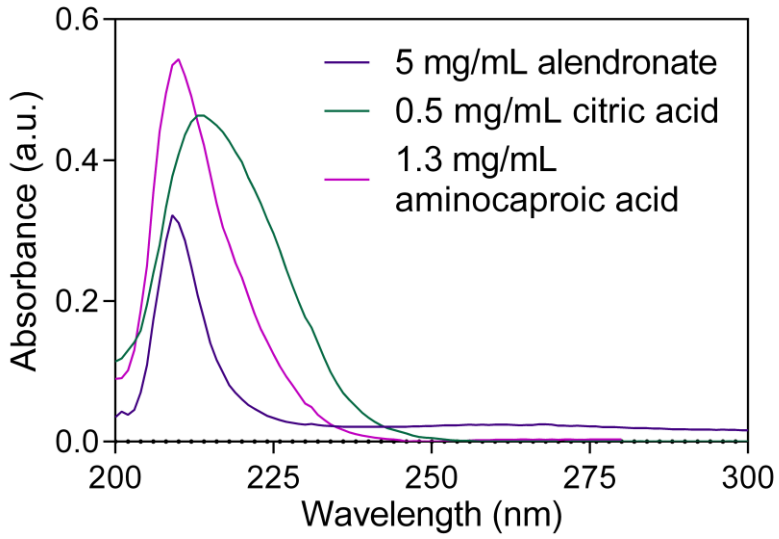

Figure B2 Absorbance spectra of some ligands used in this work. Aminocaproic acid and citric acid were used for hydrothermal synthesis and stabilization of LnNPs, and alendronate was used for ligand exchange reactions and bioconjugation. Note that the shape of the absorbance of these molecules does vary with concentration.

APPENDIX C

Supplementary information for Chapter 5

Characterization and photoluminescence of ACA-stabilized NPs and DPIX-DS complexes

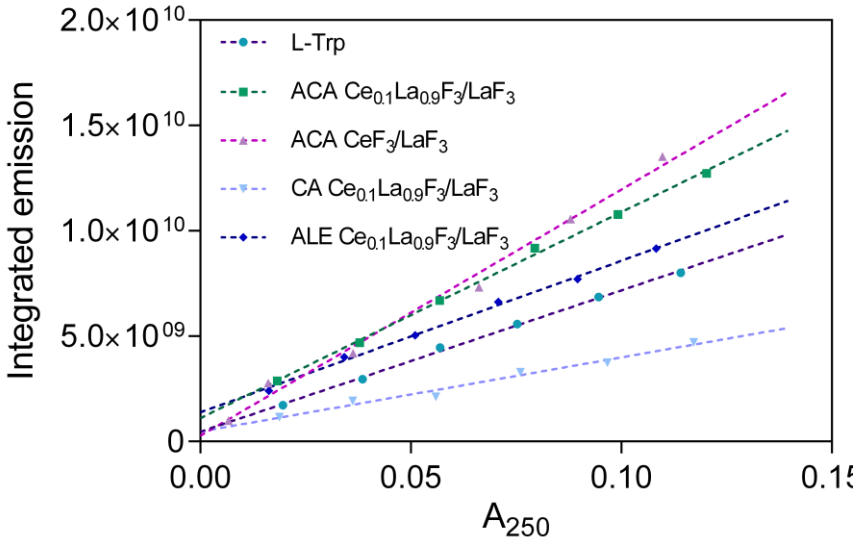

Figure C1 Data for QY measurements of ACA-, CA- and ALE-NPs compared to an L-tryptophan standard.

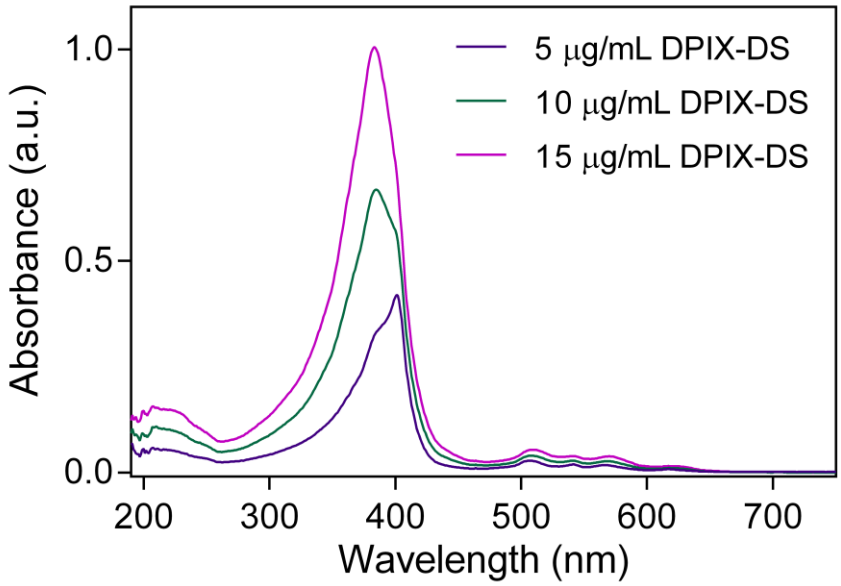

Figure C2 Absorbance spectra for different concentrations of deuteroporphyrin IX 2,4-disulfonic acid dihydrochloride in water, taken in a 1 cm path length "UVette."

Table C1 Physical characteristics of ACA-NPs. NPs were approximated as thin cylinders for surface area and volume calculations.

ACA-NP composition	Diameter (nm)	Thickness (nm)	Surface area (nm^2)	Volume (nm^3)
$Ce_{0.1}La_{0.9}F_3/LaF_3$	11.9	3.2	342.1	355.9
CeF_3/LaF_3	16.4	4.3	644.0	908.3

Table C2 Concentrations and relative amounts for all samples of ACA-NPs with DPIX-DS.

ACA-NP composition	NPs (μg/mL)	NPs (nM)	DPIX-DS (% w/w)	DPIX-DS (μg/mL)	DPIX-DS (μM)	DPIX-DS/NP	DPIX-DS/nm^2
$Ce_{0.1}La_{0.9}F_3$/LaF$_3$	50	39.2	1	0.5	0.67	17	0.05
	50	39.2	2	1	1.34	34	0.10
	50	39.2	3	1.5	2.02	51	0.15
	50	39.2	4	2	2.69	69	0.20
	50	39.2	5	2.5	3.36	86	0.25
	50	39.2	6	3	4.03	103	0.30
CeF$_3$/LaF$_3$	10	3.0	2	0.2	0.27	89	0.14
	10	3.0	4	0.4	0.54	178	0.28
	10	3.0	6	0.6	0.81	267	0.41
	10	3.0	8	0.8	1.08	356	0.55
	10	3.0	10	1	1.34	445	0.69
	10	3.0	12	1.2	1.61	534	0.83

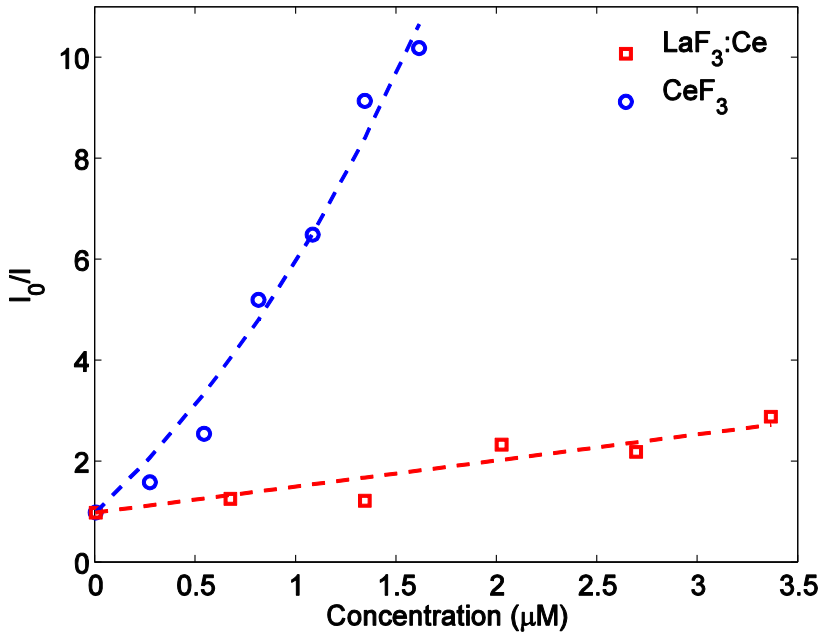

Figure C3 Stern-Volmer fitting of PL quenching data for $Ce_{0.1}La_{0.9}F_3$/LaF$_3$ NPs (red squares and dotted line) and CeF$_3$/LaF$_3$ NPs (blue circles and dotted line) after addition of DPIX-DS at indicated concentrations. Fit parameters given in the main text.

Table C3 TCSPC fit results for Ce^{3+} emission of ACA-NPs at different wavelengths with different amounts of DPIX-DS (shown in % w/w). All exponentials are shown with amplitudes as percentages of the positive decay components, with the exception of negative amplitude components (bounded by boxes), which were not included in the calculation of average lifetimes. Confidence intervals for lifetimes greater than a few ns were typically less than ±5% of the fitted value and less than ±1% for lifetimes greater than ~25 ns. For shorter lifetimes, confidence intervals were larger, up to ±50%.

$La_{0.9}F_3Ce_{0.1}/LaF_3$	I_1 (%)	τ_1 (ns)	I_2 (%)	τ_2 (ns)	I_3 (%)	τ_3 (ns)	I_4 (%)	τ_4 (ns)	$\langle\tau\rangle$ (ns)	χ^2
300 nm	—	—	**1.2**	**0.74**	**20.3**	**8.1**	**78.5**	**23.8**	**20.3**	**0.92**
+1% DPIX	—	—	2.0	0.79	23.3	7.9	74.7	23.4	19.3	0.95
+2% DPIX	—	—	2.6	0.71	22.2	6.8	75.2	22.1	18.1	0.99
+3% DPIX	—	—	5.5	0.76	24.3	6.0	70.2	20.3	15.7	1.06
+4% DPIX	—	—	4.6	0.71	21.5	5.8	73.9	20.5	16.4	1.06
+5% DPIX	—	—	12.9	0.63	31.3	4.1	55.8	16.8	10.2	1.06
+6% DPIX	—	—	21.1	0.52	40.6	2.6	38.3	11.8	5.7	0.91
330 nm	-326.4	2.2	—	—	—	—	**100.0**	**32.2**	**32.5**	**1.00**
+1% DPIX	-196.1	3.6	—	—	24.2	19.6	75.8	34.8	31.5	0.97
+2% DPIX	-127.4	4.5	—	—	24.4	19.6	75.6	34.8	31.4	0.95
+3% DPIX	—	—	1.0	0.48	19.7	12.7	79.3	31.4	27.4	1.00
+4% DPIX	—	—	0.80	0.26	17.9	15.9	81.3	32.0	28.8	0.94
+5% DPIX	—	—	2.5	0.47	15.3	8.4	82.2	28.3	24.6	1.00
+6% DPIX			8.6	0.57	21.5	4.7	69.9	28.9	21.2	1.01
380 nm	-329.9	2.3	—	—	—	—	**100.0**	**38.4**	**38.8**	**1.01**
+1% DPIX	-145.1	2.2	—	—	—	—	100.0	38.1	38.3	1.03
+2% DPIX	-191.8	2.5	—	—	—	—	100.0	38.7	39.0	1.03
+3% DPIX	—	—	0.17	0.33	17.3	20.4	41.6	41.6	37.8	1.06
+4% DPIX	—	—	—	—	44.4	29.6	55.6	46.8	39.2	0.95
+5% DPIX	—	—	0.60	0.50	10.3	14.4	89.1	40.4	37.5	0.99
+6% DPIX	—	—	1.4	0.66	5.2	7.4	93.4	42.7	40.3	1.00
CeF_3/LaF_3	I_1 (%)	τ_1 (ns)	I_2 (%)	τ_2 (ns)	I_3 (%)	τ_3 (ns)	I_4 (%)	τ_4 (ns)	$\langle\tau\rangle$ (ns)	χ^2
300 nm	**9.4**	**0.34**	**26.6**	**1.8**	**34.8**	**6.4**	**29.2**	**19.1**	**8.3**	**0.93**
+2% DPIX	11.0	0.31	25.4	1.6	35.0	6.0	28.6	18.3	7.8	0.94
+4% DPIX	17.3	0.33	31.4	1.5	27.6	5.5	23.7	15.8	5.8	0.99

+6% DPIX	36.7	0.33	46.3	1.3	17.0	5.4	—	—	1.6	0.95
+8% DPIX	37.2	0.33	47.2	1.3	15.6	6.1	—	—	1.7	1.00
+10% DPIX	38.8	0.24	50.0	0.91	11.2	3.0	—	—	0.9	1.00
+12% DPIX	40.1	0.21	46.1	0.69	13.8	2.3	—	—	0.7	1.04
330 nm	-561.0	0.31	—	—	**30.0**	**10.1**	**70.0**	**29.9**	**24.0**	**0.98**
+2% DPIX	—	—	3.3	2.5	33.2	11.5	63.5	30.5	23.3	0.92
+4% DPIX	—	—	6.6	1.3	36.1	9.5	57.3	29.2	20.2	0.99
+6% DPIX	11.0	0.43	24.5	1.6	22.2	7.5	42.3	39.4	18.8	0.94
+8% DPIX	11.2	0.41	25.0	1.6	21.5	7.4	42.3	39.8	18.9	0.97
+10% DPIX	13.1	0.36	23.4	1.1	8.6	3.7	54.9	43.6	24.6	0.98
+12% DPIX	16.3	0.35	17.2	1.1	4.6	5.1	61.9	44.0	27.7	0.92
380 nm	-1080.0	0.78	—	—	**26.3**	**15.0**	**73.7**	**37.3**	**31.8**	**1.02**
+2% DPIX	-499.0	1.1	—	—	23.8	16.9	76.2	38.8	34.0	1.01
+4% DPIX	—	—	2.5	3.9	27.2	15.6	70.3	39.6	32.2	0.98
+6% DPIX	—	—	5.4	1.1	12.3	8.3	82.3	42.1	35.7	0.98
+8% DPIX	—	—	5.1	1.0	11.1	7.5	83.8	42.5	36.5	1.03
+10% DPIX	—	—	4.5	0.67	3.5	3.7	92.0	44.5	41.1	1.01
+12% DPIX	—	—	3.3	0.54	2.5	3.5	94.2	44.5	42.0	1.00

Characterization and photoluminescence of CA- and ALE-NPs and chlorin e6 conjugates

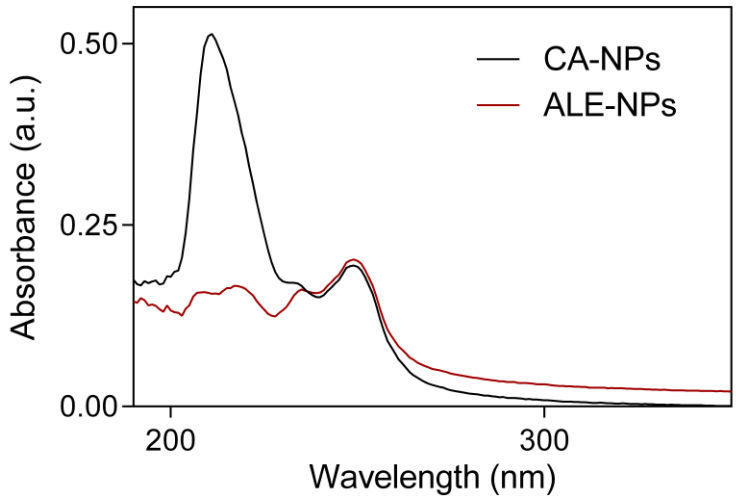

Figure C4 Absorbance spectra for $Ce_{0.1}La_{0.9}F_3/LaF_3$ NPs synthesized with citrate ligands (CA-NPs) and after ligand exchange with alendronate (ALE-NPs).

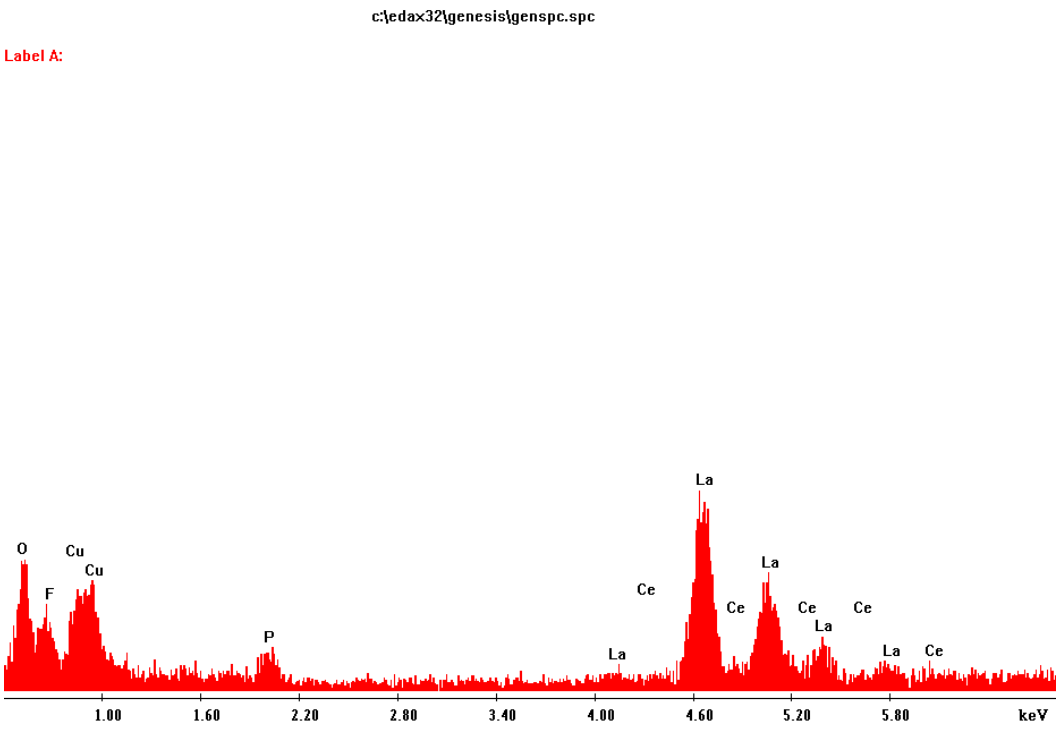

Figure C5 EDX spectrum of alendronate-stabilized $Ce_{0.1}La_{0.9}F_3/LaF_3$ NPs, displaying peaks for La, Ce, F and P.

Table C4 Center positions of Gaussian fits of PL emission spectra of $Ce_{0.1}La_{0.9}F_3/LaF_3$ NPs shown in Figure 5.7a & b.

NP ligand	μ_1 (eV)	μ_2 (eV)	μ_3 (eV)	μ_4 (eV)	R^2
Citrate	4.31	4.06	3.96	3.27	0.99
Alendronate	4.25	4.07	3.89	3.59	1.0

Quantifying Ce6 conjugation

The mass concentration of the conjugate stock was determined using rotary evaporation to be ~13.3 mg/mL. The absorbance of a 10X dilution in water was measured (shown in Figure 5.8).

Determining Ce6 concentration in conjugate samples

A standard absorbance curve was established for free Ce6 in acidic buffer. A stock solution was made by dissolving Ce6 at 1 mg/mL in DMSO, then diluted to 10 µg/mL in 1X PBS pH ~3, which was used for further dilutions to 1.7-6.7 µg/mL:

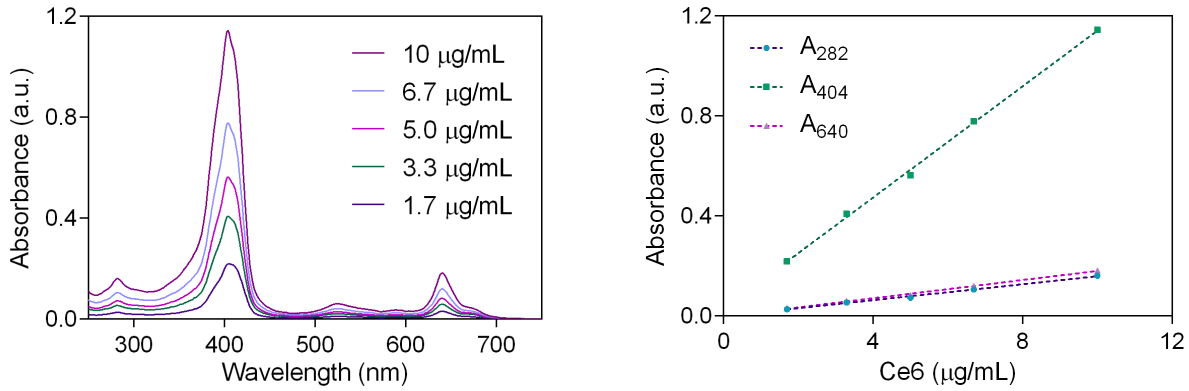

Figure C6 Absorbance spectra for Ce6 in PBS, and linear fits to Soret band and Q band values.

The fits ($R^2 = 0.99$) gave the following extinction coefficients:

$$\varepsilon_{282} = 0.016\ (\mu g/mL)^{-1}cm^{-1} = 9{,}549\ M^{-1}cm^{-1}$$

$$\varepsilon_{404} = 0.111\ (\mu g/mL)^{-1}cm^{-1} = 66{,}390\ M^{-1}cm^{-1}$$

$$\varepsilon_{640} = 0.018\ (\mu g/mL)^{-1}cm^{-1} = 10{,}890\ M^{-1}cm^{-1}$$

Using the conj. absorbance,

$$C_{Ce6} = 10*(A_{640}/\varepsilon_{640}) = 10*(0.104/0.018\ (\mu g/mL)^{-1}cm^{-1}) = 58\ \mu g/mL$$

Thus, Ce6 accounts for a small fraction of the total conjugate mass: (58/13300)*100 = 0.44%.

The molar concentration can also be determined:

$$C_{Ce6} = 10*(A_{640}/\varepsilon_{640}) = 10*(0.104/10{,}890\ M^{-1}cm^{-1}) = 96\ \mu M$$

Determining molar NP concentration in conjugate samples

The $Ce_{0.1}La_{0.9}F_3/LaF_3$ NPs are taken to be roughly spherical with a 4 nm diameter.

$$\rho_{NP} = (0.95)(5.94\ g/cm^3) + (0.05)(6.16\ g/cm^3) = 5.95\ g/cm^3 = 5.95 \times 10^{-21}\ g/nm^3$$

$$V_{NP} = (4/3)\pi r^3 = (4/3)\pi(2\ nm)^3 = 33.5\ nm^3$$

$$m_{NP} = \rho_{NP}V_{NP} = 2 \times 10^{-19}\ g/NP = \sim 120\ kDa$$

Using the mass concentration determined from rotary evaporation without discounting ligand mass gives:

$$C_{Conj} = 13.3\ mg/mL = 6.65 \times 10^{16}\ NPs/mL = 110\ \mu M$$

Using this value gives 0.87 Ce6 molecules/NP. Accounting for the ligand mass contribution would result in a lower true NP molarity, giving closer to or possibly exceeding 1 Ce6 molecule/NP.

Discussion and conclusions

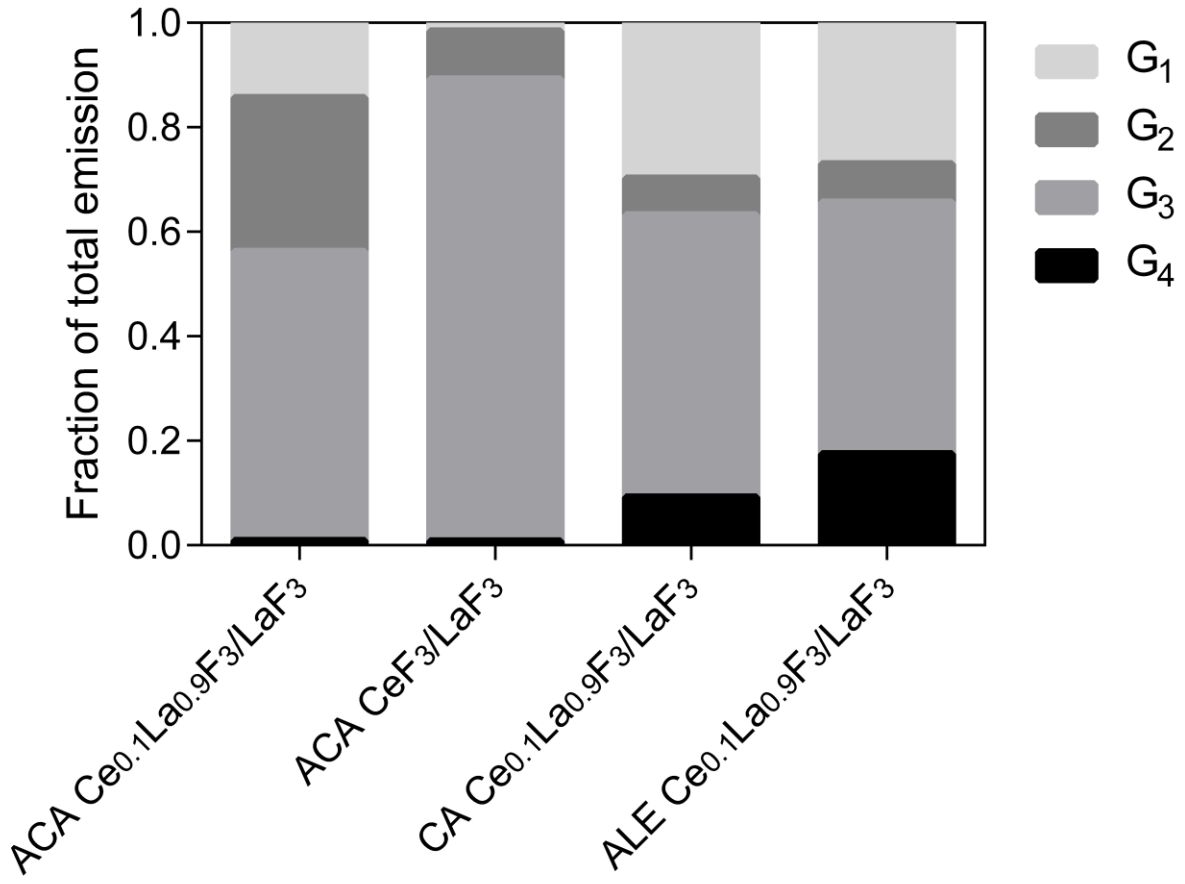

Figure C7 The contribution of different Ce^{3+} emission components depends on Ce^{3+} concentration, physical dimensions of NPs and surface coatings. Perturbed site component G_3 dominates for ACA CeF_3/LaF_3 NPs. For CA- and ALE-NPs, the G_1:G_2 ratio is dramatically altered compared to ACA-NPs, with a more prominent G_4 component representing surface sites.